Study of Thermal Oxidation of SiGe for Advanced CMOS FD-SOI Technologies

Fabien Rozé

To cite this version:

Fabien Rozé. Study of Thermal Oxidation of SiGe for Advanced CMOS FD-SOI Technologies. Electric power. Université Grenoble Alpes, 2018. English. NNT : 2018GREAI018 . tel-01809031

HAL Id: tel-01809031
https://theses.hal.science/tel-01809031
Submitted on 6 Jun 2018

HAL is a multi-disciplinary open access archive for the deposit and dissemination of scientific research documents, whether they are published or not. The documents may come from teaching and research institutions in France or abroad, or from public or private research centers.

L'archive ouverte pluridisciplinaire **HAL**, est destinée au dépôt et à la diffusion de documents scientifiques de niveau recherche, publiés ou non, émanant des établissements d'enseignement et de recherche français ou étrangers, des laboratoires publics ou privés.

Communauté
UNIVERSITÉ Grenoble Alpes

THÈSE

Pour obtenir le grade de

DOCTEUR DE LA COMMUNAUTE UNIVERSITE GRENOBLE ALPES

Spécialité : **2MGE : Matériaux, Mécanique, Génie civil, Electrochimie**

Arrêté ministériel : 25 mai 2016

Présentée par

Fabien ROZÉ

Thèse dirigée par **Elisabeth BLANQUET, Directrice de recherche, CNRS,** encadrée par **Olivier Gourhant** et co-encadrée **par François Bertin**

préparée au sein du **Laboratoire Science et Ingénierie des Matériaux et Procédés**, de **STMicroelectronics (Crolles)** et du **CEA-LETI**

dans **l'École Doctorale I-MEP2 – Ingénierie – Matériaux, Mécanique Environnement, Energétique, Procédés, Production**

Study of Thermal Oxidation of SiGe for Advanced CMOS FD-SOI Technologies

Etude de l'oxydation thermique du SiGe pour application aux technologies CMOS FD-SOI avancées

Thèse soutenue publiquement le **08/03/2018**,
devant le jury composé de :

Dr., Alain, CLAVERIE
Directeur de recherche, CEMES - CNRS, Rapporteur
Pr., Pierre, MÜLLER
Professeur, CINaM - CNRS, Rapporteur
Pr., Wilfried, VANDERVORST
Professeur, IMEC, Président
Dr., François, BERTIN
HDR, CEA-LETI, Co-encadrant
Dr., Elisabeth, BLANQUET
Directrice de recherche, SIMaP – CNRS, Directrice de thèse
Dr., Olivier, GOURHANT
PhD, Ingénieur STMicroelectronics, Encadrant

A Solène, Florian et mes parents.

Remerciements

Ce travail de thèse n'aurait pu aboutir sans l'aide et le soutien de nombreuses personnes, à commencer par mes encadrants. Un immense merci à Olivier pour m'avoir accordé sa confiance, pour sa disponibilité (en particulier pour les nombreuses relectures approfondies en cette fin de thèse), et ses encouragements dans les moments les plus délicats. J'ai particulièrement apprécié le subtil équilibre entre autonomie et encadrement que tu as imprimé dès le début de cette thèse. J'ai beaucoup appris grâce à toi sur la conduite d'un travail scientifique, et plus généralement même sur la construction d'un projet quel qu'il soit, ainsi que sur les aspects humains du travail en équipe. Cette expérience et ces compétences me seront très utiles pour la suite de ma carrière, et pour tout cela merci encore ! Je tiens à remercier Elisabeth pour sa grande disponibilité et le soutien dont tu as fait preuve chaque fois que j'en ai eu besoin. Ton soutien tout au long de cette thèse m'a vraiment permis de prendre du recul et de voir plus large que mon travail au sein de l'entreprise, de comprendre les enjeux de la thèse, et d'éviter de nombreux écueils (enfin pas tous sinon ce n'est pas drôle !). Et enfin, merci à François, qui a toujours su apporter un éclairage critique très constructif et des solutions à de nombreuses questions et problématiques rencontrées pendant cette thèse. J'ai trouvé nos discussions, scientifiques et plus générales, très enrichissantes.

Je remercie vivement tous les membres du jury. Pierre Müller et Alain Claverie pour avoir accepté d'être rapporteurs de mon travail de thèse, et merci également à Wilfried Vandervorst d'avoir présidé ce jury.

Je tiens aussi à remercier les nombreuses personnes avec qui j'ai eu la chance de travailler. Et notamment les thésards : Laurent Fauquier (je te souhaite une bonne continuation dans ta nouvelle carrière !), Aurèle Durand, Rémy Berthelon (mention spéciale au succès du LOCOS, une intégration restée … incomprise et non répétable. Un véritable one shot !), et Aurore Durel (anciennement Bonneviale, Félicitations !). Et bon courage à Damien !

Je remercie tous les collègues de l'équipe TT épi HK, tout particulièrement pour votre accueil et l'excellente ambiance de l'équipe : Rémi, Nathalie, Patrick, Clément, Bilel, Didier, Mickael, Denis, Elodie, Fabien, David, Julien, Kristell, Maud, Lucie, Franck, Yves, et Pierre (merci pour les discussions très enrichissantes et ton aide pour les simulations). Je n'aurais pas pu réaliser cette thèse sans l'aide de Karen, Laurent, Marc, Véronique, Francesco, Delphine Doloy et Delphine Le Cunff. Merci à vous. J'ai aussi beaucoup apprécié la bonne humeur des collègues de wet, Clément, Yann, Stéphane, Emilie, Thomas…

Mention spéciale à l'équipe 3D. Si nous n'avons pas travaillé ensemble, j'ai par contre eu le plus grand plaisir à venir prendre le café et manger de délicieux gâteaux (j'ai fini par amener ce fameux kouign amann tant de fois promis !) avec vous. Sans oublier l'escape game et les tontons (et son célèbre et si léger vacherin) !

Je dois aussi beaucoup aux personnes avec qui j'ai travaillé au LETI, notamment François Pierre, Denis Rouchon et Denis Jalabert (INAC je précise, je ne souhaite pas créer de problèmes !). Merci à vous également pour ces très sympathiques pauses café et l'enthousiasme communicatif dont vous faites preuve ! Merci aussi à Yves Morand, Cyrille Le Royer, Sylvie Favier, Nicolas Bernier, Eugénie Martinez, François Andrieu, Jean-Marc Fabbri. Et un grand merci à Patrice Gergaud pour ces jolies manips, en particulier celles à Soleil. J'ai beaucoup appris en travaillant avec toi. Merci à Patricia Donnadieu du SIMaP pour sa disponibilité et sa pédagogie pour la TEM GPA et à Michel Pons pour ses bonnes remarques sur l'oxydation. Je remercie aussi Nicolas Jaouen du synchrotron Soleil et l'équipe de l'ILL pour ces jolies manips !

Je tiens aussi à saluer tous les thésards du week-end ski, notamment Matthieu et Edouard (La figure de style ayant conduit à la transformation d'un de mes skis en deux petits skis était bien évidemment prévue) pour ces chouettes moments !

AFCGI에 감사드립니다 한국어를 배울 수 있었어요. 민영 선생님 고맙습니다! 민영 씨는 아주 착해요! 받아쓰기를 못 해서 미안해요. 민영 씨와Joël 씨 가 저를 집에 초대해줘서 고마웠어요. 마싰었어요 ! 마지막으로, 다른 학생들 고마워요! 한국어를 계속 공부할 거예요!

Un grand merci à l'équipe des séjours moto et en particulier aux organisateurs, Pierre (malgré l'agression de marmottes), Pascal (malgré le bruit et les odeurs de ton tromblon anglais), ainsi qu'à Yann pour les supers films souvenirs. Tout était réuni pour une joyeuse virée en moto, de beaux virages, de beaux paysages, un parcours prédéfini mais purement indicatif, de la mauvaise foi (« t'attaquais toi ? Moi j'attaquais pas »), de l'égo (« t'as vu l'exter que je lui ai fait ? »), une attaque de moutons et du spritz.

La triste fin de la colocation n'efface pas les bons moments passés avec Thomas et Cécile, depuis les vacances au Japon en passant par les nombreuses sorties dans Grenoble et l'ambiance unique du début de la colocation. Merci aux copains bretons des environs de Grenoble, à commencer par l'unique Antoine Le Du, alias « Duch », un « coloc du week-end », pour toutes les belles sorties skis (malgré des conditions parfois peu… propices), VTT, les chouettes soirées sur Grenoble et Lyon (je regrette de n'être jamais passé à Vichy City, un jour peut-être !), et les bons cadeaux tels que des balances de 60 kg. Et je n'oublie pas Eva, alias « Jean-Va », Cécile, alias « Jean-Cile ». Bonjour à Claire et Pascal, en particulier pour le bel accueil sur Bordeaux, et un coucou à Walid, la gentillesse incarnée.

Merci à Leila (mon épaule tient personnellement à te remercier !) et à Amandine. Bonne continuation à vous deux ! Coucou aux fameux bretons que sont Maxime, alias « Maxwell », et l'infatigable et intemporelle Soléna, alias « So », alias « Denver ».

J'ai aussi partagé plein de bons moments avec tous mes colocs au cours de ces trois ans : Graf, Pauline, Romain, Carole, Yasser, Sophie et Philip, merci à vous !

J'aimerais faire deux mentions spéciales. La première à Claire pour cette improbable semaine à Hawaii passée en ta compagnie (un an et demi après, je n'ai toujours pas compris… Je pense qu'on pourrait en faire un sujet de thèse). Autre mention spéciale : le courtepaille de Saint-Aubin pour son soutien moral !

Allez, citons aussi quelques super copines de Paris Bourg et de Rennes City: ma super copine Florent, alias « Le Belge », alias « Gros Flo », un personnage fort heureusement unique (mais parce que je serais jaloux qu'il y en ait un autre que je ne connais pas !), Maud, Anne-Sophie, alias « Anne-So », François, alias « François l'enfant », alias … non je ne peux pas l'écrire même dans des remerciements, Pierre Mores, et tous les autres.

Un grand merci à toute la joyeuse bande des Mathias, Margot, Maxence, Hugo, Amélie, Maël, etc… pour votre chaleureux accueil, ces chouettes soirées, sorties rafting et ces vacances passées à Uzès et à Nîmes !

Merci à toute l'équipe des trips à vélo, Etienne, Julie, Nico, Médéric, Martin et Xavier pour ces bons moments passés sur les pistes cyclables de la via rhona et de la vélodyssée et pour toutes les sorties à Grenoble et alentours. Ces deux voyages ont laissés de beaux souvenirs, tels qu'un orage mémorable à Avignon, un passage d'un bras du Rhône en conditions un brin humides ou encore un bout de parcours de 30 kilomètres retrouvé bien tardivement!

Passons à tous les copines et copains de ST et « affiliés » (faute d'un meilleur terme). Vous vous en doutez, mes remerciements sont susceptibles de contenir des propos pouvant être considérés comme des attaques (mais à prendre avec humour hein). Vous êtes prévenus, je commence.

Merci à Victorien, mon « bro » de Hawaii, pour ces sorties plages ~~pendant~~ après la conférence et nos longues interrogations sur le mode de vie de l'américain moyen. Félicitations aussi à Evan, lozérien en situation d'asile politique, un camarade de thèse à l'enthousiasme si communicatif en cette période de rédaction. Un merci aussi à Marie, Mathilde (et mention spéciale au fameux papa Noël à Marseille), Léo, Marine et Shayma pour tous ces bons moments ! Antoine, alias « Corneloutre », et Joris, qui ne sont jamais loin pour boire un coup, et qui vont souvent plus loin que tout le monde quand il s'agit d'en boire plusieurs ! Kévin, alias « Kiki », passe de 0 à 2 pintes plus vite qu'une tireuse de bar et d'une coupe de cheveux à une autre en moins de temps qu'un footballeur (mais heureusement pas les mêmes coupes). Bonne chance à Yann dans sa nouvelle carrière à Singapour ! Sois prudent, il n'est pas impossible que passer du Katy Perry dans un espace public à Singapour soit passible d'une condamnation. Un autre Kévin, alias « Kéké », goûteur émérite d'un célèbre gâteau improvisé, qui aime le bambou (et ça c'est important) et le ski sans trop se poser de questions (le bleu et le noir se confondent facilement sur une carte après tout). Félicitations à Herr Doktor Etienne, spécialiste du napalm verbal et un bon camarade de débat politique (même si tu as tort, mais personne n'est parfait).

Merci à Adeline, alias « Crystal », humour en-dessous de la ceinture garanti, thésarde aux épaules solides malgré les agressions physiques à base de lancer de sachets de sucre (c'est parce que tu me faisais peur quand tu passais la tête au-dessus de la cloison !) et psychologiques à base d'humour de Charly. Franck, alias « Francky », globe-trotter, magicien capable de se fondre dans un coucher de soleil, expert en tabourets, en guitares plutôt sexy, et passager serein d'une bicyclette en aussi bon état qu'une certaine fiat punto. Merci à un autre Franck, Anastomose de son nom, pour ses intrusions étonnantes dans nos conversations, à Julien Ferrand et Fabien Deprat pour la chouette ambiance! Marc, alias « Marcounet », alias « Zac Efron », docteur es science en fourberie, binôme assidu des sorties skis avec le CE et des « c'est la sous-couche » de Novembre (oui j'ai vu que tu avais des nouveaux skis), un très chouette camarade malgré ses faux diplômes et ses origines belges. Merci aussi à Carine pour sa bonne humeur immortelle ! Guillaume, alias « Guigui », alias « Courgoulette », mon maître jedi des sports de montagne, en commençant par les rando, et en passant par le ski hors-piste et surtout le VTT (mention spéciale pour les chouettes descentes en Italie ! Tu verras, un jour j'aurai un tout-suspendu mieux monté que le tien !). Un clin d'œil à Laure, éternelle adolescente et scénariste hollywoodienne inégalée, et ce malgré les corrections injustifiées et intempestives de mon phrasé old school et fleuri (j'espère pour toi que « bicyclette » et « cellulaire » ne reviendront jamais à la mode), et tes goûts musicaux douteux (non non je n'ai rien dit sur JJG, j'ai parlé d'attaque, pas de suicide).

Un grand merci à Charly, alias « Chaton », alias *****, le moine zen de l'équipe et co-organisateur émérite de fameux évènements culturels grenoblois. Un camarade de bureau au top doublé d'un ami qui l'est tout autant. Prix nobel des jeux de mots que l'on pourrait qualifier de « coup du lapin accidentel provoqué sur autrui » et expert en arches et colonnes antiques et pharmacopée grecque depuis une fameuse conférence.

Malgré l'éloignement géographique, j'ai toujours pu compter sur la communauté bretonne de Madame Loïc pour son soutien! Un long discours serait bien superflu, car vous n'ignorez pas à quel point vous comptez pour moi, alors je vous dis simplement merci. Merci à Julien, alias « Le Blond », à Maureen, alias « Momo », à Marion, la dernière admise au sein de la communauté, alias « Vava » (je veux bien admettre une part de responsabilité pour les porte-couteaux teckels, mais encore une fois, je n'ai rien à voir avec cette sombre histoire de bidet), à Pauline, alias « Paulo », à Julien, alias « Le Gros », et enfin à Alexandre, alias « Pedro », et en particulier pour son soutien inébranlable pendant une année 2017 mouvementée.

J'en viens maintenant à deux personnes très chères à mes yeux et qui ont su être là lors de mes premiers pas en thèse à Grenoble. Le premier fût Grenoblois mais ne l'est plus pour les plus belles raisons possibles, Romain, un « coloc » de quelques semaines devenu mon premier copain Grenoblois, et surtout l'un des meilleurs toutes villes confondues. Apôtre de la gentillesse au naturel, ta capacité à voir le bien en chacun n'a d'égale que celle de nous le montrer et de nous en convaincre. Félicitations à Héloïse et toi pour l'adorable Rebecca ! J'aurai toujours grand plaisir à venir vous voir tous les trois (peut-être plus un jour !) à Agen ou ailleurs !

La deuxième, Marion, alias « MLM » (je me suis retenu de l'écrire en toutes lettres), est une véritable grenobloise dotée d'un cœur immense et douée d'une empathie sincère et juste dont j'ai si souvent profité. Merci pour tous ces bons moments passés à Grenoble, nos longues conversations philosophiques, politiques, etc… sur le balcon, les sorties skis, et pour ce splendide voyage improvisé au Japon (Et félicitations pour la prononciation de « merci » en Japonais et pour la récupération d'un vélo (enfin) en état de marche) ! Du début à la fin de cette thèse, tu as toujours été là pour me soutenir, et je ne le dis que trop rarement (mais ça tu le sais déjà !), alors je l'écris : merci !

Et enfin, je tiens à remercier ceux qui m'ont donné la chance immense d'en arriver jusqu'ici, ceux dont le soutien m'a toujours permis d'aller chercher le meilleur de moi-même, dans les bons moments comme dans les mauvais, ceux dont je suis si fier, Florian, Solène et mes parents.

Allez, soufflez un bon coup, vous pouvez remiser ce manuscrit au grenier sans vous sentir coupable !

Table of Contents

List of Acronyms 17

Introduction 21

Chapter I - The Condensation Technique for Advanced CMOS FD-SOI Technologies 25

Introduction to Chapter I 26

I.1. Present and Future of the CMOS Technology 27

I.1.1. The Metal Oxide Semiconductor Field Effect Transistor (MOSFET) 27

I.1.1.1. History of the MOSFET 27

I.1.1.2. MOSFET Working Principles 27

I.1.1.3. Circuit Performance Enhancement 30

I.1.1.4. The Semiconductor Industry 30

I.1.1.5. MOSFET Scaling Issues 31

I.1.2. New MOSFET Architectures 32

I.1.2.1. Bulk, FD-SOI and FinFET MOSFET Architectures 32

I.1.2.2. FD-SOI Technology Nodes 33

I.1.3. High Mobility Channels 34

I.1.3.1. Mobility Definition 34

I.1.3.2. Mobility Engineering for ON Current Enhancement 35

I.1.3.3. Channel Materials 36

I.1.3.4. Crystal Orientations 37

I.1.3.5. Strained Channels 37

I.1.4. Target Application of this Thesis Work 38

I.1.5. Paths for Integration of Compressively Strained SGOI Films as pMOS Channels 39

I.2. Properties of SiGe 39

I.2.1. Materials Properties 39

I.2.1.1. Crystal Structure 39

I.2.1.2. Phase Diagram 40

I.2.1.3. Band Diagrams 40

I.2.2. Strain and Stress 41

I.2.2.1. Definition of Strain and Stress 41

I.2.2.2. Amorphous SiO_2 42

I.2.2.3. Strain of Pseudomorphic SiGe Films on Si 42

I.2.2.4. Strain-Altered Mobility of SiGe 44

I.2.3. Epitaxy of SiGe on Si 44

I.2.4. Plastic Strain Relaxation in Compressively Strained SiGe Films 46

I.2.4.1. Introduction 46

I.2.4.2. The Equilibrium and Kinetics Models 46

I.2.4.3. Mechanisms of Plastic Strain Relaxation in Compressively Strained SiGe Films 47

I.2.4.4. Crystal Defects in SiGe Films 48

I.2.5. SiGe Interdiffusion 49

I.2.5.1. Introduction and Continuum Theory of Diffusion 49

I.2.5.2. Atomic-Scale Diffusion Mechanisms ... 50
I.2.5.3. Interdiffusion in SiGe ... 50

I.3. Properties of Thermal Oxides Grown on Si and SiGe ... 51
I.3.1. Bulk Thermal SiO_2 ... 51
I.3.2. Si-Thermal SiO_2 Interface ... 52

I.4. The Condensation Technique ... 52
I.4.1. Introduction and History of the Condensation Technique ... 52
I.4.2. FD-SOI Process Flow Integration ... 52

I.5. Problematics of this Thesis Work ... 53
I.5.1. SiGe Thermal Oxidation ... 53
I.5.1.1. Study of Mechanisms and Kinetics of SiGe Thermal Oxidation ... 54
I.5.1.2. Application to Industrial Processes for Advanced FD-SOI CMOS Manufacturing ... 54
I.5.2. Strain and Crystal Quality of SGOI Films Fabricated by Condensation ... 54
I.5.2.1. Strain and Crystal Quality of Full-Sheet SGOI Layers Fabricated by Condensation ... 54
I.5.2.2. Conservation of Strain of SGOI Films during Co-integration of n-MOS and p-MOS Transistors ... 54

Conclusion of Chapter I ... 56

Chapter II - SiGe Thermal Oxidation Processes, Characterization Techniques and Simulation Method ... 59

Introduction to Chapter II ... 60

II.1. SiGe Epitaxy Processes ... 61

II.2. Thermal Oxidation Processes ... 61
II.2.1. Introduction ... 61
II.2.2. Dry Furnace Oxidation ... 62
II.2.3. Rapid Thermal Oxidation (RTO) ... 63
II.2.3.1. Dry Rapid Thermal Oxidation (RTO) ... 63
II.2.3.2. In-Situ Steam Generation (ISSG) Oxidation ... 64

II.3. Characterization Techniques ... 65
II.3.1. Spectroscopic Ellipsometry ... 65
II.3.2. X-Ray Reflectivity (XRR) ... 66
II.3.3. X-Ray Photoelectron Spectroscopy (XPS) ... 66
II.3.4. Raman Spectroscopy ... 68
II.3.5. Geometric Phase Analysis (GPA) of HRTEM Images ... 69

II.4. Characterization Techniques using Large-Scale Facilities ... 72
II.4.1. Resonant Soft X-Ray Reflectivity (R-SoXR) ... 72
II.4.1.1. Introduction ... 72
II.4.1.2. Interaction of X-Rays with Matter in Reflectivity Experiments ... 72
II.4.1.3. X-Ray Reflection by Planar Multilayers ... 73
II.4.1.4. Resonant Soft X-Ray Reflectivity (R-SoXR) ... 74
II.4.1.5. Experimental ... 74
II.4.1.6. Fitting Procedure ... 75
II.4.2. Neutron Reflectivity ... 75

II.4.2.1. Introduction ... *75*
II.4.2.2. Interaction of Neutrons with Matter in Reflectivity Experiments ... *75*
II.4.2.3. Experimental ... *76*
II.4.3. Medium Energy Ion Scattering (MEIS) ... 76
II.4.3.1. Introduction ... *76*
II.4.3.2. Electronic Energy Loss of Medium Energy Ions in Solids ... *77*
II.4.3.3. Elastic Nuclear Collision of Medium Energy Ions with Nuclei in Solids ... *78*
II.4.3.4. Channeling ... *79*
II.4.3.5. Experimental ... *79*
II.4.3.6. Simulation of MEIS Spectra ... *79*

II.5. Simulations by the Finite Element Method (FEM) ... 80
II.5.1. Introduction to the Finite Element Method (FEM) ... 80
II.5.2. Simulation of SiGe Oxidation ... 80

Conclusion of Chapter II ... 82

Chapter III - SiGe Thermal Oxidation ... 85

Introduction to Chapter III ... 86

III.A. Study of Mechanisms and Kinetics of SiGe Thermal Oxidation ... 87

III.A.1. Literature Review ... 87
III.A.1.1. Introduction ... 87
III.A.1.2. Thermodynamic Considerations ... 87
III.A.1.3. Kinetics of Oxidation of Si and SiGe ... 88
III.A.1.3.1. The Deal and Grove Model for Oxidation of Si ... *88*
III.A.1.3.2. Revised Models of Oxidation of Si ... *90*
III.A.1.3.3. Kinetics of SiGe Oxidation ... *91*
III.A.1.4. Conclusion of Section III.A.1. ... 92

III.A.2. Experimental ... 93
III.A.2.1. Oxidation Processes and Characterization Techniques ... 93
III.A.2.2. Characterization of Strain Conservation During Oxidation ... 94
III.A.2.3. Control of Within Wafer Uniformity of the Oxide Thickness ... 94

III.A.3. Characterization of Oxide Composition by X-Ray Photoelectron Spectroscopy (XPS) ... 95
III.A.3.1. Introduction ... 95
III.A.3.2. Ge Oxide Formation During Dry RTO of SiGe ... 95
III.A.3.2.1. Depth Distribution of Ge Oxide Measured by pAR-XPS ... *95*
III.A.3.2.2. Determination of the Oxidation State of Ge Oxide ... *96*
III.A.3.2.3. Ge Oxide Formation during the full Oxidation Sequence ... *96*
III.A.3.2.4. Influence of Initial Ge Concentration and Oxidation Temperature on Ge Oxide Formation ... *97*
III.A.3.2.5. Discussion about Ge Oxide Formation During Dry RTO of SiGe ... *99*
III.A.3.3. Ge Oxide Formation During Dry Furnace Oxidation and ISSG Oxidation of SiGe ... 100
III.A.3.4. Conclusion of Section III.A.3. ... 101

III.A.4. SiGe Oxidation Kinetics and SiGe Composition Evolution ... 102

III.A.4.1. Oxidation Kinetics Results 102
III.A.4.1.1. Results 102
III.A.4.1.2. Discussion about Temperature Calibration 104
III.A.4.1.3. Kinetics of Dry Oxidation of Si 105
III.A.4.1.4. Activation Energies of Oxidation of SiGe 105
III.A.4.2. Growth Rate Enhancement (GRE) 106
III.A.4.2.1. Analysis Methodology of Oxidation Kinetics Results 106
III.A.4.2.2. GRE Dependence on the Initial Ge Concentration 107
III.A.4.3. Evolution of the Ge Concentration at the Oxidation Interface 108
III.A.4.4. GRE Dependence on the Ge Concentration at the Oxidation Interface 110
III.A.4.5. Conclusion of Section III.A.4. 111
III.A.5. Correlation Between SiGe Oxidation Kinetics and Oxide Density 111
III.A.5.1. Measurement of the Oxide Density by X-Ray Reflectivity (XRR) 112
III.A.5.1.1. Methodology for Extraction of Scattering Factors from Absorption Spectra 112
III.A.5.1.2. O Scattering Factors around the K Absorption Edge 112
III.A.5.1.3. Methodology for Measurement of the Oxide Density by Fitting XRR spectra 115
III.A.5.1.4. Density of Thermal Oxides on SiGe 115
III.A.5.2. Dependence of the Oxide Density on Process Parameters 117
III.A.5.3. Dependence of Oxidation Kinetics on the Oxide Density 118
III.A.5.4. Discussion about O_2 Diffusion in SiO_2 119
III.A.5.5. Conclusion of Section III.A.5. 120
III.A.6. Conclusion of Section III.A. 121
III.B. Application to Industrial Processes for Advanced FD-SOI CMOS Manufacturing 122
III.B.1. Condensation Abacus: Oxide thickness and Ge Diffusion Length 122
III.B.2. Simulation of SiGe Thermal Oxidation 125
III.B.2.1. Introduction 125
III.B.2.2. Simulation Models 125
III.B.2.3. Kinetics of Dry RTO and ISSG Oxidation of SiGe 126
III.B.2.4. Evolution of the SiGe Composition Profile 128
III.B.2.5. Evolution of the Ge Concentration at the Interface 129
III.B.2.6. Conclusion of Section III.B.2. 133
Conclusion of Chapter III 134
Chapter IV - Strain and Crystal Quality of SGOI Films Fabricated by the Condensation Technique 137
Introduction to Chapter IV 138
IV.A. Strain and Crystal Quality of Full Sheet SGOI Films Fabricated by the Condensation Technique 139
IV.A.1. Principles of the Condensation Technique 139
IV.A.2. Experimental 140

IV.A.2.1. SiGe Epitaxy and Condensation Process 140

IV.A.2.2. Characterization of SGOI Films 143

IV.A.3. Ge Conservation during Condensation 143

IV.A.4. Strain and Crystal Defects of SGOI Layers 144

IV.A.4.1. Strain of SGOI Films Fabricated by High Temperature Condensation 144

IV.A.4.1.1. Strain Evolution as a function of the Ge Concentration for Dry RTO 144

IV.A.4.1.2. Comparison between Dry RTO and ISSG Oxidation 148

IV.A.4.1.3. Comparison with Literature 149

IV.A.4.1.4. Comparison with SiGe Equilibrium Models 150

IV.A.4.1.5. Discussion about the Influence of the SGOI Thickness on Strain 150

IV.A.4.1.6. Conclusion about Strain of SGOI Films Fabricated by High Temperature Condensation 151

IV.A.4.2. Strain of SGOI Films Fabricated by Low Temperature Condensation 152

IV.A.4.3. Extended Defects Revelation 153

IV.A.4.4. Conclusion of Section IV.A.4. 156

IV.A.5. Characterization of SGOI Composition and Crystal Quality by MEIS 156

IV.A.5.1. Experimental 157

IV.A.5.1.1. Studied Samples and Experimental Configurations 157

IV.A.5.1.2. Identification of Peaks on MEIS Spectra 157

IV.A.5.1.3. Experimental 2D MEIS Maps 158

IV.A.5.2. Experimental and Simulated Spectra 159

IV.A.5.3. Chemical Composition Analysis 160

IV.A.5.4. Crystal Quality Analysis 162

IV.A.5.4.1. Introduction and χ_{min} *Definition 162*

IV.A.5.4.2. Channeling Angle and Angular Tolerance 162

IV.A.5.4.3. The Shadowing Effect and the Surface Peak 163

IV.A.5.4.4. Crystal Quality of SGOI Films 163

IV.A.5.5. Conclusion of Section IV.A.5. 165

IV.A.6. Conclusion of Section IV.A. 167

IV.B. Strain Relaxation at the Edge of Active Areas 168

IV.B.1. Problem Definition 168

IV.B.2. Chemical Bonding at the SGOI-BOx interface Investigated by XPS 169

IV.B.2.1. Introduction 169

IV.B.2.2. Experimental 169

IV.B.2.3. Ge-O Bonding 170

IV.B.2.4. Si-O Bonding 171

IV.B.2.5. Conclusion of Section IV.B.2. 172

IV.B.3. Measurement of Hydrogen Concentration by Neutron Reflectivity Coupled with XRR 173

IV.B.3.1. Introduction 173

IV.B.3.2. Experimental 173

IV.B.3.3. Results 174

IV.B.3.4. Conclusion of Section IV.B.3. 178

Conclusion of Chapter IV 179

Conclusion 181

Bibliography 185

Appendices 195
A - Strain and Stress 195
B - Secondary Ion Mass Spectroscopy (SIMS) 197
C - Wavelength Dispersive X-Ray Fluorescence (WDXRF) 197
D - X-Ray Diffraction (XRD) 198
E - Atomic Force Microscopy (AFM) 199
F - Transmission Electron Microscopy (TEM) 200

Résumé en français 203

Bibliography of the author 229

List of Acronyms

AmALEN	Amorphous Atomic Layer Equivalent Number
AFM	Atomic Force Microscopy
BOx	Buried Oxide
cfc	cubic-face-centered
CMOS	Complementary Metal Oxide Semiconductor
DIBL	Drain-Induced Barrier Lowering
EDX	Energy Dispersive X-Ray Spectroscopy
EELS	Electron Energy Loss Spectroscopy
FD-SOI	Fully Depleted Silicon-On-Insulator
FEM	Finite Element Method
FET	Field Effect Transistor
FFT	Fast Fourier Transform
GeOI	Germanium-On-Insulator
GPA	Geometric Phase Analysis
GRE	Growth Rate Enhancement
HRTEM	High-Resolution Transmission Electron Microscopy
IC	Integrated Circuit
IoT	Internet of Things
ISSG	In-Situ Steam Generation
MEIS	Medium Energy Ion Spectroscopy
MOSFET	Metal Oxide Semiconductor Field Effect Transistor
pAR-XPS	parallel Angle-Resolved X-Ray Photoelectron Spectroscopy
PED	Precession Electron Diffraction
RBS	Rutherford Backscattering Spectroscopy
RCS	Remote Coulomb Scattering
RMS	Root Mean Squared
RPS	Remote Phonon Scattering
R-SoXR	Resonant Soft X-Ray Reflectivity
RTCVD	Rapid Thermal Chemical Vapor Deposition
RTO	Rapid Thermal Oxidation

SCE	Short-Channel Effects
SE	Spectroscopic Ellipsometry
SGOI	Silicon-Germanium-On-Insulator
SIMS	Secondary Ion Mass Spectroscopy
SOI	Silicon-On-Insulator
STI	Shallow Trench Isolation
SWE	Single Wavelength Ellipsometry
TEM	Transmission Electron Microscopy
T.E.Y.	Total Electron Yield
T.F.Y.	Total Fluorescence Yield
WDXRF	Wavelength Dispersive X-Ray Fluorescence
XPS	X-Ray Photoelectron Spectroscopy
XRD	X-Ray Diffraction
XRF	X-Ray Fluorescence
XRR	X-Ray Reflectivity

Introduction

It is somewhat intriguing that the frantic computerization of our modern world mostly relies on a minute element often compared to a faucet that is either completely open and carries the binary number "1" or completely shut and carries the binary number "0". This minute element is called a transistor and is merely a tiny electrical switch made of silicon, the most abundant element of the earth crust. Since the first Intel microprocessor in 1971, transistors have moved from gigantic computers to PCs, to laptops, to smartphones and finally to any object that may interact with any object or human being – from a watch or a fridge to traffic regulation systems – , the so-called Internet of Things (IoT). This tremendous spread of electronic devices and networks into our day-to-day life has been enabled by Moore's law, a self-fulfilling prophecy of the semiconductor industry that Gordon Moore stated in 1965. According to this law, the number of transistors crammed into a chip would double every two years.

As long as Moore's law was obeyed, the semiconductor industry followed a two-sided, technological and economic, virtuous circle: the smaller transistors get, the lower their manufacturing costs and power consumptions are and the higher their performances are. The terrific machine that Moore's law is has however been running out of steam since the beginning of the 2000's. Peter Lee, a vice-president of Microsoft Research, humorously said that "There's a law about Moore's law. The number of people predicting the death of Moore's law doubles every two years"*. People now ask what might replace it, and different stories emerge depending on which horizon people are looking at.

One of them is composed from long-term perspectives and opportunities and is about going into the unknown. It starts by telling that no matter how determined we are, the ultimate limit of the "traditional" silicon transistor is the atom, and that it will put a stop at Moore's law. This story has also the merit to highlight that Moore's law is both a blessing and a curse. Moore's law has made progress predictable, but at the same time it has been a hindrance to innovation. One might see in the death of Moore's law the opportunity to shake things up and to explore new paths. Amongst these paths, there are 3D stacking of specialized chips, nanophotonics – which uses photons instead of electrons – , spintronics – which uses the spin of the electron instead of the charge – , quantum computing, graphene and other 2D materials-based computing, and even brain-inspired computing – which strives to take advantage of the 10,000 times higher brain power efficiency over silicon-based chips. Some of them have already proven to outperform today's best silicon transistors. But fabricating a fancy device in a lab is one thing, building billions of them on a single chip, all equals in terms of performances, reliability and lifetime, and at reasonable costs, is another one. This shows that there must be another story, at least for the near-future.

This other story, sometimes called "More Moore", has actually begun and is about how much we can push forward Moore's law by introducing "non-conventional performance boosters". To answer this question, one needs to understand what stifles Moore's law. Firstly, downsizing transistors has become increasingly difficult in the past few years and requires huge R&D spending that only a few large companies can afford. Secondly, going to the nanometer scale brings new detrimental effects that have put power consumption and performances on quasi-plateaux for a few years. To overcome these limitations, new channel materials – strained Si in 2003 – , new gate materials – high-κ oxides in 2007 – , and even new transistor architectures – FinFET and FD-SOI in 2012 – , have been introduced. And new "boosters" are still needed to sustain transistor performances and power consumption enhancement until another story begins. This thesis strives to fit into this "More Moore" story by introducing a new material, compressively strained Silicon-Germanium, into the channel of a FD-SOI transistor architecture.

Fully Depleted Silicon-On-Insulator (FD-SOI) is a technology developed in Grenoble ecosystem by Soitec, the Laboratoire d'Electronique et Technologie de l'Information (LETI), and STMicroelectronics as an alternative to the FinFET technology promoted by Intel. The FD-SOI technology benefits from several advantages in terms of power consumption and performances over traditional bulk technologies while having limited manufacturing costs increase thanks to the similarity of most manufacturing processes with traditional ones.

Si hegemony over other materials in the semiconductor industry has been achieved thanks to two major assets: it is the most abundant element of the earth crust, which makes it cheap, and Si dioxide (SiO_2) is a stable oxide featuring excellent dielectric properties, which makes Si-SiO_2 an almost perfect channel-gate stack. This hegemony is however faltering. The introduction of high-κ oxides as gate materials to overcome the issue of increasing

* "*After Moore's law: Double, double, toil and trouble*" *The Economist, March 10th, 2016.*

tunneling current through ultrathin SiO_2 (a few nanometers) – the major if not the only flaw of SiO_2 – has made one of the two assets of Si obsolete. In addition, the quest for higher switching speed and lower power consumption involves increasing the carrier mobility into the channel, with a first hit in 2003 with strained Si. But growing attention has been devoted to other materials, especially Ge and III-V materials, and strain engineering techniques, to go beyond strained Si performances. Compressively strained SiGe is one of the most promising candidates amongst these materials for transistors driven by hole carriers (p-type transistors). As compressively strained SiGe is not adequate for transistors driven by electrons (n-type transistors), and as both n-type and p-type transistors must be integrated on the same chip, co-integration of compressively strained SiGe in p-type transistors with another materials – Si or III-V materials – in n-type transistors is required. SiGe assets in terms of hole mobility can be combined with the benefits of the FD-SOI transistor architecture.

In summary, this thesis seeks to integrate compressively strained SiGe in p-type FD-SOI transistor channels with an industry-compatible process called condensation. The condensation technique has been chosen based on three major advantages over other techniques:

- It allows integration of compressively strained SiGe in p-type channels only while leaving n-type channels unaffected.
- Fully strained and high crystal quality SiGe films directly on insulator (SiGe-On-Insulator: SGOI) can be fabricated up to 50% Ge concentration.
- Only conventional manufacturing processes are used.

However, several challenges still need to be taken up for an efficient and optimized use of the condensation technique in an industrial environment: controlling kinetics of SiGe thermal oxidation (addressed in *Chapter III*) and fabricating high crystal quality and highly strained SGOI films by condensation (addressed in *Chapter IV*). These two challenges are then split into two more fundamental studies (*Section III.A* and *Section IV.A*) and two other problematics that have more direct applications to advanced FD-SOI transistors manufacturing (*Section III.B* and *Section IV.B*).

The manuscript is organized as follows:

- *Chapter I*: it describes the context, the theoretical and technological underpinnings of this thesis work, and ends with the definition of the two challenges addressed in *Chapter III* and *Chapter IV*.

- *Chapter II*: Various processes and characterization techniques and a simulation tool were used during this work. Techniques I personnaly used, either for the measurement and/or the analysis, are described in *Chapter II* while the other ones are presented in Appendices.

- *Chapter III*: The condensation technique relies on thermal oxidation of SiGe. The first part of this chapter (*Section III.A*) strives to bring more understanding of the mechanisms and kinetics of SiGe oxidation. Three technology-relevant oxidation processes are investigated. The second part of this chapter (*Section III.B*) presents two tools built thanks to the former oxidation kinetics results: a numerical simulation tool of SiGe oxidation, and a graphic assessment of the oxide thickness and of the Ge diffusion length in SiGe, two key variables of the condensation process, as a function of process parameters.

- *Chapter IV*: High strain levels and high crystal quality of SGOI films are needed for increasing the hole mobility. We thus compare in the first part of this chapter (*Section IV.A*) strain levels and crystal qualities of SGOI films fabricated by two industry-compatible condensation processes. Finally, the second part of this chapter (*Section IV.B*) starts by describing a particular SGOI strain relaxation phenomenon occurring during transistor manufacturing after the condensation process. Two possible causes to this strain relaxation phenomenon, and related to the condensation process, are suggested and investigated.

Contributions of this thesis work to the integration of compressively strained SiGe in p-type FD-SOI transistor channels by the condensation technique will be summed up. Questions left hanging in the air, new ones, and perspectives will conclude this manuscript.

« Se libérer, ne croyez surtout pas que c'est être soi-même. C'est s'inventer comme autre que soi. Autres matières: flux, fluides, flammes… Autres formes: métamorphoses. Déchirez la gangue qui scande "vous êtes ceci", "vous êtes cela", "vous êtes…". Ne soyez rien: devenez sans cesse. L'intériorité est un piège. L'individu? Une camisole. Soyez toujours pour vous-mêmes votre dehors, le dehors de toute chose. »

Alain Damasio, La Zone du Dehors

Chapter I - The SiGe Condensation Technique for Advanced CMOS FD-SOI Technologies

Introduction to Chapter I **26**

I.1. Present and Future of the CMOS Technology **27**
- I.1.1. The Metal Oxide Semiconductor Field Effect Transistor (MOSFET) 27
- I.1.2. New MOSFET Architectures 32
- I.1.3. High Mobility Channels 34
- I.1.4. Target Application of this Thesis Work 38
- I.1.5. Paths for Integration of Compressively Strained SGOI Films as pMOS Channels 39

I.2. Properties of SiGe **39**
- I.2.1. Materials Properties 39
- I.2.2. Strain and Stress 41
- I.2.3. Epitaxy of SiGe on Si 44
- I.2.4. Plastic Strain Relaxation in Compressively Strained SiGe Films 46
- I.2.5. SiGe Interdiffusion 49

I.3. Properties of Thermal Oxides Grown on Si and SiGe **51**
- I.3.1. Bulk Thermal SiO_2 51
- I.3.2. Si-Thermal SiO_2 Interface 52

I.4. The Condensation Technique **52**
- I.4.1. Introduction and History of the Condensation Technique 52
- I.4.2. FD-SOI Process Flow Integration 52

I.5. Problematics of this Thesis Work **53**
- I.5.1. SiGe Thermal Oxidation 53
- I.5.2. Strain and Crystal Quality of SGOI Films Fabricated by Condensation 54

Conclusion of Chapter I **56**

Introduction to Chapter I

This chapter presents the context, the theoretical and technological underpinnings of this thesis work, and ends with the definition of the two challenges addressed in *Chapter III* and *Chapter IV*. Today's challenges for further enhancement of Metal Oxide Semiconductor Field Effect Transistors (MOSFETs) performances are firstly introduced. More specifically, with the purpose of boosting the ON current, the different paths for increasing the electron and hole mobility in deeply-scaled MOSFETs are reviewed. Among these paths, the benefits of using compressively strained SiGe-On-Insulator (SGOI) as channel material for the p-type MOSFET are highlighted. The properties of SiGe, and then of SiO_2, that are relevant to this work are reviewed. A focus is given on strain in SiGe as it is essential to control strain of channel materials. The condensation technique, which allows the fabrication of SGOI films with possibly high Ge concentrations and high strain levels is then introduced. The two fundamental studies (*Section III.A* and *Section IV.A*) and the two technology-oriented problematics (*Section III.B* and *Section IV.B*) of this thesis are finally stated in order to draw up the organization of this manuscript.

I.1. Present and Future of the CMOS Technology

I.1.1. The Metal Oxide Semiconductor Field Effect Transistor (MOSFET)

This section starts with a brief overview of the history of the MOSFET technology from the first concept in 1926 to today's applications. Then, a description of MOSFET working principles and basic architecture is given. An emphasis is put on MOSFET performance variables that could be enhanced by technological paths related to this thesis work. Having defined MOSFET key elements, the semiconductor industry, Moore's law and key MOSFET technological breakthroughs are introduced in order to draw the general context of this work. Lastly, current scaling issues that impede further conventional scaling are reported.

I.1.1.1. History of the MOSFET

In 1926, Lilienfeld filed a US patent describing the field effect transistor but it was not until 1947 that the transistor effect was actually observed and explained by W. Shockley, J. Bardeen and W. H. Brattain at the Bell Labs [Lilienfeld30] (see *Figure I.1*). The idea of Lilienfeld was to control an electric current flowing between two terminals by controlling a third potential applied between these two terminals.

The actual MOSFET technology breakthrough happened in 1960 thanks to D. Kahng and M. M. Atalla of the Bell Labs [Kahng63]. The MOSFETs were fabricated using crystalline silicon (Si) as the substrate and thermal silicon dioxide (SiO_2) as the gate dielectric. While germanium (Ge) was used for the first transistor by W. Shockley's team, it was not used for MOSFETs due to the non-existence of a stable germanium oxide that features good electrical performances. Complementary Metal Oxide Semiconductor (CMOS) has been the building block of Integrated Circuits (ICs) since it was patented in 1963 by F. Wanlass [Wanlass67]. A CMOS cell uses two MOSFETs working in tandem and driven by electron current and hole current for the so-called nMOSFET and pMOSFET respectively. Then, the first Intel microprocessor in 1971, along with the development of clean rooms and key process steps such as photolithography, were the beginnings of the history of the semiconductor industry.

While the building blocks of CMOS logic have remained unchanged, increasing needs for differentiated ICs have led to two main applications and their associated MOSFET design, i.e. high performance (HP) transistors, mainly used in computers and servers, and low power (LP) transistors for power sensitive markets such as mobile consumer multimedia or the growing "Internet of Things" market.

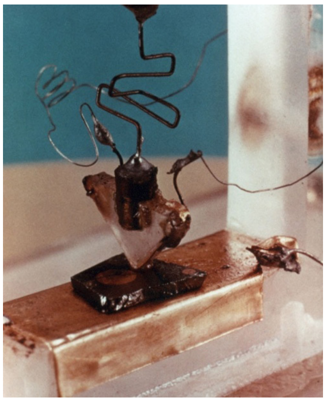

Figure I.1: The First transistor fabricated at the Bell Labs.

I.1.1.2. MOSFET Working Principles

A MOSFET is based on the unique properties of semiconductor materials, i.e. electrical conductivities between those of a conductor and an insulator. A semiconductor material may be either n-type when majority charge carriers are electrons, or p-type when majority charge carriers are holes. A "hole" is a pseudo-particle whose charge is the inverse of the charge of an electron, and which actually corresponds to the absence of an electron in the valence band. The contribution of holes to the current is equivalent to the contribution of all the electrons of the valence band, but study of the physics of semiconductor materials is much easier when considering holes rather than all the electrons of the valence band.

The electrical conductivity of a semiconductor material is controlled by introducing impurities called "dopants" which also determine the type of the semiconductor material. Silicon, a IV-column material in the Mendeleev periodic table, is the most used semiconductor material. Currently used dopants for silicon are boron (a III-column material) for p-type silicon and phosphorous and arsenic (both V-column materials) for n-type silicon.

The concept of the Field Effect Transistor (FET) is to control the conductivity of a semiconductor channel sandwiched between two ohmic contacts (the source and the drain) by applying a voltage to a third contact (the gate). In a MOSFET, the gate is separated from the channel by an insulating layer and the voltage applied to the gate controls the conductivity of the channel just below the insulator layer and thus impedes or allows the current to flow through the channel. *Figure I.2* shows schematic representations of n-type and p-type silicon-based MOSFETs. pMOSFET and nMOSFET working principles are similar and from now on, we focus only on pMOSFET. In terms of device architecture, pMOSFETs are composed of several regions:

- a n-type substrate
- heavily p doped (p+) wells that are connected to the source and the drain: they provide holes for the current flowing through the channel
- the gate: a metallic material or highly-doped polycrystalline silicon
- the dielectric layer between the gate and the channel
- the channel: the n-doped silicon region under the gate

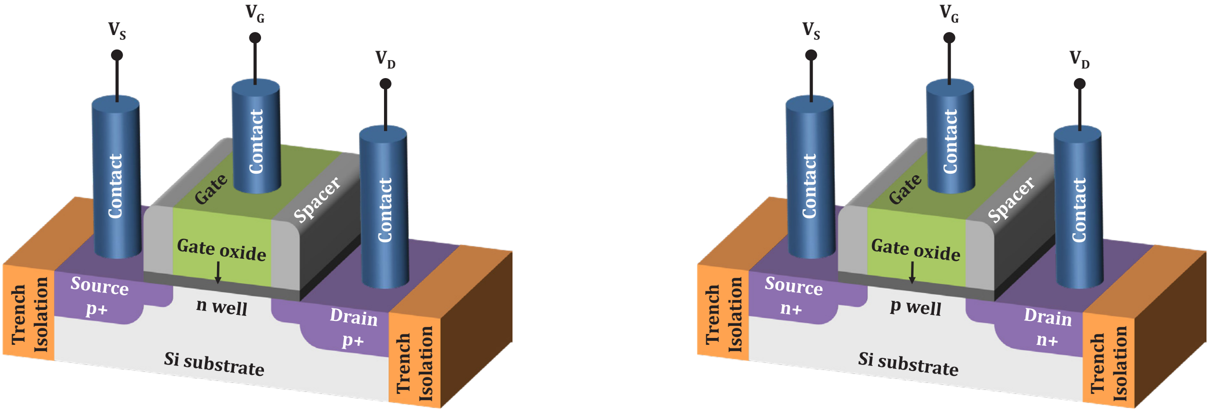
V_S
V_G
V_D
Contact
Contact
Contact
Gate
Spacer
Gate oxide
Trench Isolation
Source p+
n well
Drain p+
Si substrate
Trench Isolation
V_S
V_G
V_D
Contact
Contact
Contact
Gate
Spacer
Gate oxide
Trench Isolation
Source n+
p well
Drain n+
Si substrate
Trench Isolation

Figure I.2: Schematics of a pMOSFET (left) and a nMOSFET (right).

Three operating modes are defined depending on the applied gate voltage:

Off state

No voltage is applied to the gate: the source-channel-drain is composed of two opposite pn junctions, which prevent the current to flow through the channel from the source to the drain. The MOSFET is in off state and the current between the source and the drain is defined as $I_{DS} = I_{off}$. This current arises from leakage current in pn junctions.

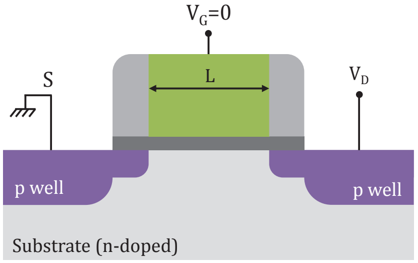
V_G=0
S
L
V_D
p well
p well
Substrate (n-doped)

Figure I.3: Schematic of a pMOSFET in off state.

On state: weak inversion regime

When a weak negative voltage is applied to the gate, majority carriers within the substrate, i.e. electrons, are expelled from the channel region: a depletion region is created. This regime is called weak inversion regime.

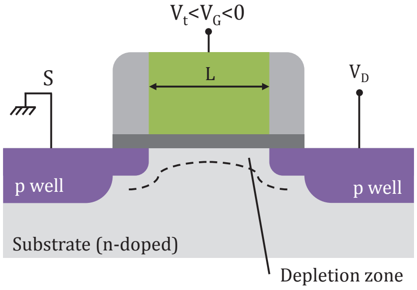
V_t<V_G<0
S
L
V_D
p well
p well
Substrate (n-doped)
Depletion zone

Figure I.4: Schematic of a pMOSFET in weak inversion regime.

In this regime, the current density is driven by diffusion in junctions and is exponentially dependent on the gate voltage [Sze06]:

$$I_{DS}=\mu_0 C_{dep}\frac{W}{L}\left(\frac{k_BT}{q}\right)^2\left[1-\exp\left(\frac{-qV_D}{k_BT}\right)\right]\exp\left(q\frac{V_G-V_T}{k_BT}\right),$$

Equation I.1

where:

- μ_0 is the intrinsic carrier mobility in the channel
- C_{dep} is the depletion zone capacitance
- q is the elemental charge, k_B is the Boltzamm constant and T the temperature
- W is the gate width

The subthreshold slope S is defined as:

$$S=\frac{\partial V_G}{\partial\log(I_{DS})}=\ln 10\frac{k_BT}{q}\left(1+\frac{C_{dep}}{C_{Ox,eff}}\right),$$

Equation I.2

where $C_{Ox,eff}$ is the oxide capacitance in the strong inversion regime. In the ideal case (C_{dep} is negligible compared to $C_{Ox,eff}$), S is equal to 60 mV/decade.

On state: strong inversion regime

When the applied gate voltage, V_G, is decreased, holes are attracted under the gate at the dielectric-channel interface. The concentration of minority carriers (holes) is higher than the concentration of majority carriers (electrons) in this region, hence the strong "inversion" regime. The threshold voltage, V_t, is defined as the applied gate voltage that corresponds to the switch between weak and strong inversion regimes. The depletion zone reaches a maximum expansion at the threshold voltage.

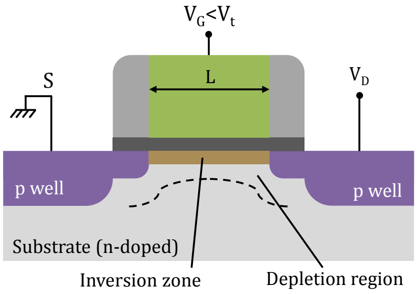

Figure I.5: Schematic of a pMOSFET in strong inversion regime.

There are two regimes depending on the drain voltage:

- The linear regime:

The channel behaves like a resistance whose resistivity depends on the minority carriers concentration in the channel. The drain current is:

$$I_{DS}=\frac{W}{L}\mu_{eff}C_{Ox,eff}\left[V_G-V_t-\frac{1}{2}V_D\right]V_D,$$

Equation I.3

where μ_{eff} is the effective mobility in the channel. For small drain voltage, the drain current is linearly dependent on the gate voltage.

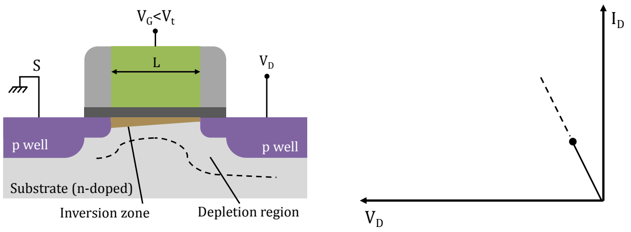

Figure I.6: Schematic (left) and drain current versus drain voltage (right) of a pMOSFET in the linear regime.

- The saturation regime:

The depletion zone thickness on the drain side is reduced to zero at a drain voltage $V_D = V_{Dsat}$. The channel current reaches a saturation value I_{Dsat}which corresponds to the ON current:

$$I_{ON} = \frac{W}{2L}\mu_{eff} C_{Ox,eff}\left(V_G - V_t\right)^2, \qquad \textbf{Equation I.4}$$

For drain voltages lower than V_{Dsat}, the inversion layer length is reduced.

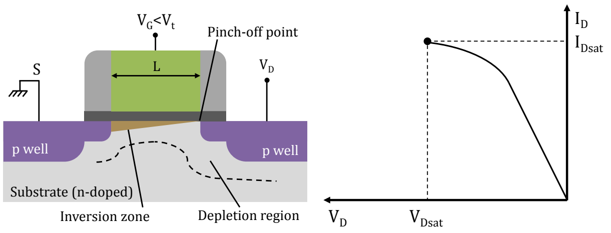

Figure I.7: Schematic (left) and drain current versus drain voltage (right) of a pMOSFET at the pinch-off point.

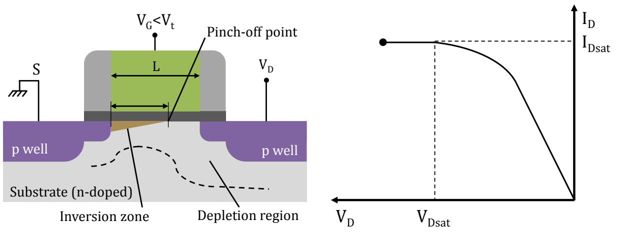

Figure I.8: Schematic (left) and drain current versus drain voltage (right) of a pMOSFET in the saturation regime.

I.1.1.3. Circuit Performance Enhancement

The two main MOSFET circuit performance specifications are the power consumption of the circuit $P_{tot}$and the commutation time τ:

$$P_{Tot} = P_{Standby} + P_{Switching}, \qquad \textbf{Equation I.5}$$

where:

$$P_{Standby} = n_{OFF} I_{OFF} V_{DD},$$

$$P_{Switching} = fC_{load} V_{DD}{}^2 \simeq n_{ON} I_{ON} V_{DD}, \qquad \textbf{Equations I.6}$$

$$\tau = \frac{C_G V_{DD}}{I_{ON}},$$

and where V_{DD}, f, C_{load}, C_G, n_{ON}, n_{OFF} are the applied gate voltage in the ON regime, also called the power supply voltage, the operating frequency, the total load capacitance, the gate capacitance, the number of transistor in ON state and the number of transistors in OFF state.

Achieving simultaneously power consumption and switching time reduction leads to MOSFET design requirements that may conflict with each other. Power consumption reduction is preferentially achieved by reducing $P_{Standby}$, in other words V_{DD} and I_{OFF}. But reducing V_{DD} induces I_{ON} reduction and consequently switching time degradation because $I_{ON} \propto V_{DD}{}^2$. We highlight that enhancement of the effective mobility μ_{eff} in the channel allows I_{ON} enhancement without conflicting power consumption requirements.

I.1.1.4. The Semiconductor Industry

Silicon-based transistors have been the foundation of the semiconductor industry since 1959, year of the first silicon-based Integrated Circuit (IC). Since then, the semiconductor industry has followed the virtuous circle schematically represented *Figure I.9* and whose key enablers have been MOSFET scaling and wafer size increasing. MOSFET scaling refers to the reduction of the transistor dimensions usually defined by the half pitch between two adjacent interconnections, the so-called technology node. *Figure I.10* shows the half-pitch of a conventional transistor.

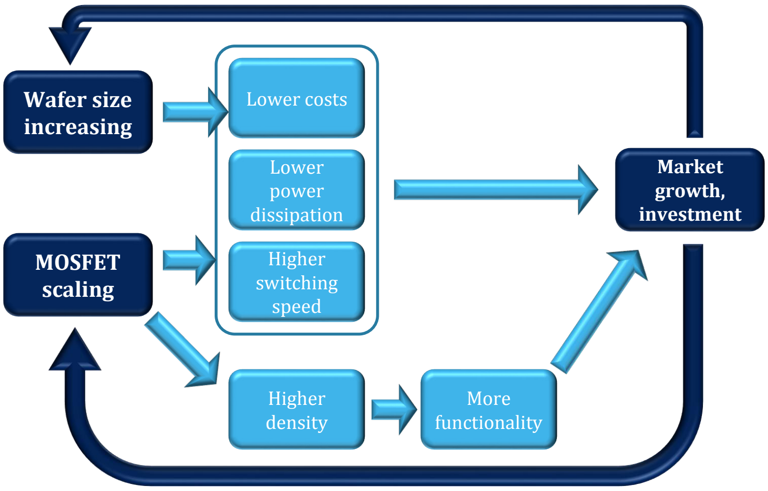

Figure I.9: The virtuous circle of the semiconductor industry.

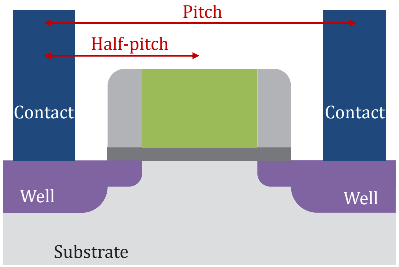

Figure I.10: Schematic of a MOSFET showing the pitch and half-pitch.

Moore’s law, an empirical rule stated in 1965 and recalibrated in 1975 by G. Moore has well described the driving force of the semiconductor industry [Moore65]. Moore’s law predicted that the number of transistors per silicon area would double every two years. Another way of stating this rule is saying that chip performances, a combination of higher transistor density and higher transistor speed, double every two years. In terms of device dimensions, Moore’s law is achieved by scaling the contacted gate pitch by a scaling factor of 0.7 every two years (see *Figure I.11*). Until 2003, Moore’s law has been synonymous with "classic" or "conventional" scaling which refers to the scaling rules described by Dennard et al. [Dennard74]. According to Dennard scaling rules, the oxide thickness, the transistor length and the transistor width (perpendicular to the channel direction) were scaled by a constant factor 1/k which in turn enhanced speed by a factor k at constant power.

But since 2003, conventional MOSFET scaling has not been sufficient to follow Moore’s law because of the scaling issues described in the following section. Therefore, "non-conventional performance boosters" were commercially introduced: strained channel in 2003, high-κ metal gate stack in 2007 and new transitor architectures, FinFET and FD-SOI in 2012. These scaling issues are expected to increase further as devices are scaled down. Henceforth, Moore’s law and its derivative term "More Moore" refer to slight scaling and technology advances which allow either cheaper, smaller or faster chips and not anymore necessarily all of them simultaneously.

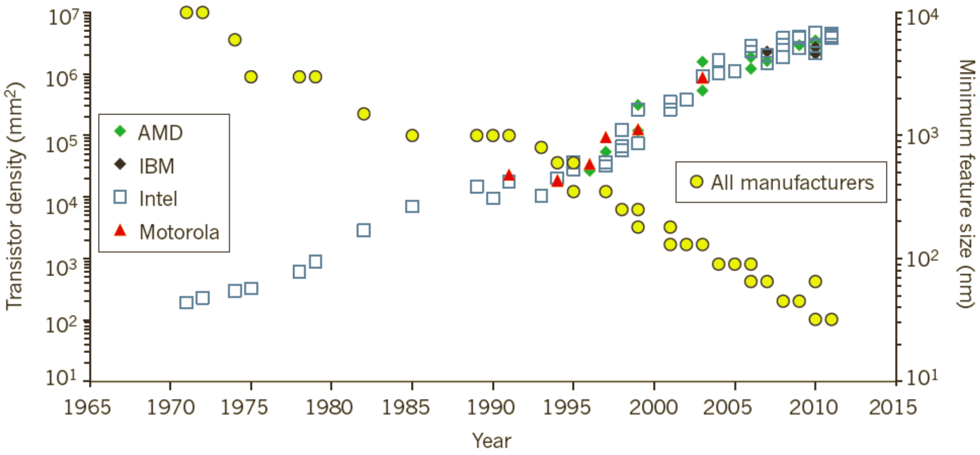

Figure I.11: Evolution of the transistor density and minimum feature size (transistor gate length) in microprocessors. From [Ferain11].

I.1.1.5. MOSFET Scaling Issues

When the gate length is scaled down to a few tens of nanometers, the drain-junction depletion region extends into the channel region, causing a reduction in the effective gate length as schematically represented *Figure I.12*. Short-channel effects (SCE) result from the sharing of electrical charges between the channel on one hand and the drain and source regions on the other hand. Therefore, the distance between the source and the drain, and the applied drain voltage influence the gate control of the transistor. SCE induce two detrimental effects: drain-induced barrier lowering (DIBL) which causes the threshold voltage to decrease when the drain voltage increases, and an increase in the subthreshold slope. Both increase the leakage current and DIBL also decreases the switching speed of the transistor. Additionally, decreasing the gate dielectric thickness induces a higher tunneling current through the gate that also increases leakage currents.

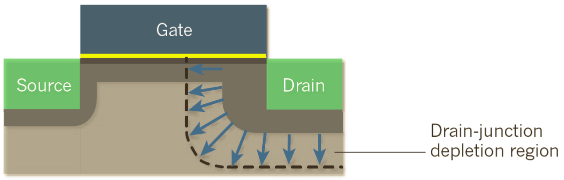

Figure I.12: Schematic view of a conventional bulk MOSFET. The depletion regions are in dark-gray. The width of the drain-junction depletion region extends into the channel as the drain voltage increases, causing DIBL. From [Ferain11].

As a consequence, the semiconductor industry is at a point where conventional transistors cannot follow Moore's law anymore. Technological innovations are thus required to overcome these scaling issues and to sustain transistor performances enhancement. Main technological innovations, such as new MOSFET architectures like FD-SOI and FinFET, and high mobility channels are described in the following sections.

I.1.2. New MOSFET Architectures

FinFET and FD-SOI are two transistor architectures whose performance advantages over conventional MOSFETs, also called bulk MOSFETs, are first introduced along with the target applications. The second part of this section focuses on FD-SOI technology nodes that are the target applications of this work.

I.1.2.1. Bulk, FD-SOI and FinFET MOSFET Architectures

Two new transistor architectures, FinFET and FD-SOI, are taking over from bulk MOSFET transistor architectures in advanced CMOS devices. Both are commercialized today and share the same crucial feature, i.e. a fully depleted channel. And as shown *Figure I.13*, both of them converge to the same architecture, merely rotated of 90° from each other.

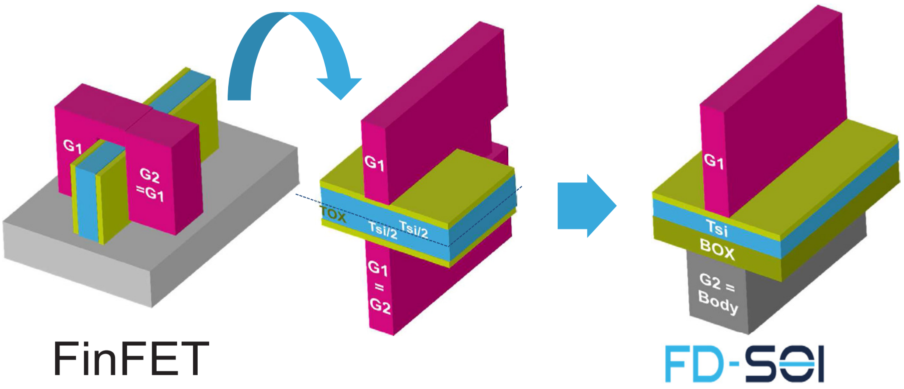

Figure I.13: Schematics of FinFET and FD-SOI architectures. FD-SOI and FinFET architectures ultimately converge, differing only from a 90° rotation, as the Buried Oxide (BOx) thickness is thinned down. From [Ouellette15].

Even if being in advanced R&D stages only, and except the FinFET architecture which has already been commercialized, multigate transistor architectures deserve to be mentionned as they may some day take over FD-SOI and FinFET architectures in most advanced CMOS devices. Multigate transistors actually refer to single gate transistors whose gate is wrapped around several sides of the channel region. FinFET, tri-gate, gate-all-around, Π-gate and Ω-gate structures are the main multigate transistor architectures [Ferain11].

Schematic profile views of a conventional bulk transistor and a FD-SOI transistor are represented *Figure I.14*. The FD-SOI technology features reduced parasitic currents and reduced junction capacitances between the source and the drain over bulk MOSFET technology. Other advantages of FD-SOI over bulk are better device-to-device isolation, reduced substrate coupling and lower sensibility to high-energy radiations that may cause computing errors.

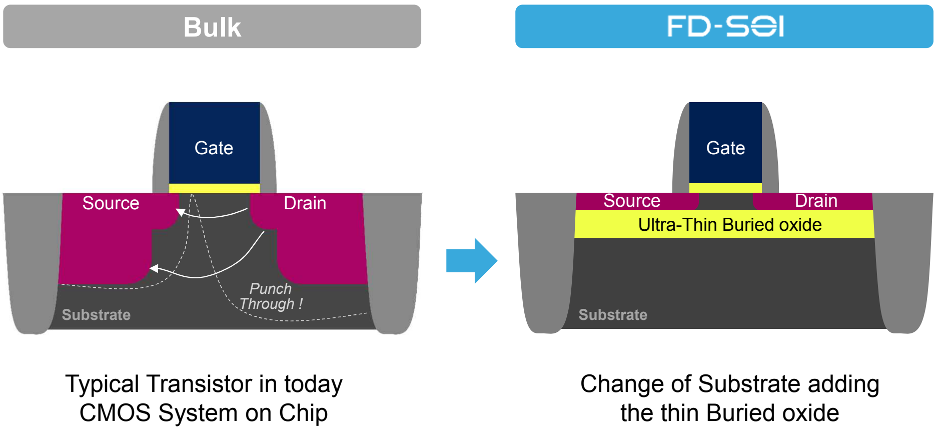
Bulk
FD-SOI
Gate
Source
Drain
Punch Through !
Substrate
Gate
Source
Drain
Ultra-Thin Buried oxide
Substrate
Typical Transistor in today CMOS System on Chip
Change of Substrate adding the thin Buried oxide

Figure I.14: Transition from bulk to FD-SOI MOSFET brings better electrostatic control over the channel and lower leakage currents. From [Ouellette15].

FinFET and FD-SOI technologies do not address exactly the same markets (see *Figure I.15*). Due to expected higher speed, density, and costs, the 3D-architecture FinFET mainly addresses high-performance markets. While FD-SOI, being manufactured by more conventional processes, benefits from lower R&D and manufacturing costs thanks to a larger accumulated knowledge. However FD-SOI requires Silicon-On-Insulator (SOI) substrates which are more expensive than bulk ones. In the end, FD-SOI better fits the needs of power sensitive markets. From now on, we focus on FD-SOI, the transistor architecture which is the target application of this work.

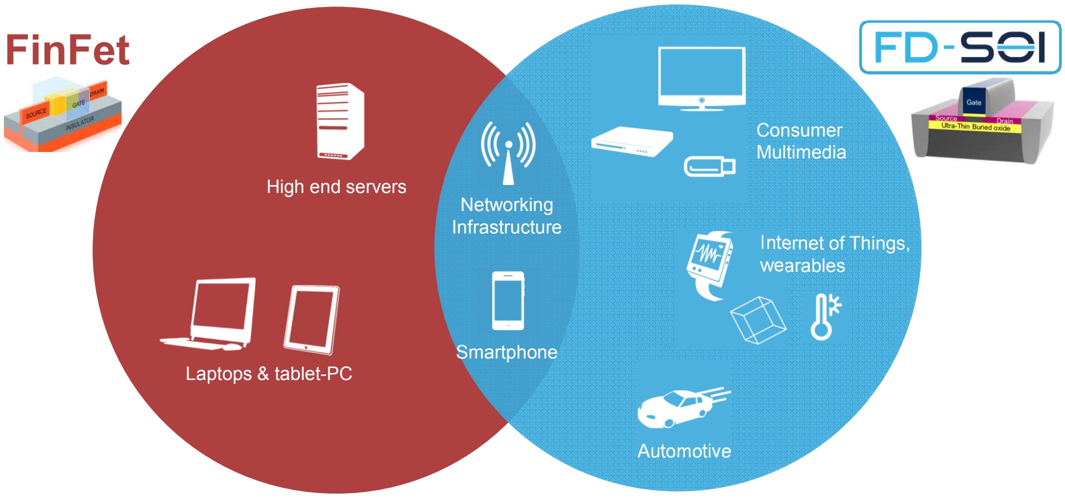
FinFet
FD-SOI
High end servers
Laptops & tablet-PC
Networking Infrastructure
Smartphone
Consumer Multimedia
Internet of Things, wearables
Automotive

Figure I.15: FD-SOI and FinFET target markets. The FD-SOI technology addresses power sensitive markets while FinFET is more suitable for high-performance markets. From [Ouellette15].

I.1.2.2. FD-SOI Technology Nodes

FD-SOI is a technology that has been developed by the LETI, Soitec, and STMicroelectronics since the beginning of the 1990’s (*Figure I.16*). SOI substrates specifications is a 20 nm Buried Oxide (BOx) thickness and a 10 nm SOI thickness and the final channel thickness is 6.5 nm. A Transmission Electron Microscopy (TEM) image of a FD-SOI pMOS device fabricated at Crolles site and featuring a SiGe channel, raised boron-doped SiGe source and drain, and high-κ metal gate is shown *Figure I.17*. This SiGe channel is a MOSFET performance booster that is described in the next section. Today’s FD-SOI specifications are in the 20% to 30% range for the Ge concentration within the SiGe channel.

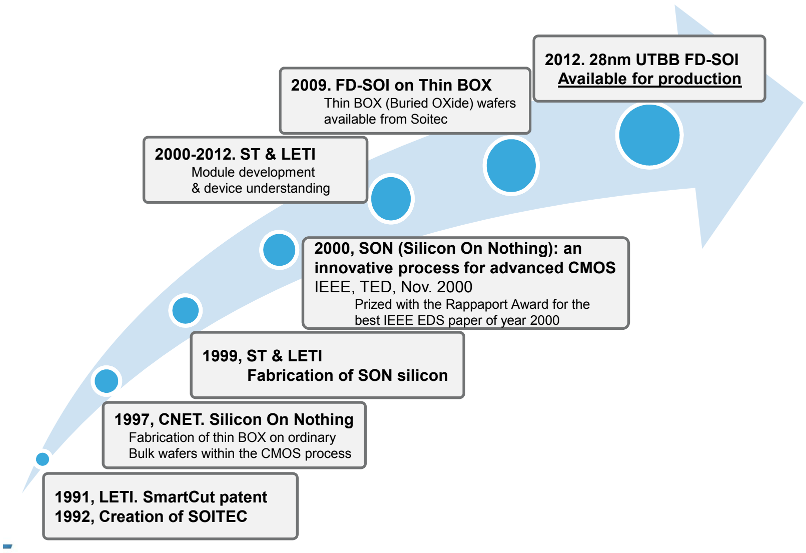
2012. 28nm UTBB FD-SOI
Available for production
2009. FD-SOI on Thin BOX
Thin BOX (Buried OXide) wafers available from Soitec
2000-2012. ST & LETI
Module development & device understanding
2000, SON (Silicon On Nothing): an innovative process for advanced CMOS
IEEE, TED, Nov. 2000
Prized with the Rappaport Award for the best IEEE EDS paper of year 2000
1999, ST & LETI
Fabrication of SON silicon
1997, CNET. Silicon On Nothing
Fabrication of thin BOX on ordinary Bulk wafers within the CMOS process
1991, LETI. SmartCut patent
1992, Creation of SOITEC

Figure I.16: R&D history of FD-SOI. From [Ouellette15].

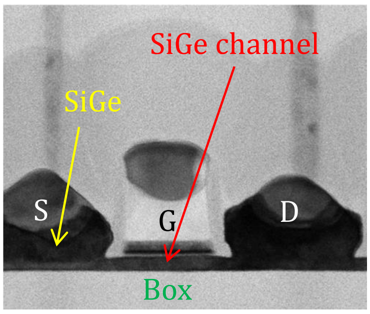
SiGe channel
SiGe
S
G
D
Box

Figure I.17: TEM image of a FD-SOI pMOS transistor fabricated at STMicroelectronics Crolles site. Internal document.

I.1.3. High Mobility Channels

As seen in *Section I.1.1.3.*, an effective way to increase the ON current is to use channels that feature high carrier mobility. We thus start by defining what mobility is and we provide more details about the relations between mobility and current in real transistors. This section then examines electron and hole mobility of various materials that could be suitable for high-mobility channels on Si substrates. Mobility dependence on crystal orientation and strain is finally reviewed.

I.1.3.1. Mobility Definition

The mobility of a carrier in a given material describes its ability to move under an applied electric field. Mobility μ is defined for a specific crystal orientation as a function of two important materials properties, i.e. the carrier effective mass m^*, and the relaxation time $\langle\tau\rangle$:

$$\mu = \frac{q\langle\tau\rangle}{m^*}. \qquad \textbf{\textit{Equation I.7}}$$

The effective mass of a carrier is used to quantify how the carrier responds to the application of external forces in a solid. Indeed, the periodic potential due to the periodic position of ions and core electrons within a crystal induces internal forces. Therefore, the behaviour of a charge carrier under an electric field in a solid is not the same as in vacuum. These internal forces may be described by the dispersion relation $E(k)$, where E is the energy of the carrier, k its wave vector, and $\hbar$ the Planck constant. The effective mass is defined by:

$$m^* = \hbar^2\left(\frac{\partial^2 E}{\partial k^2}\right)^{-1}. \qquad \textbf{\textit{Equation I.8}}$$

The relaxation time is the average carrier transit time between two collisions and depends on various scattering mechanisms caused by any change in the perfect crystal structure. In FD-SOI MOSFETs, the channel is fully depleted so that we have to consider as scattering mechanisms the interactions of the carriers not only with the gate dielectric layer but also with the BOx layer. The scattering mechanisms are:

- Broken crystal symmetry induced by confinement in deeply-scaled FD-SOI MOSFET channels.
- Thermal vibration-induced acoustic and optical phonon scattering, also referred to as Remote Phonon Scattering (RPS), is an intrinsic mobility degradation mechanism due to coupling of phonons in dielectric layers with carriers in the channel. RPS could thus represent a fundamental limit to the channel mobility of FD-SOI MOSFETs.
- Remote Coulomb Scattering (RCS) is an extrinsic mechanism of scattering of carriers by trapped charges in dielectric layers. This effect may be reduced by screening them using a layer between the channel and the dielectric layer where the charges are trapped. This layer keeps away the trapped charges from the carriers.
- Interface roughness.

The relaxation time is dominated by the scattering mechanism with the shortest scattering time (Mathiessen's rule) and we usually consider Coulomb, phonon and roughness scattering mechanisms only according to the "universal mobility model" [Takagi94]. These three scattering mechanisms have different electric field and temperature dependences as shown *Figure I.18*. At low fields, the mobility is limited by Coulomb scattering , at medium fields by phonon scattering and finally by interface roughness at high electric fields.

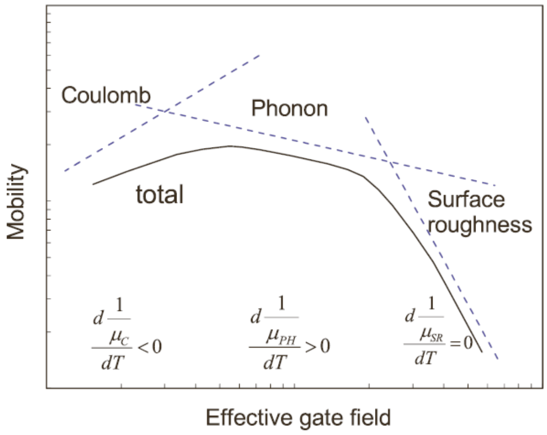

Figure I.18: Schematic illustration of the dependence of the mobility on the effective gate field of a transistor. It shows the three scattering mechanisms and at which field they limit the mobility. From [Robertson15].

I.1.3.2. Mobility Engineering for ON Current Enhancement

In *Section I.1.1.2.*, we gave the relation between the ON current and the effective mobility of the channel material. This relation do not hold anymore for short channel transistors and under high electric fields, which are today's specifications. To discuss the impact of mobility on the ON current in real devices, we provide below a simple equation of the ON current of a MOSFET per gate width [Takagi08]:

$$I_{ON} \simeq qN_S^{Source} v_s ,$$

Equation I.9

where N_S^{Source} is the surface carrier concentration near the source edge and is determined by the gate voltage and the gate capacitance, and where v_s is the carrier velocity near the source edge. On the other hand, the carrier velocity depends on the channel length. Three regimes of the velocity in MOSFETs are distinguished [Lundstrom02]:

- The stationary transport regime in long-channel MOSFETs. In this case and when velocity saturation occurs, the ON current dependence on the low field mobility becomes weaker than the linear one described by *Equation I.4.*

- The quasi-ballistic transport regime. In this case, nonstationary transport becomes dominant in short channels because the number of scattering events is reduced in the channel. The ON current is then redefined as:

  $$I_{ON} = qN_S^{Source} v_{\text{inj}} \frac{1-r}{1+r} ,$$

  Equation I.10

  where v_{inj} and r are respectively the injection velocity near the source edge and the backscattering rate near the source edge. r is related to the mobility, therefore mobility enhancement is still an important path for MOSFET performance improvement.

- Full ballistic regime of very short-channel MOSFETs. There is no scattering event in the channel and no direct mobility dependency anymore. The ON current is:

  $$I_{ON} = qN_S^{Source} v_{\text{inj}} .$$

  Equation I.11

  In this case, MOSFET performance enhancement is achieved by improving the injection velocity which follows the following relation: $v_{\text{inj}} \propto m^{-1/2}$. As shown by *Equation I.7*, decreasing the effective mass induces a mobility enhancement and therefore, mobility improvement is still an ON current enhancement path in full ballistic transport regime.

We conclude by highlighting that mobility is in all regimes a key parameter for MOSFET performances even if its impact on the final ON current is complex. There are three paths to increase mobility of carriers in transistor channels:

- Channel materials engineering: some materials feature intrinsic lower effective masses.
- Crystal engineering: the effective mass may be dependent on crystal orientation.
- Strain engineering: strain alters band structures, so that both the effective mass and the relaxation time may be decreased with certain strain levels. Strain may also change carrier densities in intrinsic semiconductor materials which in turn alters the inversion carrier density [Takagi08].

Co-integration of two combinations of these three enhancement paths are required in order to reach both high nMOS and pMOS channel mobilities on the same chip.

I.1.3.3. Channel Materials

Despite its poorer electron and hole mobility, silicon has been the chosen material for CMOS technology until these days thanks to several advantages over III-V materials and germanium. The most important ones are the existence of an associated stable oxide, SiO_2, the high electrical quality of the Si-SiO_2 interface, and the existence of low-cost and high-quality Si substrates.

Alternative materials featuring higher carrier mobility are now considered (or even reconsidered in the case of germanium since the first functional transistor was made of germanium) for next CMOS technologies. *Figure I.19* plots hole and electron mobility versus bandgap for silicon, germanium and various III-V materials, three key materials properties when considering transistor channels. A low bandgap leads to higher off-state leakage currents as a result of thermionic emission and band-to-band tunneling. Nevertheless, materials that feature a low bandgap, such as germanium, can benefit from two technology-induced changes: quantum confinement effects which arise in deeply-scaled transistor channels and which increase the effective bandgap, and the decrease in operating voltage of latest devices. On the other hand, operation at low supply voltage is prevented by the lack of a metal with a suitable work function when the bandgap is too large [Pillarisetty11].

Research has shown promising results of integration of III-V materials and germanium on silicon substrate in spite of the lattice parameter discrepancy existing between these materials [Kuhn12]. Fabrication of suitable gate stacks on these alternative materials has also been proven to be possible despite several remaining issues [Frank11].

The CMOS technology is based on co-integration of pMOS and nMOS transistors working in tandem and featuring similar performances. Therefore, while III-V materials show electron mobilities higher than 10,000 $cm^2V^{-1}s^{-1}$, they are not the most promising materials for pMOS transistors. On the other hand, germanium has the highest hole mobility (1,900 $cm^2V^{-1}s^{-1}$) of all known semiconductor materials and is thus the most promising candidate for pMOS transistors. Germanium also features a higher theoretical electron mobility than silicon, but it has never been experimentally observed and is thus not suitable for nMOS transistors. As for SiGe, the theoretical hole mobility of unstrained SiGe is dependent on calculations parameters and must be considered with caution [Fischetti96]. Co-integrating different channel materials for pMOS and nMOS on the same chip may offer the highest performance enhancement for CMOS technology but increases process and integration complexity at the same time.

We mention that decreasing the effective mass of carriers within the channel has also drawbacks because of higher quantum confinement effects. Indeed, quantum confinement effects degrade the density of states which in turn decreases the current density. Another detrimental effect is the higher leakage current induced by the increase of the tunneling current from source to drain. Trade-offs have to be found based on target applications. STMicroelectronics chosen strategy for its FD-SOI technology is co-integration of tensely strained Si for nMOS channel and compressively strained SiGe for pMOS channel, the latter being this work's target application.

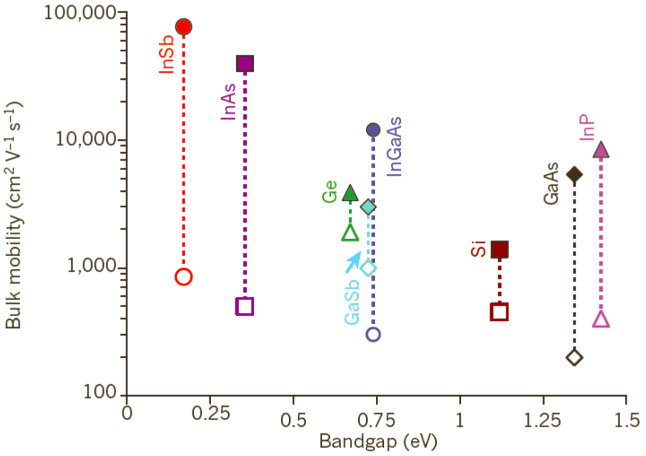

Figure I.19: Calculated bulk electron and hole mobility of silicon, germanium and some III-V materials as a function of the bandgap. Open symbols indicate hole mobility and full ones indicate electron mobility. From [Pillarisetty11].

I.1.3.4. Crystal Orientations

Crystal orientation of both the substrate and the channel alters band structures, and consequently mobility within the channel, because of the anisotropy of the effective mass of some materials such as Si and Ge. Conventional orientations for Si CMOS are <110> channels on (001) substrates. CMOS fabrication on (110) and (111) substrate orientations has been hindered because of poor gate oxide quality. Nevertheless, MOSFET performance enhancement has been recently shown on these orientations thanks to careful optimization of gate stack formation [Yang03]. Advantageous substrate-channel orientations are illustrated *Figure I.20* and have been used in commercial devices.

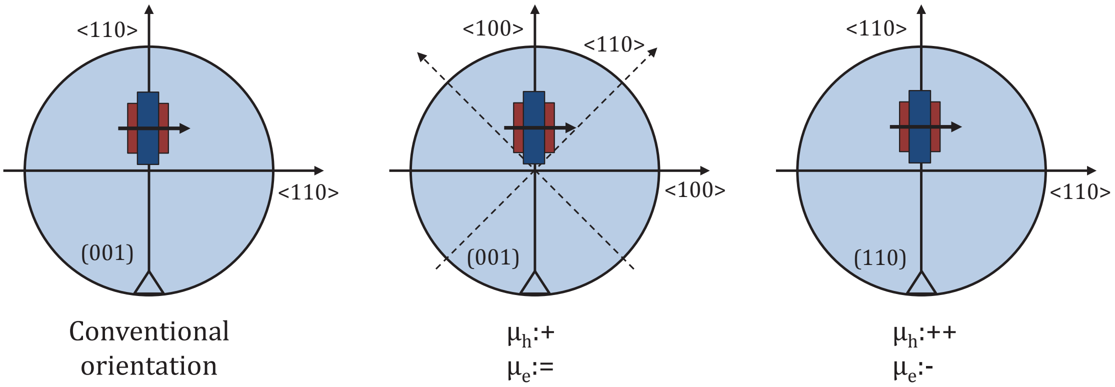

Figure I.20: Schematic representations of conventional orientation (left), (001)<100> orientation (middle) and (110)<110> orientations (right) along with mobility gains.

I.1.3.5. Strained Channels

Strain refers to the lattice deformation of a material and is either compressive or tensile. First theoretical investigation of strain-induced mobility enhancement can be traced back to the deformation potential theory formulated by J. Bardeen and W. B. Shockley in 1950 [Bardeen50] and the experimental observation of the piezoresistance effect by C. S. Smith [Smith54]. Since then, this phenomenon has been theoretically investigated by many groups, the latest extensive study based on the deformation potential theory being Fischetti and Laux's one [Fischetti96].

Strain, and subsequently stress, reduces the crystal symmetry and therefore influences band structures in two ways:

- Band warping (except for hydrostatic, in other words isotropic strain) induces a change in the effective mass.
- Band splitting changes the relative importance of intra and inter-valley scattering and therefore influences the relaxation time of charge carriers.

Figure I.21 shows calculated electron mobility gain in silicon for various strain types (uniaxial and biaxial), levels and crystallographic orientations.

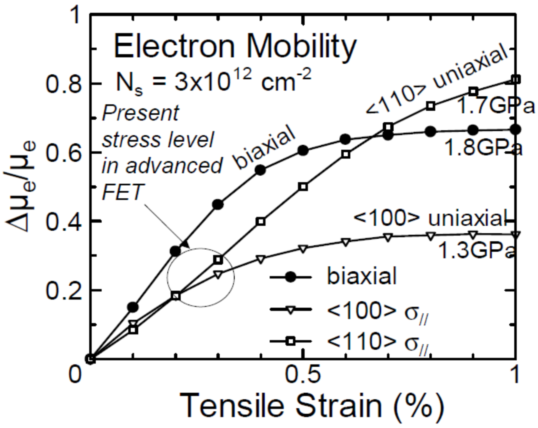

Figure I.21: Calculated electron mobility enhancement as a function of tensile strain. From [Uchida05].

On the experimental and technological side, strain within the channel has been implemented using various device and process technologies. First devices thought to benefit from strain-induced enhancement of electron and hole mobilities within the channel were Si/SiGe heterostructures [Manasevit82]. Lattice mismatch between Si and SiGe was suspected to induce strain which in turn increased mobility. Then, the Stanford group confirmed such a performance improvement in 1992 [Welser92] and Intel implemented strain in commercial devices in 2003 for the 90-nm and 45-nm nodes [Ghani03]. For the pMOSFET, the larger lattice parameter of SiGe in the source and drain regions tends to compressively strains the smaller lattice of Si within the channel, while the nMOSFET Si channel is tensely strained by engineering the stress and thickness of a silicon nitride capping layer (see *Figure I.22*).

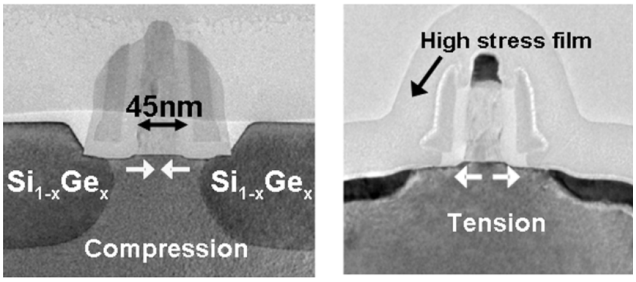

Figure I.22: pMOSFET from Intel with compressively strained Si channel using SiGe source and drain (left). And nMOSFET from Intel with tensely strained Si channel using a SiN capping layer (right). From [Thompson04].

Different strain elements, strain levels and strain orientations can be used for mobility enhancement. This work focuses on hole mobility enhancement induced by biaxial or uniaxial strain in the SiGe-based channel. For SiGe, a dramatic increase of electron and hole mobility is expected from calculations and some experimental result have shown high factor improvements [DeSalvo14].

I.1.4. Target Application of this Thesis Work

As drawn in *Section I.1.1.*, conventional MOSFET scaling has come to an end and new technology innovations are needed to sustain the dynamics of the semiconductor industry. Firstly, new transistor architectures, i.e. multi-gate transistors such as FinFET and FD-SOI, can help to extend transistor scaling. STMicroelectronics has chosen to focus on the FD-SOI transistor architecture to sustain CMOS scaling, which is why FD-SOI is the target application of this work. Then, we explained in *Section I.1.3.* why higher mobility channels are also required to enhance transistor performances. Crystal orientation, intrinsic materials mobility and strain are three paths to increase channel mobility. Compressively strained SiGe is considered to be one of the best candidates for the pMOS channel of FD-SOI transistors.

To summarize, the target application of this thesis work, schematically represented *Figure I.23*, is fabrication of high Ge-content (higher than 40%) compressively strained SiGe channel for enhancing the performances of pMOS FD-SOI transistors.

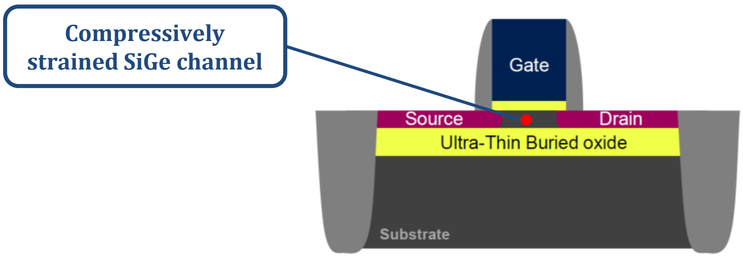

Figure I.23: Schematic of a FD-SOI transistor showing the main application of this thesis work for advanced FD-SOI technologies.

I.1.5. Paths for Integration of Compressively Strained SGOI Films as pMOS Channels

As drawn in the last section, co-integration of SOI and SiGe-On-Insulator (SGOI) channels in nMOSFETs and pMOSFETs for the next generations of CMOS devices is strongly needed. Several techniques to fabricate SGOI layers have been proposed (see [Pillarisetty11] and [Takagi15] and references therein), but many of them are either not mature, costly, or incompatible with today's CMOS manufacturing processes. The condensation technique, which will be described into more details in *Section I.4.*, shows three main advantages over the other techniques:

- It allows fabrication of SGOI layers in pMOS areas only, leaving the nMOS areas unaffected.
- Fully strained SGOI layers a few nanometers thick with Ge concentrations up to about 50% can be fabricated.
- It uses conventional SOI substrates and conventional CMOS manufacturing processes, such as SiGe epitaxial growth and thermal oxidation.

However, incorporating Ge in CMOS manufacturing processes with the condensation technique is not straightforward as new issues emerge. Firstly, kinetics of SiGe thermal oxidation, upon which the condensation technique is based, must be well controlled. And secondly, the 4% lattice mismatch between Si and Ge makes SiGe layers prone to strain relaxation and extended defects generation, which are detrimental to pMOS performances. Other issues, out of the scope of this work, such as fabrication of high-quality gate stack and source and drain with low contact resistance, etch and cleaning processes, also need to be solved.

I.2. Properties of SiGe

I.2.1. Materials Properties

In this section, essential material properties of SiGe are presented. Crystal structure of SiGe, phase diagrams, from which limitations in terms of annealing temperature are extracted, and band structures and bandgap of SiGe are reviewed.

I.2.1.1. Crystal Structure

Si and Ge are both elements of the IV column of the Mendeleev chart and their atomic numbers are 14 and 32 respectively. They both have four covalent bonds. SiGe with Ge content varying from 0% (pure Si) to 100% (pure Ge) crystallize in a diamond-like lattice structure whose space group is $O_h^7 - Fd3m$. The diamond lattice, represented *Figure I.24*, is the superposition of two cubic-face-centered (cfc) lattices shifted from a quarter of the space diagonal from each other. There are a total of eight atoms in the diamond lattice and Si and Ge atoms are undistinguishable in the whole range of composition regarding their position in the lattice.

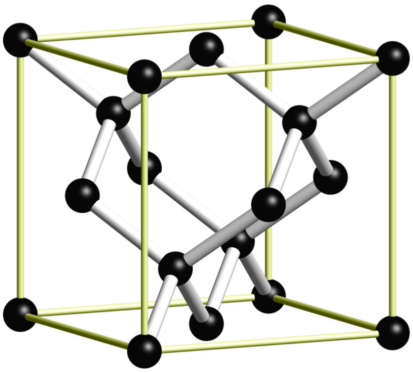

Figure I.24: Schematic of the diamond-like lattice structure of SiGe.

The lattice constants of Si and Ge are 5.431 Å and 5.658 Å respectively. Therefore, there is a 4.18% lattice mismatch between Si and Ge. $Si_{1-x}Ge_x$ lattice parameter may be described by the empirical parabolic law proposed by Dismukes et al. [Dismukes64]:

$$a_{SiGe}(x)(nm) = 0.5431 + 0.20x + 0.027x^2. \qquad \textbf{Equation I.12}$$

I.2.1.2. Phase Diagram

The phase diagram of SiGe is shown *Figure I.25*. The temperature of the solidus decreases from 1412°C, the Si melting temperature, to 937°C, the Ge melting temperature, as the Ge content increases. Thermal annealing with temperatures higher than the solidus would lead to the separation of two phases, a liquid Ge-rich one and a solid Si-rich one. Consequently, a first limitation in terms of process is that the highest temperature which can be used for thermal annealing of SiGe decreases as the Ge content increases.

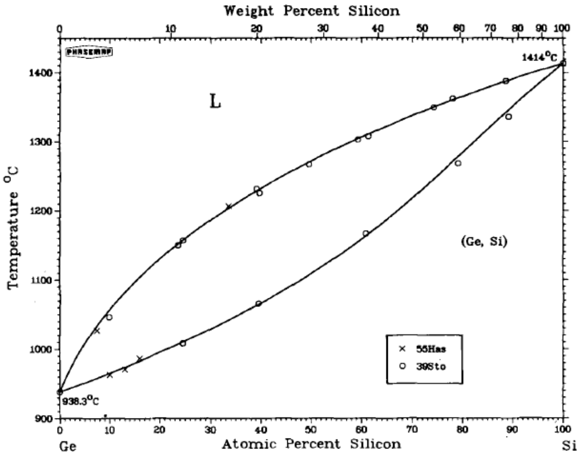

Figure I.25: SiGe Phase diagram. From [Olesinski84].

I.2.1.3. Band Diagrams

Si and Ge band diagrams are shown *Figure I.26*. They have indirect bandgaps of 1.12 eV and 0.66 eV respectively. The conduction band structure of pure Si is formed of 6 equi-energy valleys along the {100} directions with the minima at the X point (also referred to as delta minima) in the Brillouin zone (see *Figure I.27*), while the conduction band minima is eightfold degenerate in Ge and located at the L point in the {111} directions. The bandgap of unstrained and pseudomorphically strained SiGe versus Ge content is shown *Figure I.28*. The discontinuity in the evolution of the bandgap of relaxed SiGe versus Ge concentration at around 85% Ge content is caused by the crossover between the Si-like and the Ge-like band structures [Schäffler97]. Strain induces splitting of the valence band and also dramatically decreases the SiGe bandgap.

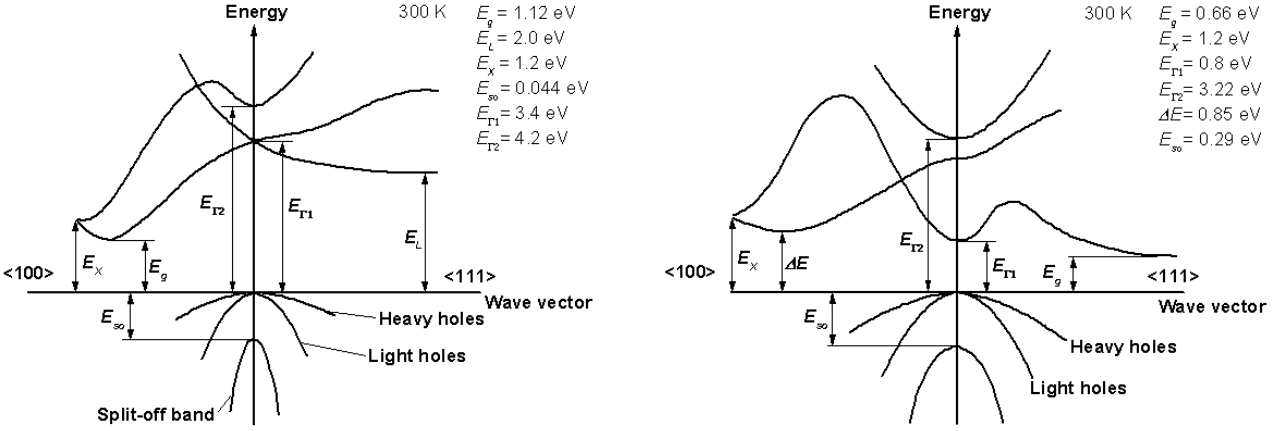
Energy
300 K
E_g = 1.12 eV
E_L = 2.0 eV
E_X = 1.2 eV
E_{so} = 0.044 eV
$E_{\Gamma1}$ = 3.4 eV
$E_{\Gamma2}$ = 4.2 eV
$E_{\Gamma2}$
$E_{\Gamma1}$
E_L
<100>
E_X
E_g
<111>
Wave vector
E_{so}
Heavy holes
Light holes
Split-off band
Energy
300 K
E_g = 0.66 eV
E_X = 1.2 eV
$E_{\Gamma1}$ = 0.8 eV
$E_{\Gamma2}$ = 3.22 eV
ΔE = 0.85 eV
E_{so} = 0.29 eV
<100>
E_X
ΔE
$E_{\Gamma2}$
$E_{\Gamma1}$
E_g
<111>
Wave vector
E_{so}
Heavy holes
Light holes

Figure I.26: Band diagrams of (left) silicon and (right) germanium. From [IOFFE].

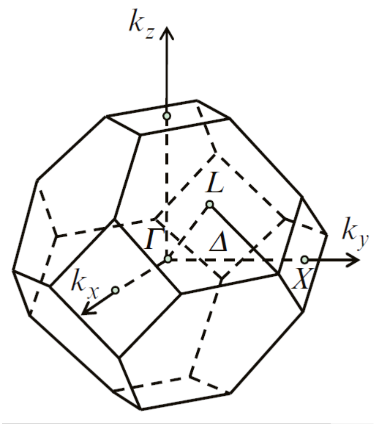

Figure I.27: Illustration of the 1st Brillouin zone.

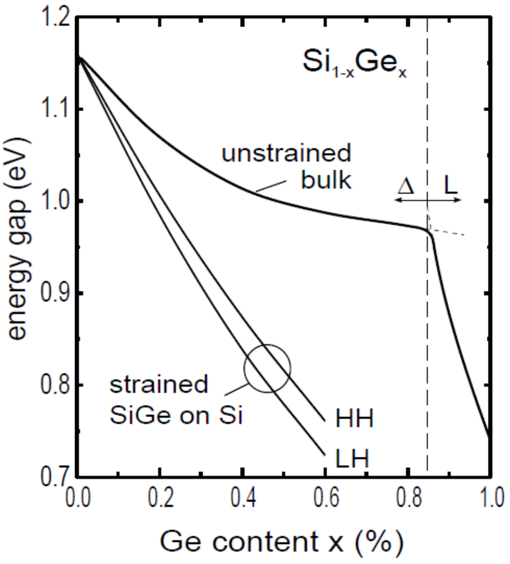

Figure I.28: Bandgap of unstrained and pseudomorphically strained SiGe versus Ge content. From [Schäfffler97].

I.2.2. Strain and Stress

The section aims to give some key elements about stress and strain. A more general description of stress and strain laws and formalism is given in *Appendice A*. After a brief introduction to the general laws of stress and strain, we give relations about stress and strain in SiO_2 and in SiGe that are specifically used in this manuscript. This section ends with an introduction to the formalism of the mathematical treatment of the influence of stress on carrier mobility.

I.2.2.1. Definition of Strain and Stress

Strain is defined as the relative lattice displacement created by deformation of the crystal structure of the material. Strain is fully characterized by the following second-order tensor:

$$\overset{=}{\varepsilon} = \begin{pmatrix} \varepsilon_{xx} & \varepsilon_{xy} & \varepsilon_{xz} \\ \varepsilon_{yx} & \varepsilon_{yy} & \varepsilon_{yz} \\ \varepsilon_{zx} & \varepsilon_{zy} & \varepsilon_{zz} \end{pmatrix}, \qquad \textbf{\textit{Equation I.13}}$$

with $\varepsilon_{\alpha\beta} = \dfrac{\partial u_\alpha}{\partial x_\beta}$, $u_\alpha = u_x, u_y, u_z$ and $x_\beta = x, y, z$ and where u_α is the displacement of the lattice point along x_α.

Stress is defined as the force responding to strain in a unit area and is fully defined by the second-order stress tensor:

$$\overset{=}{\sigma} = \begin{pmatrix} \sigma_{xx} & \sigma_{xy} & \sigma_{xz} \\ \sigma_{yx} & \sigma_{yy} & \sigma_{yz} \\ \sigma_{zx} & \sigma_{zy} & \sigma_{zz} \end{pmatrix}. \qquad \textbf{\textit{Equation I.14}}$$

As schematically represented *Figure I.29*, σ_{xy} (or τ_{xy}) is the force applied in the *x* direction to a unit area in the plane which is normal to the *y* direction.

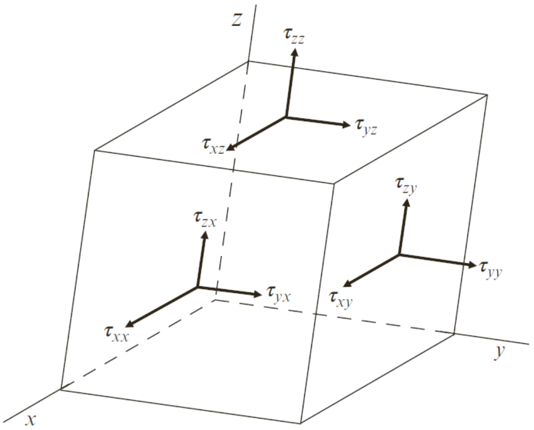

Figure I.29: Schematic representation of stress components on surfaces of an infinitesimal cube. From [Sun09].

Within the linear elastic theory, stress and strain are related by Hooke's law:

$$\overline{\overline{\sigma}} = \overline{\overline{\overline{\overline{C}}}}.\overline{\overline{\varepsilon}} \text{ or } \overline{\overline{\varepsilon}} = \overline{\overline{\overline{\overline{S}}}}.\overline{\overline{\sigma}},$$ **Equation I.15**

where $\overline{\overline{\overline{\overline{C}}}}$ and $\overline{\overline{\overline{\overline{S}}}}$ are the elastic moduli and compliances fourth-order tensors. $\overline{\overline{\overline{\overline{C}}}}$ and $\overline{\overline{\overline{\overline{S}}}}$ are inverse to each other.

I.2.2.2. Amorphous SiO_2

For a homogeneous and isotropic material such as SiO_2, strain and stress are related to each other by Young's modulus E and Poisson ratio ν:

$$\varepsilon_{xx} = \frac{1}{E}\left(\sigma_{xx} - \nu\left(\sigma_{yy} + \sigma_{zz}\right)\right)$$
$$\varepsilon_{yy} = \frac{1}{E}\left(\sigma_{yy} - \nu\left(\sigma_{zz} + \sigma_{xx}\right)\right)$$
$$\varepsilon_{zz} = \frac{1}{E}\left(\sigma_{zz} - \nu\left(\sigma_{xx} + \sigma_{yy}\right)\right)$$ **Equations I.16**

I.2.2.3. Strain of Pseudomorphic SiGe Films on Si

An usual case of this work, illustrated *Figure I.30,* is a SiGe layer biaxially strained to a (001) Si substrate.

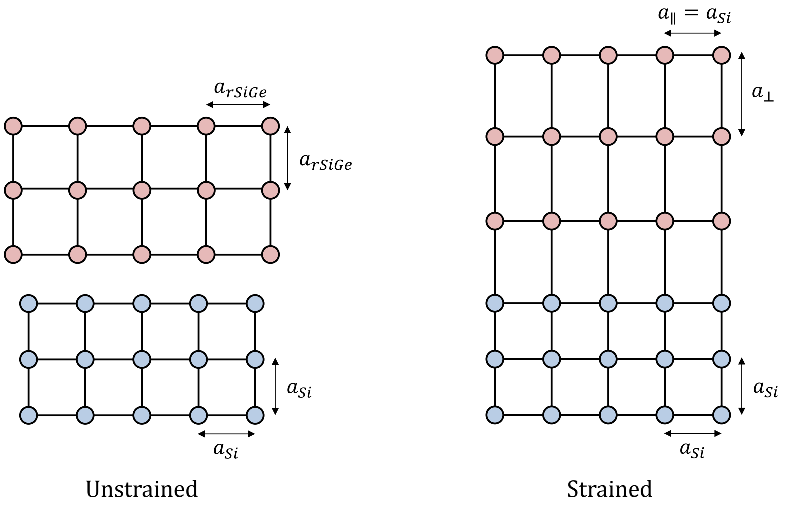

Unstrained

Strained

Figure I.30: Schematic illustration of a relaxed SiGe layer and a relaxed Si layer (left) and a pseudomorphic (fully strained) SiGe layer on relaxed Si (right).

The in-plane strain $\varepsilon_{\|}$ and out-of-plane strain $\varepsilon_{\perp}$ in the SiGe film are:

$$\varepsilon_{\|} = \frac{a_{\|} - a_{rSiGe}}{a_{rSiGe}}$$
$$\varepsilon_{\perp} = \frac{a_{\perp} - a_{rSiGe}}{a_{rSiGe}}.$$

Equations I.17

And where:

$$\varepsilon_{\perp} = \frac{2\nu}{\nu - 1}\varepsilon_{\|}.$$

Equation I.18

And:

$$\nu = \nu_{[001]} = 0.278 - 0.005x,$$

Equation I.19

where *x* is the Ge fraction and a_{rSiGe} the lattice parameter of relaxed SiGe.

Strain is sometimes confused with the in-plane deformation of the SiGe lattice parameter with respect to the Si lattice parameter. Indeed, strain of a SiGe layer is relative to the lattice parameter of relaxed SiGe and not to the Si lattice parameter. Deformations are the quantities usually measured by various strain characterization techniques such as Precession Electron Diffration (PED) and X-Ray Diffraction (XRD). Therefore, from now on, strain will always refer to the definitions given by *Equations I.17* while the in-plane deformation $d_{\|}$ and out-of-plane deformation $d_{\perp}$ are defined as:

$$d_{\|} = \frac{a_{\|} - a_{Si}}{a_{Si}}$$
$$d_{\perp} = \frac{a_{\perp} - a_{Si}}{a_{Si}}.$$

Equations I.20

When a SiGe layer is biaxially strained to a (001), the in-plane deformation is equal to zero while the out-of-plane deformation for a given Ge concentration can be calculated using Dismukes law and Poisson theory:

$$a_{\perp} = a_{rSiGe}(x)\left(1 + 2\frac{C_{12}}{C_{11}}\left(1 - \frac{a_{\|}}{a_{rSiGe}}\right)\right).$$

Equation I.21

Figure I.31 shows the out-of-plane deformation of a fully strained SiGe layer as a function of the Ge concentration.

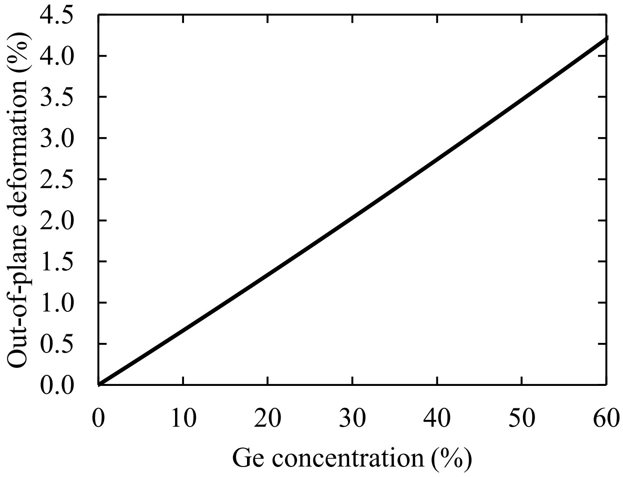

Figure I.31: Out-of-plane deformation of a pseudomorphic SiGe layer as a function of the Ge concentration.

I.2.2.4. Strain-altered Mobility of SiGe

Mobility dependency on stress and therefore on strain is usually described by the theory of the piezoresistive effect. Piezoresistivity is an effect of stress-induced resistivity change of a material that has two contributions [Sun09]: the geometrical change of the sample, and the resistivity change induced by strain-altered band structures (and subsequently the mobility). The latter is the dominant one in semiconductor materials. Piezoresistivity and stress are related by the following equation:

$$-\frac{\Delta\mu_i}{\mu} = \sum_{k=1}^{6} \pi_{ik}\tau_k ,$$

Equation I.22

where π_{ik} are the piezoresistance coefficients. The relevant stress conditions for this work are illustrated *Figure I.32*. As shown *Figure I.33*, the uniaxial stress along the [110] direction for a (001) surface-oriented substrate and [110] channel (also written (001)[110]) is the most beneficial in terms of mobility enhancement.

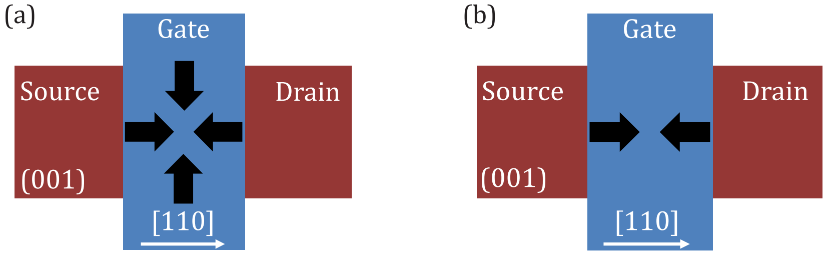

Figure I.32: Top-down schematic representation of (a) biaxial compressive stress for a (001) [110] channel and (b) uniaxial compressive stress along [110] for a (001)[110] channel.

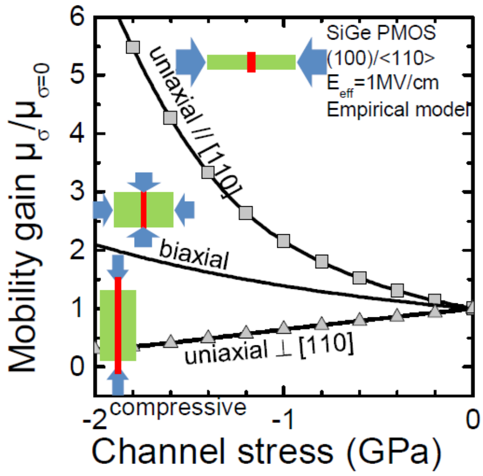

Figure I.33: Model of hole mobility variation in SiGe versus stress based on experimental piezoresistance coefficients. From [Andrieu14].

I.2.3. Epitaxy of SiGe on Si

Epitaxy refers to the deposition of a monocrystalline film on another monocrystalline film. Epitaxy is called hetero-epitaxy when the deposited material is different from the underlying material. As presented in *Section I.2.1.1.*, SiGe and Si have the same crystal structure and close lattice parameters. Thus hetero-epitaxy of SiGe on Si is possible. The most common technique used in microelectronics for growth of SiGe epitaxial layers on Si is Rapid Thermal Chemical Vapor Deposition (RTCVD). Typical gases that react to form SiGe are silane, SiH_4, or dichlorosilane SiH_2Cl_2, and Germane, GeH_4. *Figure I.34* shows a schematic view of the epitaxy process.

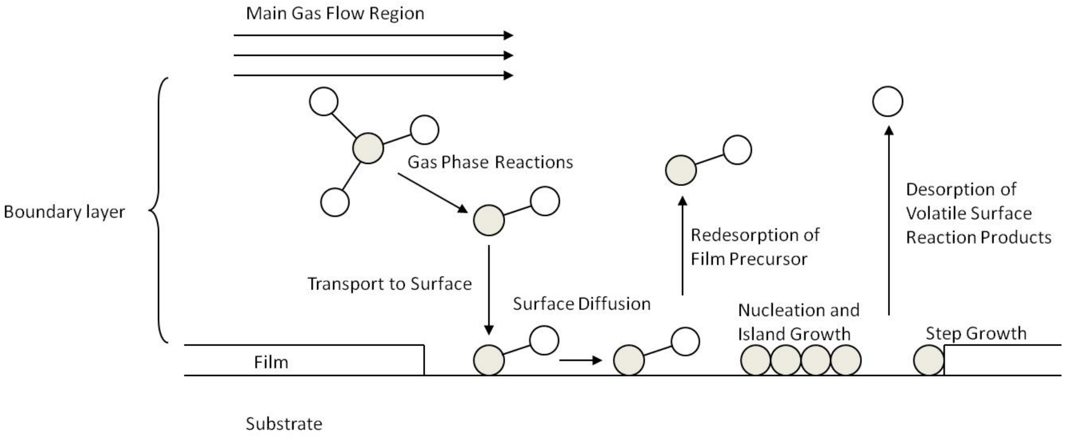
Main Gas Flow Region
Boundary layer
Gas Phase Reactions
Transport to Surface
Surface Diffusion
Redesorption of Film Precursor
Desorption of Volatile Surface Reaction Products
Nucleation and Island Growth
Step Growth
Film
Substrate

Figure I.34: Schematic illustration of the epitaxy process.

The lattice mismatch between SiGe and Si induces strain in both layers, which in turn alters thermodynamic properties of the growing film and therefore influences the growth morphology. We distinguish three main film morphologies:

- Pseudomorphic film:

The film is fully strained and its in-plane lattice parameter is equal to the one of Si. The out-of-plane lattice parameter is larger than the one of Si as described by Poisson's theory (see *Section I.2.2.3.*). *Figure I.35* shows a schematic representation of a pseudormorphic SiGe layer on Si.

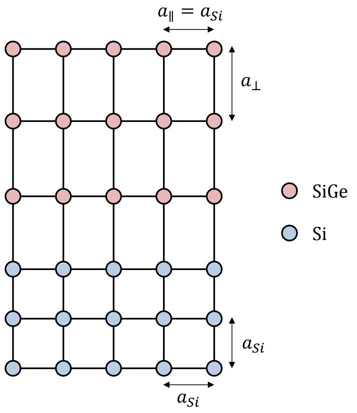
$a_{\parallel} = a_{Si}$
$a_{\perp}$
SiGe
Si
a_{Si}
a_{Si}

Figure I.35: Schematic representation of a pseudomorphic SiGe layer on top of a Si layer.

- Elastic relaxation:

As the film thickness increases, the pseudomorphic film becomes thermodynamically unstable and seeks a way to relax strain. Surface ondulations allow the accumulated energy to decrease. *Figure I.36* shows a schematic representation of the surface ondulations observed on a elastically relaxed SiGe layer on top of a Si layer.

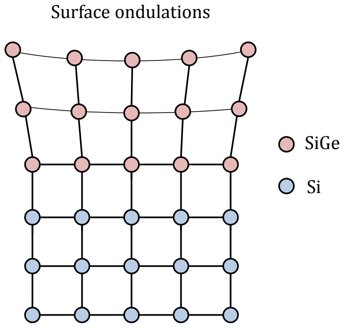
Surface ondulations
SiGe
Si

Figure I.36: Schematic representation of the surface ondulations observed on an elastically relaxed SiGe layer on top of a Si layer.

- Plastic relaxation:

When elastic relaxation is kinetically suppressed or becomes innefective, the strain relief proceeds by plastic relaxation, which refers to the formation of extended defects such as misfit dislocations (see *Figure I.37*). Introduction of misfit dislocations is the most efficient way to relieve strain, but because of the high energy cost associated with the dislocation formation, introduction of dislocations becomes energetically favorable only after a certain critical film thickness. Moreover, since the dislocation formation is a thermally activated process, the onset of plastic relaxation may be delayed to higher thicknesses due to kinetic constraints. In this case, the film is said to be metastable (see *Section I.2.4.2.*).

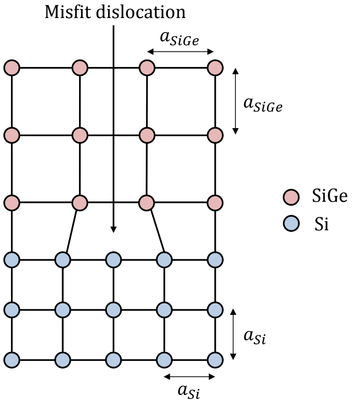

Figure I.37: Schematic representation of a plastically relaxed SiGe layer on top of a Si layer.

I.2.4. Plastic Strain Relaxation in Compressively Strained SiGe Films

After a brief introduction to the context and definition of this section, we give an overview of the two theoretical approaches to plastic strain relaxation: equilibrum and kinetic models. We then describe the mechanism of dislocation nucleation and associated specific crystal defects in the lattice structure of SiGe.

I.2.4.1. Introduction

Crystals defects are defects in the three-dimensional regular arrangement of atoms. They are classified according to their extension in space, i.e., zero, one, two and three dimensions:

- Zero-dimensional defects, also called point defects, include vacancies, which are missing atoms in the lattice, and interstitials, which are atoms incorporated in interstitial sites of the crystal lattice.
- One-dimensional defects, the so-called dislocations, occur when the regular arrangement of atoms is disturbed along a line. A schematic view of a dislocation is shown *Figure I.38.*
- Two-dimensional defects are grain and phase boundary.
- Three-dimensional defects are precipitates and inclusions.

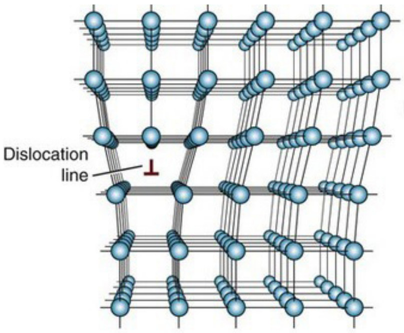

Figure I.38: Schematic view of an edge dislocation in a cubic crystal. A single vertical plane of atoms is missing and the dislocation line is located at the edge of the half plane.

This work focuses on dislocations induced by plastic relaxation in compressively strained SGOI layers formed by the condensation technique. Plastic relaxation decreases elastic strain in the layer and consequently lowers the hole mobility, and it also introduces defects that further reduce the hole mobility and may even kill transistor proper functionning in deeply-scaled transistors. Therefore, it is crucial to study the dependence of plastic relaxation of SGOI layers formed by the condensation technique on sample properties and condensation process conditions. Most of the theoretical and experimental studies are about plastic relaxation in heteroepitaxial SiGe layers on bulk Silicon. Our system, a SiGe layer sandwiched between a buried oxide layer and a thermal oxide, differs from heteroepitaxial systems because of the nature of both bottom and upper interfaces and also because of the process used to fabricate the layer.

I.2.4.2. The Equilibrium and Kinetic Models

There are two main theoretical approaches to plastic relaxation in strained layers:

- Equilibrium models based on energetic considerations only were firstly proposed [Matthews70][Matthews74]. A SiGe layer pseudomorphically strained with respect to Si has a certain amount of elastic strain energy that increases with the thickness of the SiGe layer. Above a critical amount of elastic strain energy, corresponding to a certain thickness called the critical thickness, introduction of plastic strain energy instead of elastic strain energy decreases the total energy of the layer and is therefore favorable. The most accepted expression of the critical thickness is the Matthews-Blakeslee one [Matthews74] (see *Figure I.39*). However, large discrepancies have been observed between theoretical critical thicknesses and experimental results [Bean84][Bai94]. The consensus today seems to be that the critical thickness cannot be based on energetic considerations only, and that kinetic barriers that may delay plastic strain relaxation have to be considered (the kinetic models described below).

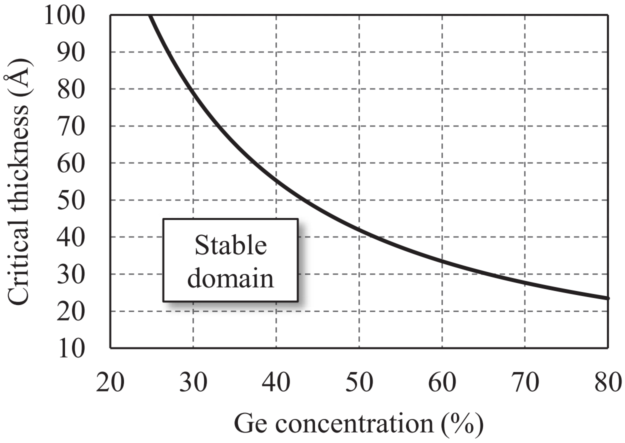

Figure I.39: Critical thickness of an epitaxial SiGe layer versus the Ge concentration calculated from the Matthews and Blakeslee model [Matthews74].

- Kinetic models consider both energetics of elastic strain and energetics and kinetics of dislocation nucleation, multiplication, glide and pinning [Dodson87][Houghon91][Wang01][Menéndez09]. Kinetic barriers to plastic strain relaxation are indeed particularly large in heteroepitaxial SiGe layers and may allow epitaxial growth of fully strained SiGe layers with thicknesses more than a decade above the equilibrium critical thickness (such as the one proposed by Matthews and Blakeslee). In this case, the system is said to be metastable and would return to the strain level defined by equilibrium models after thermal annealing. However, while equilibrium models cannot reproduce accurately most of actual epitaxial growth results, kinetic models suffer from practical limitations. Indeed, comparison with experiments and predictions are far more complexed with kinetic models because of the large number of unknown parameters. Moreover, except from the one published by Menéndez et al., they require numerical computation, making fitting to experimental data complicated.

I.2.4.3. Mechanisms of Plastic Strain Relaxation in Compressively Strained SiGe Layers

Today’s susbstrates feature very low densities of dislocations. Thus, it has been shown that technologically relevant plastic strain relaxation mechanisms are nuclation and glide of dislocations, and that dislocation multiplication from dislocations already present in the substrate and pinning can be neglected [Menéndez09]. The mechanism of dislocation nucleation, i.e. dislocation half-loop nucleation at the upper interface and its gliding and expansion within {111} planes of the SiGe layer, is illustrated *Figure I.40*. Inhomogeneities, such as impurities, local roughness, local higher Ge concentration due to the fluctuation of the distribution of Si and Ge atoms in the lattice, and point defects, increase the local stress and lower the activation energy of atomic displacements. Thus, sinks of dislocation half-loops are located at interfaces. In compressively strained SiGe layers, dislocation half-loops expand and glide within {111} planes because they are the denser ones and are thus favorable to atomic displacements. In order to attain equilibrium, the half-loops reach the bottom interface where they are split into three segments: two threading dislocations that extend from the bottom interface to the upper surface within {111} planes, and the misfit dislocation at the bottom interface. Dissociation of these dislocations into partial dislocations can occur as described in the following section.

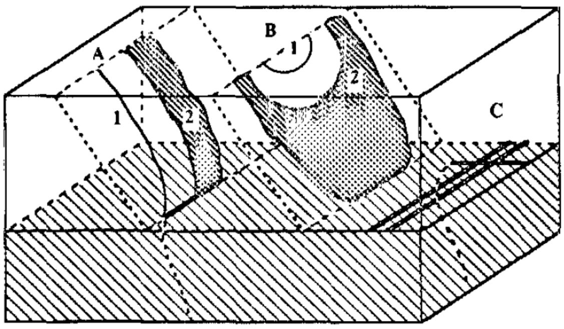

Figure I.40: Schematic representation in a (001) semiconductor of (A) the glide into a {111} plane of an existing dislocation, (B) the nucleation at the upper interface of a dislocation half-loop and its expansion into a {111} plane. Once the dislocation half-loop reaches the bottom interface, it is split into three segments, a misfit dislocation and two threading dislocations. (C) The misfit dislocation can be dissociated into two partial dislocation as described in the following section. From [Marée87].

I.2.4.4. Crystal Defects in SiGe Films

Every dislocation can be described by its dislocation vector $\vec{\xi}$ and its burgers vector $\vec{b}$. The burgers vector describes the shift of one part of the crystal with respect to the other one. It is quantitatively defined by the so-called burgers circuit illustrated *Figure I.41*. The burgers circuit is the additional step necessary to close the circuit in the reference lattice structure relative to the same lattice structure but with a dislocation.

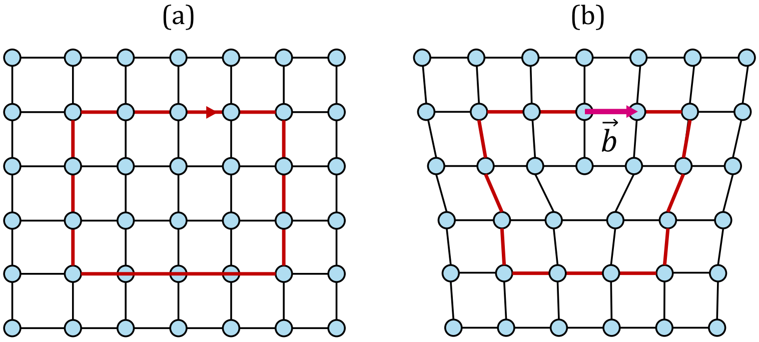

Figure I.41: Definition of the burgers circuit and the burgers vector by comparison of (a) a crystal without any dislocation with (b) the same crystal with a dislocation.

The above sections considered an elastic continuum while crystals are made of particular three-dimensional arrangements of atoms. Therefore, burgers vectors are usually lattice vectors. A dislocation has an intrinsic energy because of the elastic stress field around it. It was shown that the dislocation energy is roughly proportional to the square of its burgers vector. Thus, according to the Frank criterion, a dislocation whose burgers vector is $\vec{b}$ can be split into two dislocations of burgers vectors $\vec{b}_1$ and $\vec{b}_2$ if:

$$b^2 \rangle b_1^2 + b_2^2. \qquad \textbf{Equation I.24}$$

As a consequence, in SiGe layers whose growth direction is <100>, the dominating slip system is {111} and the stable burgers vector is a/2<100>, which is the minimum translation in <100> orientations. This dislocation is called a perfect 60° dislocation and has an angle of 60° between its dislocation line and its burgers vector [Matthews70].

As illustrated *Figure I.42 (a)*, the face-centered cubic (fcc) lattice is based on a ...ABCABCA... stacking sequence. If the correct sequence is interrupted, a stacking fault is formed. According to the Frank criterion, a 60° perfect dislocation can be dissociated into two partial dislocations whose burgers vectors are a/6<211> and a/2<1-12>, and whose angles are 90° and 30° respectively. The partial dislocations, called Shockley partial dislocations, are stacking faults gliding on {111} planes. One of the partial dislocation forms a low-energy second-nearest-neighbor stacking fault whose stacking sequence is ...ABC|BCA.... And the other one produces a high-energy nearest-neighbor stacking fault whose stacking sequence is ...ABC|CAB.... The distance between these two partial dislocations is obtained by balancing their formation energy and their repulsive energy.

Another way to produce a planar fault in the fcc lattice is to mirror the stacking sequence on one side of a {111} plane. Such a fault, called a twin, is illustrated *Figure I.42 (b)* and has the following stacking sequence type: ...ABC|BCACB....

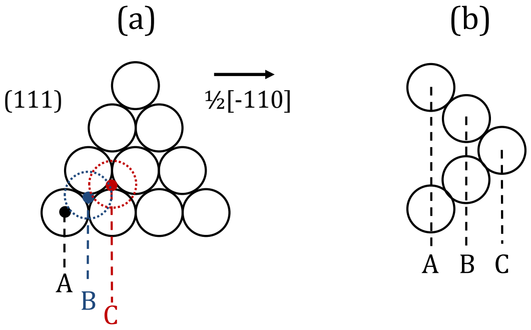

Figure I.42: (a) Arrangement of atoms on a {111} plane of a fcc lattice and (b) stacking sequence of a twin in the fcc lattice.

I.2.5. SiGe Interdiffusion

Interdiffusion is a key mechanism of oxidation of SiGe. This section starts by giving an insight about the driving forces of diffusion as well as atomic-scale diffusion mechanisms. Then, we focus on interdiffusion of SiGe since it is the specific diffusion regime during thermal oxidation of SiGe.

I.2.5.1. Introduction and Continuum Theory of Diffusion

Diffusion in solids is the transport of atoms or molecules from one point to another one. Diffusion is a complex and wide subject, and this section does not intend to give an in-depth description of it. It rather encompasses mechanisms and properties that are relevant to this thesis work. In this section, we only consider diffusion in monocrystalline SiGe that do not have extended defects, such as dislocations, that can act as diffusion short-circuits. We also do not take into account other driving forces such as electrical field or temperature gradient.

The diffusion flux is proportional to the chemical gradient and the chemical gradient is proportional to the composition gradient in dilute and ideal solid solutions [Mehrer07]. Diffusion tends to equalize concentrations of elements in the solid. The most common approach to diffusion is Fick's laws. The First Fick's law is:

$$\mathbf{J} = -D\nabla C, \qquad \textbf{\textit{Equation I.25}}$$

where $\mathbf{J}$, D and C are the flux of particles, the diffusion coefficient or diffusivity, and the particles concentration. Diffusion is driven by Brownian motion, and is therefore a thermally activated phenomenon. Diffusion depends on thermodynamic variables such as temperature, pressure and composition, as well as on strain. Diffusivity is usually found to follow an Arrhenius law:

$$D = D^0 \exp\left(-\frac{\Delta H}{k_B T}\right), \qquad \textbf{\textit{Equation I.26}}$$

where k_B is the Boltzmann constant, T is the temperature, D^0 is the pre-exponential factor, and ΔH is the activation enthalpy of the considered diffusing species. The physical interpretation of the activation energy and of the frequency factor is dependent on the considered diffusion mechanism and process, and is beyond the scope of this thesis work. Let us note that if several diffusion mechanisms are involved, for instance interstitial and vacancy mechanisms, the total diffusivity is the sum of the diffusivities associated with each diffusion mechanism.

Fick's second law is then retrieved by combining Fick's first law with the equation of continuity, which is another spelling of the law of conservation of matter. Fick's second law is:

$$\frac{\partial C}{\partial t} = \nabla.(D\nabla C). \qquad \textbf{\textit{Equation I.27}}$$

Most diffusion problems consists in solving Fick's second law, which is a second-order differential equation. Fick's laws are a purely continuum and phenomenological description of diffusion that do not derive from atomic-scale motion of particles. Comprehension of atomic-scale and discrete motion processes is also required for a proper use of Fick's laws, and is the object of the next section.

I.2.5.2. Atomic-Scale Diffusion Mechanisms

We have to consider atomic diffusion mechanisms because they strongly impact diffusivity. There are two main diffusion mechanisms in monocrystalline materials: non-defect mechanisms which refer to exchanges between lattice atoms and which are not believed to play any significant role in diffusion in SiGe, and native point defect (interstitials and vacancies) mechanisms [Kube10]. Interstitials are atoms incorporated in interstitial sites in the host lattice and vacancies refer to the absence of an atom at a lattice site. These native point defect diffusion mechanisms are represented *Figure I.44*. In the vacancy mechanism, the diffusing atom jumps into a neighboring vacancy lattice site, while in the interstitial mechanism, an interstitial atom jumps from an interstitial site to another one. Defects such as vacancies and interstitials may be present at thermal equilibrium, with Si supporting both vacancies and self-interstitials while in Ge, the vacancy diffusion mechanism predominates. These diffusion mechanisms can simultaneously contribute to diffusion in a given environment.

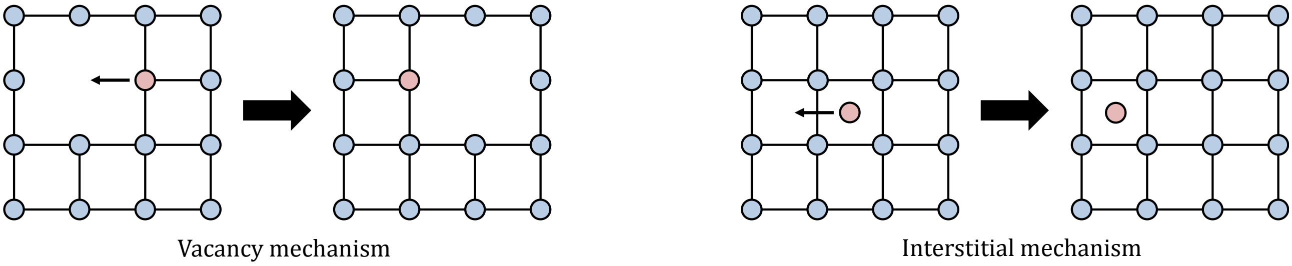

Figure I.44: Schematic representations of vacancy and interstitial diffusion mechanisms.

I.2.5.3. Interdiffusion in SiGe

Interdiffusion refers to diffusion processes in alloys with composition gradients. As will be shown *Section I.4.1.*, Si selective oxidation of SiGe induces interdiffusion in the underlying SiGe layer, hence the description of the main properties of SiGe interdiffusion in this section.

While interdiffusion is a single process described by a single interdiffusion coefficient, interdiffusion is actually driven by diffusion of Si and Ge atoms which have two different intrinsic diffusion coefficients [Merher17]. This apparent contradiction is solved when the reference frame and a vacancy flux is considered (the so-called Kirkendall effect) is considered. The interdiffusion coefficient accurately describes interdiffusion in a reference frame that is not the one of the laboratory, but the one moving with the vacancy flux. We also emphasize that the SiGe interdiffusion coefficient depends on the Ge concentration because the chemical environment of SiGe depends on the Ge concentration.

The first theoretical and mathematical description of interdiffusion in a binary alloy that takes into account the Kirkendall effect was proposed by Darken in 1948 [Mehrer07]. Without entering the details of his demonstration, the two Darken's equations relate the interdiffusion coefficient to the intrinsic and self-diffusion coefficients of the two elements of the binary alloy. Darken's equations provide a convenient framework for solving interdiffusion problems, such as the one of interdiffusion in SiGe. Darken's framework will be used for the numerical simulations of SiGe oxidation of *Section III.B.2.*.

Generally speaking, interdiffusion is SiGe increases with the Ge concentration because of the increase of the number of weaker Si-Ge and Ge-Ge bonds compared to the number of stiffer Si-Si bonds. Compressive strain also enhances SiGe interdiffusivity [Dong14]. We highlight that SiGe interdiffusivity is approximately exponentially dependent on both temperature, following an Arrhenius law, and Ge content.

Figure I.45 and *Figure I.46* show relaxed SiGe interdiffusivity and strained SiGe interdiffusivity versus Ge content at different temperatures and published by Dong et al. group.

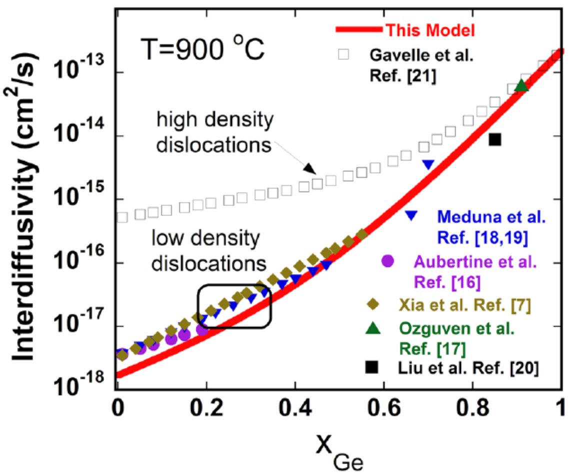

Figure I.45: Calculated SiGe interdiffusivity versus Ge content and comparison with various experimental data from literature. From [Dong12].

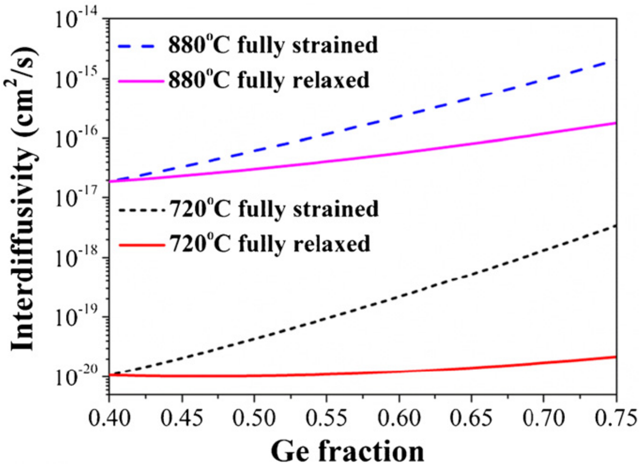

Figure I.46: Comparison of SiGe interdiffusivity versus Ge content in a SiGe layer on a fully relaxed $Si_{0.60}Ge_{0.4}$ substrate under fully relaxed and fully strained conditions and at two different temperatures. From [Dong14].

I.3. Properties of Thermal Oxides Grown on Si and SiGe

I.3.1. Bulk Thermal SiO_2

In this manuscript, SiO_2 always refers to amorphous thermally grown SiO_2, also called fused silica. The usual SiO_2 phase produced in CMOS manufacturing oxidation processes is composed of corner-shared SiO_4 tetrahedra connected together in a three-dimensional network. As illustrated *Figure I.47* and *Figure I.48*, the resulting structure features a strong short-range order with an average Si-O-Si bond angle of 145° and a bond angle range of 110° to 180°, but no long-range order. Thermally grown SiO_2 is thus considered amorphous. However, Tatsumura et al. and Munkholm et al. showed by performing X-Ray Scattering that the bulk of thermal SiO_2 retains the residual crystalline order of {111} planes of its parent Si crystal [Tatsumura04][Tatsumura05][Munkholm04]. They showed that there is no other residual crystalline order but the one originating from {111} planes and that high temperature annealing makes it disappear. They concluded that this residual crystalline order is sufficiently weak so that thermal SiO_2 should be conventionally considered amorphous.

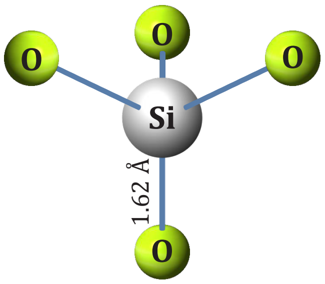

Figure I.47: Schematic view of the tetrahedron structure of thermal SiO_2.

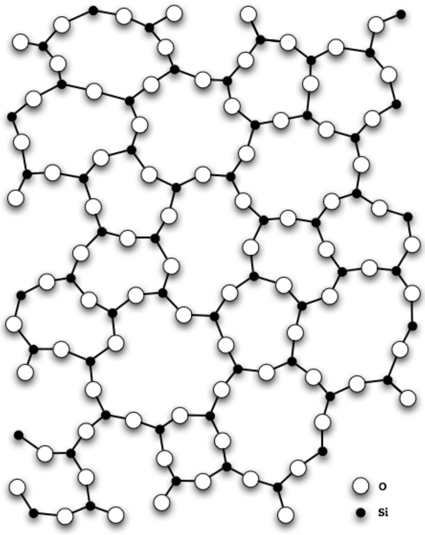

Figure I.48: Schematic view of amorphous SiO_2 showing no long-range order.

I.3.2. Si-Thermal SiO_2 Interface

The transition structure at the Si(100)-SiO_2 interface (about 1 nm-thick) cannot be considered abrupt in views of the oxide thicknesses studied in this work (from 1 nm to a few tens of nanometers). No atomic-scale structure model has gained widespread acceptance but several experiments and atomic-scale theoretical models have shed light on some of its properties, that are briefly introduced below:

- Oxidation states of Si as a function of depth into the interfacial layer have been investigated by X-ray Photoemission Spectroscopy (XPS) [Himpsel88][Rochet97][Oh01][Hirose07]. Oh et al. showed that Si^{1+} and Si^{2+} are located in the first layer of the interfacial layer while Si^{3+} species location extends into the second and third layers.
- The density of thermal SiO_2 have been measured by X-Ray Reflectivity (XRR) [Ajawi96][Kosowsky97]. They showed the existence of an approximately 1 nm-thick interfacial layer of higher density (between 2.3 $g.cm^{-3}$ and 2.4 $g.cm^{-3}$)
- Various atomistic models of the Si(100)-SiO_2 interface have been constructed using simulations methods [Bongiorno03].

I.4. The SiGe Condensation Technique

I.4.1. Introduction and History of the Condensation Technique

The condensation technique has been proposed for the first time in 2001 by Tezuka et al. [Tezuka01] from the Toshiba-MIRAI group as an innovative method for producing high-quality Germanium-On-Insulator (GeOI) or SiGe-On-Insulator (SGOI) buffer layers for the growth of tensely strained Si channels. In 2003, the idea to use the condensation technique to form a defect-free and compressively strained SiGe channel on insulator was published [Nakaharai03]. This technique was labelled "condensation" because the Ge content in the final SiGe layer may be higher than the one in the initial epitaxial layer. An appropriate term could have been "enrichment" instead of "condensation", because condensation also refers to the phase change from a gaseous phase to a liquid phase.

The condensation technique is described *Figure I.49*. After epitaxial growth of a 5-20 nm-thick fully strained SiGe layer on Si, thermal oxidation is performed. A Si-selective oxidation occurs and Ge atoms are rejected into the underlying SiGe film. Interdiffusion of Si and Ge in the underlying film tends to homogenize the Ge concentration because the BOx layer acts as a diffusion barrier. The SGOI layer thickness is also reduced because some Si is incorported into the growing oxide during the oxidation process.

Many research groups studied the condensation technique. A non-exhaustive list includes the CEA-LETI [Vincent08], the IMEC [Souriau08], the SIMIT [Di05], IBM [Bedell06], the University of Tokyo [Takagi10], Stanford University [Gunji11], and the IM2NP [David15].

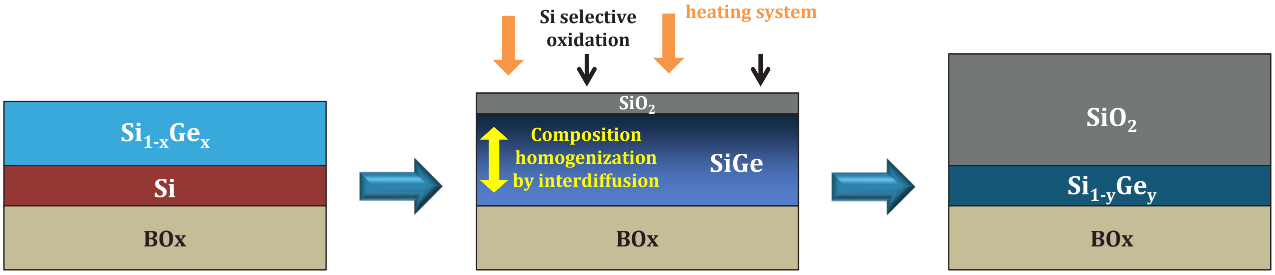

Figure I.49: Schematic representation of the condensation technique.

I.4.2. FD-SOI Process Flow Integration

One of the key advantages of the condensation technique for the FD-SOI process flow shown *Figure I.50* is that co-integration of Si-based nMOS and compressively strained SiGe-based pMOS transistors can be performed. Indeed, a SiN hard mask is deposited on top of nMOS areas to act as an oxidation barrier. We can highlight that, at the end of the condensation process, an area at the frontier between nMOS and pMOS regions is not homogeneous because of the lateral interdiffusion triggered by the thermal anneal of the condensation process. This issue is overcome thanks to the Shallow Trench Isolation (STI) fabrication step. As illustrated *Figure I.51*, the STI is fabricated in the frontier area between nMOS and pMOS areas and is larger than the width of this non-homogeneous area.

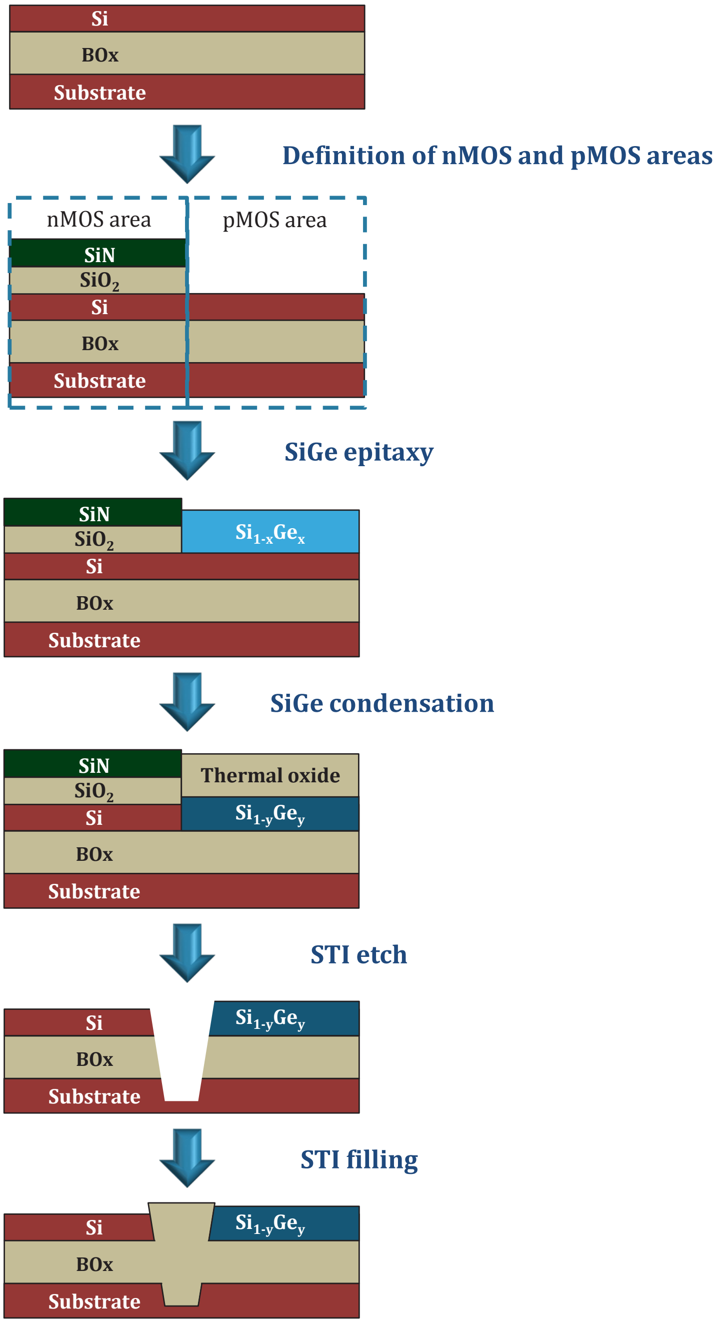
Si
BOx
Substrate
Definition of nMOS and pMOS areas
nMOS area
pMOS area
SiN
SiO2
Si
BOx
Substrate
SiGe epitaxy
SiN
SiO2
Si1-xGex
Si
BOx
Substrate
SiGe condensation
SiN
SiO2
Thermal oxide
Si
Si1-yGey
BOx
Substrate
STI etch
Si
Si1-yGey
BOx
Substrate
STI filling
Si
Si1-yGey
BOx
Substrate

Figure I.50: FD-SOI process flow showing co-integration of SGOI-based pMOS and Si-based nMOS. The figure does not show intermediary process steps, such as SiN deposition, for clarity considerations.

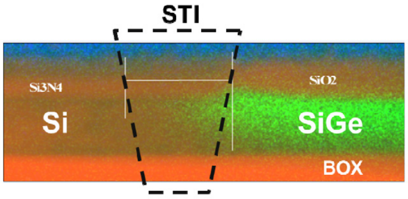
STI
Si3N4
Si
SiO2
SiGe
BOX

Figure I.51: STEM-EDX picture of the transition between the SGOI and SOI regions as well as the future location of the STI. From [Gourhant14].

I.5. Problematics of this Thesis Work

It has already been shown that the condensation technique is a powerful and convenient technique for local fabrication of fully strained SGOI layers. However, several challenges still need to be taken up for an efficient and optimized use of the technique in an industrial environment. Two main challenges were identified during this thesis work and are addressed in *Chapter III* and *Chapter IV* respectively. These two problematics are then split into two more fundamental studies (*Section III.A* and *Section IV.A*) and two other problematics that have more direct applications to advanced FD-SOI CMOS manufacturing (*Section III.B* and *Section IV.B*). They are presented in the following sections.

I.5.1. SiGe Thermal Oxidation

I.5.1.1. Study of the Mechanisms and Kinetics of SiGe Thermal Oxidation

The final SGOI layer composition and thickness must be well controlled for industrial CMOS manufacturing. Considering that the whole quantity of Ge is conserved during condensation (this will be shown *Section IV.A.3.*), the final SGOI composition depends on the amount of Si that is oxidized (this will be shown *Section IV.A.1.*). The total quantity of oxidized Si then depends on the thickness of the grown thermal oxide. It is therefore crucial to understand SiGe thermal oxidation kinetics when using industrial oxidation processes.

In spite of the widespread attention that has been devoted to the matter, there is an obvious lack of consensus regarding the oxidation kinetics of SiGe compared to that of Si. Indeed, a higher oxidation rate has been reported for dry oxidation of SiGe [Holland87][Kilpatrick97][Spadafora03], while some other authors have observed no difference between SiGe and Si [LeGoues89][Nayak92][Vincent07][Long12]. Several mechanisms have been proposed to explain oxidation kinetics of SiGe with respect to Si, but none of them has gained widespread acceptance. Moreover, the thickness of grown oxides range from a few nanometers to tens of nanometers depending on each publication, which makes comparison between published results difficult. *Section III.A* thus aims to bridge the gaps between these studies by covering various technology-relevant oxidation processes. We thus address in *Section III.A* the mechanisms and kinetics of thermal oxidation of SiGe by means of dry furnace oxidation, dry RTO and ISSG oxidation.

I.5.1.2. Application to Industrial Processes for Advanced FD-SOI CMOS Manufacturing

The second part of this chapter (*Section III.B*) presents two tools built from to the oxidation kinetics results of *Section III.A*. The first one is a graphic assessment of the oxide thickness and of the Ge diffusion length in SiGe, a key parameter of the evolution of the SiGe composition during oxidation, as a function of process parameters. It is designed for a convenient and quick evaluation of the relative importance of the Ge pile-up mechanism with respect to SiGe interdiffusion. Accurate prediction of the oxide thickness and SiGe composition profile by numerical simulation can be useful for both a finer understanding of the dynamics of oxidation (oxide growth and evolution of the SiGe composition profile) as well as for optimization of industrial processes. This is also addressed in *Section III.B*.

I.5.2. Strain and Crystal Quality of SGOI Films Fabricated by Condensation

I.5.2.1. Strain and Crystal Quality of Full-Sheet SGOI Films Fabricated by Condensation

As seen *Section I.1.3.*, high Ge content and fully strained SGOI layers are required for enhancing the hole mobility of pMOSFET FD-SOI transistors. Any atom displaced from its lattice site disrupts the crystal symmetry and may degrade the hole mobility as a consequence. Extended defects are recombination centers that degrade the mobility and may even prevent the device from functioning properly. It is therefore crucial to understand how the condensation process influences the final strain level and crystal quality of SGOI layers.

Strain and dislocations formation in SGOI layers formed by condensation as well as their dependence on initial and final layer properties (Ge concentration and SiGe layer thickness) and condensation process conditions have been assessed by several groups [Bedell04][Nakaharai06][Vincent07][Takagi10][Gunji11]. Most of these studies showed that the SGOI layer remains fully strained until a peak value, which depends on the initial SiGe concentration, SiGe thickness and condensation process conditions, is reached. The onset of strain relaxation was shown to be accompanied by dislocations formation and/or film buckling. However, the type of dislocation and the onset for for their formation vary from one publication to another. Moreover, these studies focused on condensation processes based on dry furnace oxidation, while lower thermal budget oxidation processes, such as dry Rapid Thermal Oxidation (RTO) and In-Situ Steam Generation (ISSG) oxidation, are preferred in today's semiconductor manufacturing.

We thus propose in *Section IV.A* to compare the strain level and the crystal quality of SGOI layers formed by condensation processes based on two industrial oxidations processes, i.e. dry RTO and ISSG oxidation.

I.5.2.2. Conservation of Strain of SGOI Films during Co-Integration of nMOS and pMOS Transistors

Strain, SGOI crystal quality and electrical quality of SGOI-BOx and SGOI-gate stack interfaces are required at the very end of chip manufacturing in order to reach high pMOS electrical performances. Indeed, further processing to fabricate both nMOS and pMOS on the same chip may alter the electrical properties of the SGOI channel. The effects of processes that immediately follow the condensation process (see *Figure I.50*) on the properties of the

SGOI layer at the end of chip manufacturing may be strongly correlated to the properties of the SGOI layer right after the condensation process.

As will be detailed in *Section IV.B*, strain relaxation of the SGOI layer after STI etch at the edge of pMOS active areas has been evidenced and shown to be detrimental to final pMOS electrical performances. It was suggested that the condensation process, which is performed a few processing steps before the STI etch, is most probably related to this phenomenon [Usuda13][Boureau16]. Two possible causes based on properties of the SGOI layer and of its interfaces with the thermal oxide and the BOx layer were identified and are thus studied in *Section IV.B*.

Conclusion of Chapter I

The MOSFET technology has been introduced and its limitations to further downsizing have been described. New transistor architectures and high mobility channels, two main paths for enhancement of transistor performances, were reviewed. Among these performance "boosters", the benefits of using compressively strained SGOI films as channel material for p-type MOSFETs were presented. Specificities of the condensation technique, which allows the fabrication of SGOI films with possibly high strain levels, were described. Finally, the two main challenges of this thesis, which are addressed in *Chapter III* and *Chapter IV*, were defined:

- Understanding and controlling the mechanisms and kinetics of thermal oxidation of SiGe.

- Fabricating highly strained and high crystal quality SGOI films by the condensation technique.

« N'acceptez pas que l'on fixe, ni qui vous êtes, ni où rester. Ma couche est à l'air libre. Je choisis mon vin, mes lèvres sont ma vigne. Soyez complice du crime de vivre et fuyez! »

Alain Damasio, La Horde du Contrevent

Chapter II - SiGe Thermal Oxidation Processes, Characterization Techniques and Simulation Method

Introduction to Chapter II **60**

II.1. SiGe Epitaxy Processes **61**

II.2. Thermal Oxidation Processes **61**
- II.2.1. Introduction 61
- II.2.2. Dry Furnace Oxidation 62
- II.2.3. Rapid Thermal Oxidation (RTO) 63

II.3. Characterization Techniques **65**
- II.3.1. Spectroscopic Ellipsometry 65
- II.3.2. X-Ray Reflectivity (XRR) 66
- II.3.3. X-Ray Photoelectron Spectroscopy (XPS) 66
- II.3.4. Raman Spectroscopy 68
- II.3.5. Geometric Phase Analysis (GPA) of HRTEM Images 69

II.4. Characterization Techniques using Large-Scale Facilities **72**
- II.4.1. Resonant Soft X-Ray Reflectivity (R-SoXR) 72
- II.4.2. Neutron Reflectivity 75
- II.4.3. Medium Energy Ion Scattering (MEIS) 76

II.5. Simulations by the Finite Element Method (FEM) **80**
- II.5.1. Introduction to the Finite Element Method (FEM) 80
- II.5.2. Simulation of SiGe Oxidation 80

Conclusion of Chapter II **82**

Introduction to Chapter II

Various processes and characterization techniques and a simulation tool were used to address the four problematics defined in *Section I.A.*. Techniques I personally used, either for the measurement and/or the analysis, are described in this chapter. Techniques used for characterizations I was only requester of and not involved with are presented in *Appendices*.

This chapter starts by describing the processes used to fabricate samples, with a focus on the thermal oxidation processes used in this work, i.e. dry furnace oxidation, dry Rapid Thermal Oxidation (RTO) and In-Situ Steam Generation (ISSG) oxidation.

Then, characterization techniques using equipment considered as "common" equipment are presented. Ellipsometry is the most used technique to measure thicknesses of films fabricated during this thesis work, especially thermal oxides in *Section III.A.*. X-Ray Reflectivity (XRR) measurements using standard tools were also performed to measure the thicknesses of various films, including thermal oxides for comparison with ellipsometry, and especially SGOI films fabricated by condensation in *Chapter IV*. XRR is only briefly presented as this technique is more thoroughly described later in *Section II.4.1.*. X-Ray Spectroscopy (XPS) allowed us to study the chemical composition of thermal oxides grown on SiGe in *Section III.A.3.*. Raman spectroscopy is a powerful technique for evaluation of strain, especially for very thin films (10 nm and below) when X-Ray Diffraction (XRD) is not adequate. Raman spectroscopy was thus used to measure strain levels of SGOI films fabricated by condensation in *Section IV.A.*. And finally, Geometrical Phase Analysis (GPA) of High-Resolution Transmission Electron Microscopy (HRTEM) images is introduced. We performed this analysis on a few SGOI samples of *Section IV.A.* in order to compare strain levels retrieved by GPA with the ones measured by Raman spectroscopy, and in order to reveal crystal defects such as dislocations.

Techniques that required the use of large-scale facilities are then described. It starts with XRR experiments performed on SEXTANTS beamline at Soleil synchrotron in order to measure the density of thermal oxides (*Section III.A.5.*). Neutron Reflectivity was used to identify whether or not there is hydrogen in SGOI films. The experiments were performed on D50 beamline at Institut Laue Langevin (ILL) nuclear facilities. Medium Energy Ion Scattering (MEIS) experiments were carried out at MEIS facilities at LETI, Grenoble, to study the depth distribution of crystal perturbations and defects of SGOI films in *Section IV.A.*.

Finally, a simulation tool based on the Finite Element Method (FEM) was developed in COMSOL environment in order to be able to perform numerical simulations of SiGe oxidation (*Section III.B.2.*). The FEM and the environment of the simulation tool are thus described in this chapter.

II.1. SiGe Epitaxy Processes

For hetero-epitaxy on bulk Si, thin SiGe films were grown on 300 mm bulk {001} Si substrates in an industrial single wafer reactor (Centura from Applied Materials) using Rapid Thermal Chemical Vapor Deposition (RTCVD) techniques. All SiGe epitaxy processes used in this work are based on processes developed at STMicroelectronics before this thesis work.

Prior to deposition, Si surfaces were prepared by an in-situ high temperature bake at 1040°C for 120 seconds. Two epitaxy processes were used to grow SiGe films of two different compositions. $Si_{0.7}Ge_{0.3}$ films were grown at 630°C using H_2 gas carrier and Germane (GeH_4) and to Dichlorosilane (DCS, SiH_2Cl_2) precursors. For growth of $Si_{0.9}Ge_{0.1}$ films, Silane precursor (SiH_4) was used instead of DCS and the growth temperature was raised to 700°C in order to reach a reasonable growth rate.

As for hetero-epitaxy on SOI substrates, another surface preparation was used because the high temperature bake would roughen or disrupt the SOI film. Firstly a standard HF-RCA clean was performed, and an in-situ dry cleaning process called SiCoNi [Labrot16] was then used. SiGe with about 30% Ge concentration were grown at 630°C using DCS and GeH_4 precursors.

These epitaxy processes were performed by Clément Pribat and Yves Campidelli from STMicroelectronics. Films composition, thickness and roughness were measured by X-Ray Diffraction (XRD) and Spectroscopic Ellipsometry techniques.

II.2. Thermal Oxidation Processes

II.2.1. Introduction

In semiconductor manufacturing, the tolerance of chips being fabricated to high temperature and/or long oxidation durations depend on the target application. The impact of a thermal process in the chip is usually assessed by an abstract and qualitative notion called thermal budget. The thermal budget may be represented by the couple temperature-duration. The higher the oxidation temperature and duration are, the higher the thermal budget is. Establishing relative comparisons of the thermal budget of various oxidation processes is usefull for developing processes for industrial semiconductor manufacturing.

Two main families of oxidation processes are distinguished: furnace oxidation which has the highest thermal budget because of slow temperature ramp up and down (see *Table II.1*), and Rapid Thermal Oxidation (RTO). RTO systems use incoherent light from a honeycomb halogen lamp source to heat up a single wafer located below the lamp head (see *Figure II.1*). Such a system offers drastic reduction of the thermal budget compared to furnace oxidation thanks to its much lower thermal mass. Less common oxidation processes, such as low temperature oxidation under UV or laser light exposure, are not examined in this manuscript.

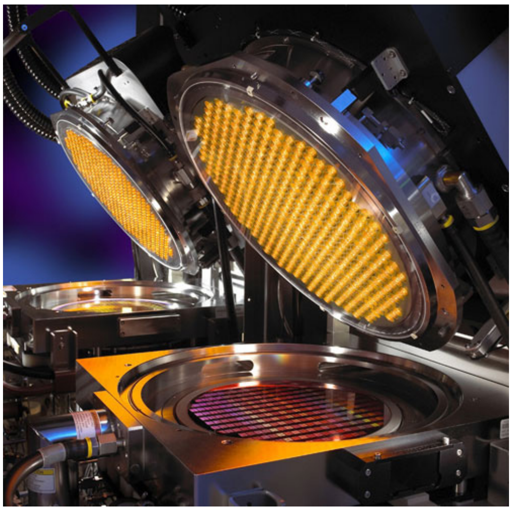

Figure II.1: Picture of a RTO tool in open situation. The honeycomb lamp head is on top while the processed wafer is below.

Oxidation Technique	Number of processed wafers in a single run	Oxidation plateau duration	Typical working temperature range	Temperature ramp up and ramp down
Furnace oxidation	Batch (100 wafers)	From tens of minutes to hours	From 800°C to 1200°C	From 10°C/min to 50°C/min
Rapid Thermal Oxidation (RTO)	Single wafer	From a few seconds to a few minutes	From 800°C to 1200°C	From 10°C/second to 50°C/second

Table II.1: Comparison of some technical specifications of furnace oxidation and RTO.

Then, we have to distinguish oxidation processes depending on the gases introduced into the chamber. The three oxidation atmospheres used in this study are:

- Dry oxidation: the atmopshere is pure O_2 or O_2 diluted in N_2.
- Wet oxidation: H_2O is introduced into the chamber. it is only used in furnace oxidation systems.
- In-Situ Steam Generation (ISSG): H_2 and O_2 are introduced into the chamber and react with each other inside it. ISSG is only used in RTO systems.

We summarize *Table II.2* the main thermal oxidation processes presented above.

	Dry Oxidation: O_2	**Wet Oxidation: H_2O**	**ISSG: $H_2 + O_2$**
Furnace Oxidation	✓	✓	
Rapid Thermal Oxidation (RTO)	✓		✓

Table II.2: Technology system along with the oxidizing gases introduced into the chamber used in the semiconductor industry.

Prior to any oxidation process, a standard HF-SPM-SC1-HCl cleaning process was performed. It resulted in the formation of an approximately 1 nm-thick chemical oxide on top of the SiGe film.

II.2.2. Dry Furnace Oxidation

Furnace oxidation was performed at 900°C in a TEL FORMULA Furnace. The temperature is the one of the O_2 gas. For each SiGe oxidized film, Si monitor wafers were oxidized in the same conditions. To ensure the relevance of a comparison with RTO processes, the maximum temperature ramp allowed was used and the chamber was filled with O_2 at the end of the temperature ramp up in order to reach one atmosphere of pure oxygen at the beginning of the oxidation plateau. A N_2 purge was immediately started at the end the oxidation plateau. Oxidation during the temperature ramps was thus kept to a minimum. A typical temperature-time profile of a dry furnace oxidation process is shown *Figure II.2*.

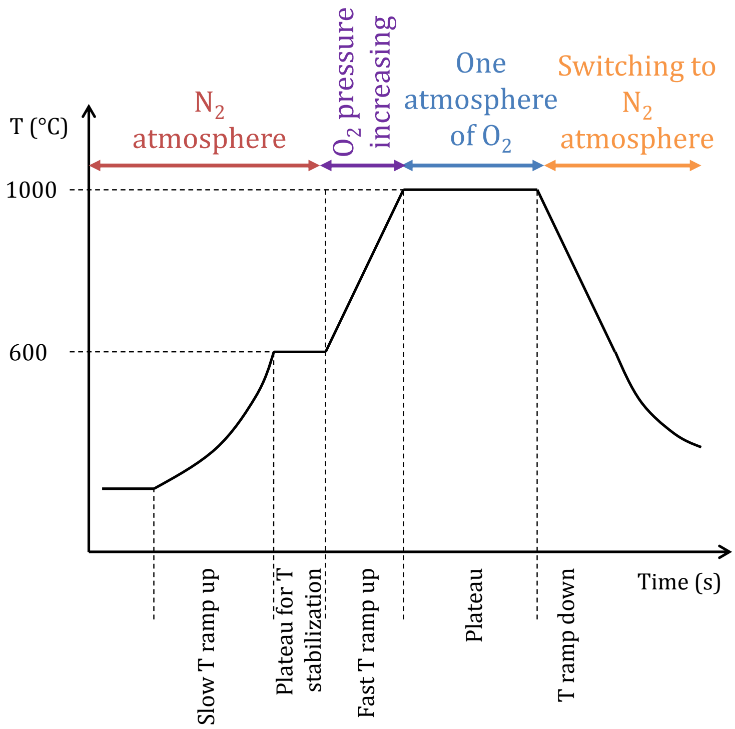

Figure II.2: Typical temperature-time profile of a dry furnace oxidation process.

II.2.3. Rapid Thermal Oxidation (RTO)

For RTO processes, it has been shown that the heat redistribution length is much larger than the light absorbing depth, and therefore that the temperature is uniform across the wafer thickness and that it can be extracted by measuring the emissivity of the back side of the wafer (by use of an instrument called pyrometer) [Borisenko97]. The wafer is also constantly rotating to allow good circular uniformity. Two RTO processes were used in this study.

II.2.3.1. Dry Rapid Thermal Oxidation (RTO)

A typical temperature-time profile of a dry RTO process is shown *Figure II.3* and has the following steps:

- It starts with a first slow temperature ramp up until reaching 550°C. In this regime, the power of the lamp is handly fixed.
- Then, there is a plateau of a few seconds at 550°C to allow the temperature to be uniform over the whole wafer surface and the temperature monitoring system (based on a pyrometer as described above) to stabilize.
- During the second temperature ramp up, the power of the lamp is controlled by a closed loop system that constantly compares the set temperature-time profile and the measured one. The temperature ramp up is usually around 50°C.s^{-1}.
- When the target temperature is reached, there is a plateau in the temperature-time profile controlled by the closed loop. The oxidation time given in this manuscript is the duration of this plateau.
- The first temperature ramp down until 550°C is controlled by the closed loop.
- Below 550°C, the temperature ramp down is in open loop with a handly set lamp power.

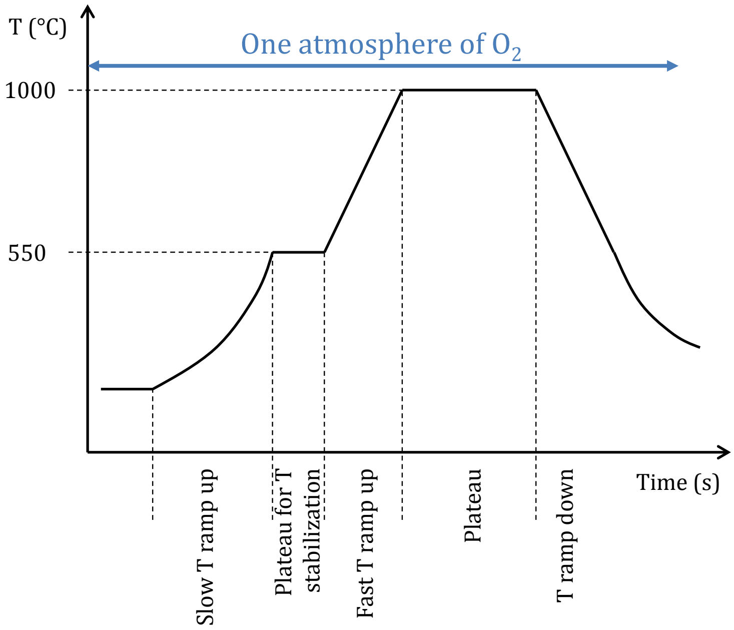
T (°C)
One atmosphere of O_2
1000
550
Time (s)
Slow T ramp up
Plateau for T stabilization
Fast T ramp up
Plateau
T ramp down

Figure II.3: Typical temperature-time profile of a dry RTO process.

Dry RTO was performed in a single wafer rapid thermal equipment (Radiance chamber from Applied Materials). The oxidizing atmosphere was 740 Torr of pure O_2 and the temperature of the wafer was monitored by a closed loop system taking as input the measurement of the emissivity of the back side of the wafer. The set atmosphere inside the chamber was reached before the temperature ramp up. Temperature ramp up and ramp down were between 25°C/s and 75°C/s to ensure that oxidation during the temperature ramps is negligible compared to oxidation during the oxidation plateau.

II.2.3.2. In-Situ Steam Generation Oxidation

ISSG oxidation was also performed into a Radiance chamber from Applied Materials. For this process, a mixture of 33% H_2 and 66% O_2 atmosphere with a total pressure of 7 Torr was used. Temperature ramps and monitoring procedure were similar to the ones of dry RTO processes. Below 600°C, the atmosphere was pure O_2 at low pressure, and H_2 was added only after the temperature exceeded 600°C, as illustrated on th temperature-time profile *Figure II.4*.

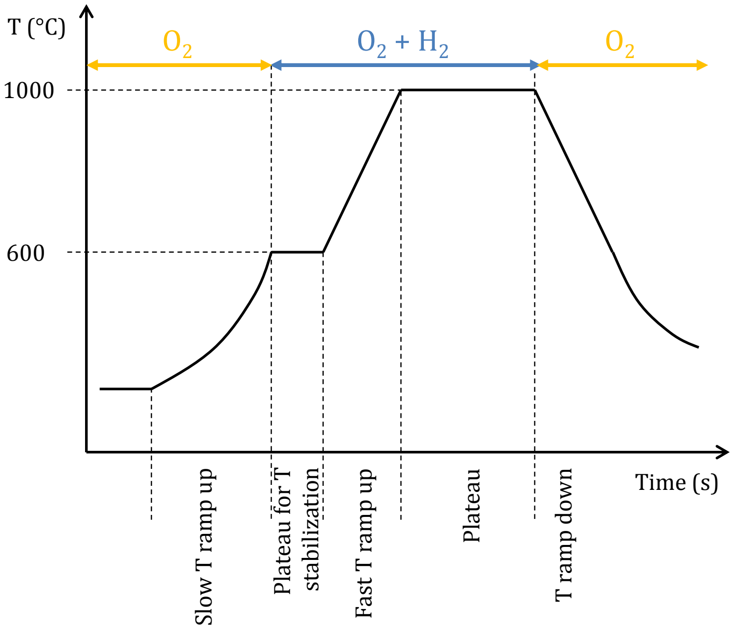
T (°C)
O_2
$O_2 + H_2$
O_2
1000
600
Time (s)
Slow T ramp up
Plateau for T stabilization
Fast T ramp up
Plateau
T ramp down

Figure II.4: Typical temperature-time profile of a ISSG oxidation.

II.3. Characterization Techniques

II.3.1. Spectroscopic Ellipsometry

Ellipsometry is a non-destructive optical characterization technique based on the measurement of the change of light polarization upon a reflection on a surface sample. Ellipsometry can be separated into two modes: Single Wavelength Ellipsometry (SWE) and Spectroscopic Ellipsometry (SE). SWE is commonly considered as the characterization technique for measuring film thicknesses since it is non-destructive, relatively fast, possibly in-line, and one of the most accurate thickness measurement techniques. However, it is highly model-dependent and input parameters must be carefully calibrated. SE allows to study more complex structures such as multilayer structures and allows access to data such as roughness or homogeneity.

The output of an ellipsometer is composed of two ellipsometric angles, Ψ and Δ, which are related to the optical indices of the sample. These angles are defined by the relation:

$$\frac{r_p}{r_s} = \tan\psi \exp(i\Delta), \qquad \textbf{\textit{Equation II.1}}$$

where r_p and r_s are the Fresnel reflection coefficients for a parallel and a perpendicular polarization respectively. The sample is described as an optical element by its Jones matrix:

$$J = \begin{pmatrix} r_p & 0 \\ 0 & r_s \end{pmatrix}. \qquad \textbf{\textit{Equation II.2}}$$

A schematic illustration of the principles of ellipsometry is shown *Figure II.5*.

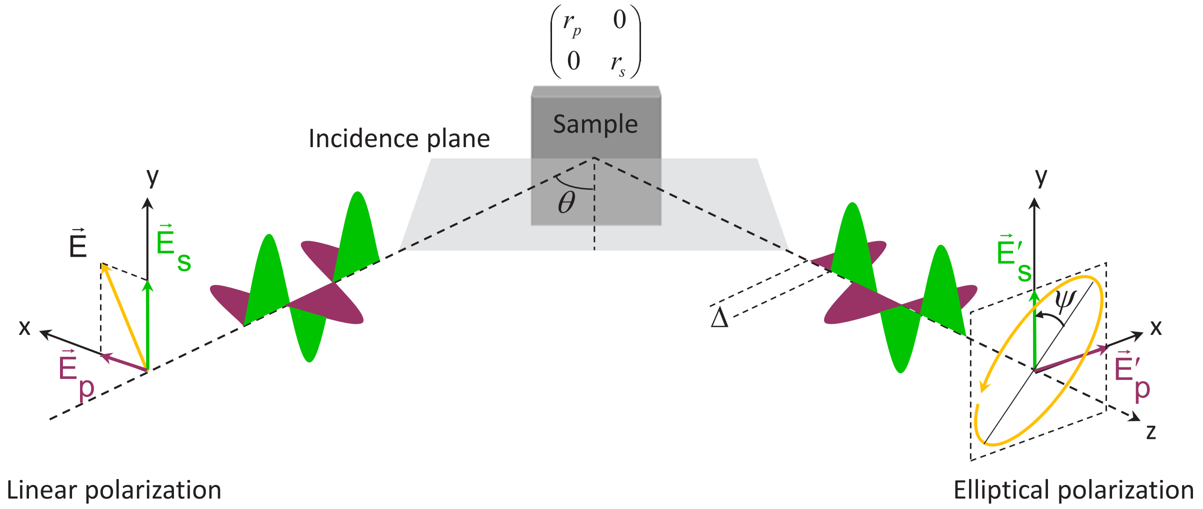

Figure II.5: Illustration of ellipsometry principles. θ is the angle of incidence. The sample is optically described by its Jones matrix. Δ and Ψ are the ellipsometry angles.

In this study, SE spectra were acquired between 240 nm and 780 nm on a Nanometrics ATLAS II. Oxide layers, either thermal oxide layers grown on SiGe or BOx layers, were considered to be pure stoichiometric amorphous layers whose optical constants were fixed to known values (see *Figure II.6*).

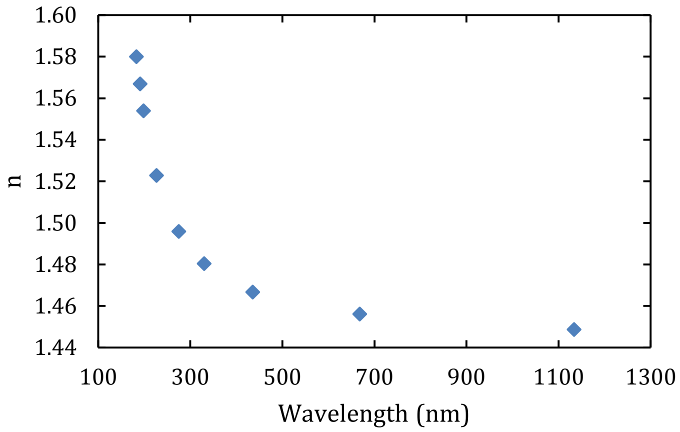

Figure II.6: Thermal SiO_2 optical index as a function of wavelength.

We used SiGe optical constants published by Nolot et al. [Nolot14] and treated the composition of the SiGe layers as unknowns. When non-homogeneous SiGe layers were expected, two or three SiGe layers were used for the fitting model in order to improve the fitting quality.

These measurements were performed with the help of Francesco Abbate from STMicroeletronics.

II.3.2. X-Ray Reflectivity (XRR)

X-Ray Reflectivity (XRR) is a thin film characterization technique based on the measurement of the reflectance of a multilayer system. The reader is referred to *Section II.4.1.* for a more thorough description of the technique. In-line (inside STMicroelectronics Crolles clean room) and off-line (at LETI) XRR characterization has been performed to measure the thicknesses of layers of various samples of this study. 0°-4° θ scans were acquired on a commercial Jordan Valley JVX7300 equipment for in-line measurement and on a Empyrean Panalytical equipment for off-line measurement. The X-Ray source uses the K-alpha emission line of copper, at a wavelength of 1.54056 Å. Reflectivity spectra were fitted with the commercial software of each equipment (JVXRR Simulator for the Jordan Valley and X'Pert Reflectivity for the Empyrean Panalytical). Fitting was limited to 0°-2° θ scans because the signal-to-noise ratio was too low above 2°. Similarly to spectroscopic ellipsometry, two or three SiGe layers were used for the fitting model in order to improve the fitting quality when non-homogeneous SiGe layers were expected.

II.3.3. X-Ray Photoelectron Spectroscopy (XPS)

X-Ray Photoelectron Spectroscopy (XPS) is a surface-sensitive chemical analysis technique based on the measurement of the kinetic energy of electrons ejected from the sample surface upon irradiation by X-Ray photons of known energy hν. This effect, known as the photoelectric effect and evidenced by Hertz (1887) and explained by Einstein (1935), corresponds to the ejection of an electron, called photoelectron, from its atomic orbital as a consequence of the absorption of a photon whose total energy is transferred to this electron. The incident photon energy (in the keV range) being known, the measurement of the kinetic energy of the photoelectron allows extraction of the binding energy of the core electron (see *Figure II.7*).

The binding energy of a core electron depends on both the element and the chemical environment of this element (such as its oxidation state). Careful analysis of XPS peak energies and shapes thus permits measurement of the composition of a sample surface and gives information about the chemical environment of each element. The depth sensitivity of the XPS technique is limited by the inelastic mean free path of an electron in a material, which is about 10 nm. XPS peaks are labelled with the element, the orbital of the ejected core electron, and when necessary information on the chemical environment of the element.

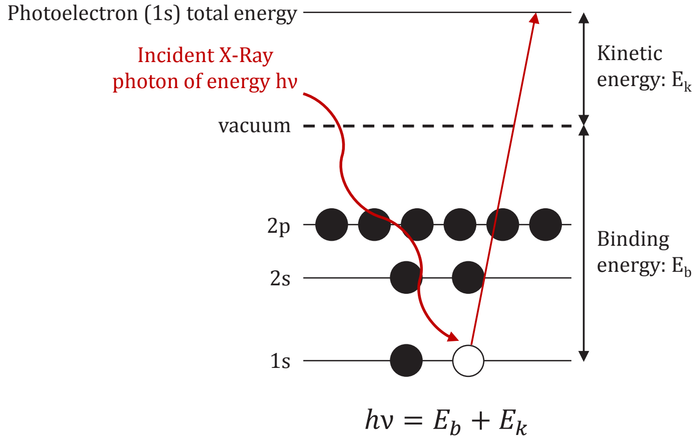

Figure II.7: Schematic illustation of the photoelectric effect. An electron (open circle) is ejected with a kinetic energy E_k from the 1s orbital.

For the quantitative analysis of Ge3d spectra acquired with the in-line XPS tool at STMicroelectronics Crolles clean room, a Shirley background from 27 eV to 31 eV was subtracted from the raw data. All spectra shown in this manuscript are data after subtraction of the background. Each spectrum is then decomposed into four peaks:

- A metallic Ge3d peak around 29.9 eV [Moulder92].
- A peak around 34 eV that we associate with the fourth oxidation state of Ge, and that we label Ge3d4+. We indeed always found a chemical shift of this peak with respect to the metallic Ge3d one of about 4.25 eV, close to values reported in the literature for the fourth oxidation state of Ge [Prabhakaran00]. We therefore fixed the chemical shift of the peak to 4.25 eV with respect to the metallic Ge3d peak.
- A Ge3d peak with an intermediary oxidation state was used for a proper fitting result only and referred as Ge3d$^{1\text{-}3+}$.
- An O2s peak at about 26 eV, which may also include hydroxide components [Moulder92].

All peak shapes were chosen to be pseudo-Voigt functions that allowed proper fit for all acquired spectra. *Figure II.8* shows an experimental spectrum with the associated background and the peaks extracted from the fitting procedure.

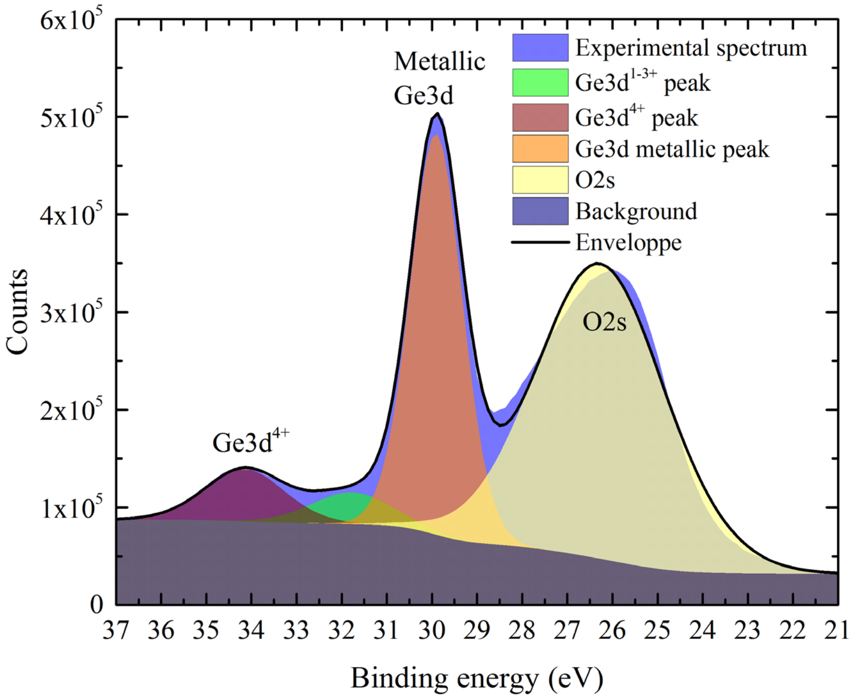

Figure II.8: Spectrum around the energy of the Ge3d XPS peak of a $Si_{0.7}Ge_{0.3}$ sample oxidized at 1100°C for 10 seconds by means of dry RTO. The measured oxide thickness is 75 Å. The envelope refers to the fitted spectrum.

XPS spectra were acquired on the direction normal to the sample surface with an in-line XPS Revera Vera-Flex II in STMicroelectronics Crolles clean room for the study discussed *Section III.A.3.* and on a direction at 45° with respect to the normal to the surface with a Versaprobe II at LETI for the study of *Section IV.B.2.*. Both equipements use a monochromatic source at 1486.6 eV. The measurements on the Versaprobe II were carried out by Eugénie Martinez from LETI.

Parallel Angle-Resolved XPS (pAR-XPS) is a specific XPS technique that uses the angular dependence of the photoemission spectra to provide chemical information as a function of depth. If the acquisition angle with respect to the normal of the sample surface is high, photoelectrons emitted at a depth of 10 nm would go through a much longer path (tens of nanometers) to escape the sample surface than a photoelecron emitted from the very top atomic layers. Using a high acquisition angle thus lowers even more than with a zero angle the intensity of the signal coming from buried atomic layers with respect to the surface. As a consequence, a high acquisition angle with respect to the normal of the sample surface provides information about the very top part of the sample.

In this study, pARXPS measurements were performed at 10^{-9} mbar in a customized ThermoScientific Theta 300 pARXPS tool at LETI using a 1486.6 eV X-Ray source. The lens design and the two-dimensional detector allowed us to perform a parallel acquisition of the photoemission signal at various angles with respect to the direction normal to the sample surface. Eight acquisition angles from 23.75° to 76.25° were used. Acquisitions and analysis of pAR-XPS spectra were performed by Laurent Fauquier [Fauquier17].

II.3.4. Raman Spectroscopy

Raman spectroscopy is a technique used for the observation of vibrational modes of atoms. The technique is based on the inelastic scattering of light, the so-called Raman scattering. The wavelength of the incoming monochromatic light, which is obtained from a laser, is therefore shifted, and the analysis of this energy shift gives information about the composition and/or strain of a material. In this study, Raman measurements were performed using a 363 nm laser beam focused on the sample using a x100 short working objective (0.9 numerical aperture). Raman spectra were acquired in backscattering geometry using a Jobin Yvon T64000 Triple Monochromator equipped with liquid N_2 cooled charge coupled device detector. The penetration depth of light at 363 nm into Si is about 15 nm, thus higher than the thicknesses of characterized SiGe layers. The presence of a thin SiO_2 layer on top of the SiGe layer does not interfere with Raman measurements as SiO_2 is transparent at 363 nm.

A Raman spectrum of a SiGe film is shown *Figure II.9* where three main peaks corresponding to the Si-Si, Si-Ge and Ge-Ge vibrational modes are identified.

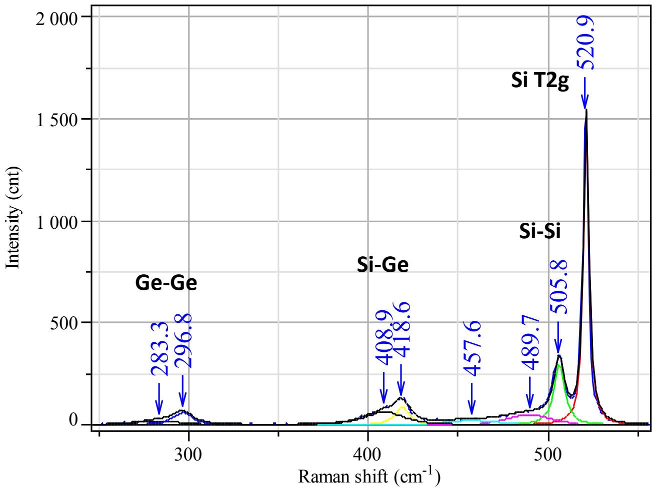

Figure II.9: SiGe Raman spectrum and its decomposition into peaks corresponding to the Si-Si, Si-Ge and Ge-Ge vibrational modes.

The frequency shift of each mode depends on both the composition and strain of the SiGe layer through the following relations:

$$\omega_i(x,\varepsilon) = \omega_{0i}(x) + \mathrm{b}_i\,\varepsilon_{\parallel}, \qquad \textbf{Equation II.3}$$

where *i* stands for Si-Si, Si-Ge, or Ge-Ge, $\omega_i(x,\varepsilon)$ is the measured Raman frequency, $\omega_{0i}(x)$ the Raman frequency of a SiGe layer with the same composition but fully relaxed, $b_{\text{Si-Si}} = -850$, $b_{\text{Si-Ge}} = -570$, $b_{\text{Ge-G}}$e = -450. b_i were extracted from measurements of Raman spectra of fully strained SiGe layers and SiGe virtual substrates [Rouchon14]. However, these empirical relations hold only for Ge concentrations below 60% because fully strained SiGe layers with Ge concentrations higher than 60% cannot be grown on Si substrates. Nevertheless, we used these relations for Ge concentrations higher than 60% because a similar tendency is expected for the Raman frequency shifts, which allows qualitative discussion above 60%.

In this study, $\omega_{0i}(x)$ were measured on SiGe virtual substrates prior to measurements of the SGOI samples. *Figure II.10* shows the measured frequencies of the three modes of SiGe virtual substrates as a function of the Ge content, along with the fitted curves that allow extrapolation of the frequencies at any Ge concentration. Therefore, knowing the dependence of $\omega_{0i}(x)$ on *x* for each mode, and having two unknows, which are *x* and $\varepsilon_{//}$, we could theoretically extract both *x* and $\varepsilon_{//}$ of each sample by using two of the three equations above. However, the "bell shape" of the Raman frequency of the Si-Ge mode as a function of the Ge content makes the use of this mode very inaccurate. Secondly, because the number of Ge-Ge bonds in low Ge content SiGe layers is low, the Ge-Ge mode peak signal is too low for accurate fitting. Therefore, only the Si-Si mode can be used for low Ge content SiGe layers. On the other hand, the Si-Si mode cannot be used for high Ge content SiGe layers for the same reasons.

As a consequence, one of the two unknown must be measured by another technique in order to extract the other one from Raman spectroscopy. Knowing the Ge concentration of the SGOI layers using another technique, we could extract strain by using the Si-Si mode for Ge concentrations below 60% and the Ge-Ge mode above 60%. Uncertainties in strain levels were calculated assuming the uncertainty of wavelength measurement is the monochromator resolution, i.e. 1 cm^{-1}.

Measurements were performed at LETI by Denis Rouchon [Rouchon14].

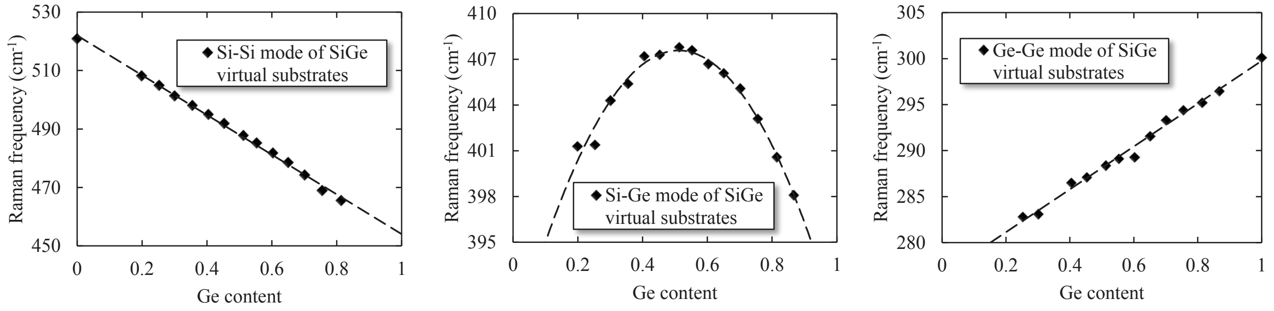

Figure II.10: Measured Raman frequencies of Si-Si, Si-Ge and Ge-Ge modes of SiGe virtual substrates [Rouchon14].

I.3.5. Geometric Phase Analysis (GPA) of HRTEM Images

Geometric Phase Analysis (GPA) is an image analysis treatment that consists in retrieving and processing the geometric phase of High Resolution TEM (HRTEM) images [Hÿtch98]. The geometric phase of the image should not be confused with the phase shift experienced by the electrons going through the TEM lamella. Since a HRTEM image can always be described as the intersections of several systems of fringes, the method can be simply illustrated *Figure II.11* on a 1D example. *Figure II.11 (a)* and *(b)* show a hypothetic HRTEM image with 1D fringes and the contrast of the image plotted along a horizontal profile respectively. As far as small deformations are considered, strain is contained in the phase of the fringe system. After retrieving the phase by numerical processing of the HRTEM image, the displacement fonction *u(x)* is obtained by substraction of the phase of a reference area (unstrained area) to the one of the distorted area. Strain is then calculated according the *Equation II.4* by chosing two non-collinear **g** vectors, $\mathbf{g}_\alpha$ and $\mathbf{g}_\beta$:

$$\varepsilon_{\alpha\beta} = \varepsilon_{\beta\alpha} = \frac{1}{2}\left(\frac{\partial u_\alpha}{\partial x_\beta} + \frac{\partial u_\beta}{\partial u_\alpha}\right). \qquad \textbf{\textit{Equation II.4}}$$

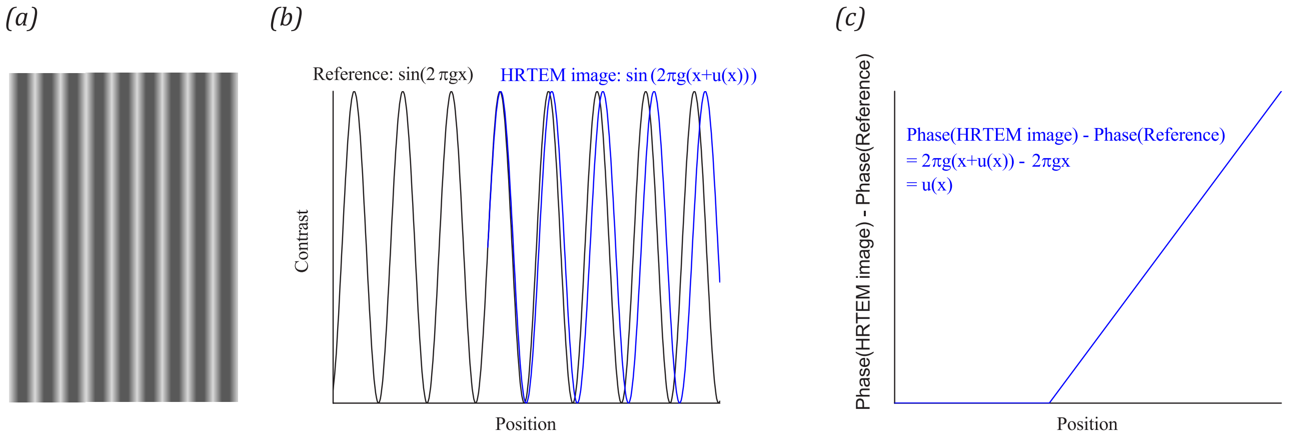

Figure II.11: (a) 1D lattice fringes of a HRTEM image,(b) contrast of the HRTEM image and of the reference area and (c) phase substraction that allows to retrieve the displacement u(x).

The complete formulation of the GPA method is firstly based on the decomposition of the intensity of the lattice fringes of the HRTEM image into local Fourier components [Hÿtch98]. The intensity is then written as:

$$I(\mathbf{r}) = \sum_{\mathbf{g}} I_{\mathbf{g}}(\mathbf{r}) e^{2\pi \mathbf{g}\cdot\mathbf{r}},$$

Equation II.5

where **g** are the reciprocal lattice vectors describing the undistorted lattice. The local Fourier components are obtained by filtering in Fourier space:

$$I_{\mathbf{g}}(\mathbf{r}) = A_{\mathbf{g}}(\mathbf{r}) e^{iP_{\mathbf{g}}(\mathbf{r})},$$

Equation II.6

where the amplitude $A_{\mathbf{g}}(\mathbf{r})$ describes the local contrast of the fringes and the phase $P_{\mathbf{g}}(\mathbf{r})$, their position. The phase can be expressed as a function of the displacement field $\mathbf{u}(\mathbf{r})$ by the following relation:

$$P_{\mathbf{g}}(\mathbf{r}) = -2\pi \mathbf{g}\cdot\mathbf{u}(\mathbf{r}).$$

Equation II.7

The two-dimentional displacement field is then calculated by measuring two phase images corresponding to two non-colinear reciprocal lattice vectors $\mathbf{g}_\alpha$ and $\mathbf{g}_\beta$:

$$\mathbf{u}(\mathbf{r}) = -\frac{1}{2\pi}\left[P_{\mathbf{g}_\alpha}(\mathbf{r})\mathbf{a}_\alpha + P_{\mathbf{g}_\beta}(\mathbf{r})\mathbf{a}_\beta\right],$$

Equation II.8

where $\mathbf{a}_\alpha$ and $\mathbf{a}_\beta$ are the basis vectors for the lattice in real space which correspond to the two reciprocal lattice vectors $\mathbf{g}_\alpha$ and $\mathbf{g}_\beta$.

GPA analysis of HRTEM images of various samples was peformed using the GPA plug-in proposed by Professor Christoph T. Koch in Digital Micrograph environment. The plug-in code is based on equations of [Hÿtch98]. The following procedure was used to get deformation maps from HRTEM images:

- FFT of the HRTEM image (*Figure II.12 (a)*) to get the diffractogram of *Figure II.12 (b))*.
- Selection of two **g** vectors and application of masks around these two frequencies
- Reverse FFT around the two selected spatial frequencies and extraction of the phase maps of *Figure II.12 (c)* after substraction of the phase of the chosen reference area (also shown *Figure II.12 (c)*).
- Deformation maps (*Figure II.12 (d)*) are obtained by combining phase maps. Shear deformation and rotations are also calculated but were always found to be uniform and close to zero so that they are not shown.

No quantitative uncertainties, deformation and spatial resolutions can be given because of the high dependence of the GPA method on the quality of the HRTEM images and on various perturbations that cannot be quantified.

HRTEM images were acquired at LMGP in collaboration with Laetitia Rapenne from LMGP and the GPA was performed with the help of Patricia Donnadieu from SIMaP.

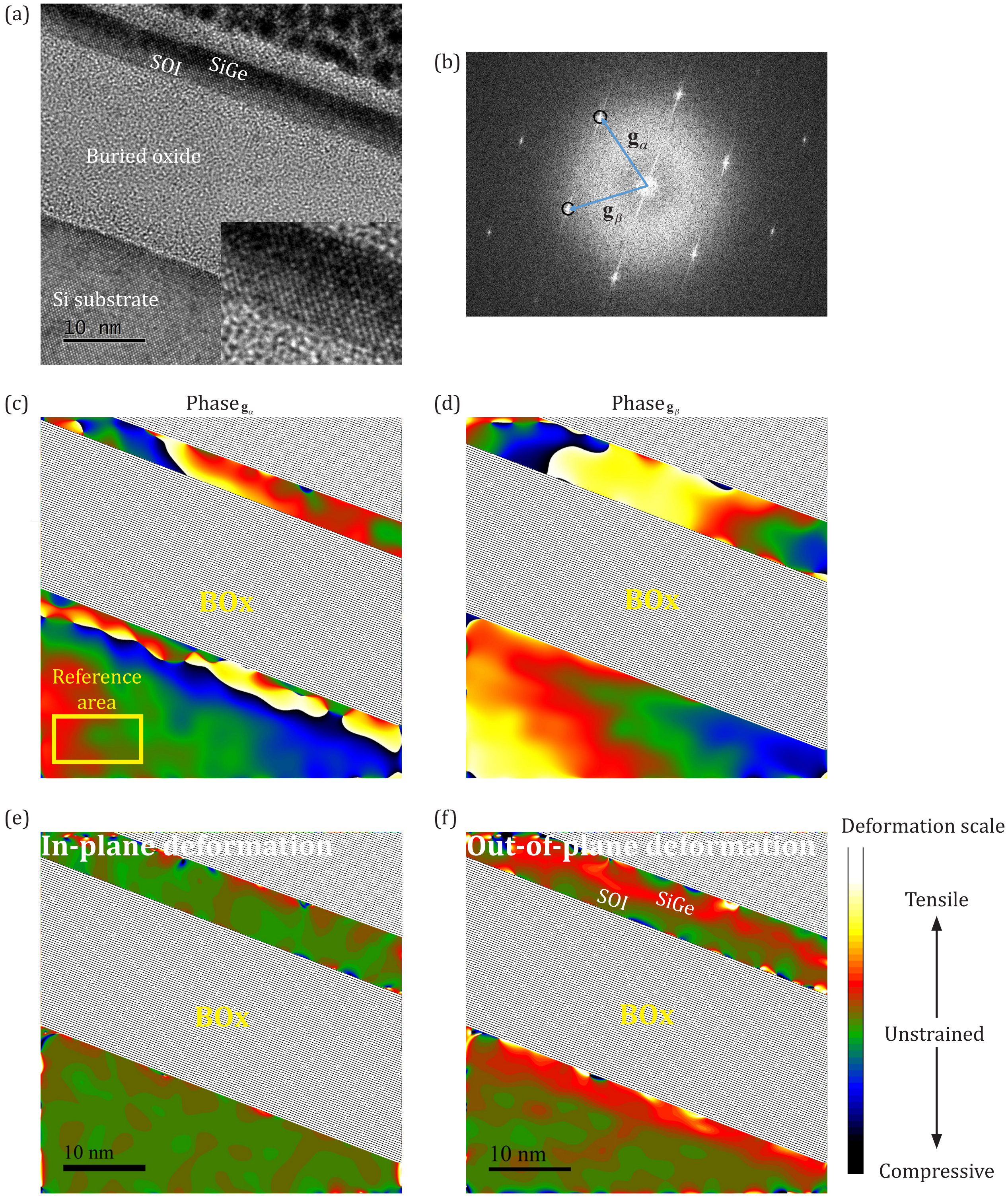
(a)
SOI
SiGe
Buried oxide
Si substrate
10 nm
(b)
$\mathbf{g}_\alpha$
$\mathbf{g}_\beta$
(c)
Phase $\mathbf{g}_\alpha$
BOx
Reference area
(d)
Phase $\mathbf{g}_\beta$
BOx
(e)
In-plane deformation
BOx
10 nm
(f)
Out-of-plane deformation
SOI
SiGe
BOx
10 nm
Deformation scale
Tensile
Unstrained
Compressive

Figure II.12: (a) HRTEM image of a fully strained SiGe epitaxial layer on a SOI substrate. (b) Diffractogram of the HRTEM image showing the selected **g** *vectors and the masked areas around these frequencies. (c) and (d) are phase maps associated with the two* **g** *vectors and showing the chosen reference area in the unstrained Si substrate. And (e) and (f) are deformation maps calculated from phase maps. Amorphous areas (the BOx layer, the thermal oxide on top and layers used for the TEM lamella preparation) are masked as the GPA is not relevant in these areas.*

II.4. Characterization Techniques using Large-Scale Facilities

II.4.1. Resonant Soft X-Ray Reflectivity (R-SoXR)

II.4.1.1. Introduction

X-Ray Reflectivity (XRR) is a technique that probes the profile of optical index along the normal of a thin film system. It can also probe the roughness at the interface between two layers of different optical indices. In the specular geometry illustrated *Figure II.13 (a)*, a monochromatic X-Ray beam is directed towards the surface of the sample with an incident angle θ, and the reflected intensity is measured at a scattering angle of 2θ with respect to the incident beam. The reflected intensity is measured as a function of the incident angle θ in a so-called θ-2θ scan, and plotted sometimes as a function of the modulus of the wave vector transfer ***q*** (see *Figure II.13 (a)*). As the reflected intensity rapidly decreases with θ, the typical θ scan range is 0°-5° for the most commonly used experimental set-up (such as the one presented *Section II.3.2.* that uses the K-alpha emission line of copper as the X-Ray source). However, for XRR experiments based on low-energy X-Rays produced with synchrotron radiation, angular scans up to a few tens of degrees can be performed.

As illustrated *Figure II.13 (b)*, the reflected intensity is modulated by constructive and destructive interferences between waves scattered at different interfaces of a multilayer system. Thicknesses and optical indices of a multilayer system can be extracted from fitting the experimental reflectance with numerical models. As will be seen into the next section, the optical index of a material at X-Ray energies directly depends on the electron density.

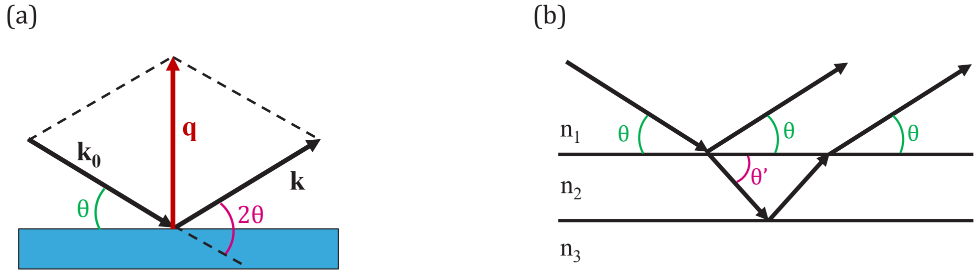

Figure II.13: Schematic illustration of (a) the scattering geometry of θ-2θ reflectivity and (b) bilayer interference.

II.4.1.2. Interaction of X-Rays with Matter in Reflectivity Experiments

Electromagnetic radiations, such as X-Rays, interact with electrons mainly but hardly with atomic nuclei. More precisely, the interaction is between the electric field of the radiation and the electron. Two main types of interactions can be distinguished:

- Elastic scattering, also called Thomson scattering, in which the incident wave is scattered by the charged particle, here an electron, without any energy loss.
- Absorption: all the energy is transferred to an electron which is excited to an empty upper state and the photon vanishes. The excited electron may be expelled from the atom (photoelectric absorption), or the atom releases the energy through the emission of another photon (fluorescence). Important transitions for X-Rays are the ones involving the electrons on the inner shells such as the K and L ones.

At the atomic level, these two interaction processes with an atom k are described by the complex atomic factor f_k which is defined by the following equation [Daillant08]:

$$\mathbf{A}_{\mathbf{sca}} = -\mathbf{A}_{\mathbf{inc}} \frac{r_0}{r} P(\phi) f_k, \qquad \textbf{Equation II.9}$$

where $\mathbf{A}_{\mathbf{sca}}$ is the scattered electric field by an atom k, $\mathbf{A}_{\mathbf{inc}}$ the incident electric field, r_0 the classical electron radius, Φ the scattering angle, $P(\Phi)$ the polarization factor, and r the distance from the atom to the observation point.

Giving an exact and complete description of all these processes, only possible in the frame of the quantum theory, is out of scope of this work. However, key results of this theory are used in the optical formalism described below. The interaction of X-Rays with matter in reflectivity experiments is presented according to an optical formalism in which the properties of materials are described by the refractive index. The use of the optical formalism is made possible because materials can be considered as a homogeneous continuum for X-Ray radiations even if they are actually not at the atomic scale. The index of refraction is commonly expressed as:

$$n = 1 - \delta - i\beta,$$ ***Equation II.10***

where δ and β account for scattering and absorption of the material respectively. For X-Rays and far from any absorption edge, the index of refraction is very close to 1 (slightly lower). One can show that:

$$\delta = \frac{r_e \lambda^2}{2\pi} \rho_e = \frac{r_e \lambda^2}{2\pi} \sum_k \frac{Z_k + f_k^{'}(\lambda)}{V_m}$$
$$\beta = \frac{r_e \lambda^2}{2\pi} \sum_k \frac{f_k^{"}(\lambda)}{V_m}$$
$$f_k = Z_k + f_k^{'} + i f_k^{"},$$ ***Equations II.11***

where r_e is the classical electron radius of the electron, λ is the wavelength of the incident X-Ray wave and ρ_e is the electron density, Z_k is the number of electrons of the atom k in the unit cell, V_m is the volume of the unit cell, and f_k' and f_k'' are the real and imaginary parts of the anomalous factor at the specific wavelength λ.

Let us give some insight about the meaning of each factor of the index of refraction shown *Equations II.11*. In a classical description of Thomson scattering of X-Rays by the electrons of an atom k, and when assuming that the frequency of X-Rays is large compared to the atomic frequency, one can show that the atomic scattering factor f_k of the atom k is simply its atomic number Z_k. This contribution accounts for the Z_k term in *Equations II.11* and is much larger that f_k' and f_k'' as long as the incident wave frequency is far from the any absorption edge of the element k. However, the frequency of the incident X-Ray wave may not be greater than the atomic frequencies for the inner electron shells such as the K and L ones. The correction factors f_k' and f_k'' are introduced in order to take into account this effect. This correction is called dispersion correction.

II.4.1.3. X-Ray Reflection by Planar Multilayers

When the X-Ray wave propagates in a heterogeneous medium with regions of different electron densities, hence of different X-Ray optical indices, calculation of the reflectance is performed by applying the boundary conditions of the electric and magnetic fields at each interface. The fact that multiple reflections have to be considered for multilayer systems requires a matrix formalism. The reader is referred to [Daillant08] for the complete calculation based on the theory of reflection.

An example of the theoretical X-Ray reflectivity curve of a homogeneous SiGe layer on a Si substrate is shown *Figure II.14*. As the optical index is slightly less than 1 for X-Rays, total reflection is observed below a critical angle θ_c that depends on the electron density of the top layer only. The oscillations, also called Kiessig fringes, are the results of interferences between the waves reflected at the surface and at the interface between the two layers. We can show that the period of these fringes depends on the layer thickness only, while the amplitude of the fringes depends on the optical contrast, that is on the electron density contrast between the two layers. The critical angle and the fringe period are indicated on *Figure II.14*.

One last important effect to consider in X-Ray reflectivity is the interface roughness. Roughness tends to decrease the total reflected intensity in the specular reflectivity geometry by scattering a part of the incident radiation towards non-specular directions. Roughness can be taken into account by introducing a transition layer.

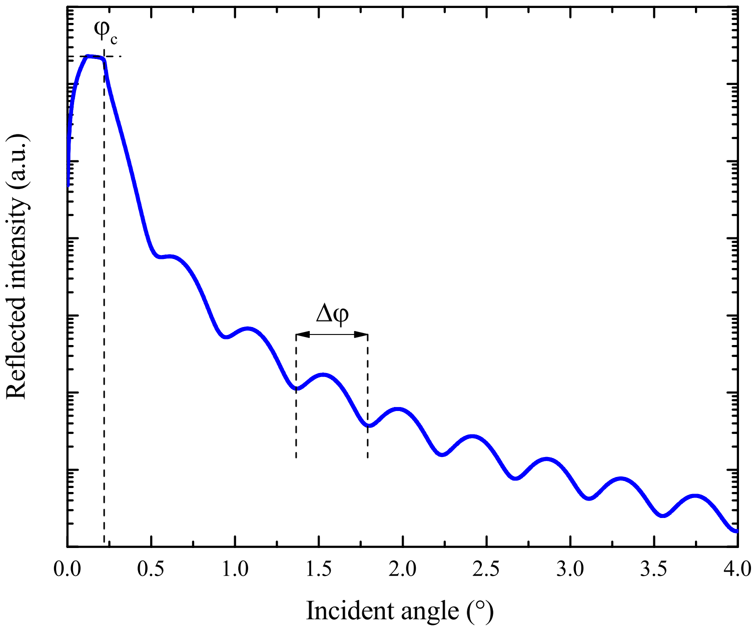

Figure II.14: XRR spectra of a SiGe layer on a Si substrate simulated at the wavelength of the K-alpha emission line of copper.

II.4.1.4. Resonant Soft X-Ray Reflectivity (R-SoXR)

Resonant X-Ray Reflectivity (R-SoXR) is called "resonant" because the energy of the incident X-ray radiation coincides and resonates with the absorption edge of an element of the multilayer system. By choosing specific X-ray energies around an absorption edge, R-SoXR can be used to tune and enhance the optical contrast between layers [Nayak15]. Indeed, large changes of reflectivity at an interface, and as a result of interferences in multilayer systems, are induced by the considerable variation of the complex index of refraction *n* around an absorption edge. These large changes arise from the correction factors *f'* and *f''*. An accurate determination of scattering factors of each element of the multilayer system is thus required for extraction of electron densities from R-SoXR spectra. As will be detailed into *Section III.A.5.1.1.*, the imaginary part *f''* of the scattering factor can be retrieved by absorption measurements and the real part *f'* is then calculated from the imaginary part using Kramers-Kronig transformation. Synchrotron radiation is needed as R-SoXR experiments require the use of several energies around an absorption edge.

II.4.1.5. Experimental

The XRR experiments were performed at SEXTANTS beamline at Soleil Synchrotron. The SEXTANTS beamline, which covers the 50-1700 eV energy range, is dedicated to the investigation of electronic and magnetic properties of materials using soft X-Ray scattering techniques. The experiments were performed using a dedicated diffractometer working under high vacuum (in the 10^{-9} mbar) in order to lower soft X-Ray absorption by air: the RESOXS reflectometer [Jaouen04]. The RESOXS reflectometer features resolution and reproducibility smaller than 0.005°, largely sufficient for soft X-Ray reflectivity experiments where the θ range is large (up to 60° in these experiments). The intensity of the reflected beam is measured by a silicon photodiode.

Prior to reflectivity experiments, absorption of several samples was measured in Total Electron Yield (T.E.Y.) and Total Fluorescence Yield (T.F.Y.) modes in order to extract O scattering factors around the K absorption edge (The extraction procedure is detailed in *Section III.5.1.1.*). T.E.Y. refers to the measurement of the current generated in the sample by absorption of soft X-Ray photons while T.F.Y. refers to measurement of X-Ray fluorescence emission by a detector close to the sample. The escape depth for the fluoresced X-Rays is larger than the one of electrons generated by absorption. It is difficult to give precise values of the probed depth of each mode because it depends both on the energy of the incoming photon and on the probed material. The T.E.Y. mode usually probes between 1 and 5 nm while the T.F.Y. probes between 10 nm and 50 nm. The polarization of the incoming beam for XRR measurements was circular.

These experiments were carried out in collaboration with Patrice Gergaud from LETI and Nicolas Jaouen from Soleil synchrotron.

II.4.1.6. Fitting Procedure

XRR spectra were fitted using the Dyna software. Dyna, which stands for "Dynamic" X-Ray Reflectivity, is a program that simulates conventional, resonant and magnetic X-Ray reflectivity in the Matlab environment. The algorithm is based on Parrat formalism [Elzo12]. Densities, thicknesses and roughnesses of each defined layer of the stack can be either fixed or free parameters. Details and assumptions specific to the experiments performed during this thesis are presented in *Section III.A.5.1.3.*.

II.4.2. Neutron Reflectivity

II.4.2.1. Introduction

In the past decades, neutron scattering was mainly used to determine positions and motions of atoms in condensed matter (1994 Nobel Prize to Shull and Brockhouse) as well as to study polymers and biological systems thanks to a high sensitivity to isotopes labeling (especially ^{1}H versus ^{2}H). In the past few years, neutron scattering started to exhibit usefulness for the characterization of materials in the semiconductor industry [Diebold99][Segura15].

Neutron Reflectivity is a technique similar to X-Ray Reflectivity (XRR) in the sense that neutrons can also be reflected at interfaces between two different materials. The formalism presented in *Section II.4.1.* can be transposed to neutron reflectivity provided that scattering factors are not the ones seen by X-Rays but the ones seen by neutrons. We thus emphasize in *Section II.4.2.* aspects that are specific to neutrons.

The combination of neutron reflectivity with XRR allows the measurement of hydrogen content in multilayer stacks, the purpose of this technique in this work, while XRR alone is not sensitive enough for such a light element [Segura15].

II.4.2.2. Interactions of Neutrons with Matter in Reflectivity Experiments

Scattering of neutrons by nuclei comes mainly from the strong interaction. Far from any nuclear resonance, which is the case of the experiments carried out in this work, absorption is negligible so that neutron scattering is considered elastic. The reader is referred to [Daillant08] for details of neutron-matter interactions.

While XRR is usually described in an optical formalism based on either the scattering factor or the optical index, neutron reflectivity formalism usually uses the nuclear scattering length. For neutrons, *Equation II.9* is written differently:

$$A_{sc} = -A_{in} b \frac{e^{-ikr}}{r}, \qquad \textbf{\textit{Equation II.12}}$$

where A_{in}, A_{sc}, b and r are the incoming wave amplitude, scattered amplitude, scattering length and distance from the scattering element. As a convention, the minus sign is in b definition in order for b to be positive for most elements. The scattering length characterizes the scattering power of an element. Contrary to X-Rays, the neutrons scattering length depends on the atomic number in a non-monotonous way, as illustrated *Figure II.15*. We emphasize that ^{1}H has a negative scattering length, which makes neutron reflectivity very sensitive to its presence.

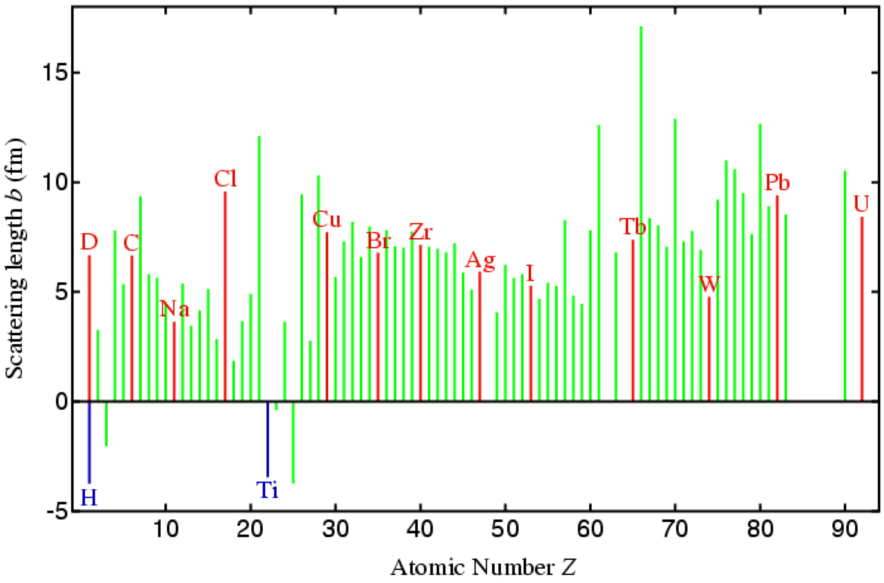

Figure II.15: Nuclear scattering lengths as a function of the atomic number Z. From [pd.chem].

Then, the index of refraction *n* seen by neutrons is:

$$n \simeq 1 - \frac{\lambda^2 \rho b}{2\pi},$$ ***Equation II.13***

where λ, ρ and b are the neutron wavelength, atomic density and scattering length.

II.4.2.3. Experimental

Neutrons reflectivity experiments were carried out at Institut Laue Langevin (ILL) facilities, Grenoble, on D50 beamline, and within the Institut de Recherche Technologique (IRT) nanolec framework. Neutrons reflectivity experiments were performed by Jaime Segura, Robert Cubbit and Philip Gutfreund, all from ILL. As will be detailed in *Section IV.B.3.*, the mass density must be measured by another technique to allow the determination of hydrogen concentration by neutron reflectivity (which is the purpose the experiments described in details in *Section IV.B.3.*). We measured the mass density of the same samples by XRR with Patrice Gergaud from LETI on a Empyrean Panalytical equipment (see *Section II.3.2.*).

II.4.3. Medium Energy Ion Scattering (MEIS)

II.4.3.1. Introduction

Medium Energy Ion Scattering (MEIS) is a technique derived from the Rutherford Backscattering Spectroscopy (RBS) technique used to measure the composition and to determine structural properties of thin films [Jalabert17]. While RBS uses ion energies in the MeV range, MEIS is based on ions accelerated at so-called medium energies, between 50 keV and 500 keV. MEIS benefits from the use of an electrostatic detector, which allows much better energy resolution than the silicon diodes of RBS systems, and which in turn allows better depth resolution (a few Å for MEIS against about 15 nm for RBS). MEIS is much less commonly used than RBS with a dozen tools worldwide only, and long acquisition durations (~10h) are usually required to get reasonable statistics. MEIS equipment can thus be considered as "quasi large-scale facilities".

Basically, a parallel H^+ or He^+ ion beam is accelerated between 50 keV and 500 keV towards the sample surface. Most of the medium-energy ions are implanted into the sample at depths much greater than the probed surface. However, a small fraction of these ions travel close enough to atoms of the samples so that they are scattered by the Coulomb interaction with nucleus. Then, another fraction of these scattered ions see their trajectories deflected backward and may consequently escape the surface of the sample.

Chemical composition profiles as well as some structural properties are extracted from the measurement of the energy and of the angle of ions backscattered by the atoms of the sample (see *Figure II.16*). Ions that encounter only one scattering process are considered for the MEIS analysis as a second scattering process before the ion escapes the sample surface is highly unlikely. The energy and angle of backscattered ions are governed by two types of ion-atom interactions, which are described in the next two sections. Specific angle configurations between the ion beam and the crystal orientation of the sample, called channeling conditions, are used to probe the crystal quality and are described in *Section IV.A.5.1.*.

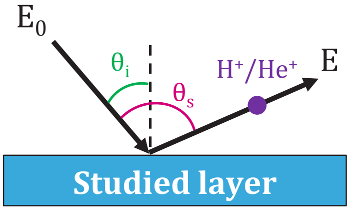

Figure II.16: Schematic illustration of the principles of the MEIS technique. E_0 refers to the energy of incident ions, E to the energy of backscattered ions, and θ_i and θ_s to the incident and scattering angles respectively.

II.4.3.2. Electronic Energy Loss of Medium Energy Ions in Solids

Ions that travel through a solid lose kinetic energy because of inelastic Coulomb interactions with the electrons of atoms of the sample. Ions that are backscattered by atoms thus lose energy during the inward travel until they are backscattered and during the backward travel until they escape the sample surface. At fixed incidence and collection angles, the deeper the atom that backscattered the ion is, the higher the lost kinetic energy is when the ion escapes the sample surface. The kinetic energy of the backscattered ions thus carry information about the depth at which they are backscattered.

The average kinetic energy of ions as a function of depth can be calculated based on the stopping power of each element of the sample, which is defined as:

$$\varepsilon(E)=\frac{1}{\rho}\frac{dE}{dx}, \qquad \textbf{Equation II.14}$$

where ρ (g.cm^{-3}) is the mass density of the material and x the depth (cm). The stopping power of compounds are calculated according to the Bragg-Kleemann rule:

$$\varepsilon_C(E)=\sum_{i=1}^{N} w_i\varepsilon_i(E), \qquad \textbf{Equation II.15}$$

where w_i is the mass fraction of element *i*.

Figure II.17 shows the stopping powers of Si, Ge and O which are the three elements of the samples of this study, as a function of the kinetic energy of ions.

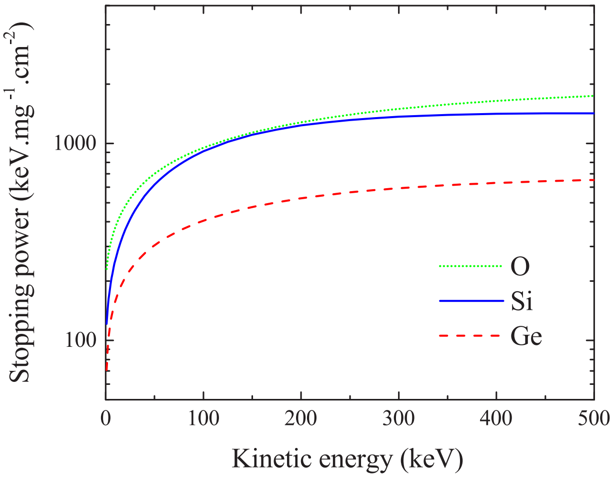

Figure II.17: Calculated stopping powers of O, Si and Ge as a function of ion energy. Calculated from [Jalabert17].

The random nature of inelastic Coulomb energy loss induces some dispersion commonly referred to as straggling. Models that take into account the straggling effect for the MEIS energy range were developed [Jalabert17]. Gaussian distributions around the average energy at the certain depth are usually used as a consequence of the straggling effect.

II.4.3.3. Elastic Nuclear Collision of Medium Energy Ions with Nuclei in Solids

Ions that travel close enough to the sample nuclei undergo elastic nuclear collision (also called Coulomb or Rutherford scattering) with the nuclei. This interaction is said to be elastic because no energy is lost in the spatial system of the mass center of the ion+nuclei system. However, in the spatial system of the laboratory, some impulse is transferred from the ion to the nucleus during the collision process, which results in the ion losing some kinetic energy. The ratio of the ion final and incident energy is called kinematic factor and can be calculated by considering energy and momentum conservation in the ion+nuclei mass center system [Busch00]:

$$K\left(\theta_S\right)=\left\{\frac{\sqrt{1-\left(M_i/M_n\right)^2\sin^2\theta_S}+\left(M_i/M_n\right)\cos\theta_S}{1+\left(M_i/M_n\right)}\right\}^2, \qquad \textbf{Equation II.16}$$

where θ_s is the scattering angle of the ion in the laboratory frame, M_i the ion mass and M_n the nuclei mass. The kinematic factor does not depend on the ion energy. *Figure II.18* shows that the energy that is transferred from the ion to the nuclei increases with the scattering angle, hence the difficulty to separate the elements with the MEIS technique at small scattering angles. We also highlight that the heavier the nuclei is, the lower the transferred energy is at a fixed scattering angle.

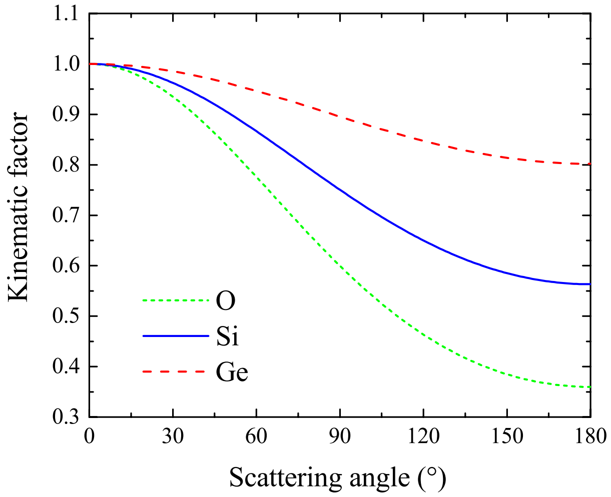

Figure II.18: Kinematic factor as a function of the scattering angle for O, Si and Ge target atoms and a He^+ ion beam.

Quantification of each element can be performed by considering the scattering cross section of each element, which represents the probability of collision. The scattering cross section, also called Rutherford cross section, in the laboratory frame for a problem of collision between two elements is:

$$\sigma\left(E,\theta_S\right)=\left(\frac{Z_iZ_n}{4E}\frac{e^2}{4\pi\varepsilon_0}\right)^2\frac{4\left(\sqrt{1-\left(\frac{M_i}{M_n}\sin\theta_S\right)^2}+\cos\theta_S\right)^2}{\sin^4\theta_S\sqrt{1-\left(\frac{M_i}{M_n}\sin\theta_S\right)^2}}, \qquad \textbf{Equation II.17}$$

where Z_i and Z_n are the atomic numbers of the ion and of the target nuclei respectively. For the MEIS energy range, there are some corrections taking into account the partial screening of the nuclei charge by the electrons of the target atom [Jalabert17]. We highlight that the higher the atomic numbers of the ion and the target nuclei are, the higher the cross section is. For a given ion type and a fixed energy, Ge has consequently a higher scattering cross section than Si.

II.4.3.4. Channeling

Channeling is a mechanism that takes place when the ion beam is aligned along a crystallographic direction of a single crystal. Ions that are not scattered by the first atomic layer see their trajectories deflected towards the space between rows of atoms. As illustrated *Figure II.19*, this mechanism induces the formation of a shadow cone which drastically reduces the probability of an ion to be scattered by deeper atoms. Ions that are deflected into the space between rows of atoms have oscillating trajectories because of small angle scattering processes occurring when ions get close to atoms.

As a consequence, except from the first atomic layer, channeling reduces the number of scattering events with a reduction factor called χ_{min}. The χ_{min} factor is the percentage of atoms displaced from theoretical lattice sites. Vibrational amplitudes of atoms, surface rearrangements, or de-channeling of the ion beam through a top amorphous layer such as a native oxide layer make the channeling process not perfect. χ_{min} ranges from about 4% for a high-quality Si crystal to 100% for totally amorphous materials. However, when there is an atom located at an interstitial site of a crystal, scattering on this atom occurs as described in the former section. Structural defects such as dislocations thus decrease the channeling efficiency. In other words, structural defects increase the χ_{min} factor to intermediary values. Crystal defects profiles as a function of depth can be extracted from the comparison of MEIS spectra acquired in non-channeling conditions, also called random conditions, with MEIS spectra acquired in channeling conditions.

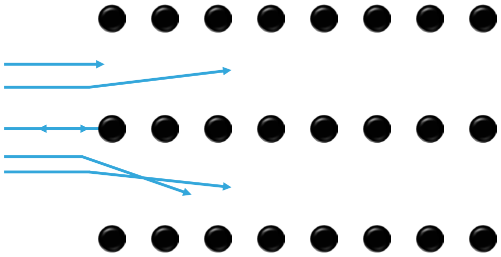

Figure II.19: Schematic illustration of the channeling mechanism showing the formation of a shadow cone behind the first atomic layer.

II.4.3.5. Experimental

The MEIS study was performed at the MEIS facilities of Minatec, Grenoble, with a 100 keV He$^+$ ion beam. The ion beam diameter was about 1 mm. The detector was an electrostatic detector with a 40° angle detection amplitude around the central angle. For instance, when the detector is set in a 90° scattering angle configuration, it detects ions that are backscattered with scattering angles between 70° and 110°. Narrow angle bands were selected and energy scans in this band were summed to get reasonable statistics. However, no more than a few consecutive scans at the same sample location could be used because ion bombardment tends to damage the sample. The ion beam location on the sample was thus regularly changed in order not to include any biased data into the final summed spectra. Several random and channeling configurations were used and will be detailed in *Section IV.A.5.1.*. Channeling conditions were fixed by finding the minimum intensity of the Ge peak.

Measurements were performed by François Pierre from LETI.

II.4.3.6. Simulation of MEIS Spectra

Simulation of MEIS spectra was performed using a homemade program developed by Denis Jalabert from INAC [Jalabert17]. This program is based on the mechanisms and equations introduced in the former sections. The program inputs are:

- General inputs which are fixed in this work:
  - Particle type (He+)
  - Ion energy (100 keV)
  - Detector resolution (0.6%)
- Angle configuration:
  - Incident angle
  - Detection angle, which is also the scattering angle because it takes the incident angle as the reference

- Inputs for each layer of the model:
  - Composition
  - Atomic density
  - Thickness
  - Channeling factor χ_{min}

As there is no fitting algorithm included in the program, simulated spectra were manually adjusted to the experimental spectra following the procedure described below:

- The incident angle was always the set value.
- An energy shift less than 0.6 keV and a detection angle shift less than 0.5° were applied to each experimental spectra. The energy shift comes from slight variations of the ion source with time while the angle shift arises from limitations of mechanical precision. When both the Si surface peak and O surface peak could be identified, the actual energy and detection angle could be exactly calculated. Indeed, both elements are present in the first atomic layer of the sample, so that the energy of backscattered ions depend on two factors only, the nature of the element and the scattering angle. When the O surface peak could not be identified, the energy and detection angle shifts were adjusted between realistic values (0.6 keV and 0.5°) in order to get the best fit.
- In random configuration, an iterative manual adjustment of all layers parameters was performed in keeping with realistic possible variations with XRR and ellipsometry results:
  - Ions that are backscattered by the Ge atoms located at the very top of the SiGe layer lose energy through two processes: elastic Coulomb scattering induces an energy loss that is known once the ion incident energy and scattering angle are calibrated (see former step of the procedure), and inelastic loss through the inward and outward travels through the top oxide only. When fixing the top oxide composition to SiO_2, its thickness could be determined by considering the energy of ions backscattered by Ge atoms at the top of the SiGe layer (which corresponds to the highest energy of the Ge peak).
  - As will be detailed into *Section IV.A.5.1.2.*, the Ge peak is isolated on the spectra while the Si peaks of the oxide, the SiGe, the BOx layer and the substrate overlap with each other. Moreover, Ge has a higher scattering cross section than Si and O, which results into higher statistics for the Ge peak even for low Ge concentrations. As a consequence, adjustment of the SiGe layer thickness and composition is more robust and easier when considering the Ge peak. Matching of the experimental and simulated Si peaks was checked for consistency considerations.
- In channeling conditions:
  - The composition, thickness and atomic density of each layer were fixed to the values determined by the analysis of random spectra. χ_{min} factors were adjusted by considering the Ge peak for the reasons mentioned above, and consistency with the Si peak was also checked.

II.5. Simulation by the Finite Element Method (FEM)

II.5.1. Introduction to the Finite Element Method (FEM)

The Finite Element Method (FEM) is described in depth in [Zienkiewicz77]. Most space and time-dependent problems are described by laws of physics that are expressed by Partial Differential Equations (PEDs). In most cases, PDEs cannot be solved analytically. The most general definition of the FEM is a numerical method for solving PDEs. The FEM is based on the division, or discretization, of the system into a finite number of elements. Then, PEDs are approximated by linear equations for each discretized element. Solutions of these linearized PDEs are computed at each node of the system, which are the intersections of the discretized elements. The solutions, called discrete solutions, are extrapolated between the nodes and an approximate continuous solution is finally obtained to the non-discretized initial problem by merging the solutions for each element. The convergence to a unique solution is guaranteed by the definition of initial and boundary conditions well adapted to the problem and by a well-refined discretization of the system. The denser the discretization, also referred to as the mesh, the closer the approximate solution is to the actual solution. However, a denser mesh induces longer computing durations, so that a trade-off has to be found for each problem. The FEM was used to simulate thermal oxidation of SiGe.

II.5.2. Simulation of Thermal Oxidation of SiGe

Oxidation kinetics of SiGe and Ge redistribution during SiGe oxidation by means of dry RTO and ISSG oxidation were studied by the FEM in COMSOL Multiphysics environment. The model was derived from the model built by Pierre Morin [Morin15]. The key elements of the environment of the model are:

- **Modeling environment**: Two physical modules were used:
  - Transport of Ge: the model of SiGe interdiffusion is based on Darken's equations.
  - Deformed geometry: the deformed geometry module was used to model the growth of the oxide.
- **Geometry and Materials**: a 1D geometry with moving interfaces was used.
- **Specific conditions**: Initial conditions of the simulations are the initial layer compositions and thicknesses.
- **Mesh**: A fine mesh was defined in Si and SiGe layers while a much wider mesh was chosen for the oxide because there is no Ge diffusion in the oxide and thus no need for calculation.

The details of the model will be presented in *Section III.B.2.2.*.

Conclusion of Chapter II

The processes to fabricate samples of this study, techniques that were used to characterize them, and the environment of a developed simulation tool were described in this chapter.

More precisely, the three oxidation processes used in this study were presented, i.e. dry furnace oxidation, dry RTO and ISSG oxidation. Then, characterization techniques using equipment considered as "common" equipment were reviewed: ellipsometry and XRR for thickness measurement, XPS for studying the chemical composition of thermal oxides grown on SiGe, Raman spectroscopy for measurement of strain of SGOI films, and GPA of HRTEM images for measurement of strain levels as well as for revealing crystal defects. Techniques that required the use of large-scale facilities were also reviewed: XRR experiments performed on SEXTANTS beamline at Soleil synchrotron in order to measure the density of thermal oxides, neutron reflectivity to identify whether or not there is hydrogen in SGOI films, and finally MEIS experiments to study the depth distribution of crystal perturbations and defects of SGOI films. This chapter ended with a description of the FEM and the environment of the developed simulation tool.

« La liberté est une chose toute bête, une maladie dont l'hygiène sociale la plus stricte ne vous guérit pas. Non content d'être malade, on veut encore contaminer les autres, leur passer nos miasmes. »

Alain Damasio, La Zone du Dehors

Chapter III - SiGe Thermal Oxidation

Introduction to Chapter III 86

III.A. Study of Mechanisms and Kinetics of SiGe Thermal Oxidation 87

III.A.1. Literature Review 87

III.A.2. Experimental 93

III.A.3. Characterization of Oxide Composition by X-Ray Photoelectron Spectroscopy (XPS) 95

III.A.4. SiGe Oxidation Kinetics and SiGe Composition Evolution 102

III.A.5. Correlation Between SiGe Oxidation Kinetics and Oxide Density 111

III.A.6. Conclusion of Section III.A. 121

III.B. Application to Industrial Processes for Advanced FD-SOI CMOS Manufacturing 122

III.B.1. Condensation Abacus: Oxide thickness and Ge Diffusion Length 122

III.B.2. Simulation of SiGe Thermal Oxidation 125

Conclusion of Chapter III 134

Introduction to Chapter III

We showed in *Section I.5.1.1.* that understanding and controlling SiGe oxidation mechanisms and kinetics is crucial for an efficient use of the condensation technique in an industrial environment.

The first part of this chapter (*Section III.A*) strives to bring more understanding of the mechanisms and kinetics of SiGe oxidation.

After a literature review of SiGe oxidation in terms of mechanisms, thermodynamics and kinetics, the composition of the oxide is investigated, with a focus on the formation of a small quantity of Ge oxides. As these Ge oxides may affect the condensation technique and/or further manufacturing processes, we identify the mechanisms and conditions that lead to their formation.

Then, an in-depth study of the kinetics of SiGe oxidations by means of three technology-relevant processes is carried out. Oxidation kinetics is correlated with the evolution of the SiGe composition during oxidation. The evolution of the SiGe composition during oxidation is discussed within the framework of a competition between the Ge pile-up mechanism that tends to increase the Ge concentration below the oxide and SiGe interdiffusion which tends to smooth the SiGe composition. The influence of the Ge concentration at the oxidation interface on the oxide density measured by X-Ray Reflectivity (XRR) and as a result on oxidation kinetics is then studied. The dependence of O_2 diffusivity on the oxide density is finally discussed.

The second part of this chapter (*Section III.B*) presents two tools built from to the former oxidation kinetics results. The first one is a graphic assessment of the oxide thickness and of the Ge diffusion length in SiGe, a key parameter of the evolution of the SiGe composition during oxidation, as a function of process parameters. It is designed for a convenient and quick evaluation of the relative importance of the Ge pile-up mechanism with respect to SiGe interdiffusion. The second one is a numerical simulation tool of oxidation of SiGe which can be used both for a finer understanding of the dynamics of SiGe oxidation and for accurate prediction of output parameters of the condensation process (such as the oxide thickness and the SiGe composition profile in the SGOI film).

III.A. Study of Mechanisms and Kinetics of SiGe Thermal Oxidation

III.A.1. Literature Review

III.A.1.1. Introduction

Oxidation comes from the archaic French word "oxide" (changed later into "oxyde") coined by L.-B. Guyton de Morveau (1737 – 1816) and A. Lavoisier (1743 – 1794), while the archaic French word "oxide" derives from the Ancient Greek "όξύς" (sharp, acid, thrill). Oxidation refers to a loss of electrons in bonding between atoms, or, more generally, to an increase of the oxidation state of an element. It is considered that, when determining the oxidation state of Si in silicon oxide, the electrons involved in bonding with O atoms are attributed to O. Each bond between a Si atom and a O atom gives a higher oxidation state to Si. Si has four covalent bonds with O atoms in stoichiometric SiO_2, which results in the oxidation state of Si in SiO_2 to be +4. The case of Ge is similar to Si.

The literature review of *Section III.A.1.* starts with thermodynamic considerations about the SiGe oxidation reaction in order to determine the expected oxide composition. Then, the Deal and Grove model of kinetics of Si oxidation is presented [Deal65]. Its limitations and attemps to revise it to better fit experimental results are summed up. Finally, SiGe oxidation kinetics with respect to Si is discussed and shown to remain a matter of debate.

III.A.1.2. Thermodynamic Considerations

Early studies of oxidation of SiGe were performed in the 1970’s [Balk71][Margalit72], but it was not until the late 1980’s that models describing thermodynamics, physical mechanisms and kinetics were proposed. Experiments of oxidation of SiGe have been performed in steam, dry oxygen, at various temperatures, pressures and on various SiGe films.

The following thermodynamic considerations are made at atmospheric pressure since considered thermodynamic activities change only slightly with pressure [Paine91], and at 1000 K, a temperature close to those used in this work. We do not consider silicon and germanium sub-oxides (SiO_x and GeO_x) which have much lower formation enthalpies. Therefore, we consider the ternary system Si-Ge-O and the following standard Gibbs energies of formation at 1000 K from [Barin77]:

	Si	**SiO_2**	**Ge**	**GeO_2**	**O_2**
Standard Gibbs energy of formation (kJ.mol^{-1})	-30.39	-981.78	-44.12	641.31	-220.93

Table III.1: Standard Gibbs energies of formation of various phases of the Si-Ge-O ternary system at 1000 K. Adapted from [Barin77].

In order to determine what is the stable oxide in the Si-Ge-O ternary system, we consider the following reaction:

$$GeO_2 + Si = SiO_2 + Ge$$

The Gibbs energy of this reaction is -353.81 kJ.mol^{-1} at 1000 K, therefore the SiO_2-Ge phase dominates and Ge is thermodynamically stable with SiO_2.

$Si_{1-x}Ge_x$ is considered as an ideal solid solution whose Gibbs energy of formation is given as a function of *x*:

$$\Delta G^o Si_{1-x}Ge_x = RT\left[\left(1-x\right)\ln\left(1-x\right)+x\ln x\right], \qquad \textbf{\textit{Equation III.1}}$$

where *R* is the gas constant and *T* the temperature in Kelvin. In order to determine whether GeO_2 reduction by Si in $Si_{1-x}Ge_x$ is favorable, we consider the following reaction:

$$GeO_2 + Si_{\left(Si_{1-x}Ge_x\right)} = SiO_2 + Ge_{Si_{1-x}Ge_x}$$

The equilibrium constant of this reaction is:

$$K = \frac{a_{SiO_2}^{SiO_2} \times a_{Ge}^{SiGe}}{a_{GeO_2}^{GeO_2} \times a_{Si}^{SiGe}} = \frac{x}{1-x},$$ **Equation III.2**

where a_i^j is the activity of *i* in *j*. This reaction is favorable if:

$$\Delta G_R < 0$$
$$\Delta G_R^o + RT\ln\left(K\right) < 0$$
$$\ln\left(\frac{x}{1-x}\right) < -\frac{1}{RT}\left(G_{SiO_2} + G_{Ge} - G_{GeO_2} - G_{Si}\right).$$ **Equation III.3**

The previous equation holds at 1000 K if $1-x \geq 3.22\times10^{-19}$, meaning that unless the Si content is lower that 3.22×10^{-19}, GeO_2 will be reduced by Si to form SiO_2. $3.22.10^{-19}$ being extremely small, oxidation of SiGe is considered thermodynamically Si-selective in the whole range of Ge concentration.

III.A.1.3. Kinetics of Oxidation of Si and SiGe

Kinetics of furnace oxidation of Si has received much attention since the 1960's because it is a crucial process of CMOS manufacturing. We thus start with a description of the pioneering work of Deal and Grove that laid the foundations of all studies of oxidation of Si and SiGe that followed. Its limitations are then emphasized, and revised models are reviewed to conclude with today's most accepted models. Finally, the specificities of oxidation of SiGe with respect to Si are discussed.

III.A.1.3.1. The Deal and Grove Model for Oxidation of Si

Oxidation of pure Si has been thoroughly investigated since the 1960's for various applications such as gate oxide formation, masks against implant or diffusion, surface passivation, dielectric isolation between adjacent devices, etc… The two following chemical reactions describe the thermal oxidation of pure Si when a silicon surface is exposed to an oxygen or a vapor water atmosphere:

- "Dry" oxidation in O_2 ambient: $Si_{(s)} + O_{2(g)} \rightarrow SiO_{2(s)}$
- "Wet" oxidation in H_2O ambient: $Si_{(s)} + 2H_2O_{(g)} \rightarrow SiO_{2(s)} + 2H_{2(g)}$

It has been shown that oxidation involves diffusion of the oxidizing species, either O_2 or H_2O, through the thermal oxide to the Si-SiO_2 interface where the oxidation reaction occurs [Ligenza60]. Taking into account Si and SiO_2 densities and molecular weights, we can show that growth of a SiO_2 layer of thickness t_{ox} corresponds to the "consumption" of a Si layer of thickness $0.44t_{ox}$.

In 1965, Deal and Grove published a seminal work on kinetics of Si thermal oxidation which is in good agreement with most published oxidation data [Deal65]. Their model describes both dry and wet oxidation chemical reactions for temperatures between 700°C and 1300°C, partial pressures between 0.2 atm and 1 atm, and oxide thicknesses in the 30 nm to 2000 nm range. The Deal and Grove model is based on the following three-step process and is illustrated *Figure III.1*:

- The oxidizing species is transported from the outer gas to the surface of the oxide.
- The oxidizing species diffuses from the surface of the oxide through the oxide layer and towards the oxide-Si interface.
- The oxidizing species reacts with Si atoms at the oxide-Si interface to form SiO_2.

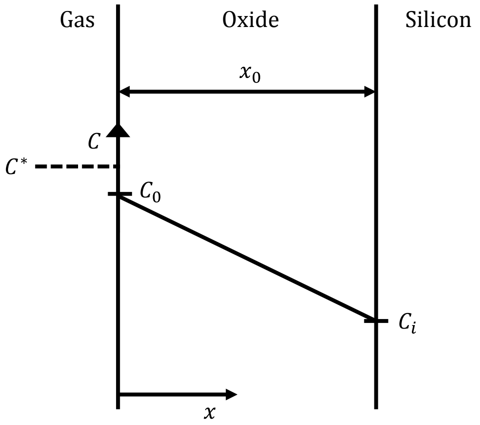

Figure III.1: The Deal and Grove model for the oxidation of silicon. Adapted from [Deal65].

C^*, C_0, C_i are respectively the equilibrium concentration of the oxidizing species in the gas phase, the concentration of the oxidizing species at the outer surface of the oxide, and the concentration of the oxidizing species at the Si-SiO$_2$ interface.

The authors made the following assumptions in their model:

- Steady-state regime.
- Growth in the direction perpendicular to the surface of the sample.
- Constant temperature and pressure in the oxidizing gas.
- They assumed that the flow of oxidizing species from the gas to the vicinity of the outer surface follows a law analogous to Newton's law of cooling: $F_1 = h(C^* - C_0)$.
- C^* is related to the partial pressure of the oxidizing species in the gas by Henry's law: $C^* = Kp$. Henry's law holds for ideal dilute solutions and in the absence of dissociation or reactions of the oxidizing species at the outer surface.
- D_{eff} if the diffusion coefficient of the oxidizing species in the oxide layer. It is assumed to be constant, and since steady-state regime is assumed, diffusion of the oxidizing species follows Fick's laws: $F_2 = D_{eff}\dfrac{C_0 - C_i}{x_0}$.
- The oxidation reaction between the oxidizing species and Si occurs at the abrupt oxide-Si interface only and the flow corresponding to this reaction is assumed to be governed by the first-order relation: $F_3 = kC_i$ where *k* is the reaction constant.

Considering these asumptions, the oxide thickness versus oxidation time is found to follow the following linear-parabolic law:

$$\frac{x(t)}{A/2} = \left[1 + \frac{t+\tau}{A^2/4B}\right]^{\frac{1}{2}} - 1, \qquad \textbf{\textit{Equation III.4}}$$

where $x(t)$ is the oxide thickness, *t* the oxidation time, τ accounts for the duration needed to form an initial 20 to 30 nm-thick oxide layer, and *A* and *B* are constants related to the physical parameters of the model. The authors examined two limiting forms of *Equation III.5*:

- For short oxidation times: $t \ll \dfrac{A^2}{4B}$,

$$x(t) \simeq \frac{B}{A}\left(t+\tau\right). \qquad \textbf{\textit{Equation III.5}}$$

The growth regime follows a linear law, with $\dfrac{B}{A}$ being referred to as the linear rate constant, and is surface-reaction limited.

- For long oxidation times: $t \gg \dfrac{A^2}{4B}$,

$$x\left(t\right)^2 \simeq Bt. \qquad \textbf{\textit{Equation III.6}}$$

The general linear-parabolic law is reduced to a parabolic law, with a parabolic rate constant B. In this regime, the oxidation rate is limited by diffusion of the oxidizing species through the thermal oxide.

The Deal and Grove model accurately describes wet oxidation for all oxide thicknesses and dry oxidation for oxides thicker than 30 nm. However, the main limitation of the Deal and Grove model appears to be dry oxidation for thin oxide formation (thickness below 30 nm). As illustrated *Figure III.2*, a faster oxidation rate compared with the Deal and Grove model is observed for oxides thinner than 30 nm. As today's needs are to control oxidation kinetics by means of dry oxidation for oxides thinner than 30 nm, revised models trying to accurately describe Si oxidation below 30 nm have been proposed and are introduced into the next section.

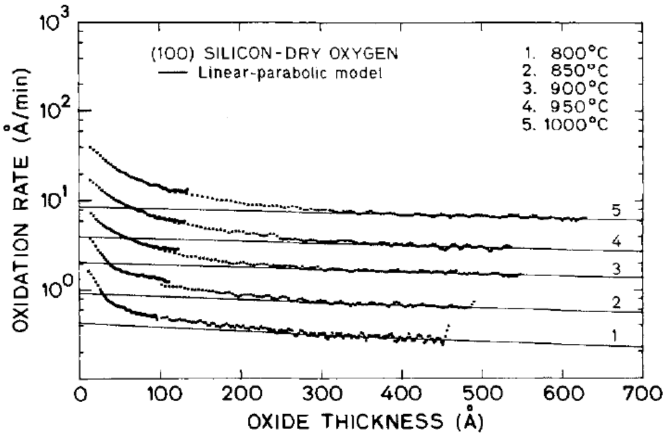

Figure III.2: Experimental oxidation rate in dry environment and at various temperatures. Solid lines are the oxidation rate predicted by the Deal and Grove model and dotted lines are experimental data. From [Massoud85].

III.A.1.3.2. Revised Models of Oxidation of Si

Nuclear reaction resonance [Rosencher79][Rochet84][Trimaille89], Secondary Ion Mass Spectroscopy (SIMS) [Costello84] and Medium Energy Ion Scattering (MEIS) experiments based on ^{16}O-^{18}O sequential oxidation [Gusev95] have shown that no oxygen atom is incorporated into the bulk of the oxide and that the oxide grows at the Si-oxide interface. These experiments have thus clearly confirmed the Deal and Grove sequential oxidation process described in the former section. However, kinetics of these mechanisms, especially in the thin oxide regime, have been put into question. Attempts at explaining Si oxidation kinetics can be separated into two main groups, depending on the limiting mechanism of oxidation in the thin oxide regime, either the interfacial reaction of O_2 with Si, or more recently, diffusion of O_2 through the oxide.

In keeping with Deal and Grove, Massoud et al. assumed an interfacial reaction-limited oxidation in the thin oxide regime and discussed various mechanisms to explain the higher oxidation rate [Massoud85][Massoud85']. They will not be discussed here as they have been dismissed later.

The hypothesis according to which the interfacial reaction is the limiting mechanism for thin oxides has been questioned by various investigations [Doremus84][Doremus89][Bongiorno04][Bongiorno04']. Some experiments and first-principles calculations show that the interfacial reaction is almost instantaneous and thus cannot be a limiting mechanism of oxidation [Bongiorno04'][Tsetseris06][Akiyama08]. These studies support that even for thin oxides, the limiting mechanism of oxidation is diffusion of O_2 through the growing oxide. To our knwoledge, Doremus was among the first ones to claim that O_2 diffusion is always the limiting mechanism and that the linear regime experimentally observed by Deal and Grove for thin oxides could be explained by modulation of O_2 diffusivity by strain in the thermal oxide.

Awaji et al. and Kosowsky et al. showed by X-Ray Reflectivity (XRR) experiments the presence of a higher density oxide layer about one nanometer thick at the Si-oxide interface [Awaji96][Kosowsky97]. The existence of this higher density interfacial oxide layer was also supported by first-principles calculations of the structure of the Si-SiO_2 interface conducted by Bongiorno et al. [Bongiorno03']. The same authors also showed by calculations that O_2 diffusion through a higher density oxide is decreased. Two disruptive models of Si oxidation based on the results of these investigations have been published [Watanabe06][Cui09].

As a conclusion, most recent investigations of Si dry furnace oxidation claim that the limiting mechanism is diffusion of O_2 through the growing oxide even for thin oxides. According to these studies, O_2 diffusion, and as a consequence oxidation kinetics, would be influenced by the oxide density.

While there is extensive data on dry furnace oxidation in the literature discussed above, there is a lack of data for RTO of Si. Other mechanisms, such as drift of ionic oxygen species, may have to be considered for RTO [Young87][Young87'][Kazor95]. While some models have been proposed for RTO of Si, none of them was widely accepted, especially because of the important dependency of RTO mechanisms on differences from one RTO apparatus to another (such as the lamp spectrum and the distance between the lamp and the wafer) [Borisenko97].

III.A.1.3.3. Kinetics of SiGe Oxidation

An enhancement of the wet oxidation rate has been observed for SiGe relative to Si [LeGoues89], while both faster [Spadafora05] and identical [Long12] dry oxidation rates for SiGe versus Si have been reported, illustrating an obvious lack of consensus. Moreover, an intrinsic difficulty that arises when studying the dynamics of oxidation of SiGe films is the evolution of the composition of the film during the oxidation process. Indeed, depending on the process parameters, Ge tends to accumulate at the oxidizing interface at various rates. Most authors only considered the initial composition of the film when reporting SiGe oxidation rates and not the Ge concentration at the oxidation interface. It makes the analysis of the influence of Ge on the oxidation rate difficult [Long12]. In addition, the range of oxide thicknesses varies widely from one study to another, so that comparisons between published experimental data is complicated.

Several mechanisms have been proposed to explain SiGe oxidation kinetics and can be separated into two main categories depending on the assumed limiting mechanism, either the interfacial reaction or diffusion of the oxidizing species:

- Interfacial reaction limited oxidation:

  - The lower Si-Ge binding energy compared to the Si-Si binding energy would increase the interfacial reaction rate and therefore the oxidation rate [Holland87]. Such a mechanism would induce a higher oxidation rate in both dry and wet oxidation conditions.

  - GeO formation followed by immediate reduction by Si at the oxide-SiGe interface was proposed as a transient reaction occuring in parallel to direct Si oxidation [Prabkakaran93]. This catalytic reaction would increase the oxidation rate in both wet and dry oxidation environments.

  - Oxidation of pure Si induces stress at the Si-SiO_2 interface because a unit volume of Si is converted into 2.25 volumes of SiO_2. This stress is partially relieved by generation and injection of Si atoms in interstitial positions into the oxide and into the Si substrate. The majority of these interstitials are injected toward the oxide and is oxidized by incoming O_2, while the minor part causes interstitials supersaturation in the Si film [Dunham86].

  It has been observed that interstitials supersaturation is suppressed for oxidation of SiGe [LeGoues89][Napolitani05]. As for the causes of the lower interstitials injection toward the substrate in the case of oxidation of SiGe, LeGoues et al. proposed that the larger lattice parameter of SiGe accounts for a part of the stress generated at the oxidizing interface. As a result, the interstitials injection required to relieve the interfacial stress would be lower. It was also suggested that the presence of SiGe at the oxidizing interface changes the balance between interstitials injected toward the oxide and those injected toward the substrate [Napolitani05]. Indeed, interstitials have higher formation energies in SiGe than in Si, which results in a lower interstitials concentration in SiGe.

  The model schematically illustrated *Figure III.3* and based on this mechanism was proposed to explain kinetics of oxidation of SiGe [LeGoues89]. Due to the high oxidation rate under wet oxidation conditions, interstitials do not have time to diffuse away from the oxidizing interface and accumulate in a thin layer below the oxide. This accumulation would slow down the oxidation rate of pure Si compared to SiGe, which in fact results in an enhancement of the wet oxidation rate of SiGe with respect to Si. As for dry oxidation conditions, there is no interstitials accumulation at the oxidizing interface for oxidation of both Si and SiGe because interstitials have time to diffuse away in both cases. Indeed, the oxidation rate is much lower for dry oxidation conditions than for wet oxidation conditions. Assuming that the interfacial reaction is the limiting step, LeGoues et al. argued that the oxidation rate of SiGe should not be higher than the one of Si in dry oxidation conditions.

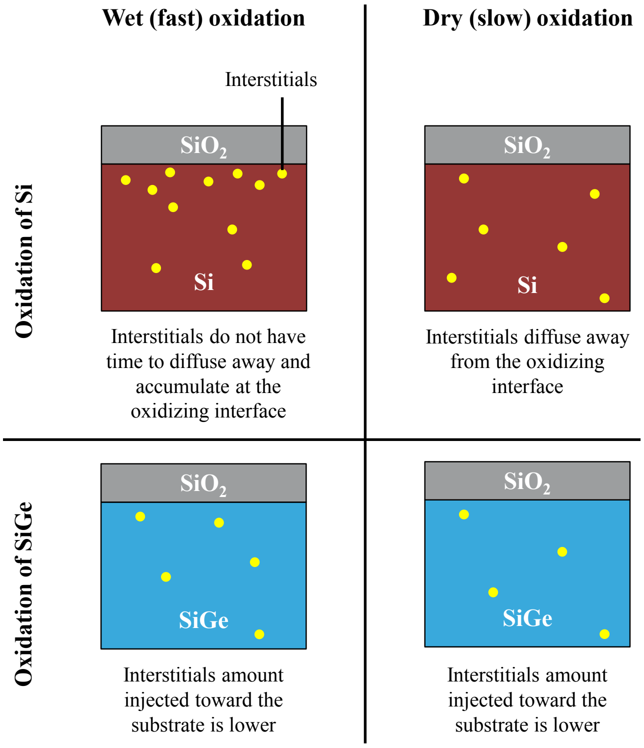
Wet (fast) oxidation
Dry (slow) oxidation
Oxidation of Si
Oxidation of SiGe
Interstitials
SiO2
Si
SiGe
Interstitials do not have time to diffuse away and accumulate at the oxidizing interface
Interstitials diffuse away from the oxidizing interface
Interstitials amount injected toward the substrate is lower
Interstitials amount injected toward the substrate is lower

Figure III.3: Schematic illustration of interstitials injection during oxidation of Si and SiGe in dry and wet oxidation conditions.

- Diffusion limited oxidation:

  - Shimura et al. proposed that the higher oxidation rate of SiGe in wet conditions is caused by the lower Si-Ge binding energy because the limiting mechanism is the interfacial reaction in wet conditions [Shimura10]. While in dry environment, there is no or hardly any difference between Si and SiGe according to the authors. Based on Watanabe et al. model [Watanabe06] of oxidation of Si, they proposed that O_2 diffusion through the thermal oxide layer is the rate limiting mechanism of oxidation of SiGe in dry ambient, whatever the oxide thickness is. And since they showed that the atomic structures of thermal oxides grown on Si and on SiGe are nearly identical, they claimed that the oxidation rate of SiGe should not be higher than the one of Si.

We emphasize that all proposed explanations, except the one of Shimura et al., assumed an interfacial reaction-limited oxidation in the thin oxide regime in dry atmosphere. Indeed, these explanations were proposed before the recent investigations about oxidation of Si reviewed in *Section III.A.1.3.2.* argued that the limiting mechanism is diffusion of O_2 through the oxide. In keeping with conclusions drawn in *Section III.A.1.3.2.*, the higher oxidation rate of SiGe should arise from different O_2 diffusivities through the thermal oxide depending on the oxidized material, Si or SiGe. Finally, we also note that no specific model or explanation has been proposed for RTO of SiGe while it has been shown that mechanisms, and as a result kinetics, of furnace oxidation and RTO of Si may be different [Kazor95].

III.A.1.4. Conclusion of Section III.A.1.

In summary, we showed that thermal oxidation of SiGe is thermodynamically Si-selective in the whole range of Ge concentration. We will study by X-Ray Spectroscopy (XPS) the composition of the oxides grown on SiGe in *Section III.A.3.* in order to check if thermal oxidation of SiGe actually keeps with thermodynamic predictions.

It is widely accepted that thermal oxidation of Si follows a three-step sequence:

- The oxidizing species is transported from the outer gas to the surface of the oxide.
- The oxidizing species diffuses from the surface of the oxide through the oxide layer and towards the oxide-Si interface.
- The oxidizing species reacts with Si atoms at the oxide-Si interface to form SiO_2.

We showed that most recent investigations claim that the limiting mechanism is diffusion of O_2 through the growing thermal oxide. These studies also argue that O_2 diffusion, and as a result oxidation kinetics, is influenced by the oxide density.

As for SiGe, there is no consensus about kinetics of dry oxidation of SiGe with respect to Si. We highlighted that the fact that the Ge concentration in the SiGe film, and especially at the SiGe-oxide interface, evolves during oxidation makes analysis of SiGe oxidation kinetics more difficult. In addition, oxidation kinetics of both Si and SiGe by means of RTO has not received much attention while RTO is commonly used today. Kinetics of oxidation of SiGe by means of various processes (dry furnace oxidation, dry RTO and ISSG oxidation) will be covered in *Section III.A.4.* and *Section III.A.5.*.

III.A.2. Experimental

III.A.2.1. Oxidation Processes and Characterization Techniques

$Si_{0.9}Ge_{0.1}$ and $Si_{0.7}Ge_{0.3}$ films were epitaxially grown on bulk Si substrates. Film thicknesses were about 20 nm. We mention that we observed slight differences of composition (less than 1% for the Ge concentration) and of film thicknesses depending on the moment when these layers were grown. It induces slight differences in terms of SIMS profiles as will be seen later in this manuscript, but without invalidating the results and the analysis methodology.

Prior to any oxidation process, a standard HF-SPM-SC1-HCl cleaning process was performed. It resulted in the formation of an approximately 1 nm-thick oxide on top of the SiGe film.

Dry furnace oxidation at 900°C, dry RTO at 900°C, 1000°C and 1100°C, and finally ISSG Oxidation at 850°C, 950°C and 1050°C were performed on SiGe and Si layers. From three to seven oxidation durations were chosen for each couple of process type and temperature. All oxidation durations refer to the duration of the oxidation plateau and were chosen to target oxide thicknesses in the 30-150 Å range, which are typical oxide thicknesses at the end of the condensation process.

The composition of grown oxides as a function of depth was firstly characterized on four representative samples by parallel Angle-Resolved X-Ray Spectroscopy (pAR-XPS). Ge oxide formation during SiGe oxidation was investigated on all samples by XPS data acquired on the in-line XPS equipment. While the in-line XPS tool cannot provide depth-resolved information, it is optimized for fast and easy XPS data acquisition, and is therefore suitable for basic characterization of such a high number of samples.

Oxide thicknesses were measured by Spectroscopic Ellipsometry (SE) between 240 nm and 780 nm using the SiGe optical constants published by Nolot et al. [Nolot14]. A three-layer model composed of the oxide and two SiGe layers was used for fitting spectra. Thicknesses of the three layers and index of refraction of SiGe layers were treated as unknowns while the index of refraction of the thermal oxide and of the Si substrate were fixed to known values. The oxide thicknesses were also measured by XRR to validate ellipsometry results. Indeed, XRR is much less model-dependent than ellipsometry for the measurement of oxide thickness on SiGe. XRR also benefits from a high contrast between SiO_2 and SiGe thanks to large density difference between these two materials. XRR is thus a robust and reference technique for measurement of the oxide thickness on SiGe. We chose to use a three-layer model for ellipsometry because it matches pretty well XRR results for all samples, and using an ellipsometry model with more SiGe layers does not bring any significant improvement.

However, XRR is not suitable for measurement of oxide on Si because of the low density contrast between Si and SiO_2 [Diebold99]. While XRR is suitable for oxide on SiGe only, ellipsometry is suitable for oxide measurement on both Si and SiGe, and was thus chosen for consistency of results. The relative difference between ellipsometry and XRR for the oxide thickness was found to be always in the 3 to 4 Å range. The uncertainty on the measured oxide thickness was set to ± 2 Å. All uncertainties given in this chapter come from uncertainty calculations taking as input this oxide thickness uncertainty. The calculated uncertainties show how confident we can reasonably be about the results and the conclusions of this work.

SIMS was performed to measure the Ge concentration as a function of depth after oxidation in order to correlate oxidation kinetics with Ge redistribution.

Oxidation kinetics will also be discussed in view of the density of thermal oxides. To this end, the density of grown oxides was measured by XRR on the SEXTANTS Beamline at Soleil Synchrotron. Details of the experimental apparatus are presented in *Section II.4.1.* and results are shown and discussed in *Section III.A.5.*.

III.A.2.2. Characterization of Strain Conservation During Oxidation

The crystallinity and strain of SiGe films after epitaxy and after oxidation have been evaluated by X-Ray Diffraction (XRD). *Figure III.4* shows the experimental and fitted rocking curves along the (004) direction of a $Si_{0.7}Ge_{0.3}$ layer after epitaxy and after dry RTO at 1100°C for 40 seconds. Curves after RTO were vertically shifted for clarity considerations. After epitaxy, the rocking curve was fitted with a single SiGe layer, which shows that the epitaxial layer is monocrystalline and homogenous. After RTO, a three-layer model was used for SiGe. As will be shown in the following sections, the composition of the SiGe layer after RTO is not homogeneous anymore, which explains why the main diffraction peak is broader and why a three-layer model was needed for fitting. Interference fringes are still observed and prove that the SiGe layer is still a monocrystal and that the broadening of the peak is not due to a polycrystalline structure, but from composition non-homogeneity. However, XRD could not be performed on samples oxidized by means of dry furnace oxidation and ISSG oxidation.

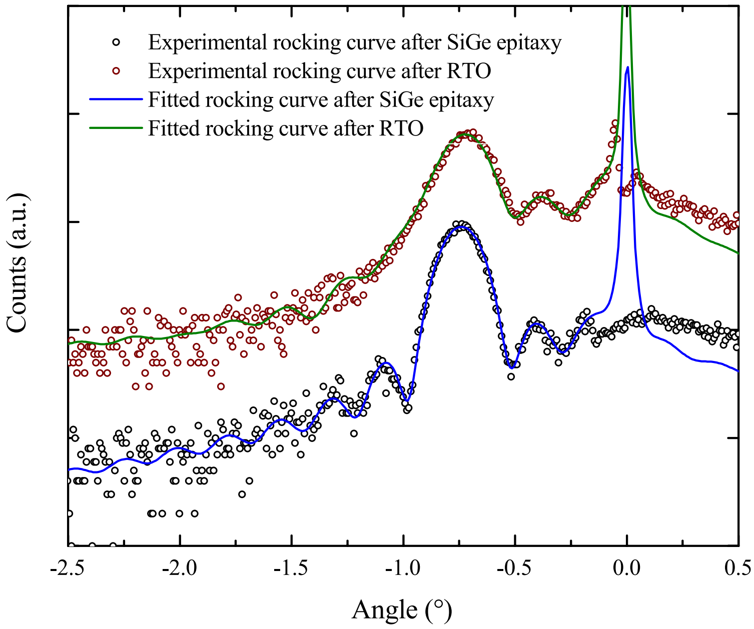

Figure III.4: Experimental and fitted (004) rocking curves of a $Si_{0.7}Ge_{0.3}$ *layer after epitaxy on bulk Si and after dry RTO at 1100°C for 40 seconds. Curves after RTO are vertically shifted for clarity considerations. The Si peak located at 0° was cut on experimental curves.*

III.A.2.3. Control of Within Wafer Uniformity of the Oxide Thickness

The oxide thickness was also measured along the wafer radius to ensure that the oxidation processes are uniform enough within a wafer. *Figure III.5* shows the oxide thickness measured by ellipsometry along the wafer radius for two oxidized samples, one by means of dry RTO and one by means of ISSG oxidation. All samples were found to feature the same profile of oxide thickness along the wafer radius. It is found that the oxide thickness along the radius of the wafer is comprised in a few Å range. XRR measurement was also performed and found to agree well with ellipsometry measurements with a 3 Å to 4 Å offset. We chose to consider the oxide thickness measured at the center of the wafer by spectroscopic ellipsometry for the analysis of oxidation kinetics in the next sections.

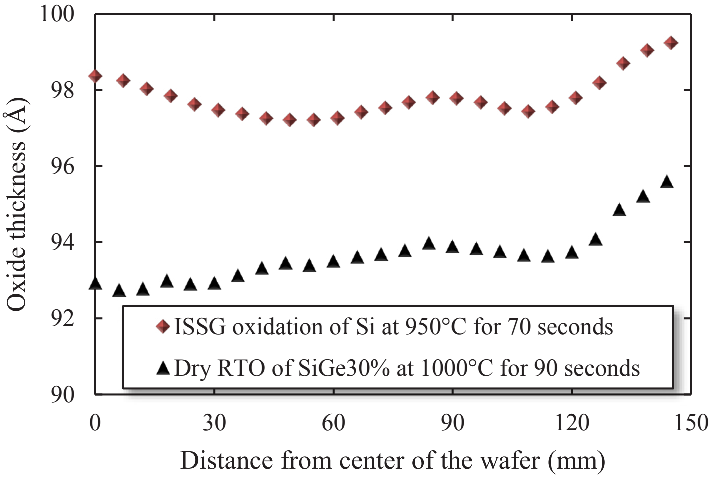

Figure III.5: Oxide thickness measured by ellipsometry along the radius of the wafer for two oxidized samples.

III.A.3. Characterization of Oxide Composition by X-Ray Photoelectron Spectroscopy (XPS)

III.A.3.1. Introduction

Formation of Ge oxide during the first stages of SiGe oxidation has already been evidenced by XPS [Long12]. Firstly, understanding the formation process of Ge oxide during SiGe oxidation could bring some insight into SiGe oxidation mechanisms. Secondly, very precise control of the Ge content in the condensed SGOI channel, which is reduced from the quantity of Ge incorporated into Ge oxide, is required for efficient industrial manufacturing. Moreover, Ge oxide properties are different from the ones of SiO_2, and may therefore influence further processing, such as wet etching of the oxide. And finally, formation of high-κ gate stacks usually requires the formation of a thin SiO_2 interfacial layer between the SiGe channel and the high-κ layer. Such thin layers are formed by specific oxidation processes, and Ge oxide formation may influence the electrical properties of the gate stack [Park08].

The presence of Ge oxide on XPS Ge3d spectra of SiGe layers oxidized by means of dry RTO has been noticed. We therefore sysmetically characterized the presence of Ge oxide during thermal oxidation of SiGe as a function of process parameters.

III.A.3.2. Ge Oxide Formation During Dry RTO of SiGe

III.A.3.2.1. Depth Distribution of Ge Oxide Measured by pAR-XPS

We performed pAR-XPS characterization of four SiGe samples oxidized by means of dry RTO to measure the depth distribution of each element, and especially Ge oxide. *Figure III.6* shows the Ge3d spectrum as a function of the collection angle of a $Si_{0.7}Ge_{0.3}$ layer oxidized by means of dry RTO at 900°C for 20 seconds. As explained in *Section II.3.3.*, the contribution to XPS spectra of a buried atom decreases when the collection angle increases. This is the case of the Ge3d peak of metallic Ge atoms (bonded to either Si or Ge atoms). On the other hand, the area of the peak associated with Ge oxide is independent from the collection angle, which shows that Ge oxide is exclusively located in the very top part of the oxide.

Reconstruction of depth profiles of atomic concentrations was perfomed from the analysis of Ge3d, Si2p, O1s and C1s spectra. *Figure III.7* shows the reconstructed chemical profile of the $Si_{0.7}Ge_{0.3}$ layer oxidized by means of dry RTO at 900 seconds for 20 seconds. We firstly noticed the usual presence of carbon contamination on top of the sample. We also observe that the proportion of O atoms to Si atoms is roughly 2 to 1 in the oxide, as expected for stoichiometric SiO_2. The depth resolution is degraded below a few nanometers so that it does not allow very accurate reconstruction of the chemical profile of the SiGe layer below the oxide. The metallic Ge observed in the oxide must not be taken as a piece of evidence of the presence of Ge in the oxide. However, qualitatively speaking, there is no or hardly any metallic Ge atom in the oxide while Ge oxide is exclusively located in the first nanometer of the oxide (referred as "Top of the oxide" on *Figure III.7*).

We performed the same analysis on three other samples oxidized by means of dry RTO: a $Si_{0.7}Ge_{0.3}$ layer oxidized at 900°C for 180 seconds, a $Si_{0.7}Ge_{0.3}$ layer oxidized at 1000°C for 30 seconds and a $Si_{0.9}Ge_{0.1}$ layer oxidized at 1000°C for 60 seconds. The same conclusion was reached: a small quantity of Ge oxide (a few percent) is located in the very top of the oxide (the top 10 Å). We believe that these four samples are representative enough to extend this conclusion to all SiGe samples of this study oxidized by means of dry RTO.

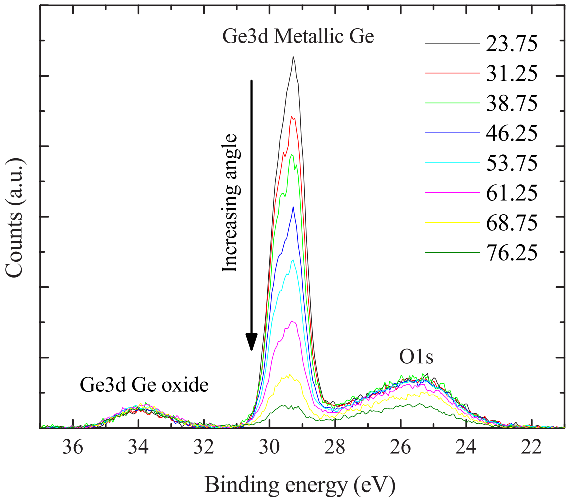

Figure III.6: Ge3d spectra of a $Si_{0.7}Ge_{0.3}$ film oxidized by means of dry RTO at 900°C for 20 seconds for different collection angles (indicated on the Figure).

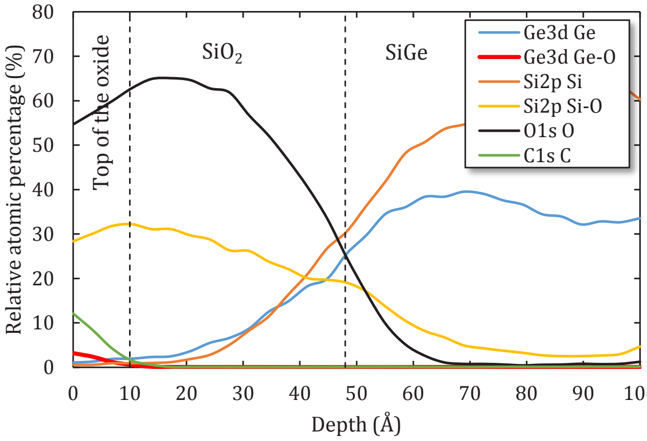

Figure III.7: Chemical profile of the same sample reconstructed from Ge3d, Si2p, O1s and C1s spectra.

III.A.3.2.2. Determination of the Oxidation State of Ge Oxide

For all investigated samples, we followed the fitting procedure described in *Section II.3.3.* which uses two peaks for the Ge oxide. We found that the main peak is always centered at a binding energy about 4.25 eV above the one of metallic Ge. Such a chemical shift is associated with the fourth oxidation state of Ge [Prabhakaran00]. Moreover, we also noticed the disappearance of the peak associated with Ge oxide on Ge3d spectra after the sample surface has been rinsed with water (Figure not shown). As GeO_2 is known to be water soluble, it confirms that the Ge oxide observed after dry RTO of SiGe is mainly composed of GeO_2 and that it is located in the very top part of the oxide.

III.A.3.2.3. Ge Oxide Formation During the Full Oxidation Sequence

As oxidation proceeds by formation of oxide at the SiGe-oxide interface, the top of the oxide corresponds to the first stages of oxidation. Ge oxide is therefore likely formed at the beginning of the oxidation plateau. In order to precisely determine at which step(s) of the SiGe epitaxy-cleaning process-dry RTO sequence Ge oxide is formed, we performed XPS measurements after each key step of the sequence. XPS measurements were performed after SiGe epitaxy, after the cleaning process prior to oxidation, after the temperature ramp up until 550°C, after the temperature ramp up until 900°C, and after a complete dry RTO process. *Figure III.8 (a)* shows on a typical temperature-time profile of a dry RTO process at which steps measurements were performed.

Figure III.8 (b) shows Ge3d spectra after each of these steps. No Ge oxide is noticed after SiGe epitaxy and after the cleaning process prior to oxidation while some Ge oxide is observed right after the temperature ramp up until 550°C. The O1s peak is also noticeable after the temperature ramp up until 550°C, which shows that the oxide started to grow even at temperatures below 550°C. The O1s peak area keeps increasing as the temperature goes up and oxidation at the target temperature proceeds. There is still some Ge oxide observed after the temperature ramp up until 900°C and after the complete oxidation process. Comparison of $Ge3d^{4+}$ peak areas after each of these process steps show that there are more Ge oxide after the temperature ramp up until 900°C than after the temperature ramp up until 550°C only (*Figure III.11* shown and discussed into more details in *Section III.A.3.2.4.*). Within measurement and fitting errors, no clear difference between peak areas has been evidenced between the temperature ramp up until 900°C and the complete oxidation process.

As a conclusion, Ge oxide is formed during the temperature ramp up until at least 550°C. Some Ge oxide is still formed above 550°C but we cannot precisely determine at which moment they are not formed anymore based on these results only.

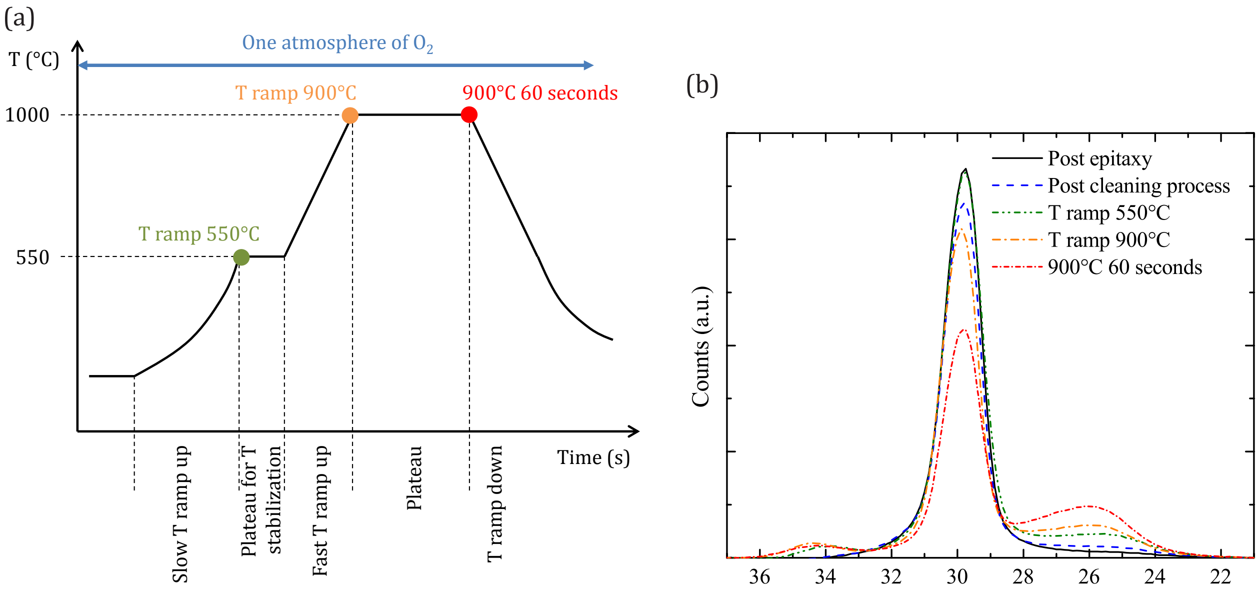

Figure III.8: (a) Typical temperature-time profile of a dry RTO process showing at which moment oxidation was stopped to perform XPS measurements. And (b) Ge3d spectra acquired after each key step of the SiGe epitaxy-cleaning process-dry RTO sequence.

III.A.3.2.4. Influence of Initial Ge Concentration and Oxidation Temperature on Ge Oxide Formation

Figure III.9 allows us to study the influence of the initial Ge concentration on the quantity of Ge oxide formed during dry RTO of SiGe. The metallic Ge peak area depends on various parameters, especially the thickness on top of the SiGe layer because of the depth sensitivity of the XPS technique (see *Section II.3.3.*) and of the pile-up mechanism which leads to various SiGe composition profiles. Analysis of the area of the metallic Ge peak is thus complex while the one of the Ge3d^{4+} and O2s is easier because they both directly depend on the total amount of GeO_2 and SiO_2 in the thermal oxide. We chose to compare samples that have close oxide thicknesses. For all investigated temperatures, the Ge oxide peak area is larger for $Si_{0.7}Ge_{0.3}$ layers than for $Si_{0.9}Ge_{0.1}$ layers. All other parameters being equals, there is more Ge oxide after oxidation of SiGe when the initial Ge concentration is higher.

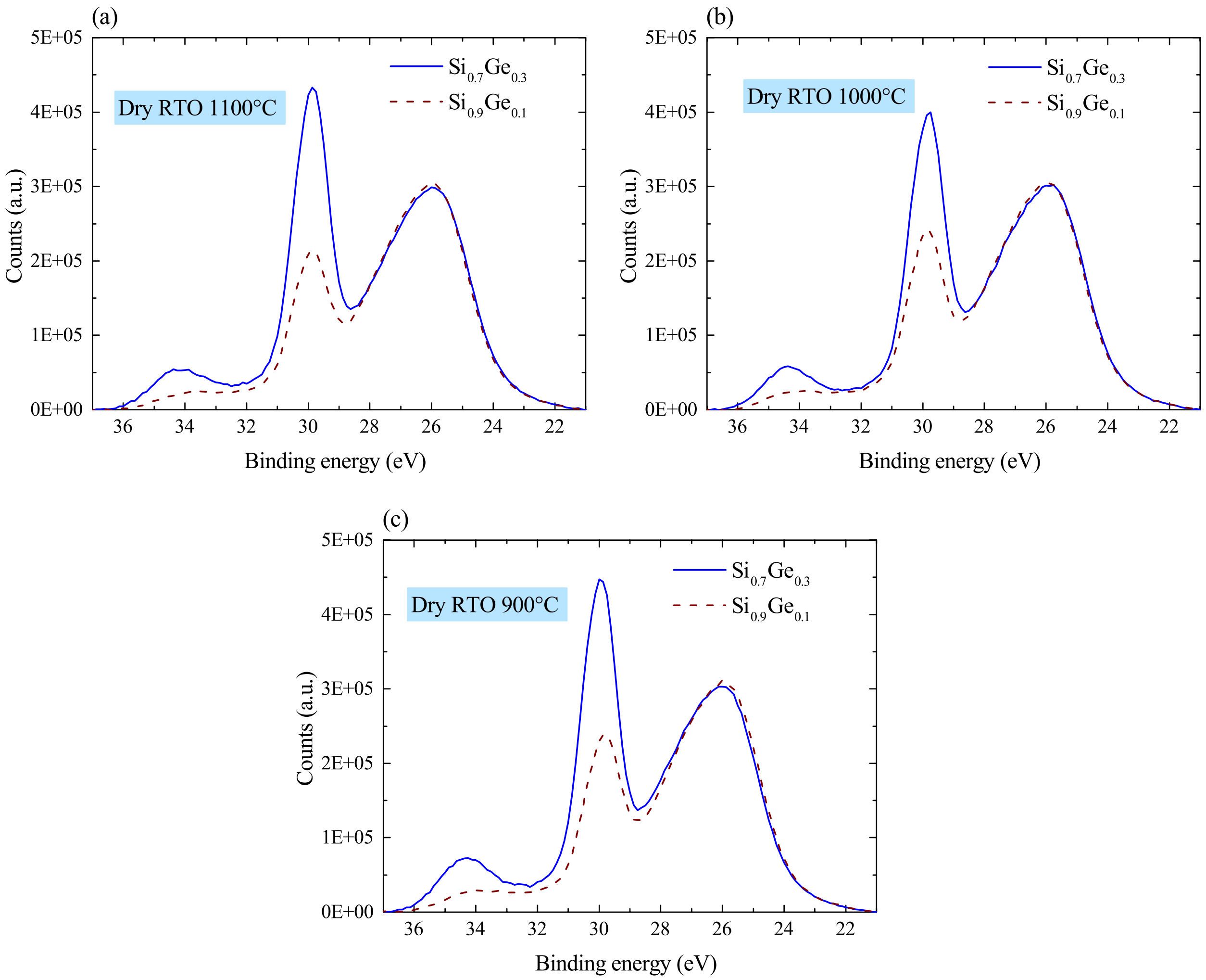

Figure III.9: Ge3d XPS spectra acquired after dry RTO of SiGe layers at (a) 1100°C, (b) 1000°C and (c) 900°C.

As for the effect of the temperature of dry RTO on the quantity of Ge oxide, we observe on *Figure III.10* that the area of the Ge3d^{4+} peak is slightly higher when the oxidation temperature is lower.

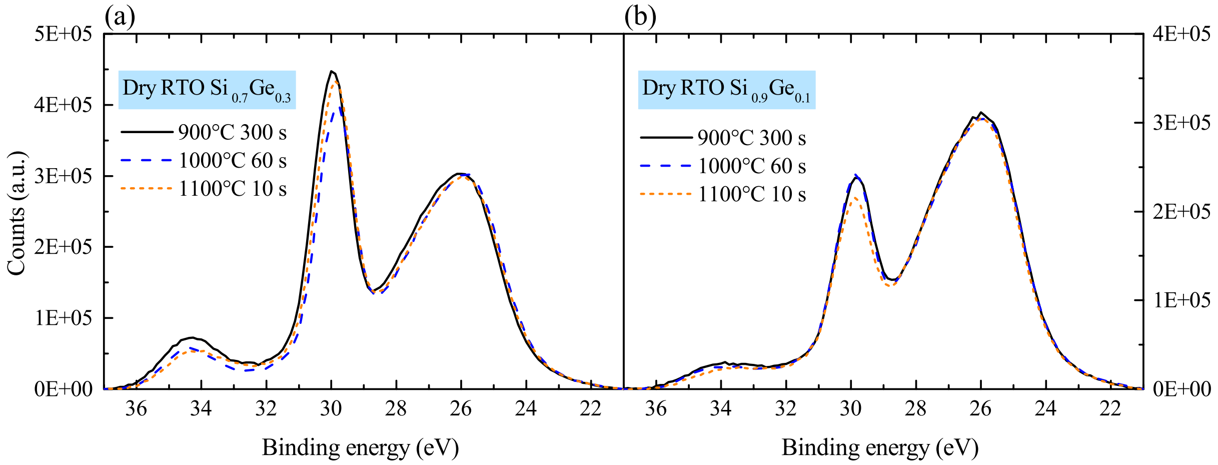

Figure III.10: Ge3d XPS spectra acquired after dry RTO of SiGe layers with initial (a) 10% Ge concentration and (b) 30% Ge concentration.

Figure III.11 shows the area of the fitted Ge3d^{4+} peak after dry RTO of SiGe as a function of the initial Ge concentration and of the oxidation temperature. There are several points for a single temperature and a single initial Ge concentration because measurements were performed for several oxidation durations. No clear evidence of variation of the quantity of Ge3d^{4+} peak area with the oxidation duration was found. But due to different Ge3d metallic and O2s peak shapes at different oxide thicknesses, precise analysis of the evolution of the Ge3d^{4+} peak area with the oxidation time is less accurate.

The measured peak areas after the temperature ramp up until 550°C and 900°C for the case of $Si_{0.7}Ge_{0.3}$ are also shown as full lines over the total range of temperature for comparison. As already mentionned, Ge oxide is formed below and above 550°C, so that the peak area is higher after a temperature ramp up until 900°C than after a temperature ramp up until 550°C only. *Figure III.11* also confirms that the higher the initial Ge concentration is, the higher the quantity of Ge oxide is. More precisely, the quantity of Ge oxide for dry RTO of $Si_{0.7}Ge_{0.3}$ seems to be roughly three times as high as the one for $Si_{0.9}Ge_{0.1}$. The Ge oxide quantity would therefore be proportional to the initial Ge concentration of the SiGe layer. Thirdly, the Ge oxide quantity seems to decrease when the oxidation temperature increases, but the variations are lower than the one caused by the initial Ge concentration.

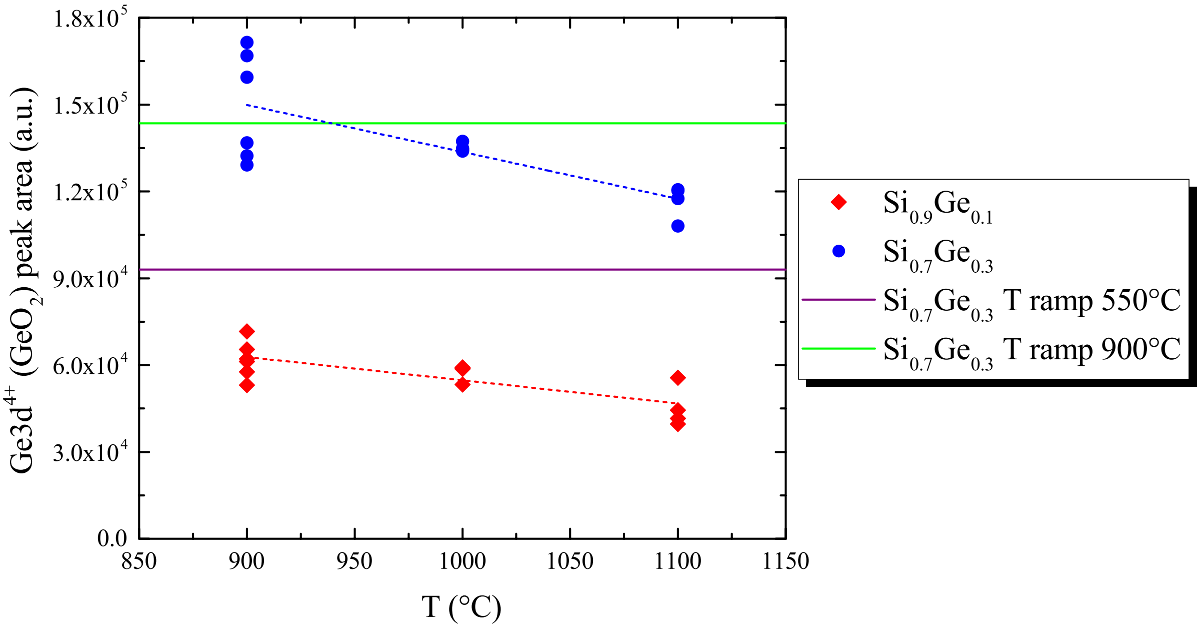

Figure III.11: Areas of the fitted Ge3d^{4+} peak for all SiGe samples oxidized by dry RTO. Dotted lines are linear trend lines for each initial Ge concentration. Full lines are for the temperature ramp up and are plotted over the full range of oxidation temperature for comparison only.

III.A.3.2.5. Discussion about Ge Oxide Formation During Dry RTO of SiGe

Paine et al. and Kilpatrick et al. showed that despite of the thermodynamic tendency to form pure SiO_2 during oxidation of SiGe, mixed $SiGeO_x$ may be formed when considering kinetic factors [Paine91][Kilpatrick03]. Such mixed oxide formation occurs when using low temperature and/or high oxidant pressure oxidation conditions. Paine et al. also showed that the mixed oxide formed under these oxidation conditions is mostly composed of SiO_2-GeO_2, with a GeO_2 to SiO_2 fraction roughly similar to the Ge to Si fraction in the SiGe layer at the oxidation interface. They argued that when using these oxidation conditions, the interdiffusion rate of Si towards the oxidation interface is much lower than the oxidation rate, so that we can almost consider that diffusion is suppressed. The huge gap between the oxidation rate and the diffusion rate is responsible for the mixed oxide formation.

We showed in *Section III.A.3.2.1.* that Ge oxide is always located in the top part of the oxide (the top 10 Å) (see *Figure III.7*). Based on XPS results, no Ge oxide was observed after either SiGe epitaxy and after the standard chemical cleaning process used prior to any oxidation process (see *Figure III.8*). There is thus no Ge oxide just before thermal oxidation of SiGe. As the top of the oxide layer corresponds to the beginning of oxidation, we argued that Ge oxide is formed during the first stages of oxidation only.

In *Section III.A.3.2.2.*, we showed that in all samples where the presence of Ge oxide is observed by XPS, there is a major contribution of the Ge3d^{4+} peak, which makes us think that formed Ge oxide is mainly GeO_2, in agreement with Paine et al..

We suggest that during the temperature ramp up of dry RTO, the atmosphere being already pure O_2 at 740 Torr, some oxidation occurs even below 550°C and leads to mixed $SiGeO_x$ formation. The formation of $SiGeO_x$ seems to continue between 550°C and 900°C as the Ge3d^{4+} peak area increases between 550°C and 900°C (see

Figure III.11). We argue that, during temperature ramp up of dry RTO, the oxidation temperature is low enough and the oxidation rate high enough (the oxide is very thin, which results in a high oxidation rate as will be seen in *Section III.A.4.1.*) for the oxidation regime to be the one described by Paine et al. and Kilpatrick et al. that corresponds to mixed oxide formation. We also observed that the Ge3d^{4+} peak area after temperature ramp up until 900°C is close to the ones of samples oxidized at 900°C for various oxidation durations, while the Ged^{4+} peak areas of samples oxidized at higher temperatures are lower (see *Figure III.11*). It shows that there is no Ge oxide formation after the temperature ramp up.

In summary, we claim that Ge oxide is formed during the temperature ramp up, mostly until 900°C, and that the quantity of formed Ge oxide is be roughly proportional to the initial Ge concentration, in agreement with Paine et al.. Indeed, the GeO_2 quantity for dry RTO of $Si_{0.7}Ge_{0.3}$ seems to be roughly three times as high as the one for $Si_{0.9}Ge_{0.1}$ (see *Figure III.11*). One possible mechanism for the smaller GeO_2 quantity at higher temperatures could be recombination of GeO_2 into GeO during dry RTO followed by desorption of GeO [Prabhakaran00].

III.A.3.3. Ge Oxide Formation during Dry Furnace Oxidation and ISSG Oxidation of SiGe

Figure III.12 (a) and *(b)* show that there are no Ge oxide after either the temperature ramp up until 900°C or after complete oxidation for the case of dry furnace oxidation. As described in *Section II.2.3.2.*, the atmosphere is pure N_2 until 600°C, so that there is no oxidation during the temperature ramp up until 600°C. Then, the partial pressure of O_2 gradually increases from 600°C to 900°C and oxidation starts. However, because the O_2 partial pressure is increasing into the chamber during the temperature ramp up, oxidation is most likely less important. We argue that there is no Ge oxide formation during the temperature ramp up because the oxidation rate is not high enough compared with the diffusion rate for the mixed oxide formation conditions to be fulfilled.

Some Ge oxide contribution on Ge3d spectra is noticed for the temperature ramp up until 900°C of ISSG oxidation and after complete ISSG oxidation at 850°C (see *Figure III.12 (a)* and *(c)*). For ISSG oxidation, the chamber is filled with pure O_2 at low pressure until 600°C is reached, and H_2 starts to flow into the chamber when the temperature exceeds 600°C. Some $SiGeO_x$ is also formed during this temperature ramp up, but the Ge oxide quantity seems to be smaller than for the temperature ramp up of dry RTO (see *Figure III.12 (a)*). Further investigation is required to identify the contributions of the temperature ramp up below and above 600°C, which correspond to different oxidation atmospheres (see *Section II.2.3.2.*), to Ge oxide formation. Similarly to dry RTO, one possible mechanism for the smaller GeO_2 quantity at higher temperatures could be recombination of GeO_2 with other species of the oxide and of the atmopshere (such as O* which has a strong oxidizing power) to form GeO which then desorbs [Prabhakaran00].

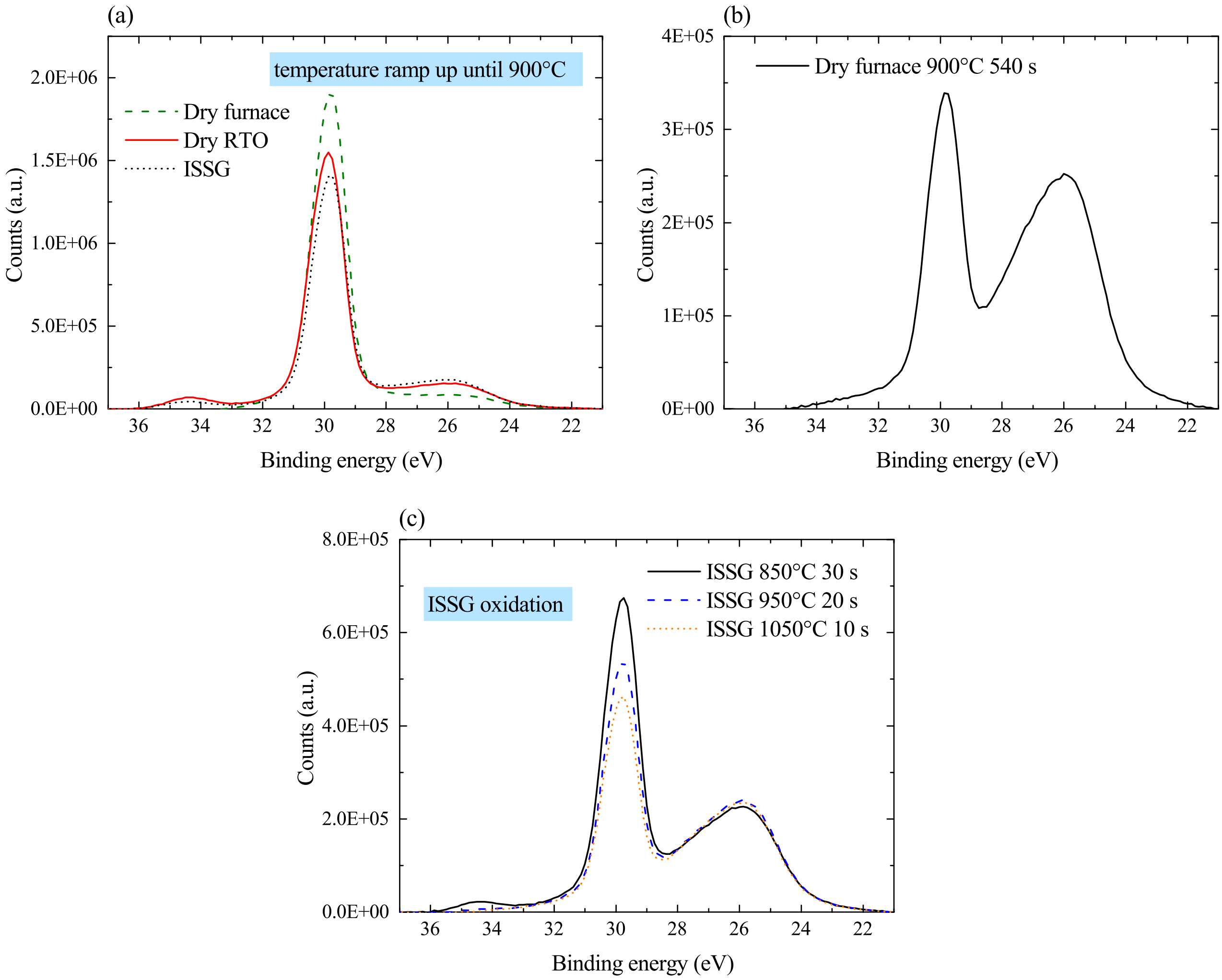

Figure III.12: (a) Ge3d spectra acquired on a $Si_{0.7}Ge_{0.3}$ layer which underwent the temperature ramp up until 900°C of dry furnace oxidation, and (b) which underwent a full dry furnace oxidation at 900°C for 540 seconds. And (c) Ge3d spectra acquired on $Si_{0.7}Ge_{0.3}$ layers oxidized by means of ISSG oxidation performed at three different temperatures.

III.A.3.4. Conclusion of Section III.A.3.

We found that in spite of the thermodynamic tendency to form SiO_2 during oxidation of SiGe, mixed $SiGeO_x$ may be formed due to kinetic factors. We investigated the formation of Ge oxide by pAR-XPS and XPS. We observed that mixed $SiGeO_x$ are formed when the oxidation rate largely exceeds the Ge diffusion rate. These mixed oxide formation conditions are fulfilled during the temperature ramp up of dry RTO under one atmosphere of O_2. The quantity of formed Ge oxide, found to be mainly GeO_2, is roughly proportional to the Ge concentration of the SiGe epitaxial layer.

We also claimed that the oxidation rate during the temperature ramp up of dry furnace oxidation is not high enough for Ge oxide to be formed. As for ISSG oxidation, some GeO_2 are formed during the temperature ramp up but disappear afterwards if the oxidation temperature is above 950°C. More experiments are required to clarify GeO_2 formation and disappearance during ISSG oxidation of SiGe.

To conclude, we showed that, except possibly during the very first stages of oxidation, the composition of oxides grown on SiGe is pure SiO_2 for all investigated oxidation processes, in agreement with thermodynamic considerations of *Section III.A.1.2.*. Having studied the composition of the grown oxide, the next section focuses on the kinetics of oxidation of SiGe.

III.A.4. SiGe Oxidation Kinetics and SiGe Composition Evolution

The goal of this section is to identify the oxidation mechanisms that govern oxidation kinetics and to correlate oxidation kinetics with the process parameters and with the evolution of the Ge concentration during oxidation. Experimental oxidation rates of dry furnace oxidation, dry RTO and ISSG oxidation of SiGe are firstly compared with the Deal and Grove linear-parabolic regime. A quantitative analysis methodology based on the definition of a term called Growth Rate Enhancement (GRE) is then introduced. After having shown that SiGe oxidation kinetics does not depend on the Ge concentration of the initial SiGe epitaxial film only, we study the evolution of the Ge concentration profile during oxidation as a function of process parameters. The last part of this section shows that oxidation kinetics and the Ge concentration at the oxidation interface are correlated.

III.A.4.1. Oxidation Kinetics Results

III.A.4.1.1. Results

Figure III.13 shows the measured oxide thickness as a function of time for dry furnace oxidation, dry RTO and ISSG oxidation. We observe that, for all investigated oxidation processes, and for identical oxidation temperature and duration, the higher the initial Ge concentration is, the higher the oxide thickness is. However, the differences between the oxide thicknesses for SiGe and for Si are much lower for ISSG oxidation than for dry furnace oxidation and dry RTO.

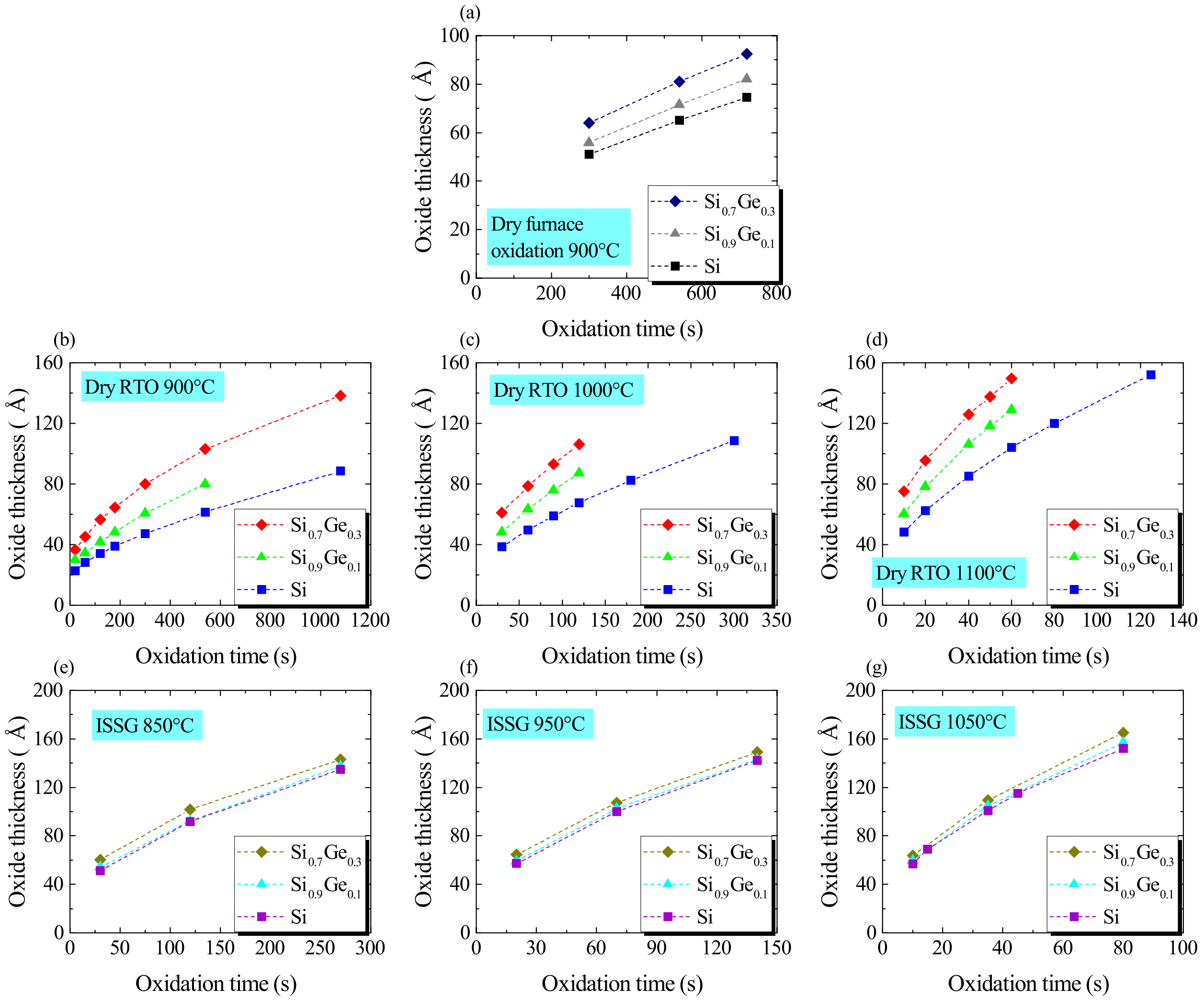

Figure III.13: (a) Oxide thickness as a function of the oxidation time for dry furnace oxidation of Si, $Si_{0.9}Ge_{0.1}$ and $Si_{0.7}Ge_{0.3}$ at 900°C. (b) (c) and (d) show the oxide thickness as a function of the oxidation time for dry RTO of Si, $Si_{0.9}Ge_{0.1}$ and $Si_{0.7}Ge_{0.3}$ at 900°C, 1000°C and 1100°C respectively. (e) (f) and (g) show the oxide thickness as a function of the oxidation time for ISSG oxidation of Si, $Si_{0.9}Ge_{0.1}$ and $Si_{0.7}Ge_{0.3}$ at 850°C, 950°C and 1050°C respectively. Dots are experimental points and dotted lines are guides for the eye.

We also highlight that the oxidation rate decreases with time during oxidation for all samples. The oxidation regime is thus not linear, in contradiction with the Deal and Grove model for thin oxides (thinner than 20 nm) [Deal65]. However, to highlight in a more quantitative manner the discrepancy with the Deal and Grove model, we tried to fit our experimental data with the Deal and Grove model with two methods:

- If we fix the parabolic constant to the value provided by the Deal and Grove model (the parabolic constant can be determined from oxidation kinetics for oxides much thicker than 200 Å according to the Deal and Grove model, which is not the case in our study), the fit quality is highly degraded as illustrated *Figure III.14*.
- If we let free all parameters of a linear-parabolic model to fit our experimental data, the fitting procedure tends to a purely parabolic regime. There is thus hardly any linear contribution, even for short oxidation times.

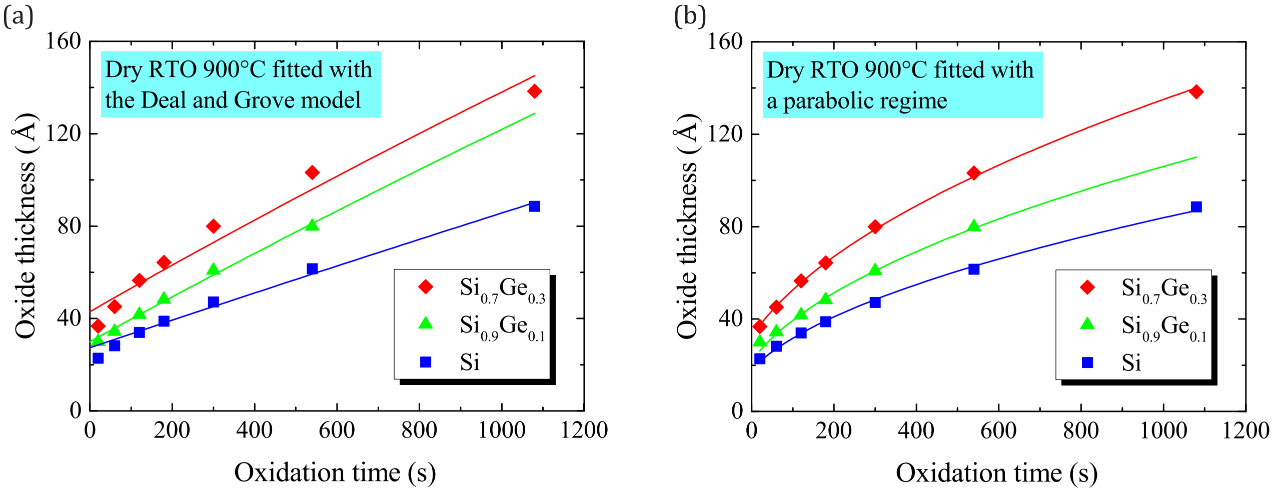

Figure III.14: Experimental oxide thickness as a function of time of $Si_{0.7}Ge_{0.3}$ *oxidized by means of dry RTO at 900°C along with curves fitted with the two methods described in text.*

The Deal and Grove model is thus not adequate for fitting the experimental data. As shown *Figure III.15*, all oxidation processes follow parabolic regimes with the following equation type:

$$x^2 = \alpha t + \beta, \qquad \textbf{\textit{Equation III.7}}$$

where x is the oxide thickness and α and β are coefficients that depend on the temperature, the initial Ge concentration and the oxidation process type.

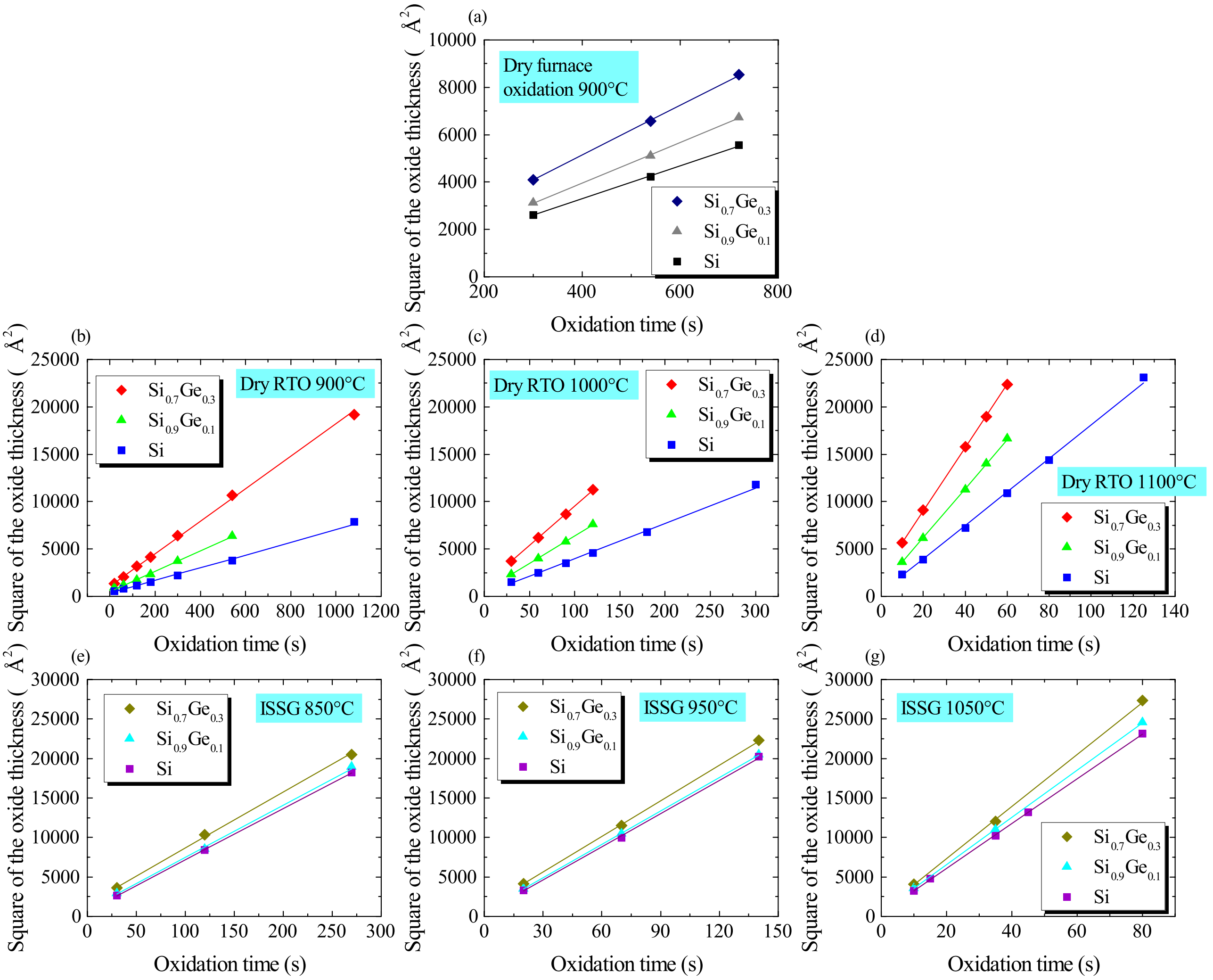

Figure III.15: (a) Square of the oxide thickness as a function of the oxidation time for dry furnace oxidation of Si, $Si_{0.9}Ge_{0.1}$ and $Si_{0.7}Ge_{0.3}$ at 900°C. (b) (c) and (d) show the square of the oxide thickness as a function of the oxidation time for dry RTO of Si, $Si_{0.9}Ge_{0.1}$ and $Si_{0.7}Ge_{0.3}$ at 900°C, 1000°C and 1100°C respectively. (e) (f) and (g) show the square of the oxide thickness as a function of the oxidation time for ISSG oxidation of Si, $Si_{0.9}Ge_{0.1}$ and $Si_{0.7}Ge_{0.3}$ at 850°C, 950°C and 1050°C respectively. Dots are experimental points and lines are fitted curves (see text).

In this section, we thus showed that firstly, the oxidation regime is parabolic in the whole range of oxide thicknesses. According to the Deal and Grove model, oxidation parabolic regimes refer to an oxidation rate limited by diffusion of the oxidizing species through the thermal oxide [Deal65]. Secondly, the oxidation rate is higher for a higher initial Ge concentration for the three studied oxidation processes.

III.A.4.1.2. Discussion about Temperature Calibration

Prior to any attempt to analyze and discuss differences of oxidation kinetics between Si and SiGe, one question that needs to be answered is that if the observed differences of oxidation kinetics do not arise from different actual oxidation temperatures between Si and SiGe samples.

For furnace oxidation, the equipment used was a batch equipment with a good spatial temperature homogeneity. Since Si and SiGe samples were oxidized in the same oxidation run, the possibility of different temperatures between Si and SiGe samples is thus ruled out.

For dry RTO and ISSG oxidation, we highlight that the measured temperature is the one of the back-side of the wafer, which is identical for Si and SiGe samples. But let us assume that the observed differences in oxidation kinetics are actually a temperature effect, in other words, that the parabolic constant α is only dependent on the oxidation process type and the temperature, and not on the Ge concentration. Knowing the activation energies of the parabolic constants α of dry RTO and ISSG oxidation of Si (they will be discussed in *Section III.A.4.1.4.*), we can extract the temperature that would correspond to the observed oxidation kinetics of SiGe.

There would be approximately 25°C and 50°C gaps between the set oxidation temperature and the actual one for dry RTO of $Si_{0.9}Ge_{0.1}$ and $Si_{0.7}Ge_{0.3}$ respectively. Such differences are much higher than possible temperature calibration errors. As for ISSG oxidation, gaps are much lower, between 3°C and 7°C. ISSG oxidations were performed in a similar equipment as dry RTO and in a single run. We are thus confident that the observed differences of oxidation kinetics for ISSG oxidation of SiGe arise from truly different oxidation kinetics between Si and SiGe and not from temperature calibration errors.

Therefore, we believe that possible temperature errors have a minor contribution in any oxidation process of this study, and that the differences of oxidation rates arise from truly Ge-based and oxidation process type effects.

III.A.4.1.3. Kinetics of Dry Oxidation of Si

As illustrated *Figure III.16*, there is hardly any difference between oxidation kinetics of Si oxidized at 900°C by means of dry furnace oxidation and dry RTO. The slightly systematic higher oxide thickness for furnace oxidation compared to dry RTO could arise from the contribution of oxidation during temperature ramps, which are longer for furnace oxidation than for dry RTO. These results suggest that O_2 diffusion properties through the thermal oxide grown on Si are identical for both processes.

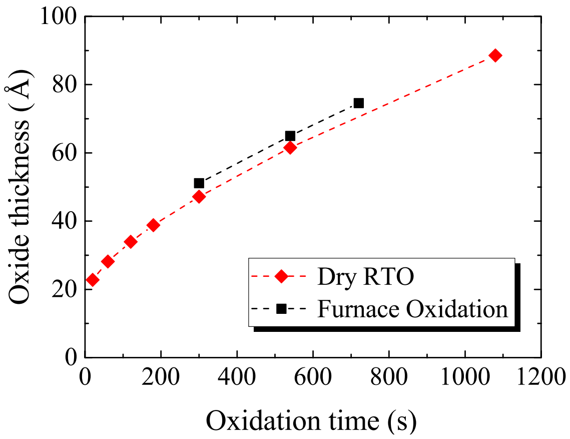

Figure III.16: Oxide thickness as a function of oxidation time for dry furnace oxidation and dry RTO of Si at 900°C.

III.A.4.1.4. Activation Energies of Oxidation of SiGe

As shown *Figure III.17*, the parabolic constants α of dry RTO and ISSG oxidation both follow Arrhenius laws (only one oxidation temperature was investigated for dry furnace oxidation, which does not allow extraction of an activation energy). Extracted activation energies are shown in *Table III.2*.

Deal and Grove found that the activation energy of the parabolic constant is 1.24 eV and assumed that it corresponds to the one of diffusion of O_2 through the thermal oxide, in good agreement with the one reported by Norton (1.17 eV) [Norton61]. The activation energy of the parabolic constant of dry RTO of Si was found to be 2.29 eV in our study, in disagreement with the ones reported by Deal and Grove and Norton for dry furnace oxidation. However, it is in better agreement with the ones reported by Kazor for dry RTO of Si (2.17 eV) and by David et al. for dry RTO of SiGe (2.1 eV) [Kazor95][David16]. As suggested by Kazor, mechanisms specific to one of the two oxidation processes likely take place and affect activation energies of oxidation. The activation energy of dry RTO found in our study is also in fairly good agreement with the activation energy of diffusion of O_2 in strained thermal SiO_2 calculated by Bongiorno et al., Tsetseris et al. and Akiyama et al. (about 2.0 eV) [Bongiorno04][[Tsetseris06][Akiyama08]. In keeping with these observations, kinetics of dry RTO of Si would be limited by diffusion of O_2 through the thermal oxide and the activation energy of diffusion would be about 2.3 eV. We also note that the activation energy of dry RTO of SiGe decreases when the initial Ge concentration increases.

As for ISSG oxidation, according to literature, ISSG oxidation is mainly limited by diffusion of O* radicals through the growing oxide, which results in a parabolic regime [Kee00]. The extracted activation energy of the parabolic constant of ISSG oxidation is therefore the one of diffusion of O* in SiO_2. We observe that ISSG oxidation follows parabolic regimes with activation energies around 1 eV for all initial Ge concentrations.

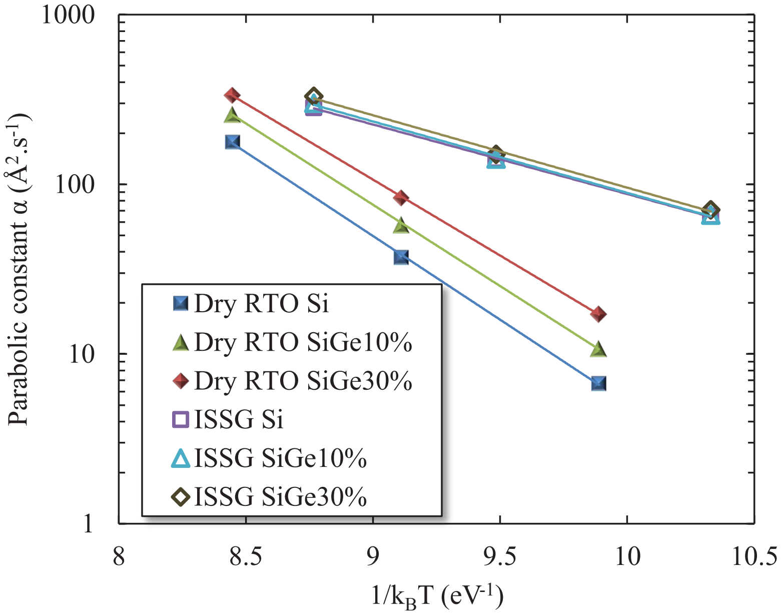

Figure III.17: Symbols are experimental parabolic constants α of dry RTO and ISSG oxidation of Si, $Si_{0.9}Ge_{0.1}$ and $Si_{0.7}Ge_{0.3}$ as a function of $1/k_BT$, and lines are results of fits with Arrhenius laws.

	Si	**$Si_{0.9}Ge_{0.1}$**	**$Si_{0.7}Ge_{0.3}$**
Dry RTO	2.29 ± 0.04	2.21 ± 0.05	2.06 ± 0.03
ISSG Oxidation	0.95 ± 0.03	0.97 ± 0.03	0.99 ± 0.03

Table III.2: Activation energies of the parabolic constant α of dry RTO and ISSG oxidation of Si, $Si_{0.9}Ge_{0.1}$ and $Si_{0.7}Ge_{0.3}$ (eV).

To go further into the analysis of oxidation kinetics of SiGe, the next section will quantitatively compare the oxidation rate of SiGe with the one of Si.

III.A.4.2. Growth Rate Enhancement (GRE)

III.A.4.2.1. Analysis Methodology of Oxidation Kinetics

In order to quantitatively examine oxidation kinetics of SiGe with respect to Si, we need to define a meaningful term that compares oxidation rates of SiGe and Si. We could not find such a definition in literature. We define a Growth Rate Enhancement (GRE): the GRE is the ratio of the SiO_2 growth rate for the case of oxidation of SiGe to the one for Si at identical oxide thickness. As a consequence of the observed parabolic regime, the GRE does not depend on the oxide thickness and has a unique value for a unique combination of oxidation process type, initial Ge concentration and oxidation temperature. Finally, the GRE is reduced to:

$$GRE = \frac{\alpha\left(SiGe\ initial\ concentration, oxidation\ process\ type, T\right)}{\alpha\left(Si, oxidation\ process\ type, T\right)}, \qquad \textbf{Equation III.8}$$

where *SiGe initial concentration* is either 10% or 30% Ge concentration in this study, the *oxidation process type* is either dry furnace oxidation, dry RTO, or ISSG oxidation, *T* is the oxidation temperature, and *α* the coefficients extracted from the fitted parabolic laws of *Figure III.15*. For instance, let us consider the case of $Si_{0.7}Ge_{0.3}$ oxidized by means of dry RTO at 1000°C illustrated *Figure III.18*. The GRE of this case could be evaluated at an oxide thickness of 67 Å, which corresponds to 40 seconds and 120 seconds of oxidation for $Si_{0.7}Ge_{0.3}$ and Si respectively. And it could also be evaluated at an oxide thickness of 93 Å, which corresponds to 90 seconds and 225 seconds of oxidation for $Si_{0.7}Ge_{0.3}$ and Si respectively.

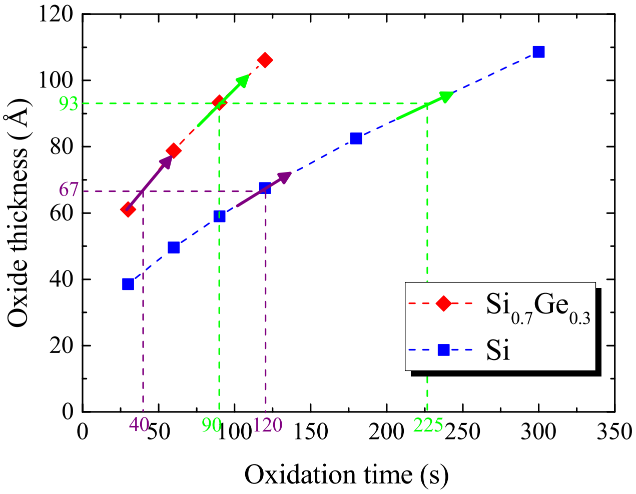

Figure III.18: Illustration of the GRE for the case of $Si_{0.7}Ge_{0.3}$ *oxidized at 1000°C after 90 seconds. The oxide thicknesses mentioned in text for illustration are 67 Å and 93 Å. Arrows are tangents to the curves and represent the growth rates of* $Si_{0.7}Ge_{0.3}$ *and Si at these oxide thicknesses.*

We propose this GRE definition for the following reasons. Firstly, in order to quantitatively examine the effect of Ge on oxidation kinetics, what must be considered is the oxidation rate and not directly the oxide thickness. Indeed, whatever the mechanisms that govern oxidation kinetics are, oxidation models such as the ones of Deal and Grove, Watanabe et al. and Cui et al. are based on oxidizing species flux and oxidation rates [Deal65][Watanabe06][Cui09]. Secondly, because the oxidation regime is parabolic, the oxidation rate tends to decrease with time. With this GRE definition, the contribution of the increasing oxide thickness to the oxidation rate is thus excluded and only the effects of both the oxidation process type and Ge on oxidation kinetics are analyzed.

III.A.4.2.2. GRE Dependence on the Initial Ge Concentration

As seen previously, the initial Ge concentration influences the oxidation rate of SiGe. *Figure III.19* shows the GRE as a function of the initial Ge concentration. We observe that, for either dry furnace oxidation, dry RTO or ISSG oxidation, the GRE is always higher for $Si_{0.7}Ge_{0.3}$ than for $Si_{0.9}Ge_{0.1}$ (see (1) on *Figure III.19*). We also observe that the GRE is higher for dry RTO than for dry furnace oxidation (see (2) on *Figure III.19*). Therefore, for a given oxidizing species, how the thermal energy is provided influences oxidation kinetics of SiGe.

If we now compare the GRE values of dry RTO and ISSG oxidation, two RTO process types, the GRE is much lower for ISSG than for dry RTO. The nature of the oxidizing species thus also influences the GRE. Then, for both dry RTO and ISSG oxidation, the GRE depends not only on the initial Ge concentration, but also on the oxidation temperature (see (3) on *Figure III.19*). However, the GRE of dry RTO and of ISSG oxidation depend on the oxidation temperature in the opposite way. The higher the oxidation temperature is for a fixed initial Ge concentration, the lower the GRE is for dry RTO. On the contrary, the higher the oxidation temperature is, the higher the GRE of ISSG oxidation is.

Therefore, further investigation is required to understand how the nature of the oxidizing species, the initial Ge concentration and the temperature influence oxidation kinetics of SiGe. As described in *Section III.A.1.3.3.*, the SiGe composition depth profile evolves during oxidation. We hence propose to consider into the next section the Ge redistribution during oxidation of SiGe to further examine the GRE.

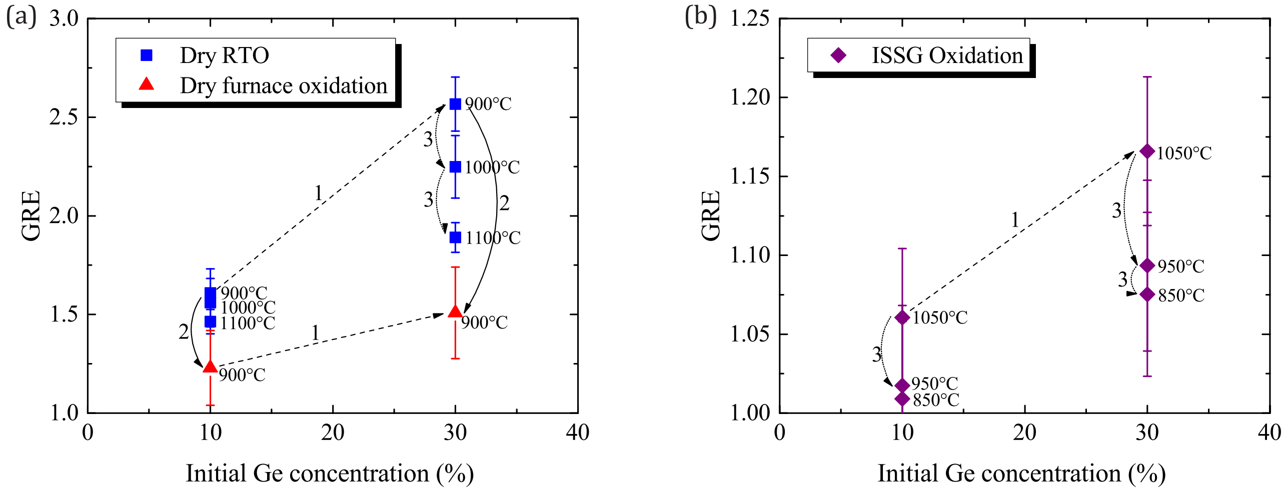

Figure III.19: GRE as a function of the initial Ge concentration for (a) dry RTO and furnace oxidation, and (b) ISSG oxidation of SiGe. The influences indicated by numbers on the figure are explained in text.

III.A.4.3. Evolution of the Ge Concentration at the Oxidation Interface

Figure III.20 shows the SIMS profiles of Ge concentration after oxidation of various samples oxidized by means of dry RTO. For clarity considerations, the *x* axis is shifted so that the SiGe-oxide interfaces are all close to zero. We observe that the Ge concentration just below the oxide, so that at the oxidation interface, is always higher than the initial Ge concentration of the SiGe epitaxial layer. The pile-up mechanism caused by the Si-selective oxidation of SiGe is therefore clearly evidenced. The Ge concentration profile after oxidation, and especially at the oxidation interface, obviously depends on the initial Ge concentration and oxidation temperature.

For dry RTO at 900°C, a few nanometers-thick layer with a high Ge concentration is observed below the oxidation interface. Plateaux at 10% and 30% Ge concentration corresponding to the initial SiGe epitaxial layer and a quite abrupt interface between the SiGe epitaxial layer and the Si substrate are still clearly visible on *Figure III.20 (a)* and *(b)*. While for dry RTO at 1000°C and 1100°C, no layer with abrupt interfaces and formed by the pile-up mechanism can be identified on *Figure III.20 (c)*, *(d)* and *(e)*. The plateaux at 10% or 30% Ge concentration have also disappeared and interfaces between the SiGe epitaxial layer and the Si substrate are now much graded. The higher the oxidation temperature is, the less noticeable the pile-up mechanism is. As a consequence, the Ge concentration at the oxidation interface is lower at higher oxidation temperatures.

With the oxidation conditions used in this study, all Ge atoms at the oxidation interface are piled-up below the oxidation front in the underlying SiGe crystal [Paine91] (see *Section IV.A.3.*). Stated differently, there is no Ge segregation in the oxide. The Ge concentration profile below the oxide, and especially at the oxidation interface, depends on a competition between oxidation that piles-up Ge atoms below the oxidation front and SiGe interdiffusion that tends to smooth the Ge concentration profile below the oxide. Oxidation and diffusion in SiGe are both thermally activated mechanisms that follow Arrhenius-type laws. As shown in *Section III.A.4.1.4.*, the activation energy of dry RTO of SiGe is about 2 eV. While the ones of Ge and Si diffusion in SiGe are in the 4 eV to 5 eV range [Kube10]. Phrased in qualitative terms, the temperature dependence of diffusion is much higher than the one of both dry RTO and ISSG oxidation. Therefore, the diffusion rate increases faster with temperature than the oxidation rate does, which makes the Ge pile-up less pronounced as Ge atoms diffuse away.

The second key point of this section is that the Ge concentration at the oxidation interface seems to be constant after a transient regime. For dry RTO of $Si_{0.7}Ge_{0.3}$ at 1100°C (see *Figure III.20 (c)*), the first ten seconds at least likely correspond to a transient regime when the oxidation rate is particularly high because of the very thin oxide. In that case, the oxidation rate largely exceeds the diffusion rate. Therefore, we will not consider this transient regime for the analysis of the GRE, and will assume that the Ge concentration at the oxidation interface is rather constant at about 33% during almost all the investigated oxidation durations range. For dry RTO of $Si_{0.7}Ge_{0.3}$ at 1000°C (see *Figure III.20 (b)*), the Ge concentration at the oxidation interface is 41.7% and 42.4% after 60 seconds and 120 seconds of oxidation respectively. As for dry RTO of $Si_{0.7}Ge_{0.3}$ at 900°C (see *Figure III.20 (a)*), the Ge concentration at the oxidation interface increases from 45.9% after 120 seconds of oxidation to 49.8% after 1080 seconds of oxidation. Nevertheless, this 3.9% variation of the Ge concentration with time is rather low compared to the gap induced by the oxidation temperature, from 33% Ge concentration at the oxidation interface at 1100°C to more than 46% at 900°C.

The Ge concentration at the oxidation interface after dry RTO of $Si_{0.9}Ge_{0.1}$ at 1100°C for 50 seconds and at 900°C for 540 seconds are 16% and 21% respectively. By analogy with the case of $Si_{0.7}Ge_{0.3}$, we can reasonably assume that there is also a plateau for the Ge concentration at the interface for dry RTO of $Si_{0.9}Ge_{0.1}$, taken as 16% at 1100°C and 21% at 900°C (see *Figure III.20 (d)* and *(e)*).

The evolution of the Ge profile below the oxide, and especially at the oxidation interface, depends on the interdependence of the pile-up mechanism caused by the Si-selective oxidation and SiGe interdiffusion. This manuscript does not intend to quantitatively explain the observed quasi-plateau of the Ge concentration at the oxidation interface during dry RTO, but rather keeps to the observed tendencies to discuss oxidation kinetics.

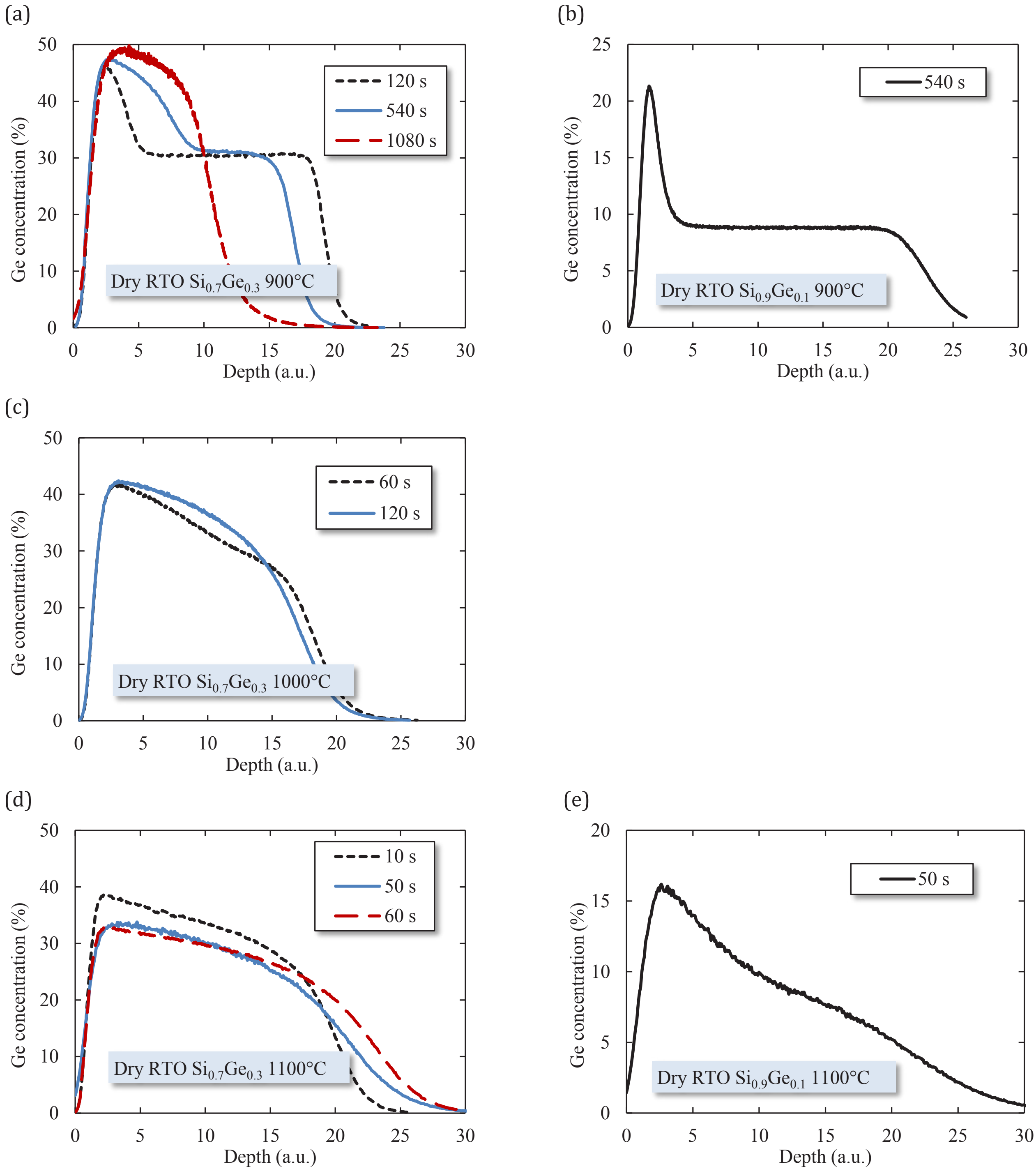

Figure III.20: SIMS profiles of the Ge concentration below the oxide after dry RTO of (a) $Si_{0.7}Ge_{0.3}$ at 900°C, (b) 1000°C, (c) 1100°C, and of (d) $Si_{0.9}Ge_{0.1}$ at 900°C and (e) at 1100°C. For clarity considerations, the x axis is shifted so that the SiGe-oxide interfaces are all close to zero.

As shown *Figure III.21 (a)*, with a Ge concentration at the oxidation interface of 45.5% for dry furnace oxidation at 900°C of $Si_{0.7}Ge_{0.3}$, there is hardly any difference with dry RTO. The differences in terms of total quantities of Ge atoms in both layers arise from a thinner epitaxial SiGe film for the case of dry furnace oxidation. As for ISSG oxidation, the same tendency as for dry RTO is obserbed, with a strong pile-up layer with a maximum Ge concentration of 59.7% observed for ISSG oxidation of $Si_{0.7}Ge_{0.3}$ at 850°C. Indeed, ISSG oxidation at 850°C is much faster than dry RTO, which increases even more the gap between the oxidation rate that piles up Ge atoms and the diffusion rate. The Ge concentration at the oxidation interface for ISSG oxidation of $Si_{0.9}Ge_{0.1}$ at 1050°C is 22.3%.

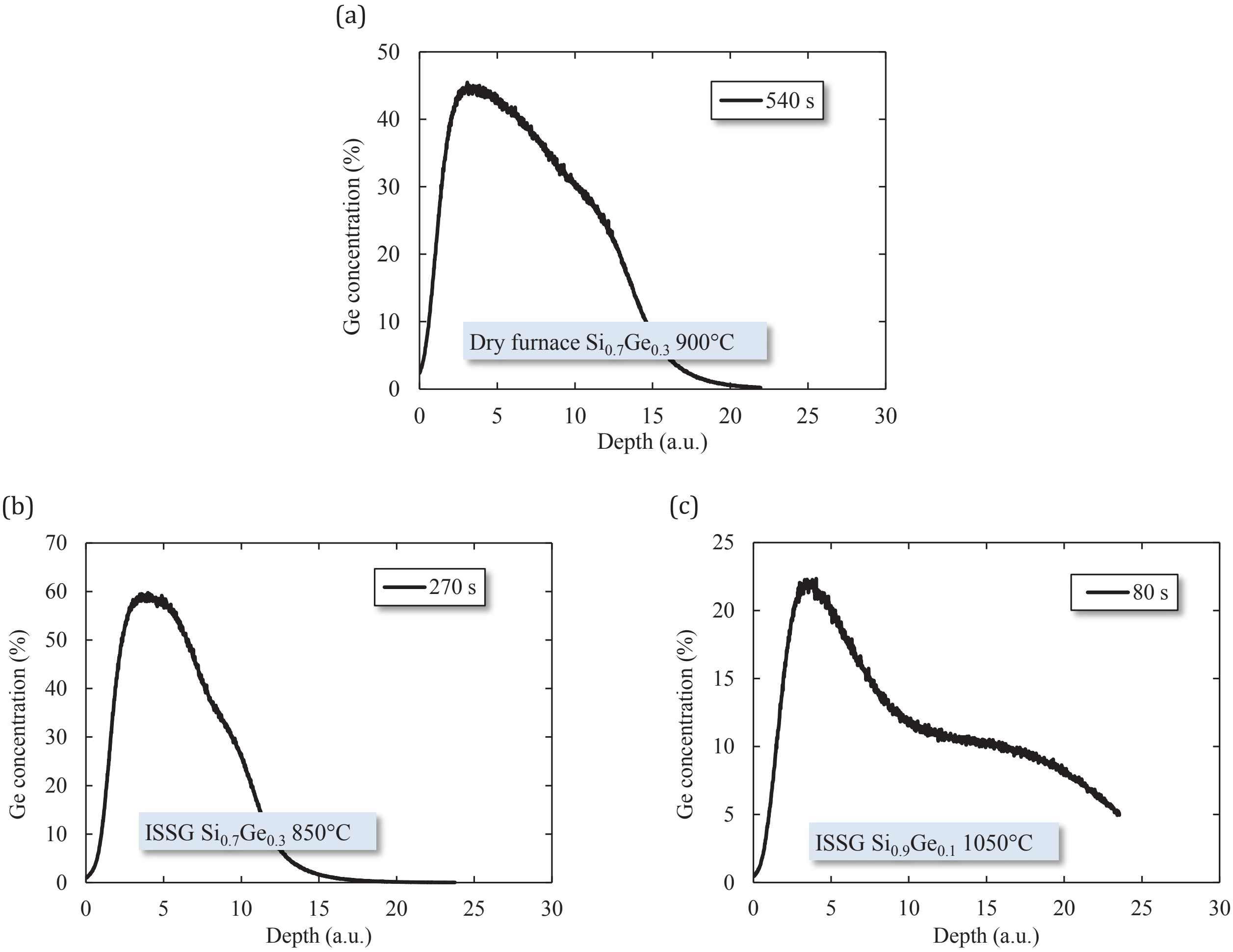

Figure III.21: SIMS profiles of the Ge concentration below the oxide after (a) dry furnace oxidation of $Si_{0.7}Ge_{0.3}$ at 900°C, (b) ISSG oxidation of $Si_{0.7}Ge_{0.3}$ at 850°C, (c) and ISSG oxidation of $Si_{0.9}Ge_{0.1}$ at 1050°C. For clarity considerations, the x axis is shifted so that the SiGe-oxide interfaces are all close to zero.

To summarize the main conclusions of this section, we firstly claim that for all investigated dry RTO processes, a pile-up layer is rapidly formed below the oxide, and that after a transient regime, the Ge concentration at the oxidation interface is quite constant with time over the range of studied oxidation durations. We also observe that the higher the oxidation temperature is, the lower the Ge concentration at the oxidation interface is.

III.A.4.4. GRE Dependence on the Ge Concentration at the Oxidation Interface

Following *Section III.A.4.3.* conclusions, *Figure III.22* shows the GRE as a function of the Ge concentration at the oxidation interface measured by SIMS, except for dry RTO of $Si_{0.7}Ge_{0.3}$ at 1100°C for 10 seconds that likely correspond to a transient regime. We found that the higher the Ge concentration at the oxidation interface is, the higher the GRE for dry RTO is. For dry RTO, the GRE dependence on the initial Ge concentration and on the temperature shown *Figure III.19 (a)* can be summed up by its dependence on the Ge concentration at the oxidation interface. Due to the GRE definition given *Equation III.9*, the oxidation rate of SiGe by means of dry RTO is therefore the one of Si oxidized in the same conditions multiplied by a factor that depends only on the Ge concentration at the interface.

As already shown *Figure III.19 (a)*, the GRE of dry furnace oxidation at 900°C is lower than the one of dry RTO at the same temperature. It was also evidenced that the Ge concentrations at the oxidation interface for dry furnace oxidation and dry RTO are similar. It thus shows that the Ge concentration at the oxidation interface is not the only parameter that affects oxidation kinetics of SiGe for dry oxidation, and that the process type also influences oxidation kinetics of SiGe.

Finally, kinetics of ISSG oxidation is only slightly dependent on the Ge concentration at the oxidation interface, as already shown *Figure III.19 (b)*.

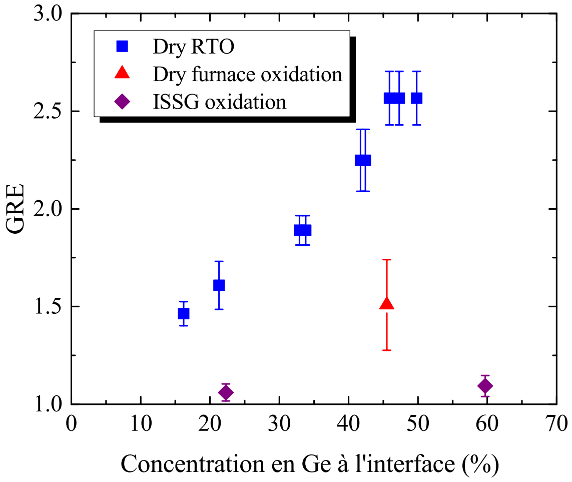

Figure III.22: GRE of dry furnace oxidation, dry RTO and ISSG oxidation of SiGe as a function of the Ge concentration at the oxidation interface.

III.A.4.5. Conclusion of Section III.A.4.

To conclude *Section III.A.4.*, we showed that oxidation of SiGe by means of either dry furnace oxidation, dry RTO and ISSG oxidation is limited by diffusion of the oxidizing species through the growing oxide. The oxidation rate of SiGe was found to be weakly dependent on the presence of Ge for ISSG oxidation, while it is significantly higher for the cases of dry furnace oxidation and dry RTO. A factor called Growth Rate Enhancement (GRE) was then defined to quantitatively compare the oxidation rates of Si and SiGe.

We also evidenced that a Ge pilled-up region below the oxide is rapidly formed during oxidation and that afterwards, the Ge concentration at the oxidation interface is rather constant with time over the range of studied oxidation durations. For dry RTO, our results show that the oxidation rate of SiGe increases with the Ge concentration at the oxidation interface. It was shown that the gap between the GRE of SiGe oxidized by means of dry RTO with the one for dry furnace oxidation cannot be explained based solely on the comparison of the Ge concentrations at the oxidation interface, which was found to be almost equals for both processes. The process type thus influences oxidation kinetics of SiGe.

Various studies showed or suggested that the oxide density can influence diffusion of O_2 through the oxide and that this density is influenced by oxidation process parameters (see *Section III.A.1.3.2.*). The next section thus discusses further oxidation kinetics of SiGe in light of the measurement of the oxide density by X-Ray Reflectivity (XRR).

III.A.5. Correlation Between SiGe Oxidation Kinetics and Oxide Density

We showed in the previous section that oxidation of SiGe is governed by diffusion of the oxidizing species through the growing thermal oxide. As the density of the oxide is known to influence diffusion of the oxidizing species, this section aims to understand how oxidation kinetics of SiGe depends on the oxide density, and how the process parameters and the Ge concentration at the oxidation interface affect the oxide density.

This section starts by describing the methodology of measurement of the oxide density by X-Ray Reflectivity (XRR). Then, we investigate how the process parameters and the Ge concentration at the oxidation interface influence the oxide density. Oxidation kinetics is correlated with the oxide density and discussed in light of the influence of the oxide density on the diffusivity of O_2 through the thermal oxide. Finally, the dependence of O_2

diffusion on the oxide density, a subject that the study of oxidation kinetics allows to investigate, is discussed.

III.A.5.1. Measurement of the Oxide Density by X-Ray Reflectivity (XRR)

III.A.5.1.1. Methodology for Extraction of Scattering Factors from Absorption Spectra

We intended to measure the density of thermal oxides grown on SiGe by Resonant Soft X-Ray Reflectivity (R-SoXR) around the O K-absorption edge. Indeed, R-SoXR can be a powerful technique for measurement of small variations of electron densities (see *Section II.4.1.4.*). As drawn in *Section II.4.1.2.*, scattering factors of all elements in the sample must be known for analysis of XRR spectra, hence the description of their measurement in this section.

While the tabulated values of the scattering factors do not accurately reproduce the precise variations of the scattering factors close to an absorption edge, they are reliable far from it. Si and Ge scattering factors below and above the O K-absorption edge used in the fitting procedure are thus tabulated values [CXRO].

The following procedure was used to measure O scattering factors around its K-absorption edge:

- Measurement of absorption spectra: absorption of several samples was measured in Total Electron Yield (T.E.Y.) and Total Fluorescence Yield (T.F.Y.) modes between 520 eV and 550 eV. Differences between the two modes are introduced in *Section II.4.1.5.* in terms of experimental set-up and will be discussed in *Section III.A.5.1.2.*.
- Normalization: the following linear normalization allows extraction of the imaginary part of the O scattering factor because absorption is proportional to the imaginary part of the scattering factor f_2:

$$f_2(E) = aI(E) + b, \qquad \textbf{Equation III.9}$$

where *I(E)* is the absorption spectrum as a function of the X-Ray energy *E*, and *a* and *b* are constants. *a* and *b* are calculated using two tabulated values for the O scattering factor respectively below and above the absorption edge (here 520 eV and 550 eV) [CXRO]:

$$\begin{aligned} f_2(520\ eV) &= aI(520\ eV) + b \\ f_2(550\ eV) &= aI(550\ eV) + b. \end{aligned} \qquad \textbf{Equations III.10}$$

As a result:

$$\begin{aligned} a &= \frac{f_2(520\ eV) - f_2(550\ eV)}{I(520\ eV) - I(550\ eV)} \\ b &= \frac{f_2(550\ eV)I(520\ eV) - f_2(520\ eV)I(550\ eV)}{I(520\ eV) - I(550\ eV)}. \end{aligned} \qquad \textbf{Equations III.11}$$

We also highlight that Si and Ge atoms absorb X-Ray photons, and thus contribute to the measured absorption spectra. However, the variations of their scattering factors between 520 eV and 550 eV are much lower than the one of O atoms. Therefore, their contributions in the measured absorption spectra has no effect on calculation of the imaginary part of the O scattering factor using *Equations III.10*.

III.A.5.1.2. O Scattering Factor around the K-Absorption Edge

Figure III.23 shows the O scattering factors retrieved from measurement of absorption spectra of three different samples in T.E.Y. and T.F.Y. modes. The samples are Si and $Si_{0.7}Ge_{0.3}$ films oxidized by means of dry RTO. While the T.E.Y. mode probes the top few nanometers of the oxide (between 1 nm and 5 nm), the T.F.Y. mode probed depth is larger than 10 nm and thus probes all O atoms of the oxide, including the O atoms at the interface with the Si(Ge) layer.

Hardly any difference can be observed between O scattering factors of the three samples for the T.E.Y. mode (see *Figure III.23 (a)*). The T.E.Y. mode shows that the O scattering factor of the top of the oxide is not or hardly influenced by Ge and by the oxidation temperature. A hollow can be observed at around 528 eV while no noticeable variation is expected below the absorption edge. This hollow is likely due to absorption caused by residual oxygen in the beamline (absorption of the beamline was measured independently from these experiments and shows some absorption at around 528 eV).

O scattering factors acquired in T.F.Y. mode are shown *Figure III.23 (b)*. The O scattering factor of the Si sample oxidized at 1100°C and measured in T.E.Y. mode is also plotted for comparison. The same hollow is observed at about 528 eV, which supports the suggestion of absorption by residual oxygen in the beamline. In T.F.Y. mode only, a pre-edge "bump" is observed at around 532 eV. This pre-edge "bump" can thus be associated with O atoms close to the interface with Si(Ge). We also observe that the intensities of this pre-edge "bump" and of the maximum of absorption at 535 eV are different between the three samples. It is noticed that the O scattering factor of the Si sample in T.F.Y. mode unexpectedly decreases from about 1.6 at 520 eV to 0.3 at 528 eV. We believe that this is due to measurement issues and that this decrease has no physical meaning.

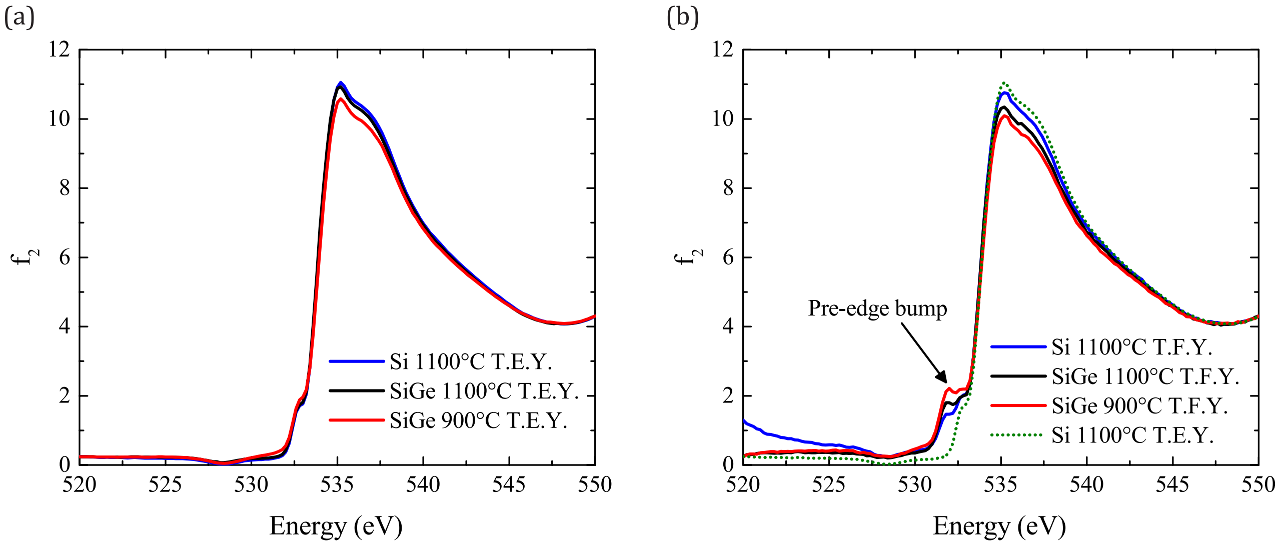

Figure III.23: Imaginary part of the O scattering factor around its K-absorption edge measured in (a) T.E.Y. and (b) T.F.Y. modes. The O scattering factor of the Si sample oxidized at 1100°C and measured in T.E.Y. mode is also plotted in (b) for comparison.

In order to discuss further about this pre-edge "bump", the O scattering factors of the Si sample oxidized at 1100°C are compared with the ones of O atoms in the bulk of the oxide and at the interface with Si measured by Muller at al. [Muller99]. Muller et al. used a microscopy technique (Electron Energy Loss Spectroscopy: EELS) to probe the O scattering factor at the atomic scale as a function of the position with respect to the Si-oxide interface. The O scattering factors spectra published by Muller et al. were normalized following the procedure of *Section III.5.1.1.* and shifted in the *x* axis so that the one of the bulk of the oxide coincides at 533.6 eV with the one that we measured (such a shift is expected because of different experimental set-up and thus different absolute energy measurements).

We observe on *Figure III.24* that the scattering factor of O atoms in the bulk of the oxide from Muller et al. is very similar to the one that we measured in T.E.Y. mode until at least 550 eV. Differences, especially at the onset of the absorption edge (about 532 eV) and at the maximum of absorption (about 535 eV) may partially due to different energy resolutions between EELS measurements of Muller et al. and our measurements.

Muller et al. found that the scattering factor of O atoms located at the Si-oxide interface is very different from the one of O atoms in the bulk of the oxide. More precisely, they found that the edge onset is reduced by 3 eV and that there is no sharp peak at 535 eV. They claimed that this sharp peak is associated with O-O scattering and is strongly reduced when the number of O second-nearest neighbours around the excited O atom is reduced. The number of O second-nearest atoms being reduced in the vicinity of the Si-oxide interface, the sharp peak tends to disappear close to the interface.

The energy shift of the pre-edge "bump" with respect to the edge onset of the T.E.Y. mode is lower than but in qualitative agreement with the one observed by Muller et al.. These results support that the pre-edge "bump" observed in T.F.Y. mode arises from O atoms close to the oxide-Si(Ge) interface.

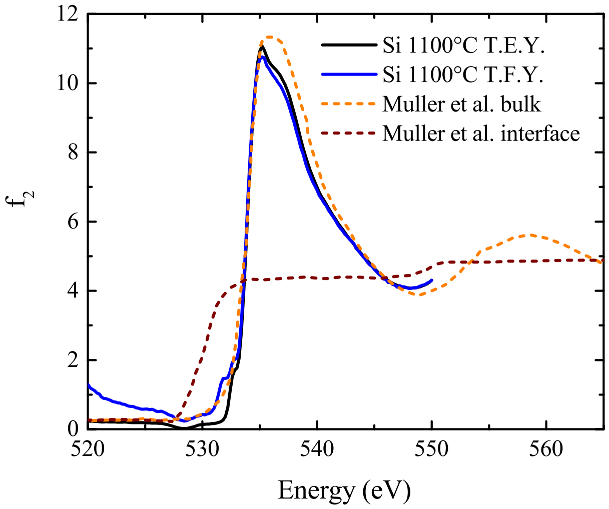

Figure III.24: Imaginary part of O scattering factors of the Si sample around the K-absorption edge and measured in T.E.Y. and T.F.Y. modes, as well as the ones measured by Muller et al. in the bulk of thermal oxide on Si and at the Si-thermal oxide interface [Muller99].

However, it is difficult to perform a quantitative analysis of O absorption at the Si(Ge)-oxide interface such as the one published by Muller et al. using the T.F.Y. mode. Indeed, this mode measures absorption of all O atoms of the oxide, including O atoms at the surface of the oxide which also have a reduced number of second-nearest O neighbours, and O atoms in the vicinity of the Si(Ge)-oxide interface. Moreover, the contribution of O atoms to the spectrum depends on the depth of the O atoms because of absorption of X-Ray photons in the SiO_2 film. A dedicated study would be required to retrieve this dependency.

A simple quantitative method is now attempted in order to draw tendencies. We assume that the T.F.Y. mode simply adds up absorption of O atoms from the bulk of the oxide, whose scattering factor is assumed to be the one of the Si sample in T.E.Y. mode, with the one of O atoms in an interfacial layer where all O atoms have the scattering factor at the interface published by Muller et al.. The equation of this linear combination is then:

$$f_{2-T.F.Y.} = (1-z)\, f_{2-T.E.Y.} + z f_{2-interface-Muller}, \qquad \textbf{Equation III.12}$$

where $f_{2\text{-}T.F.Y.}$ and $f_{2\text{-}T.E.Y.}$ are imaginary parts of O scattering factors of the Si sample acquired in T.F.Y. mode and T.E.Y. mode respectively, $f_{2\text{-}interface\text{-}Muller}$ is the O scattering factor at the interface published by Muller et al., and z a coefficient. Absorption being proportional to the total quantity of O atoms, it is also proportional to the thickness of the considered layer. So, the thickness of the interfacial layer is:

$$Interfacial\ thickness\ =\ z.total\ oxide\ thickness. \qquad \textbf{Equation III.13}$$

Firstly, we chose to apply this method at 532 eV because at this energy, the contribution of O atoms of the bulk of the oxide is minimum and equal to the tabulated values while the one of the interface is maximum. *Table III.3* summarizes the total oxide thicknesses of the three samples measured by ellipsometry and the interfacial layer thickness calculated using *Equation III.12* and *Equation III.13*. In summary, the thickness of the layer that has O atoms having scattering factors different from the one of the bulk of the oxide is higher for SiGe than for Si, even if reported values must not be taken as absolute values. In summary, there are more O atoms having scattering factors different from the one of the bulk of the oxide at the SiGe-oxide interface than at the Si-oxide interface.

LeGoues et al. and Kilpatrick et al. showed by XPS that the SiGe-oxide interface has more Si atoms in intermediate oxidation states than the Si-oxide interface [LeGoues89’][Kilpatrick08]. In other words, there are more Si sub-oxides at the SiGe-oxide interface. The sharp absorption peak at 535 eV arises from O-O scattering, so that we can expect O atoms in Si sub-oxides to have scattering factors close to the one at the interface published by Muller et al.. Our results are thus consistent with a higher quantity of Si sub-oxides at the SiGe-oxide interface observed by LeGoues et al. and Kilpatrick et al.

	Si 1100°C	$Si_{0.7}Ge_{0.3}$ 1100°C	$Si_{0.7}Ge_{0.3}$ 900°C
Total thickness	95.4 Å	138.8 Å	99.5 Å
Interfacial layer thickness	26.5 Å	50 Å	46.3 Å

Table III.3: Total oxide thicknesses measured by ellipsometry and interfacial layer thicknesses calculated using Equation III.12 and Equation III.13. Samples were oxidized by means of dry RTO at the temperature indicated in the Table.

We found no sound results with this procedure when applied to the whole spectra between 520 eV and 550 eV. We believe that the linear combination of *Equation III.12* is not sophisticated enough to match reality. For instance, we could imagine a graded O scattering factor from the one at the interface published by Muller et al. to the one of bulk for the O atoms in a sub-oxide region in close proximity with the interface. And the dependence of the contribution of each O atom on depth was neither taken into account.

The fact that we cannot accurately retrieve the O scattering factors as a function of the distance from the Si(Ge)-oxide interface does not allow proper fitting of XRR spectra except below the absorption edge. Indeed, the O scattering factor below the absorption edge is not dependent on the environment of the scattering O atom and is tabulated. As a consequence, XRR spectra acquired at 500 eV only will be analyzed in the next sections using tabulated values of Si, Ge and O scattering factors [CXRO].

III.A.5.1.3. Methodology for Measurement of the Oxide Density by Fitting XRR Spectra

All XRR spectra were fitted using Dyna program (see *Section II.4.1.6.*). The thickness, the density and the roughness of each layer except the Si substrate were free fitting parameters. The roughness of the Si substrate was a free parameter while its density was fixed to its known value. Uncertainties of the measurement of the oxide density were calculated assuming that the statistical error is governed by Poisson statistics, which is the statistical error of a photon source [Tiilikainene07]. We included a synthetic error into the count of photons at each measurement angle of XRR experiments using the following formula:

$$I_S(\theta) = I(\theta) + \eta(\theta)\sqrt{I(\theta)},$$ **Equation III.14**

where I, Is, θ and η are the measured count of photons, the synthetic count of photons, the angle between the incoming X-Ray beam and the surface of the sample, and a random number in the [-1,1] interval. We then fitted numerous synthetic XRR spectra to get the statistical error on the oxide density. We report as error bars on all following figures the maximum deviation obtained with this method.

III.A.5.1.4. Density of Thermal Oxides Grown on Si and SiGe

XRR experimental spectra were fitted with two different models depending on the oxidized material:

- Oxides grown on Si: a single SiO_2 layer on top of the Si substrate. The density, the thickness, the roughness of the oxide and the roughness of the Si substrate were free parameters. The density of the Si substrate was fixed to its known value.
- Oxides grown on SiGe: a single SiO_2 layer on top of two SiGe layers and the Si substrate. The densities, thicknesses and roughnesses of the oxide and of the SiGe layers were free parameters. The density of the Si substrate was fixed to its known value.

Figure III.25 shows the experimental and fitted XRR spectra of Si and SiGe samples oxidized in various conditions. Some portions of experimental curves are missing because signal jumps were removed. For oxides on Si, very high fit qualities were obtained with a single SiO_2 layer on top of the Si substrate.

As for SiGe, we observe that all spectra have major interference fringes and some minor contributions which warp the main interference fringes. The major fringes are due to reflection at the oxide-SiGe interface and minor fringes are due to reflections in the SiGe and Si layers. The thickness of the major fringes is related to the oxide thickness while their amplitudes are related to the optical contrast between the oxide film and the SiGe layer. For X-Rays, the optical contrast is related to gaps in terms of electron densities. The electron density is also related to the mass density, which is a more common and used parameter. The mass density of thermal oxides is around 2.2 $g.cm^{-3}$ while the one of SiGe goes from about 2.3 $g.cm^{-3}$ for Si to 4 $g.cm^{-3}$ for $Si_{0.5}Ge_{0.5}$. Therefore, the higher the Ge concentration at the oxidation interface is, the higher the optical contrast between the oxide and the SiGe layer is. It explains why fringes are more pronounced for oxides on SiGe than for oxides on Si.

Rather good fit quality are obtained by using a model with a single oxide layer on top of two SiGe layers and the Si substrate. The fit quality is very good around the critical angle, which only depends on the oxide density (see *Section II.4.1.3.)*. This gives us confidence about the reported oxide density values. In general, the fit quality is better for low *q* values, where spectra are more sensitive to the density contrast between the oxide and the SiGe layer, than for high *q* values where reflections at deeper interfaces have a higher contribution. We are thus confident about values of the oxide density extracted from these spectra and discussed into the next sections.

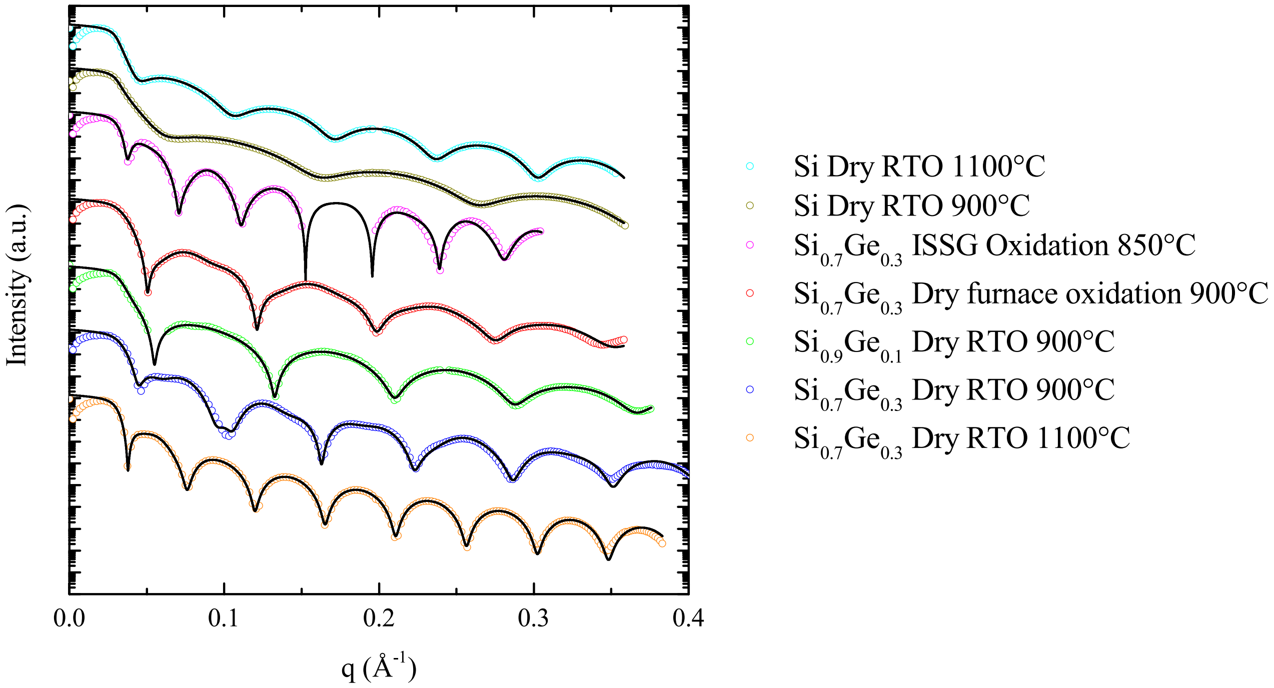

Figure III.25: XRR spectra of thermal oxide-SiGe samples. Dots are experimental XRR spectra acquired at 500 eV and lines are results of fits.

The density of oxides grown on Si and on SiGe is plotted *Figure III.26* as a function of the oxidation temperature. The effects of the initial Ge concentration, of the process type and of the oxidation temperature are summarized below and indicated by arrows on *Figure III.26*:

- 1: Initial Ge concentration: for both dry RTO and ISSG oxidation, the higher the initial Ge concentration is, the lower the oxide density is.
- 2: Process type: the density of the oxide grown on $Si_{0.7}Ge_{0.3}$ is higher for dry furnace than for dry RTO.
- 3: Temperature: the oxide density of oxides grown on $Si_{0.7}Ge_{0.3}$ by means of dry RTO increases with the temperature, as opposed to the case of Si.

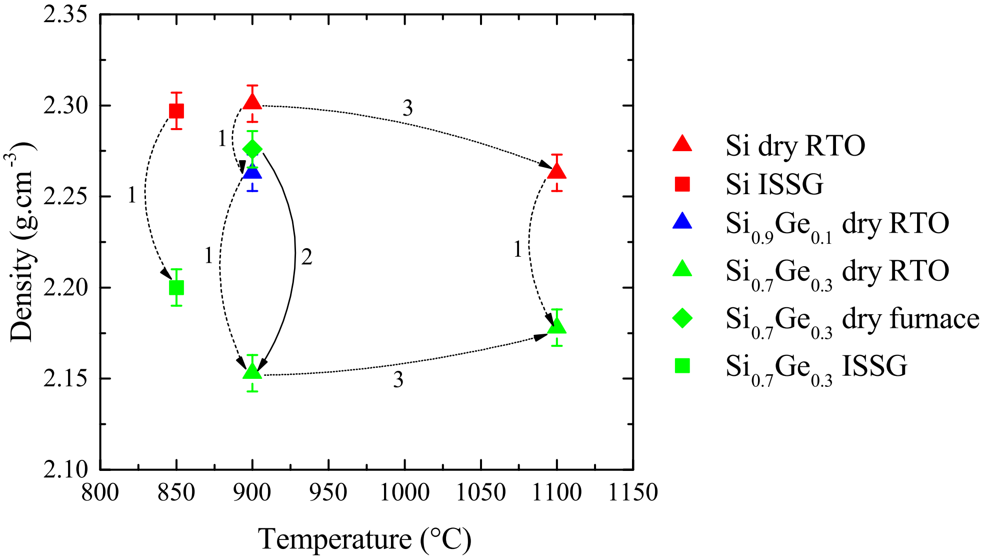

Figure III.26: Evolution of the density of oxides grown on Si and on SiGe as a function of the oxidation temperature. The effects of the initial Ge concentration, of the process type and of the oxidation temperature on the oxide density are indicated by arrows (see text).

These results confirm the conclusion of *Section III.A.4.2.2.*: the oxide density is influenced by a combination of process type, initial Ge concentration and oxidation temperature. Following *Section III.A.4.* logical procedure, the next section considers the Ge concentration at the oxidation interface to study further SiGe oxidation kinetics.

III.A.5.2. Dependence of the Oxide Density on Process Parameters

Figure III.27 shows the measured oxide density as a function of the Ge concentration measured by SIMS at the oxidation interface. We observe that the higher the Ge concentration at the oxidation interface is, the lower the oxide density is for dry RTO and ISSG oxidation. A shift is also observed between dry RTO at 900°C and dry RTO at 1100°C. We suggest that SiO_2 stress relaxation via viscous flow at high temperature (> 960°C) may account for the influence of temperature on the oxide density for the case of SiGe as well.

One mechanism can be proposed to explain the oxide density dependence on the Ge concentration at the oxidation interface. As suggested by Holland et al., the higher lattice parameter of SiGe compared with Si, at least the out-of-plane one for a fully strained SiGe film, would tend to accommodate the mismatch of atomic spacing between Si and SiO_2 [Holland87]. As a result, the interfacial compressive stress in the grown oxide would be lower for oxides grown on SiGe. The lower compressive stress at the oxidation interface would correspond to a less dense oxide generated at the oxidation interface. The Ge concentration at the oxidation interface being rather constant during oxidation, except during a transient regime at the beginning of oxidation (see *Section III.A.4.3.*), the density of the grown oxide would be rather homogeneous in depth.

We also observe that the oxide density for the case of dry furnace oxidation at 900°C is not aligned with dry RTO at 900°C. We suggest that the longer temperature ramp up of furnace oxidation may influence strain in the SiGe layer prior to oxidation. Strain of the SiGe film after dry furnace oxidation could not be measured, so further experiments are required to study this suggestion.

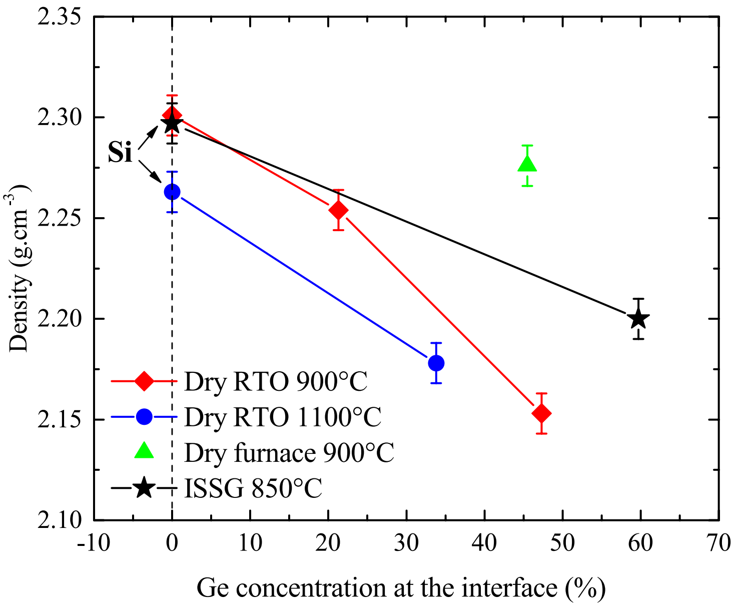

Figure III.27: Evolution of the oxide density as a function of the Ge concentration at the oxidation interface.

To conclude, we discussed in this section the dependence of the oxide density on process parameters, i.e. oxidation process type and temperature, and on the Ge concentration at the oxidation interface. Into the next section, we show a correlation between the measured oxide density and oxidation kinetics by considering the dependence of the GRE on the oxide density.

III.A.5.3. Dependence of Oxidation Kinetics on the Oxide Density

The GRE of ISSG oxidation, dry furnace oxidation and dry RTO is plotted *Figure III.28* as a function of the measured oxide density. The GRE of dry RTO at 900°C decreases when the oxide density increases. It is consistent with oxidation kinetics limited by diffusion of O_2 through the oxide and with the O_2 diffusivity that decreases when the oxide density increases. We also observe that the GRE of dry furnace oxidation at 900°C is close to the trend line of the evolution of the GRE of dry RTO at 900°C with the oxide density. It further confirms the dependence of the oxidation rate on diffusion of O_2 through the oxide. A similar decrease of the GRE when the oxide density increases is also observed for dry RTO at 1100°C. However, there seems to be a shift of the GRE of dry RTO at 1100°C to lower values than dry RTO at 900°C. This will be discussed in *Section III.A.5.4.*.

As for ISSG oxidation, the GRE also decreases when the oxide density increases. However, the oxidation rate of SiGe by means of ISSG oxidation is close to the one of Si (the GRE is close to 1) while the oxide density gap is significant between the two measured samples. ISSG oxidation is mainly limited by diffusion of O* through the oxide (see *Section III.A.4.1.4.*). It thus shows that O* diffusivity is not or hardly dependent on the oxide density. However, we can still discuss the slight GRE dependence on the oxide density. The GRE could be due to a slightly higher O* diffusivity when the oxide density decreases. But O* is not the only oxidizing species for ISSG oxidation [Kee00], so that the GRE of ISSG oxidation could also be due to a higher diffusivity of another oxidizing species (such as O_2) when the oxide density decreases.

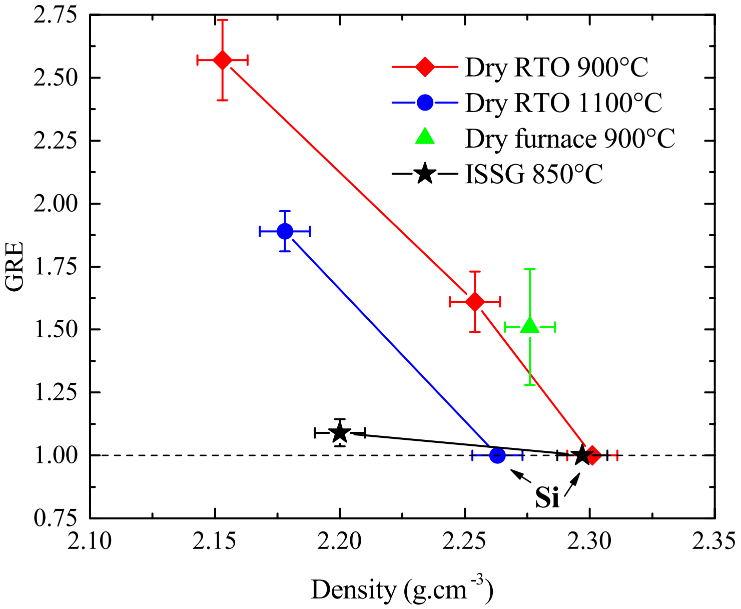

Figure III.28: Evolution of the GRE as a function of the measured oxide density.

In this section, it was shown that oxidation kinetics depends on the oxide density: the higher the oxide density is, the lower the GRE is. Into the next section, thanks to the dependence of the GRE on O_2 diffusivity and on the oxide density, we will open a window on a mechanism which is not specific to this study: the influence of the oxide density on O_2 diffusivity.

III.A.5.4. Discussion about O_2 Diffusion in SiO_2

According to thermodynamic considerations about the temperature and pressure dependence of the diffusion coefficient detailed in [Mehrer07], the diffusion coefficient of O_2 in SiO_2 is:

$$D = D_0 \exp\left(-\frac{\Delta H}{k_B T}\right) = D_0 \exp\left(-\frac{E + p\Delta V}{k_B T}\right), \qquad \textbf{\textit{Equation III.15}}$$

where D_0, ΔH, k_B, T, E, p and ΔV are a pre-exponential constant, the activation enthalpy of diffusion, the Boltzmann constant, the temperature in K, the activation energy of diffusion, the pressure and the activation volume. Some authors choose to express $p\Delta V$ as a function of another parameter because $p\Delta V$ is sometimes not known and less convenient to use than other related parameters in real diffusion problems. Doremus, Watanabe et al., Akiyama et al. and Cui et al. expressed the diffusivity as a function of strain, depth into the oxide, pressure and activation volume, and density respectively [Doremus84][Watanabe06][Akiyama08][Cui09]. Whatever the parameter they chose to use is, their models are very similar in their forms and can be generalized to:

$$D = \begin{cases} D_0 \exp\left(-\dfrac{E}{k_B T}\right) & \text{through oxide grown on Si} \\ D_0 \exp\left(-\dfrac{E + \Delta E}{k_B T}\right) & \text{through oxide grown on SiGe} \end{cases}, \qquad \textbf{\textit{Equation III.16}}$$

where E and ΔE are the activation energy in eV of O_2 diffusion in SiO_2 grown on Si and the diffusion barrier modulation in eV due to the density variation. The density variation due to the temperature only is included into the activation energy E and not in ΔE. In other words, the activation energy E is dependent on T because of the density variation with the temperature. We will use this more generalized model because we do not know stress levels in the oxide and will not make any assumption on the dependence of $p\Delta V$ on any other parameter such as density.

According to *Equation III.8*, the GRE is equal to the ratio of O_2 diffusivity in the oxide grown on SiGe to the one in the oxide grown in Si. Combining *Equation III.8* with *Equation III.16*, the GRE is:

$$GRE = \exp\left(-\frac{\Delta E}{k_B T}\right).$$ **Equation III.17**

As shown *Figure III.29*, the diffusion barrier modulation *ΔE* increases with the oxide density. There seems to be a linear increase of the diffusion barrier for the case of SiGe (see trend line on *Figure II.29*), in agreement with Cui et al. who assumed that the diffusion barrier modulation is proportional to the density [Cui09]. Due to the fact that the density variation due to the temperature is included into the activation energy *E* and not in *ΔE*, we cannot compare densities of oxides grown in Si with the ones of oxides grown on SiGe on *Figure III.29*.

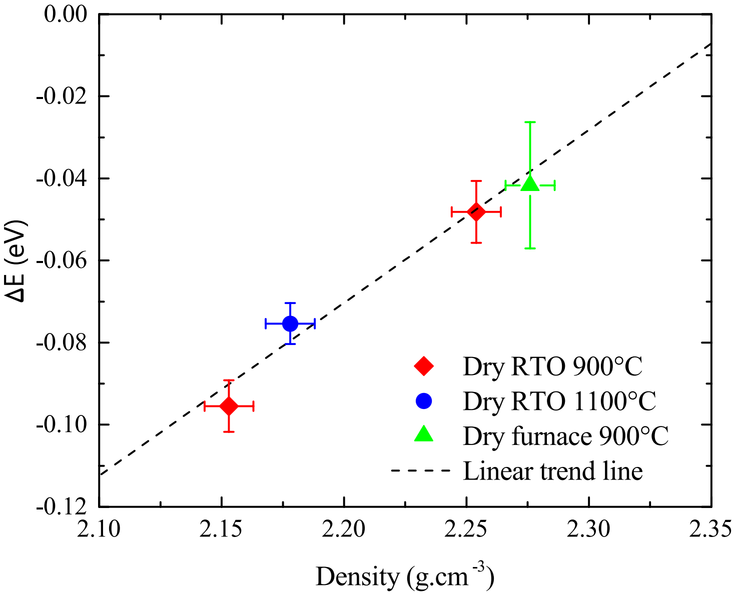

Figure III.29: Evolution of the modulation of the diffusion barrier of O_2 through thermal SiO_2 as a function of the oxide density.

III.A.5.5. Conclusion of Section III.A.5.

We previously showed in *Section III.A.4.* that oxidation kinetics of SiGe is limited by diffusion of the oxidizing species through the oxide. As the oxide density is known to influence diffusion, this section aimed for studying SiGe oxidation kinetics in light of the measurement of the oxide density.

After having presented the experimental method based on XRR measurements, we studied the dependence of the density of oxides grown on SiGe on the initial Ge concentration, on the process type and on the oxidation temperature. We showed that the oxide density decreases when the oxidation temperature increases and suggested that SiO_2 stress relaxation via viscous flow at high temperature (> 960°C) may account for this temperature influence. We also found that the density of the oxide grown on SiGe by means of dry furnace oxidation is higher than for dry RTO, thus showing a strong influence of the process type. And finally, we found that the higher the Ge concentration at the oxidation interface is, the lower the oxide density is. It was suggested that the higher lattice parameter of SiGe with respect to Si would tend to accommodate the lattice mismatch between Si and SiO_2, and as a consequence lower the density of the growing oxide.

Then, we showed that the lower the density of the oxide is, the higher the oxidation rate for dry oxidation is, in agreement with an oxidation regime that is governed by diffusion of O_2 through the growing oxide.

Finally, we proposed a model of O_2 diffusivity that depends on the oxide density through the modulation of the diffusion barrier. This model is consistent with experimental oxide densities measured on SiGe samples and with the model of O_2 diffusivity proposed by Cui et al. [Cui09].

III.A.6. Conclusion of Section III.A.

In *Section III.A.*, based on a literature review, we defined two problematics:

- What is the composition of the thermal oxide grown on SiGe and does it agree with thermodynamic predictions (*Section III.A.3.*)?
- What are the mechanisms and kinetics of thermal oxidation of SiGe (*Section III.A.4*. and *Section III.A.5.*)?

In *Section III.A.3.*, we showed that, except possibly during the very first stages of oxidation (the temperature ramp up), the composition of oxides grown on SiGe is pure SiO_2 for all investigated oxidation processes, in agreement with thermodynamic considerations of *Section III.A.1.2.*. We found that a very small quantity of Ge oxide (less than 5%) may be formed during the temperature ramp up when the oxidation rate largely exceeds the SiGe diffusion rate.

Then, we showed that oxidation of SiGe by means of dry furnace oxidation, dry RTO and ISSG oxidation is limited by diffusion of the oxidizing species through the growing oxide. A factor called Growth Rate Enhancement (GRE) was then defined to quantitatively compare the oxidation rates of Si and SiGe. We found that the GRE, and consequently oxidation kinetics, is correlated with the oxide density via the modulation of O_2 diffusivity. The influence of the process parameters on the oxide density, and as a result on oxidation kinetics, was finally clarified: the oxide density decreases when the oxidation temperature and the Ge concentration at the oxidation interface increase. Finally, we proposed a model of O_2 diffusivity that depends on the oxide density through the modulation of the diffusion barrier and which is consistent with our experimental data.

Some mechanisms that could account for the dependence of the oxide density on the oxidation temperature and on the Ge concentration at the oxidation interface have been suggested. The higher lattice parameter of SiGe with respect to Si would tend to accommodate the lattice mismatch between SiGe and SiO_2, and as a consequence decrease the density of the oxide. As for the effect of temperature, it was proposed that stress relaxation of SiO_2 via viscous flow could decrease the oxide density.

In the second part of this chapter (*Section III.B.*), two technological applications based on these results are presented.

III.B. Application to Industrial Processes for Advanced FD-SOI CMOS Manufacturing

The second part of this chapter presents two tools built based on the former oxidation kinetics results. The first one is a graphic assessment of the oxide thickness and of the Ge diffusion length in SiGe, a key parameter of the evolution of the SiGe composition during oxidation, as a function of process parameters. It is designed for a convenient and quick evaluation of the relative importance of the Ge pile-up mechanism with respect to SiGe interdiffusion. The second one is a numerical simulation tool of oxidation of SiGe which can be used both for a finer understanding of the dynamics of SiGe oxidation and for accurate prediction of output parameters of the condensation process (such as the oxide thickness and the SiGe composition profile in the SGOI film).

III.B.1. Condensation Abacus: Oxide Thickness and Ge Diffusion Length

There are two key variables of the condensation process that can be used for optimizing it:

- The oxide thickness after condensation: indeed, when fixing the epitaxial SiGe layer thickness and Ge concentration, the final SGOI layer thickness and Ge concentration directly depend on the oxide thickness at the end of the condensation process (this will be be shown in *Section IV.A.1.*). The oxide thickness may therefore be considered as a target specification of the condensation process.
- The self-diffusion length of Ge in SiGe: depending on the needs in terms of SGOI composition after the condensation (for instance, full homogenization or on the contrary hardly any diffusion of Ge into the SOI layer may be required), SiGe interdiffusion must be more or less pronounced. How far Si and Ge atoms diffuse into SiGe describes how homogeneous the SGOI layer will be after condensation. We will use a deliberately simple model for SiGe interdiffusion: the Ge self-diffusion length in SiGe is a fairly good variable of how far atoms diffuse and may therefore be considered as a variable of the condensation process.

Precise prediction of SGOI layer thickness and composition profile requires the use of simulations such as the ones presented in *Section III.B.2.*. However, these simulations are not appropriate for an easily understandable display of key variables of the condensation process. We thus give *Figure III.30* and *Figure III.31* two graphic and convenient tools for assessing the key variables of the condensation process as a function of two process parameters: oxidation temperature and duration.

These tools are temperature-time charts showing isolines of oxide thicknesses and of Ge self-diffusion lengths for two SiGe compositions relevant to the condensation process (0% and 25%). Isolines of oxide thicknesses and Ge self-diffusion were chosen to be plotted on temperature-time charts with *x* and *y* axis ranges relevant to Rapid Thermal Processes (dry RTO and ISSG oxidation), i.e. from 850°C to 1150°C for the oxidation temperature and from 10 seconds to 1000 seconds for the oxidation duration. Isoline values were also chosen to be relevant to the condensation process, from 100 Å to 200 Å for the oxide thicknesses and from 10 Å to 200 Å for the Ge self-diffusion lengths.

Oxidation kinetics and SiGe interdiffusion are inter-dependent. Therefore, the fact that the BOx layer plays the role of a diffusion barrier in the condensation process influences SiGe composition evolution and consequently oxidation kinetics of the condensation process. Oxidation kinetics and SiGe composition evolution are thus different depending on the substrate, either bulk Si or SOI, on which SiGe is epitaxially grown. We compared the oxide thickness after oxidation of SiGe on bulk Si (samples of *Section III.A.*) and after condensation (samples of *Section IV.A.*). We found that differences between the two substrate types are negligible for SGOI final Ge concentrations below 50%. And as already stated before, these charts aim at giving a visual assessment of the key variables of the condensation process and not at precisely predicting SGOI composition profiles. Oxide thicknesses are calculated using equations of *Section III.A.4.1.1.* and Ge self-diffusion lengths are calculated using data published by Kube et al. [Kube10] according to the equation:

$$L = \sqrt{Dt}. \qquad \textbf{\textit{Equation III.18}}$$

where *L* is the diffusion length, *D* the diffusion coefficient and *t* the oxidation duration. Napolitani et al. have shown that oxidation of Si and SiGe induces injection of Si interstitials into the Si/SiGe film below the oxidation interface [Napolitani05]. They also observed that the interstitials injection mechanism depends on the Ge content. SiGe interdiffusion being mediated by interstitials and vacancies, the oxidizing environment most likely alters SiGe interdiffusion. We do not have quantitative data on the injection of interstitials for our processes, so that we can only use published data while assuming that tendencies are similar in an oxidizing environment.

The temperature dependence of dry RTO is higher than the one of ISSG oxidation because the activation energy of dry RTO is higher than the one of ISSG oxidation (about 2 eV for dry RTO against 1 eV for ISSG oxidation). At 1100°C, dry RTO and ISSG oxidation have similar oxidation rates. While at lower temperatures, ISSG oxidation yields a much higher oxidation rate, which induces much shorter oxidation durations for ISSG oxidation for the same target oxide thickness. This temperature dependence of ISSG oxidation versus dry RTO can be seen in the slopes of isolines: the steeper the slope is, the lower the temperature dependence is. Dry RTO at temperatures lower than 900°C is not suitable for oxides thicker than 100 Å because oxidation times would have to be higher than 10 minutes, which is out of specification for a Rapid Thermal Process.

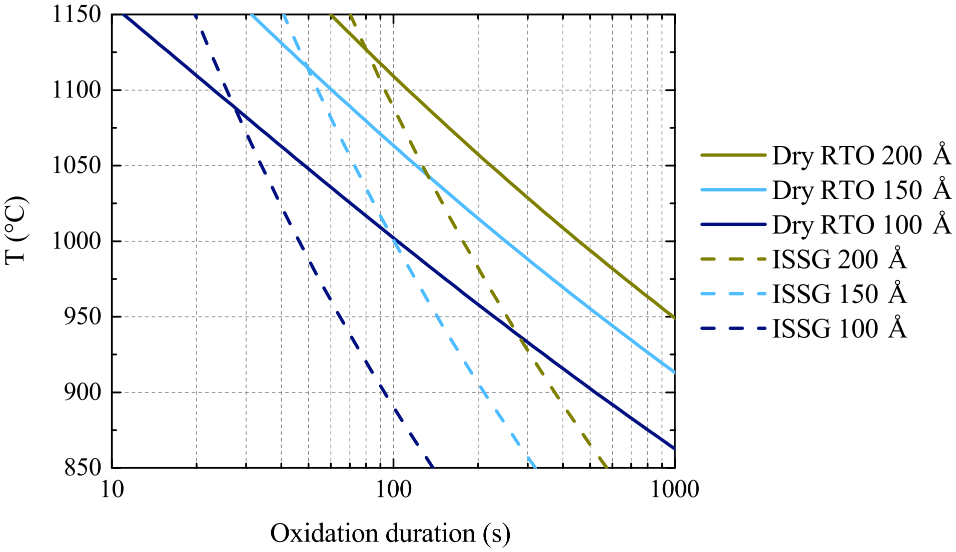

Figure III.30: Oxidation temperature-time charts for oxidation of $Si_{0.7}Ge_{0.3}$*. Isolines of oxide thicknesses for both dry RTO and ISSG oxidation are displayed on chart.*

The activation energy of SiGe interdiffusion is about 4 eV, thus much higher than the one of dry RTO (around 2 eV) and ISSG oxidation (1 eV). Similarly to oxidation, such a temperature dependence can be seen in the slopes of isolines, which are gentler than the ones of dry RTO and ISSG oxidation plotted on *Figure III.30*. Isolines for diffusion in Si and $Si_{0.75}Ge_{0.25}$ are almost parallel on this chart because the activation energies of Ge self-diffusion in Si and in $Si_{0.75}Ge_{0.25}$ are close (4.83 eV for Si against 4.71 eV for $Si_{0.75}Ge_{0.25}$). We emphasize that isolines are highly dependent on the SiGe composition: the higher the Ge concentration is, the higher the Ge self-diffusion length is. For instance, isolines of 50 Å for diffusion in Si and of 200 Å for diffusion in $Si_{0.75}Ge_{0.25}$ are very close.

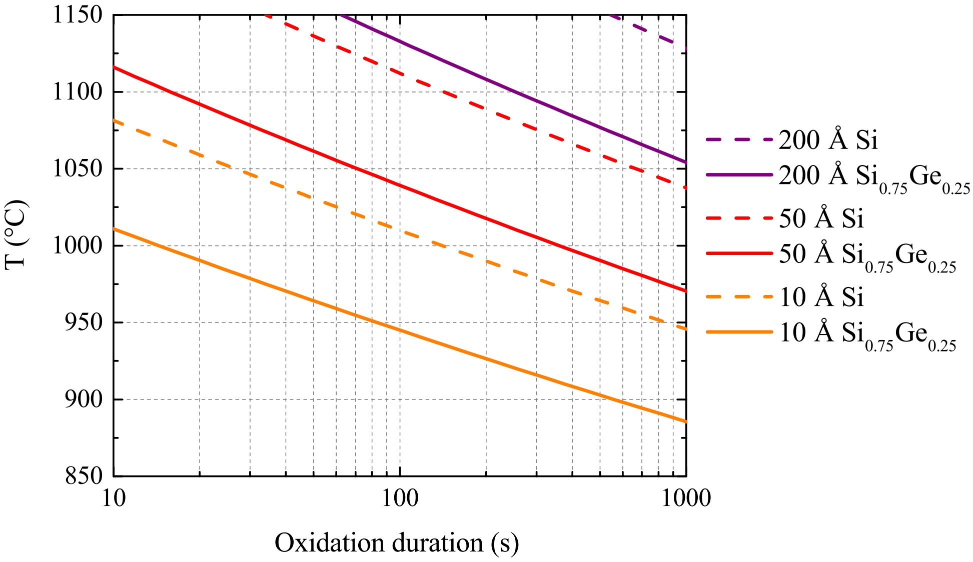

Figure III.31: Oxidation temperature-time charts for Ge self-diffusion in SiGe. Isolines of Ge self-diffusion lengths are displayed on chart.

Let us illustrate how these charts can be used with an example relevant to this work. Let us assume that, for some technology-related reasons, we need to grow a 100 Å-thick oxide film on a $Si_{0.7}Ge_{0.3}$-SOI stack while keeping a very steep interface between the $Si_{0.7}Ge_{0.3}$ and the SOI films. The later constraint can be translated into a constraint on the Ge diffusion length in Si, for instance that it cannot exceed 10 Å. This example is illustrated *Figure III.32*.

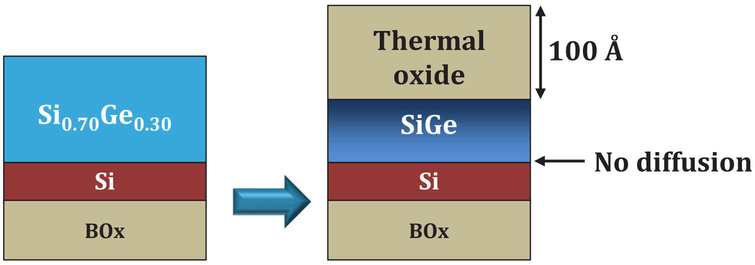

Figure III.32: Schematic illustration of the target specifications of the example of how the charts of Figure II.30 and Figure III.31 can be used (see text)

We can draw the isoline of 10 Å Ge self-diffusion length in Si on *Figure III.31*. The isoline defines the process window that respects this criterion and is plotted *Figure III.33*. Within this process window, we could for instance perform ISSG oxidation at 1035°C for 37 seconds, or at 900°C for 93 seconds, or dry RTO at 1015°C for 82 seconds. This methodology can be extended to other criteria such as the diffusion length of a dopant, or the maximum temperature that does not induce phase change of another material.

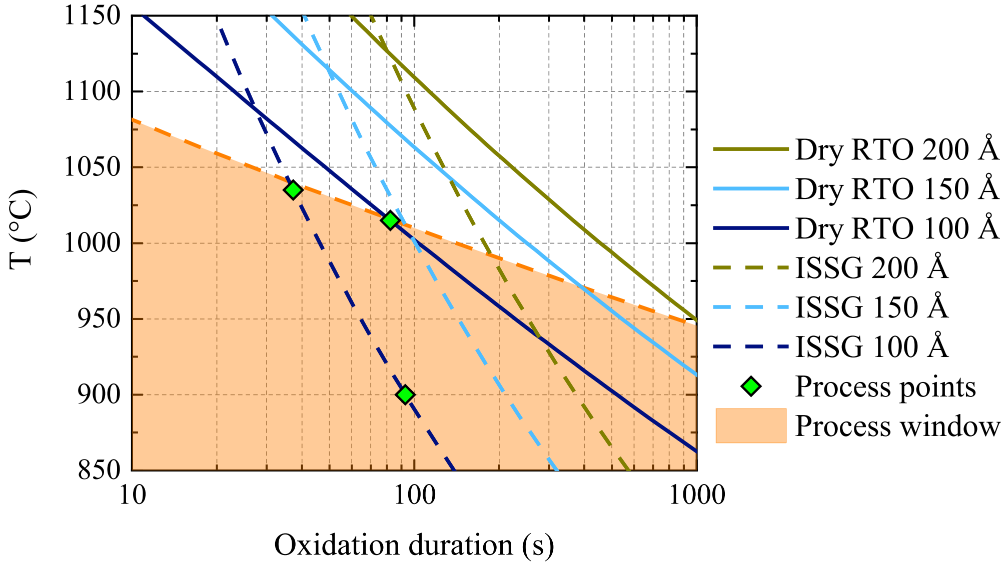

Figure III.33: Oxidation temperature-time charts for oxidation of $Si_{0.7}Ge_{0.3}$. The isoline of 10 Å Ge self-diffusion length in Si is also drawn in orange dashed line and defines the process window as the area below the line (see text).

III.B.2. Simulation of SiGe Thermal Oxidation

III.B.2.1. Introduction

As already stated in *Section I.5.1.2.*, numerical simulation of thermal oxidation of SiGe has two interests at stake: it can be used for a finer understanding of mechanisms and kinetics of SiGe oxidation; and it could also be used to accurately predict two key outputs of the condensation process: the oxide thickness and the SiGe composition profile. In this section, we present the very first results of simulation of thermal oxidation of SiGe using a FEM simulation tool developed in COMSOL Multiphysics environment. After introducing the main features and assumptions of the model, we compare simulated kinetics and SiGe composition profiles evolution during dry RTO and ISSG oxidation of SiGe with experimental data. As a conclusion, we highlight some key findings about oxidation of SiGe evidenced by simulation as well as current limitations and perspectives about simulation of thermal oxidation of SiGe.

III.B.2.2. Simulation Model

The model was derived from the model built by Pierre Morin [Morin15]. There are three main mechanisms that govern thermal oxidation of SiGe and that must be modeled:

- **Oxide growth rate**: According to the definition of the GRE given *Section III.A.4.2.1.*, the oxide growth rate on SiGe is:

$$\frac{dx}{dt}\Big|_{SiGe}(x)=\frac{dx}{dt}\Big|_{Si}(x)\,GRE, \qquad \textbf{\textit{Equation III.19}}$$

where x is the oxide thickness. The oxide growth rate on Si is:

$$\frac{dx}{dt}\Big|_{Si}(x)=\frac{\alpha_{Si}}{2x}=\frac{A\exp\left(\frac{-E_{ox}}{k_B T}\right)}{2x}, \qquad \textbf{\textit{Equation III.20}}$$

where α_{SiGe} is the parabolic constant of dry RTO of Si and where A and E_{ox} are the pre-exponential constant and the oxidation activation energy. Both parameters are calculated according to *Section III.A.4.1.4.* (E_{ox} is equal to 2.29 eV for dry RTO and 0.95 eV pour ISSG oxidation, and A is equal to 1.32×10^{10} Å^2.t^{-1} for dry RTO and 3.01×10^5 Å^2.t^{-1} for ISSG oxidation).

For ISSG oxidation, there is no strong correlation between the oxidation rate and the Ge concentration. We thus consider that the GRE is equal to 1.

For dry RTO, we found that the GRE is dependent on the Ge concentration at the oxidation interface (see *Section III.A.4.4.*). *Figure III.34* shows the experimental data along with the best fit we found, which is an exponential function of the Ge concentration at the oxidation interface Ge$\%_{\mathrm{ox}}$ (in percent):

$$GRE = \exp\left(0.0188 Ge\%_{ox}\right). \qquad \textbf{Equation III.21}$$

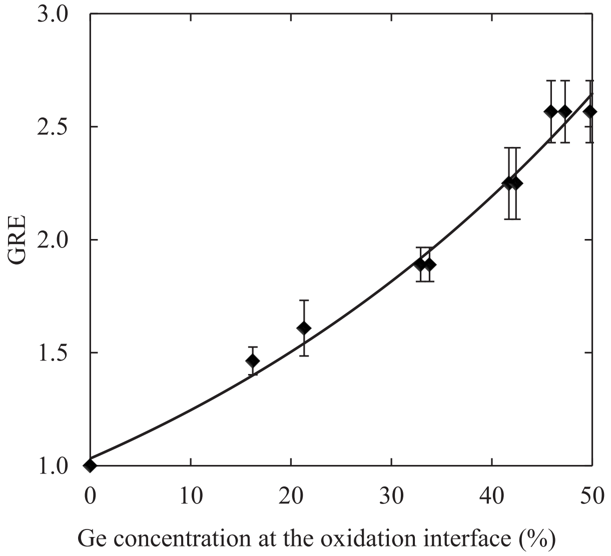

Figure III.34: GRE as a function of the Ge concentration at the oxidation interface. Dots are experimental data and the line is the fitted exponential function.

- **Ge injection below the SiGe-oxide interface**: As shown in *Section IV.A.3.*, there is no significant Ge loss during oxidation and all Ge atoms are repelled below the oxide. The flux of Ge atoms injected at the oxidation interface towards the SiGe film is calculated at each step based on the consumption of Si atoms by the oxidation reaction.

- **SiGe interdiffusion**: the model of SiGe interdiffusion is based on Darken's equations with a unique self-diffusion coefficient calibrated by Morin et al. [Morin15]:

$$D_S(x) = D_0 \exp\left(S(x)\right) \exp\left(-\frac{E_a(x)}{kT}\right) \exp\left(-\frac{PV_a}{kT}\right) \exp\left(-\frac{E_C}{kT}\right), \qquad \textbf{Equation III.22}$$

where x is the Ge fraction, k and T are respectively the Boltzmann constant and the temperature, S the SiGe mixture entropy, E_a the enthalpy (related to the formation and migration of vacancies in SiGe), P the pressure related to the stress components, V_a the activation volume. The effect of strain on diffusion is accounted by the product PV_a where $P = (\sigma_x + \sigma_y + \sigma_z)/3$. Hence the model also calculates the stress components in the SiGe layer according to the formalism presented in *Appendice A*. The term E_c was added to account for the injection of interstitials at the oxidation interface (see *Section III.A.1.3.3.*). The values of the parameters of the diffusion coefficient have been fitted on published self-diffusion data [Kube10] and experimental data acquired previously to this work at IBM Albany Alliance site.

III.B.2.3. Kinetics of Dry RTO and ISSG Oxidation of SiGe

Equation III.20 shows that the oxide thickness must not be null. We thus enter an initial oxide thickness into the simulation model. Experimental and simulated oxides thicknesses of dry RTO of Si at 1000°C as a function of oxidation time are shown *Figure III.35*. It appears logical in the first instance to enter the native oxide thickness as the initial oxide thickness (about 1 nm). However, as illustrated *Figure III.35*, it may not be the initial conditions that correspond to the best fit of experimental data. In the case of dry RTO of Si at 1000°C, the best initial conditions seem to be an initial 2 nm-thick oxide.

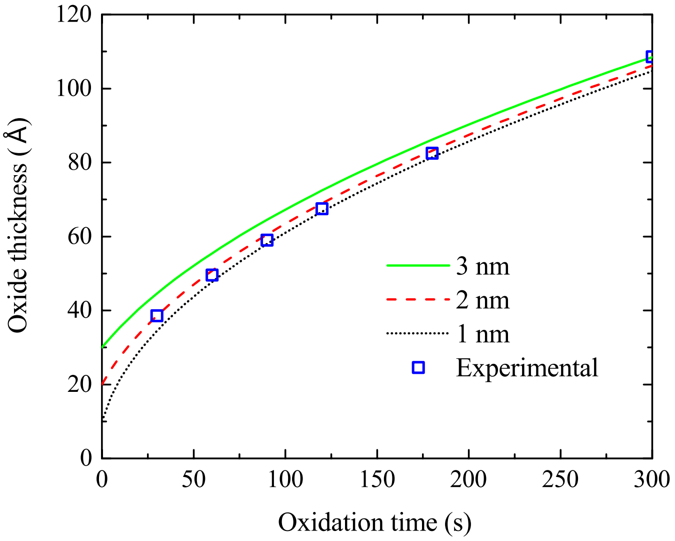

Figure III.35: Oxide thickness as a function of the oxidation time for dry RTO of Si at 1000°C. Lines are simulations with starting oxide thicknesses indicated in the legend and squares are experimental data.

This apparent contradiction is due to the fact that there is a transient regime at the very beginning of oxidation. Indeed, the oxide thicknesses extrapolated from the fitted parabolic laws of *Section III.4.1.1.* are not equal to zero or one nanometer when the oxidation time is zero. This transient regime may be due to oxidation during the temperature ramp up and/or altered oxidation kinetics for very thin oxides. As we do not know what this regime is, we should enter the initial conditions of the simulation that correspond to the beginning of the actual parabolic regime. A further problem that arises with SiGe is that the Ge concentration at the oxidation interface changes very rapidly during the first stages of oxidation (see *Section III.A.4.3.*). The SiGe composition profile at the beginning of the parabolic regime is not known either. We chose to start simulations with an initial oxide layer on top of a single SiGe layer in the first instance.

We determined for each oxidation conditions the initial oxide thickness that corresponds to the best fit of experimental data. *Figure III.36* compares the oxide thicknesses simulated with the best initial oxide thickness with experimental data for all dry RTO and ISSG oxidation conditions. Simulation of dry furnace oxidation of SiGe cannot be performed as we do not know the dependence of the GRE on the Ge concentration at the oxidation interface. Simulation of ISSG oxidation kinetics does not depend on the Ge concentration (the GRE is fixed to one as explained *Section III.B.2.2.*), hence data of ISSG oxidation of Si only are shown.

We observe a rather good agreement between simulated and experimental data except for the case of dry RTO of $Si_{0.9}Ge_{0.1}$ at 900°C. It seems that starting simulations with an initial oxide layer on top of a single SiGe layer does not drastically alter the simulated oxide growth kinetics. In summary, the simulation model based on the GRE equation is rather consistent with experimental data in terms of oxide growth kinetics. We examine into the next section the evolution of the Ge concentration profile and compare it with SIMS measurements already shown in *Section III.A.4.3.*.

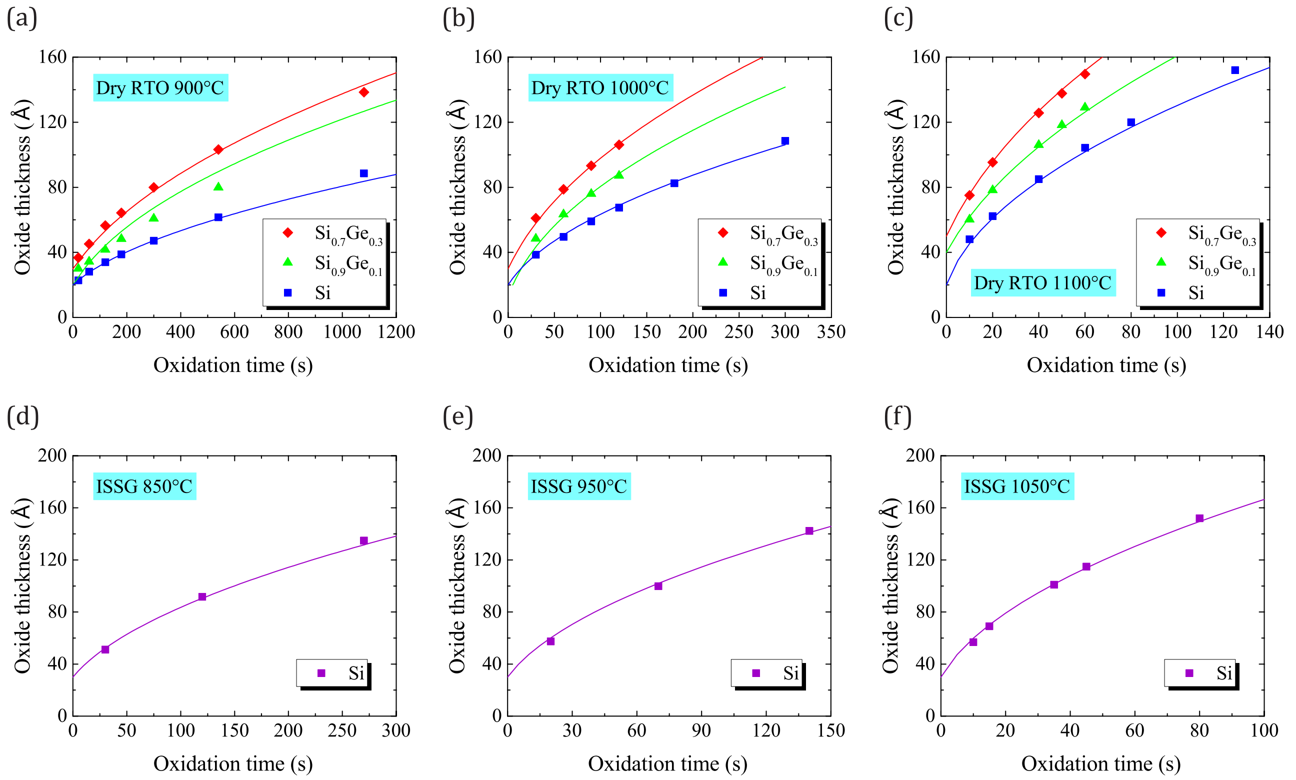

Figure III.36: Experimental and simulated oxide thicknesses as a function of the oxidation time of dry RTO of Si, $Si_{0.9}Ge_{0.1}$ *and* $Si_{0.7}Ge_{0.3}$ *at (a) 900°C, (b) 1000°C and (c) 1100°C. And experimental and simulated oxide thicknesses as a function of the oxidation time of ISSG oxidation of Si at (a) 850°C, (b) 950°C and (c) 1050°C. Dots are experimental data and lines are simulations.*

III.B.2.4. Evolution of the SiGe Composition Profile

Experimental SIMS and simulation profiles of the Ge concentration after various dry RTO and ISSG oxidation processes are shown *Figure III.37*. Due to simulation constraints, the same initial SiGe epitaxial thickness was used while it was not the case of experiments. However, these differences are not expected to influence the tendencies observed on *Figure III.37*.

In agreement with the discussion of *Section III.A.4.3.*, we notice that the higher the oxidation temperature is, the lower the simulated Ge concentration at the oxidation interface is. Simulations show the same dependence on temperature of the competition between oxidation that tends to pile-up Ge atoms below the oxidation interface and SiGe interdiffusion that tends to smooth Ge concentration gradients.

Yet, in terms of absolute values, we observe that the Ge concentration gradients are smoother in experiments than in simulations in all cases. The systematically higher Ge concentration at the interface in simulations shows that the pile-up mechanism is more pronounced in simulations. In addition, the Ge concentration gradients between the pile-up layer and the epitaxial SiGe film and between the SiGe film and the Si substrate are also smoother in experiments. Even if SIMS measurements tend to smooth concentration gradients due to the snow-plow effect, we do not expect it to cause such differences.

We have shown in the former section that the experimental and simulated oxidation rates are very similar so that these differences can only arise from SiGe interdiffusion rates slower in simulations than in experiments. The SiGe diffusion coefficient used in simulations was the one calibrated by Morin et al. [Morin15] (see *Section III.B.2.2.*) with published self-diffusion data [Kube10] and dedicated experiments. These dedicated experiments are different from the experiments performed during this thesis in two ways.

Firstly, oxidation processes performed in this study are different in various ways from the ones performed by Morin et al. (the details cannot be disclosed). As oxidation of Si(Ge) is known to inject a certain amount of Si and/or Ge interstitials into the Si(Ge) film (see *Section III.A.1.3.3.*), the concentrations of interstitials and vacancies are most likely influenced by oxidation conditions. SiGe interdiffusion being mediated by diffusion of interstitials and vacancies (see *Section I.2.5.2.*), the SiGe diffusion coefficient is consequently influenced by oxidation conditions.

Secondly, they calibrated their model with condensation experiments, therefore with a SOI substrate, while these experiments are performed with bulk Si substrates. Si(Ge)-oxide interfaces, as any interface in diffusion experiments, likely play a role in recombination and generation of interstitials and vacancies, and as a result on SiGe interdiffusion.

Whatever the reasons for these differences are, there is a discrepancy between the simulated oxidation rates, which are very close to the experimental ones, with the simulated Ge concentration at the oxidation interface, from which the oxidation rate is calculated in simulations. Due to time constraints, we could not further investigate about this discrepancy. As tendencies are still consistent with experiments, we will discuss into the next section the evolution of the Ge concentration at the oxidation interface during oxidation, and its dependence on process parameters.

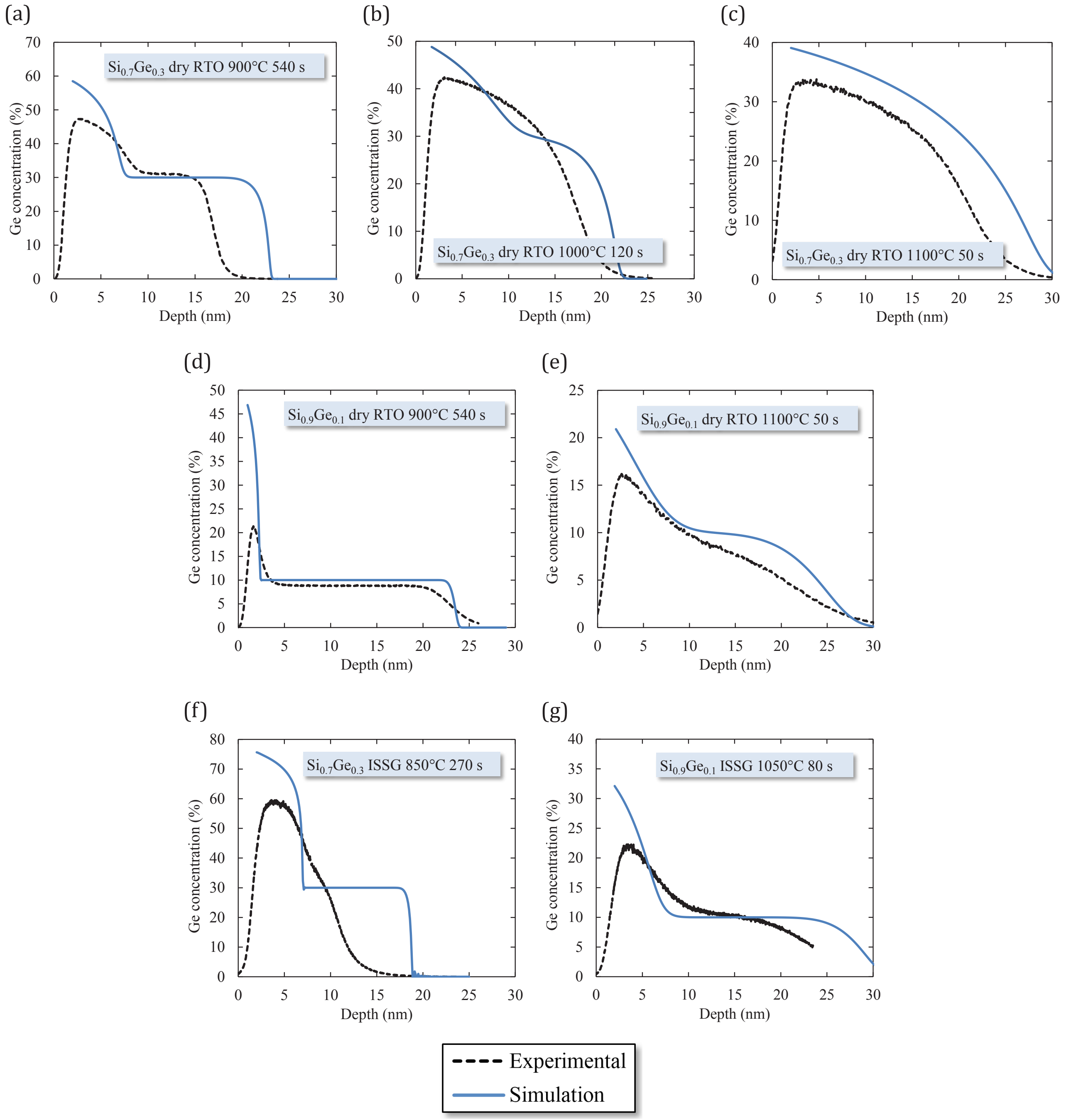

Figure III.37: Experimental SIMS and simulated Ge concentration profiles.

III.B.2.5. Evolution of the Ge Concentration at the Interface

Figure III.38 shows the simulated and experimental Ge concentration at the oxidation interface as a function of oxidation time for various dry RTO and ISSG oxidation conditions. In all cases, the simulated Ge concentration at the interface rapidly increases until it reaches a plateau. As previously observed, the higher the oxidation temperature is, the lower the Ge concentration at the oxidation interface is. The same discrepancy in terms of absolute values is noticed: the simulated Ge concentration at the interface is systematically higher than the experimental one.

The only case that is slightly different is dry RTO of $Si_{0.7}Ge_{0.3}$ at 1100°C: the Ge concentration at the interface starts to decrease after about 30 seconds. It is consistent with experiments, where the Ge concentration at the interface decreases from 38.6% after 10 seconds to 32.9% after 60 seconds.

Investigating why the Ge concentration at the oxidation interface is rapidly increasing until a plateau would require to compare in a quantitative manner the oxidation rate with the diffusion rate as a function of time. Such a problem cannot be solved analytically (hence the simulations) so that further discussion about this phenomenon is difficult at the present time.

In summary, we highlight that despite of the discrepancy between experimental and simulated results in terms of absolute values, simulations are consistent with what was experimentally shown in *Section III.A.4.3.*: the Ge concentration at the oxidation interface is rather constant after a transient regime.

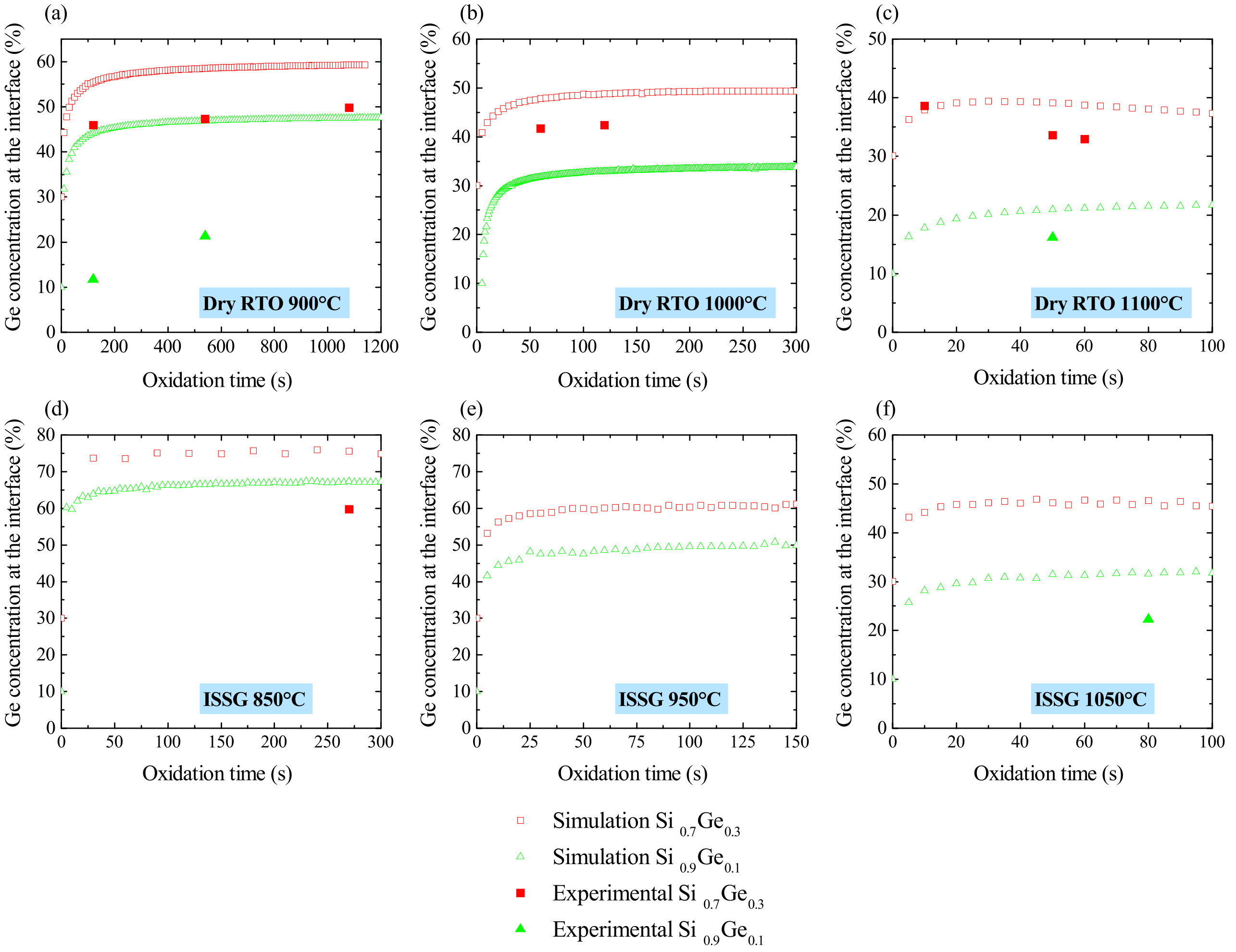

Figure III.38: Experimental and simulated Ge concentration at the interface as a function of time.

The Ge concentration at the interface is crucial not only for dry RTO kinetics, but also in terms of oxide density (see *Section III.A.5.*). The oxide density can also influence further processing of CMOS devices (such as chemical etching of the oxide), so that it may be useful to be able to predict the Ge concentration at the interface as a function of process parameters. Even if simulated values must not be considered as absolute values, tendencies are valid and valuable information.

Figure III.39 shows the simulated Ge concentration at the interface once the plateau is reached, and plotted as a function of the initial Ge concentration and oxidation temperature. We noticed that in all cases, the plateau is reached when the oxide is 13 nm-thick (figure not shown), so that we decided to extract the Ge concentration at the interface at this thickness.

As expected, the higher the initial Ge concentration and the lower the temperature are, the higher the Ge concentration at the interface is. The temperature dependence of ISSG oxidation is higher than of dry RTO. Indeed, as already discussed in *Section III.A.4.3.* and in *Section III.B.1.*, ISSG oxidation at low temperatures is much faster than dry RTO, which makes the gap between the oxidation rate and the diffusion rate higher, and results in a higher Ge concentration at the oxidation interface. The dependence on the initial Ge concentration seems similar for dry RTO and ISSG oxidation. Then, two trends can be emphasized for both processes:

- The dependence of the Ge concentration at the interface on the initial Ge concentration is higher at higher temperatures.
- The dependence of the Ge concentration at the interface on temperature is higher at lower initial Ge concentrations.

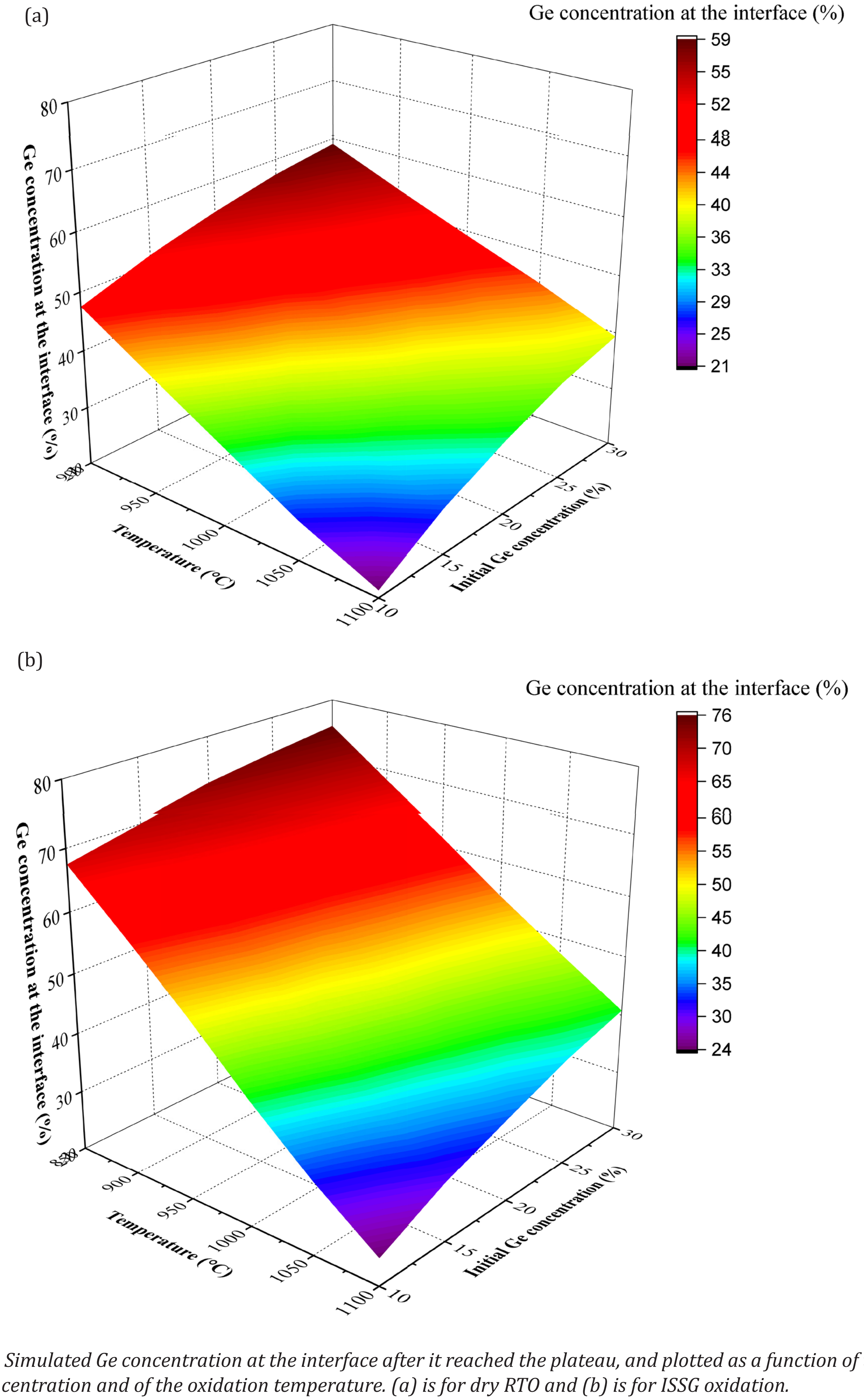

Figure III.39: Simulated Ge concentration at the interface after it reached the plateau, and plotted as a function of the initial Ge concentration and of the oxidation temperature. (a) is for dry RTO and (b) is for ISSG oxidation.

Table III.4 summarizes the dependence of the Ge concentration at the oxidation interface on the process type, the initial Ge concentration and temperature.

	Initial Ge concentration	Oxidation temperature
Dry RTO	**+**	**++**
ISSG oxidation	**+**	**+++**

Table III.4: Relative weight of the dependence of the Ge concentration at the interface on the process type (dry RTO and ISSG oxidation), the initial Ge concentration and the oxidation temperature. + refers to a low dependency while +++ to a high one.

III.B.2.6. Conclusion of Section III.B.2.

We implemented the experimentally observed GRE dependence on the Ge concentration at the interface into the simulation model built by Morin et al. [Morin15]. We showed that simulated kinetics of dry RTO and ISSG oxidation of SiGe is in good agreement with experiments, in spite of the difficulty to model the transient regime of the beginning of oxidation. We evidenced a discrepancy between experiments and simulations in terms of SiGe composition profile evolution, especially at the oxidation interface. We believe that this discrepancy is due to a non-adapted calibration of SiGe interdiffusion parameters. Nevertheless, it allowed us to highlight some tendencies, and especially the dependence of the Ge concentration at the oxidation interface on process parameters.

In a summary, the simulation tool already proved its usefulness in studying the dynamics of thermal oxidation of SiGe as it successfully reproduces tendencies in terms of oxidation kinetics and SiGe composition profile evolution. However, as expected given that the simulation model is an initial approach, it requires further improvement to be able to accurately predict a condensation process.

Conclusion of Chapter III

In *Section III.A.*, based on a literature review, we defined two problematics:

- What is the composition of the thermal oxide grown on SiGe and does it agree with thermodynamic predictions (*Section III.A.3.*)?
- What are the mechanisms and kinetics of thermal oxidation of SiGe (*Section III.A.4*. and *Section III.A.5.*)?

In *Section III.A.3.*, we showed that, except possibly during the very first stages of oxidation (the temperature ramp up), the composition of oxides grown on SiGe is pure SiO_2 for all investigated oxidation processes, in agreement with thermodynamic considerations of *Section III.A.1.2.*. We found that a very small quantity of Ge oxide (less than 5%) may be formed during the temperature ramp up when the oxidation rate largely exceeds the SiGe diffusion rate.

Then, we showed that oxidation of SiGe by means of dry furnace oxidation, dry RTO and ISSG oxidation is limited by diffusion of the oxidizing species through the growing oxide. A factor called Growth Rate Enhancement (GRE) was then defined to quantitatively compare the oxidation rates of Si and SiGe. We found that the GRE, and consequently oxidation kinetics, is correlated with the oxide density via the modulation of O_2 diffusivity. The influence of the process parameters on the oxide density, and as a result on oxidation kinetics, was finally clarified: the oxide density decreases when the oxidation temperature and the Ge concentration at the oxidation interface increase. Finally, we proposed a model of O_2 diffusivity that depends on the oxide density through the modulation of the diffusion barrier and which is consistent with our experimental data.

Some mechanisms that could account for the dependence of the oxide density on the oxidation temperature and on the Ge concentration at the oxidation interface have been suggested. The higher lattice parameter of SiGe with respect to Si would tend to accommodate the lattice mismatch between SiGe and SiO_2, and as a consequence decrease the density of the oxide. As for the effect of temperature, it was proposed that stress relaxation of SiO_2 via viscous flow could decrease the oxide density. As a perspective to this work, we suggest that studying oxidation kinetics of fully relaxed SiGe films and varying the conditions of the temperature ramp up of each oxidation process (which are largely different from dry RTO to dry furnace oxidation) could shed light on the mechanisms that induce this dependence.

In the second part of this chapter (*Section III.B.*), two technological applications based on the former results were presented. The first one is a graphic assessment of the oxide thickness and of the Ge diffusion length in SiGe, a key parameter of the evolution of the SiGe composition during oxidation, as a function of process parameters. The tool compares the relative importance of the Ge pile-up mechanism caused by the Si-selective oxidation with respect to SiGe interdiffusion. And secondly, a numerical simulation tool of thermal oxidation was adapted from the one of Morin et al. [Morin15]. The simulation model proved its worth in bringing more understanding of the dynamics of SiGe oxidation in spite of some remaining discrepancies with experimental data. We concluded with some suggestions that could improve the model, i.e. dedicated experiments to calibrate the diffusion model on the specific processes performed in this work.

« D'une certaine façon, être vivant ne s'atteint que par ce triple combat: contre les forces de gravité en nous – la paresse, la fatigue, la quête du repos ; contre l'instinct de répétition – le déjà-fait, le connu, le sécurisant ; et enfin contre les séductions du continu – tous les développements durables, le réformisme ou ce goût très fréole de la variation plaisante, du pianotement des écarts autour d'une mélodie amusante. »

Alain Damasio, La Horde du Contrevent

Chapter IV - Strain and Crystal Quality of SGOI Films Fabricated by the Condensation Technique

Introduction to Chapter IV 138

IV.A. Strain and Crystal Quality of Full Sheet SGOI Films Fabricated by the Condensation Technique 139

IV.A.1. Principles of the Condensation Technique 139

IV.A.2. Experimental 140

IV.A.3. Ge Conservation during Condensation 143

IV.A.4. Strain and Crystal Defects of SGOI Layers 144

IV.A.5. Characterization of SGOI Composition and Crystal Quality by MEIS 156

IV.A.6. Conclusion of Section IV.A. 167

IV.B. Strain Relaxation at the Edge of Active Areas 168

IV.B.1. Problem Definition 168

IV.B.2. Chemical Bonding at the SGOI-BOx interface Investigated by XPS 169

IV.B.3. Measurement of Hydrogen Concentration by Neutron Reflectivity Coupled with XRR 173

Conclusion of Chapter IV 179

Introduction to Chapter IV

After *Chapter III* has brought about understanding of the mechanisms and kinetics of thermal oxidation of SiGe, this chapter strives to study strain and crystal quality of SGOI films fabricated by condensation. Indeed, we highlighted in *Section I.5.2.* that high strain levels and high crystal quality are needed for increasing the hole mobility of SGOI channels.

Strain of full-sheet SGOI films is evaluated as a function of process parameters. The conditions for strain relaxation and its correlation with the formation of extended crystal defects are discussed for both dry Rapid Thermal Oxidation (RTO) and In-Situ Steam Generation (ISSG) oxidation processes. The process conditions and mechanisms that lead to strain relaxation and formation of dislocations are discussed. Then, the amount of atoms displaced from lattice sites in SGOI films is measured as a function of depth by the Medium Energy Ion Scattering (MEIS) technique. This amount of atoms displaced from lattice sites is a crystal quality indicator. The effects of the condensation process and of the Ge concentration on SGOI crystal quality are discussed.

Finally, the second part of this chapter starts by describing a particular SGOI strain relaxation phenomenon occurring during CMOS fabrication after the condensation process. The mechanical properties of the BOx-SGOI and SGOI-thermal oxide interfaces are thought to play a key role in this phenomenon. Two possible causes of these weaker mechanical properties are suggested and studied in *Section IV.B.2.* and *Section IV.B.3.* respectively. *Section IV.B.2.* studies the chemical bonding at the BOx-SGOI interface by X-Ray Spectroscopy (XPS) and *Section IV.B.3.* examines by neutron reflectivity the presence or not of hydrogen in BOx-SGOI-thermal oxide stacks.

IV.A. Strain and Crystal Quality of Full Sheet SGOI Films Fabricated by the Condensation Technique

IV.A.1. Principles of the Condensation Technique

The condensation technique is based on concurrent Si-selective thermal oxidation of a SiGe layer epitaxially grown on a SOI substrate and homogenization of the SGOI layer by interdiffusion. As shown by other groups [Nakaharai09][Boureau16] and in *Section IV.A.3.*, there is no significant Ge loss during condensation, except possibly at the very beginning of the process (see *Section III.A.3.*). It was also shown that there is no Ge diffusion into the BOx layer within measurement error. The Ge quantity provided by the SiGe epitaxy process can thus be considered to be fully conserved in a well-defined SGOI layer sandwiched by the thermal oxide and the BOx layer. Moreover, thermal annealing processes that follow the condensation process for fabrication of functional devices are important enough to fully homogenize the SGOI layer if some composition gradient remains after the condensation process.

From the point of view of technologists, there are a few key variables related to both the SiGe epitaxy process and the condensation process that need to be well controlled. Especially, at the end of the condensation process, the Ge concentration and the thickness of the SGOI film are crucial because the final transistor performances directly depend on them. In this work, various Ge concentrations and SGOI thicknesses were targeted, so that a clear understanding of how these variables are interdependent was required for calibrating the condensation processes. For this purpose we consider the following model:

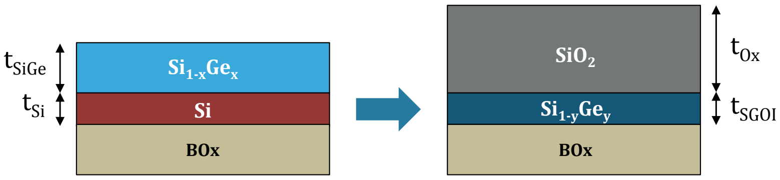

Figure IV.1: Condensation model.

Where t_{Si}, t_{SiGe}, x, t_{Ox}, t_{SGOI} and y are the SOI thickness, the epitaxial SiGe thickness, the Ge content in the epitaxial SiGe film, the final oxide thickness, the final SGOI thickness and the Ge content in the SGOI film.

When assuming negligible atomic density changes with Ge content (the lattice volume of Si and Ge are very close), the conservation of Ge can be written as:

$$t_{SiGe}x = t_{SGOI}y. \qquad \textbf{Equation IV.1}$$

And within the same assumptions and because 1 volume of Si is converted into 2.25 volumes of SiO_2, the conservation of Si can be written as:

$$t_{Si} + t_{SiGe}(1-x) = t_{SGOI}(1-y) + t_{Ox}/2.25. \qquad \textbf{Equation IV.2}$$

As the oxide thickness t_{Ox} may be a reference parameter when calibrating an oxidation or a condensation process, it is useful to predict the final SGOI thickness t_{SGOI} and Ge content y for a given structure as a function of the thermal oxide thickness t_{Ox}. Combining *Equation IV.1* and *Equation IV.2*, we provide the following equations for the SGOI thickness and Ge content in the SGOI layer as a function of the initial structure parameters and of the oxide thickness:

$$\begin{aligned} t_{SGOI} &= t_{Si} + t_{SiGe} - t_{Ox}/2.25 \\ y &= \left(t_{SiGe}x\right)/\left(t_{Si} + t_{SiGe} - t_{Ox}/2.25\right). \end{aligned} \qquad \textbf{Equations IV.3}$$

Let us now consider for example that a 60 Å-thick SGOI layer ($t_{SGOI} = 60$ Å) with 40% Ge concentration ($y = 0.4$) is targeted. We could consider the Ge total amount instead of the Ge concentration for this example. But for clarity considerations, we assume that the SGOI layer is fully homogeneous at the end of the condensation process, and that we can therefore use the Ge concentration, a more striking and used parameter. Let us also assume that the Ge concentration of the epitaxial SiGe layer x is fixed to either 25% or 35% ($x = 0.25$ or 0.35) and that the SOI thickness t_{Si} is 70 Å. According to *Equation IV.1*, the thickness of the epitaxial SiGe layer t_{SiGe} is 96 Å and 69 Å for 25% and 35% respectively. We will refer to C1 and to C2 for the cases of 25% and 35% initial Ge concentrations respectively.

Figure IV.2 shows graphic representations of the model of condensation for C1 and C2 cases.

Based on *Equation IV.1*, the Ge concentration of the SGOI layer as a function of its thickness is plotted *Figure IV.2 (a)*. The more the SiGe layer is oxidized, or "condensed", the lower the SGOI layer thickness is because of Si atoms incorporation in the oxide. At the same time, the Ge concentration of the SGOI layer increases during condensation. *Figure IV.2 (a)* also shows the target point of the condensation process. We highlight that both C1 and C2 have the same evolution of the Ge concentration as a function of the SGOI thickness. Indeed, they have the same total Ge quantity in the starting epitaxial SiGe layer, with C1 having a SiGe layer that has a higher thickness but a lower Ge concentration.

Now, in order to reach the target SGOI specifications, we need to calculate the target oxide thickness for C1 and C2 cases according to *Equation IV.2*. *Figure IV.2(b)* shows the evolution of the oxide thickness as a function of the Ge concentration of the SGOI layer, along with the target oxide thicknesses, which are 239 Å and 177 Å for C1 and C2 respectively. As long as oxidation proceeds, the thickness of the oxide and the Ge concentration of the SGOI film increase. We notice that the targeted oxide thickness of C1 is higher than C2. Indeed, the total Si quantity of C1 is higher than the one of C2 while the Ge quantity of C1 and C2 are identical. So, in order to reach the same SGOI target specifications, more Si atoms must be consumed by the oxidation process for C1 than for C2. In other words, the grown oxide must be thicker for C1 than for C2.

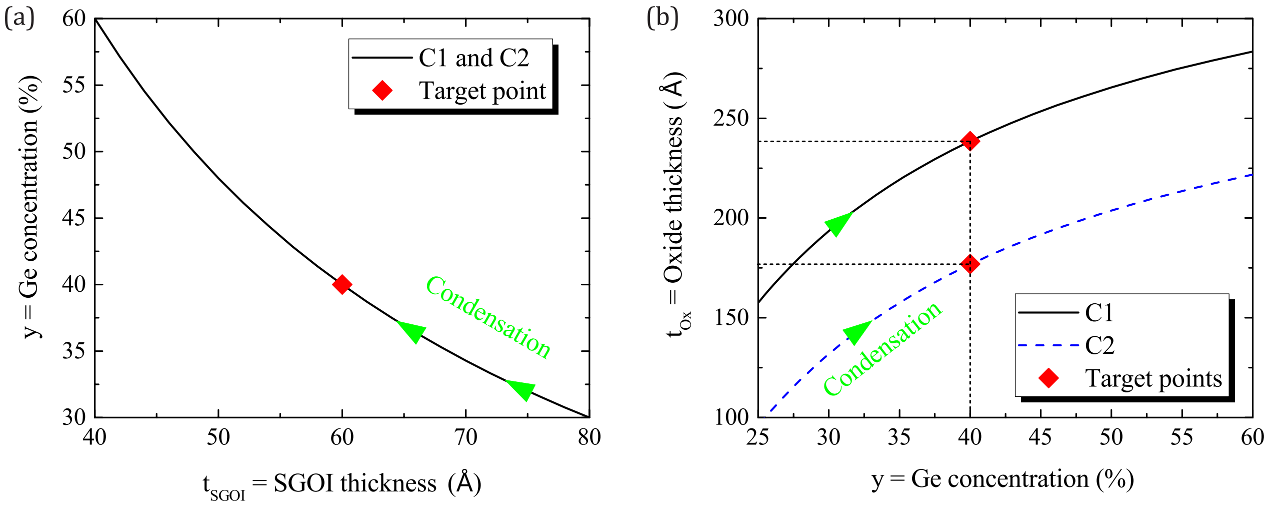

Figure IV.2: (a) The full line is the Ge concentration of the SGOI layer as a function of its thickness for the both C1 and C2 and the symbol is the SGOI thickness and Ge concentration target point. (b) The full line is the oxide thickness as a function of the Ge concentration of the SGOI layer for C1 and C2 and the symbols are target oxide thicknesses.

All condensation processes presented *Section IV.A.2.* and performed in this work were calibrated based on this model of condensation. Having presented the condensation technique into more details, the next section describes the experiments conducted to address the problematic defined in *Section I.5.2.1.*.

IV.A.2. Experimental

IV.A.2.1. SiGe Epitaxy and Condensation Process

SOI substrates with a 100 Å-thick SOI layer and a 200 Å-thick BOx layer were used. Dry furnace oxidation was performed in order to decrease the SOI layer thickness to about 75 Å. After removal of the grown thermal SiO_2 layer, three types of SiGe layers were epitaxially grown full sheet, in other words on the whole surface of the wafer. The compositions and thicknesses of the grown layers were measured by ellipsometry.

Condensation was performed by either dry RTO or ISSG oxidation. At each moment of the condensation process, the temperature must be kept below the melting temperature of the SGOI layer in order to prevent melting of

SiGe. As shown *Section IV.A.1.*, if we assume that the SGOI composition is homogeneous at every moment of the condensation process, the SGOI composition as a function of the oxide thickness is known. Then, as SiGe oxidation kinetics can be predicted (see *Chapter III*), the evolution of the SGOI composition during condensation can be predicted too.

For Ge concentrations below 50%, the melting temperature is higher than the maximum oxidation temperature used in this study (1100°C). However, above 50% Ge concentration, the condensation temperature must be decreased. Most of the oxidation recipes were designed so that the temperature decreases stepwise from 1100°C to 1000°C and finally to 900°C, as illustrated *Figure IV.3*. Temperature ramp down between temperature steps were 25°C.s^{-1}. A margin of about 50°C was kept at every moment between the condensation temperature and the SGOI predicted melting temperature because of three sources of bias on the prediction of the SGOI melting temperature:

- During condensation, the Ge concentration is never fully homogeneous because of the pile-up mechanism, even when using high temperatures such as 1100°C. The maximum Ge concentration of the SGOI layer is the one at the oxidation interface and is higher than the one calculated when assuming a homogenous composition of the SGOI layer. The predicted melting temperature of the SGOI layer when assuming homogeneous SGOI layers is thus lower than the actual melting temperature of the top part of the layer.

- The type of substrate, bulk or SOI, influences SiGe interdiffusion (the BOx layer actually acts as a diffusion barrier, and interfaces are known to play a role in interstitials and vacancies generation and recombination, so on diffusion processes as well), which may in turn affect the Ge concentration at the oxidation interface. As we know from the results of *Chapter III* that kinetics of dry RTO depend on the Ge concentration at the oxidation interface, dry RTO kinetics thus depend on the type of substrate.

- Oxidation kinetics can be predicted according to the results of *Chapter III* for Ge concentrations at the oxidation interface below 50% only. However, some SGOI layers of this study have Ge concentrations above 50%, especially at the oxidation interface. As we cannot predict oxidation kinetics for Ge concentrations above 50%, we cannot either predict the evolution of the SGOI composition during condensation above 50% Ge concentrations.

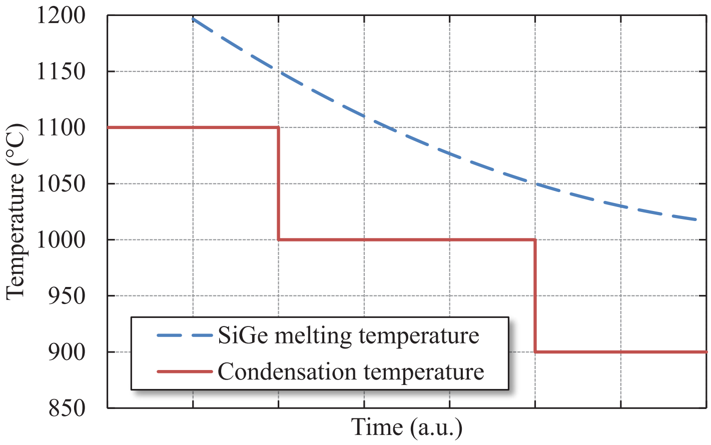

Figure IV.3: Evolution of the melting temperature of SiGe during condensation and of the condensation temperature which is decreased stepwise as soon as the melting temperature is only 50°C above the condensation temperature.

Oxidation process durations are limited by the specifications of the Rapid Thermal Processes equipment used for performing dry RTO and ISSG oxidation. The required process durations to form high-Ge content SGOI layers by a single condensation process exceed the equipment specifications. In those cases, two condensation processes which both comply with the equipment specifications were performed consecutively. A HF treatment was used to thin down the oxide between the two condensation processes in order to decrease the duration of the second condensation process. Indeed, the oxidation rate was shown to decrease when the oxide thickness increases (see *Chapter III*). Therefore, the thinner the oxide thickness before the second condensation process is, the shorter the second condensation process is for a fixed target SGOI composition. This sample preparation sequence is schematically illustrated *Figure IV.4*.

For low Ge content films (lower than 50% Ge concentration), the temperature of oxidation (1100°C) is high enough for the SGOI film to be homogeneous in depth. And when, the temperature is decreased to 1000°C for high Ge content films, the diffusion rate increases fast enough with the Ge concentration (see *Section III.B.1.*) to still consider that the SGOI film is homogeneous at the end of the condensation process.

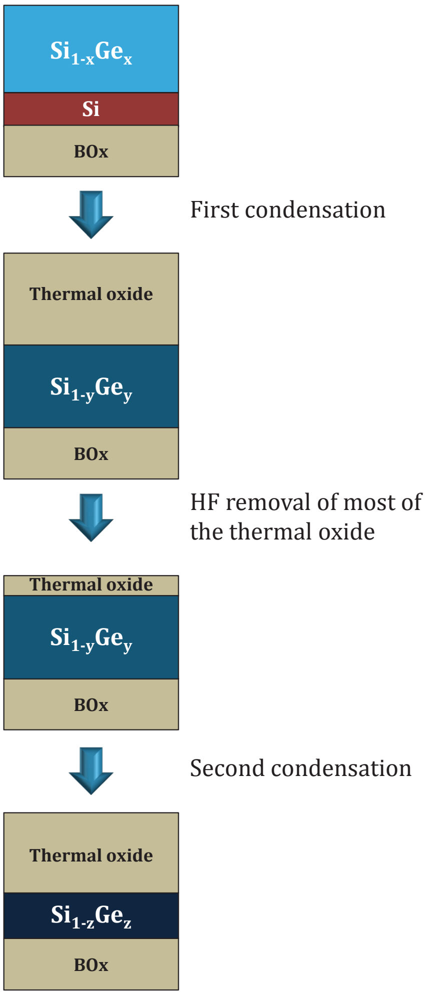

Figure IV.4: Schematic illustration of the condensation-oxide removal-condensation sequence for the fabrication of high-Ge content SGOI films. Here x<y<z.

IV.A.2.2. Characterization of SGOI Films

A dedicated method was used to measure SGOI layer thicknesses and compositions. Spectroscopic ellipsometry could not be used because SiGe optical constants are not known for Ge concentrations above 54%. On the other hand, while compositions cannot be accurately determined by XRR measurements, XRR is a reliable technique for measuring the thickness of SGOI and oxide layers for the whole range of SGOI compositions. The roughness of the SGOI-BOx and SGOI-thermal oxide interfaces and of the oxide surface increases with the Ge concentration, especially when strain relaxation occurs for high Ge-content SGOI layers (this will be shown later). The roughness of these interfaces were therefore treated as unknown during the fitting process of XRR spectra. For the sake of comparability, the SGOI layer thicknesses mentioned in this manuscript are the ones measured by XRR even for Ge concentrations below 54%.

Then, the SGOI composition was calculated assuming no Ge loss during condensation, as described *Section IV.1.*. We mention that methods based on other techniques, such as X-Ray Fluorescence (XRF) coupled with XRR and a technique based on hybridization of XRR and XPS [Fauquier17], allow measurement of SGOI thickness and/or composition as well. However, they could not be used during the whole duration of this study and were thus ruled out for the sake of comparison.

Then, various techniques were used to study strain and crystal quality of SGOI films fabricated by condensation.

Top surface Atomic Force Microscopy (AFM) imaging was performed on 5 x 5 µm^2 SGOI surfaces after oxide removal by HF treatment in order to reveal dislocations. As will be shown *Section IV.A.4.1.3.*, dislocations may induce atomic steps on the surface of the SiGe film along specific crystallographic directions, and AFM can be used to reveal these specific surface steps.

Strain levels were measured by Raman Spectroscopy assuming that the SGOI composition is the one determined by the method described above. Si-Si and Ge-Ge raman peak shifts were used for Ge concentrations below and above 60% respectively (see *Section II.3.4.*). Uncertainties in strain levels were calculated assuming the uncertainty of wavelength measurement is the monochromator resolution, i.e. 1 cm^{-1}. X-Ray Diffraction (XRD) could not be used because SGOI films are too thin for accurate strain determination with this technique.

HRTEM images of a few representative samples were acquired. GPA of these images, taking as a reference an unperturbed area of the Si substrate below the BOx layer was performed to measure the in-plane and out-of-plane deformation of SiGe for comparison with Raman spectroscopy.

The MEIS technique was used to study the composition and the depth distribution of crystal defects of three reprentative samples. Angle configurations and details of the samples will be given *Section IV.A.5.1.*.

IV.A.3. Ge Conservation during Condensation

The model of condensation described in *Section IV.A.1.* relies on Si and Ge conservation during thermal oxidation of SiGe. Other groups have already shown that there is no significant Ge loss during condensation, and we also checked that this is also the case for the condensation processes used in this study.

Spectra of the Ge K-α and L-α spectral lines were measured by Wavelength Dispersive X-Ray Fluorescence (WDXRF) to compare Ge doses before and after condensation (see *Appendice C* for the description of the WDXRF technique). *Figure IV.5* shows WDXRF intensities of a reference sample, i.e. after SiGe epitaxy, and of the same sample after condensation by means of dry RTO at 900°C and at 1100°C. As peak intensities only are compared, no absolute energy calibration is required.

Ge K-α and L-α intensities of all three samples are very close to each other, which shows that there is no significant variation of the Ge amount before and after condensation. We showed in *Section III.A.3.* that there is significant Ge in the thermal oxide. Therefore, all Ge atoms are repelled below the growing oxide during oxidation and conserved in the sample. We could not perform the same measurement for condensation by means of ISSG oxidation but we will assume that there is no significant Ge loss for this process as well. In summary, there is no significant Ge loss during condensation of SiGe and that the model of condensation presented in *Section IV.A.1.* is valid.

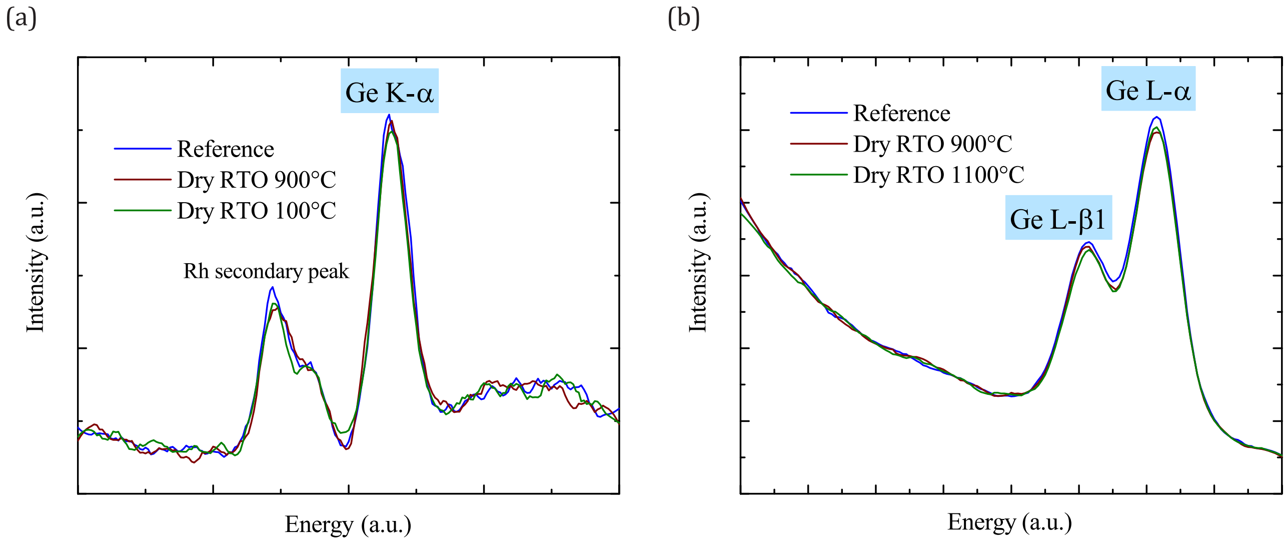

Figure IV.5: (a) Ge K-α and (b) L-α lines WDXRF spectra for a sample before condensation (Reference) and after condensation by means of dry RTO at 900°C and 1100°C.

IV.A.4. Strain and Crystal Defects of SGOI Layers

The section starts by examining the evolution of elastic strain of SGOI films fabricated by condensation based on high temperature oxidation by means of either dry RTO or ISSG oxidation. Results are compared with literature state-of-the-art and discussed in terms of strain energy balance. Condensation based on low temperature ISSG oxidation is then performed to investigate the influence of the temperature and of the nature of the interfaces with the SiGe film on strain. Finally, the formation of dislocations in partially strain relaxed SGOI films is evidenced by AFM imaging of SGOI surfaces.

IV.A.4.1. Strain of SGOI Films Fabricated by High Temperature Condensation

IV.A.4.1.1. Strain Evolution as a function of the Ge Concentration for Dry RTO

Before any discussion, we highlight that the in-plane strain of a fully or partially strained SiGe layer on Si is negative. However, absolute values are usually reported in literature. Following common practices, we will consider absolute values of the in-plane strain and will refer to it as "compressive" in-plane strain to avoid any confusion.

Figures IV.6, *IV.7*, *IV.8* and *IV.9* show HRTEM images of various samples along with the in-plane and out-of-plane deformation maps measured by GPA. Some caution must be observed when analysing GPA deformation maps because of all perturbations that alter the results. This is illustrated on *Figure IV.7 (d)* by the local fluctuations of the compressive in-plane deformation averaged over the thickness of the layer and plotted along an in-plane profile.

The contrast difference of the HRTEM image of the "Post Epitaxy" sample shows the presence of two distinct layers. The quite homogeneous green color for the in-plane deformation of the SOI-SiGe bilayer indicates that the in-plane deformation is close to zero, as expected for a fully strained SiGe layer. The out-of-plane deformation is close to zero (in green) in the bottom part of the layer, which corresponds to the SOI film, and positive in the top part of it (in red) because of the Poisson effect in the SiGe layer. The out-of-plane deformation is averaged along the in-plane direction over the whole HRTEM image and is plotted as a function of depth on *Figure IV.6 (d)*. The spatial and strain resolutions of the GPA technique for this particular study do not allow a precise reconstruction of the out-of-plane deformation depth profile, but gives rather good qualitative agreement with what can be expected for a fully strained SiGe layer. Indeed, the out-of-plane deformation goes from about zero at the SOI-BOx interface to about 2% in the SiGe layer, in agreement with theoretical calculations detailed in *Section I.2.2.3*..

HRTEM images and in-plane and out-of-plane deformation maps of SGOI layers with Ge concentrations of 26%, 57% and 77%, referred to as SGOI26, SGOI57 and SGOI77, are also shown on *Figures IV.7*, *IV.8* and *IV.9*. For both SGOI26 and SGOI57, the dominant color on the in-plane deformation map is green, hence the in-plane deformation is close to zero. SGOI26 and SGOI57 would therefore have no or limited strain relaxation. As for the out-of-plane deformation, it is positive for SGOI26 and SGOI57 samples due to the Poisson effect.

The red shift of the in-plane deformation map for SGOI77 indicates that it is positive for the SGOI77 film, which thus shows strain relaxation. If it is fully relaxed, the in-plane and out-of-plane deformations should be identical (the in-plane and out-of-plane lattice parameters would be equal) while if the film is partially relaxed only, the out-of-plane deformation is expected to by higher because of the Poisson effect. However, we cannot determine if it is partially or fully relaxed because of the high uncertainty on absolute deformation values determined by GPA of HRTEM images.

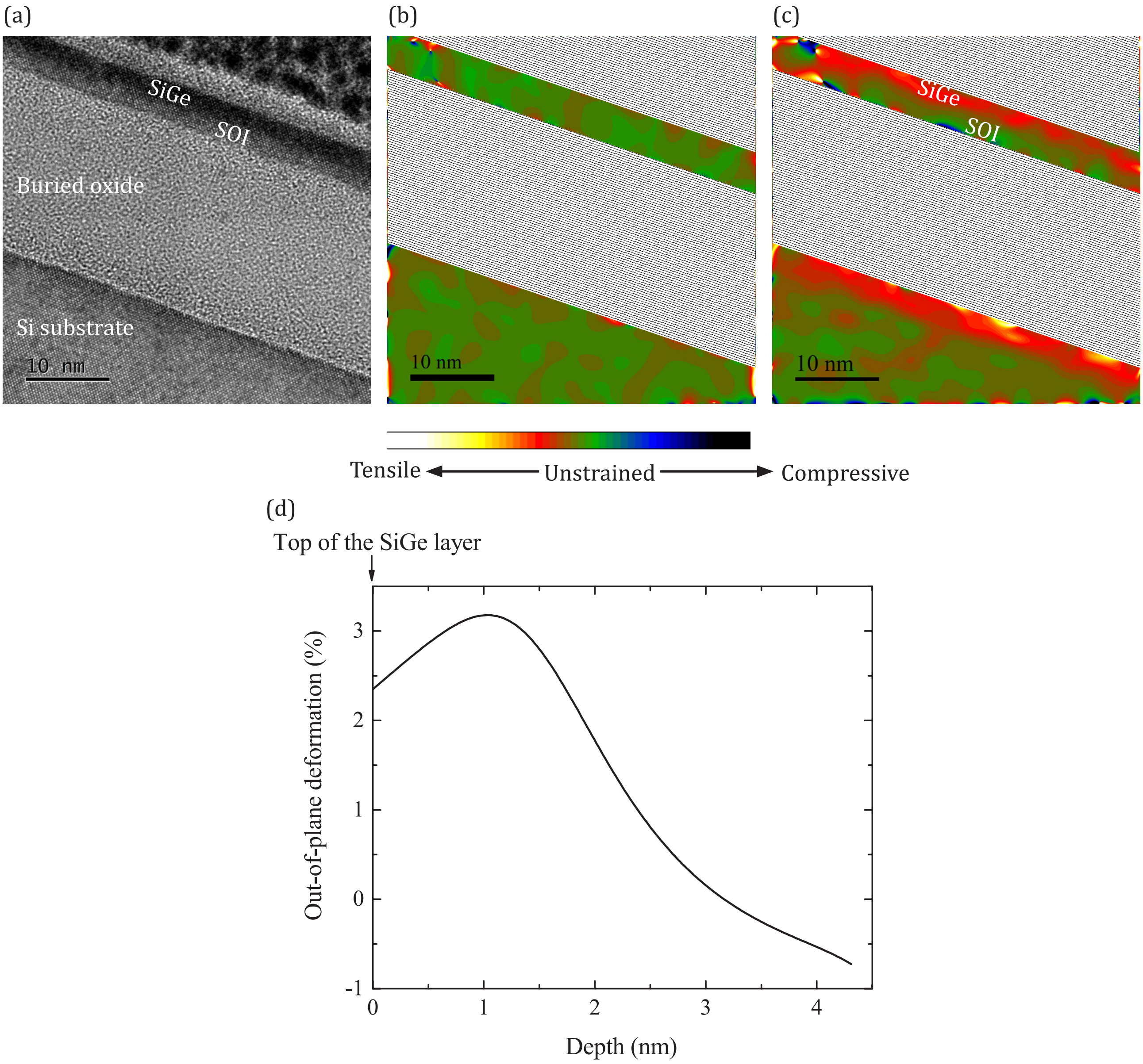

Figure IV.6: (a) HRTEM image of a post epitaxy sample with 30% Ge concentration, (b) in-plane and (c) out-of-plane deformation maps, and (d) depth profile of the out-of-plane deformation measured by GPA.

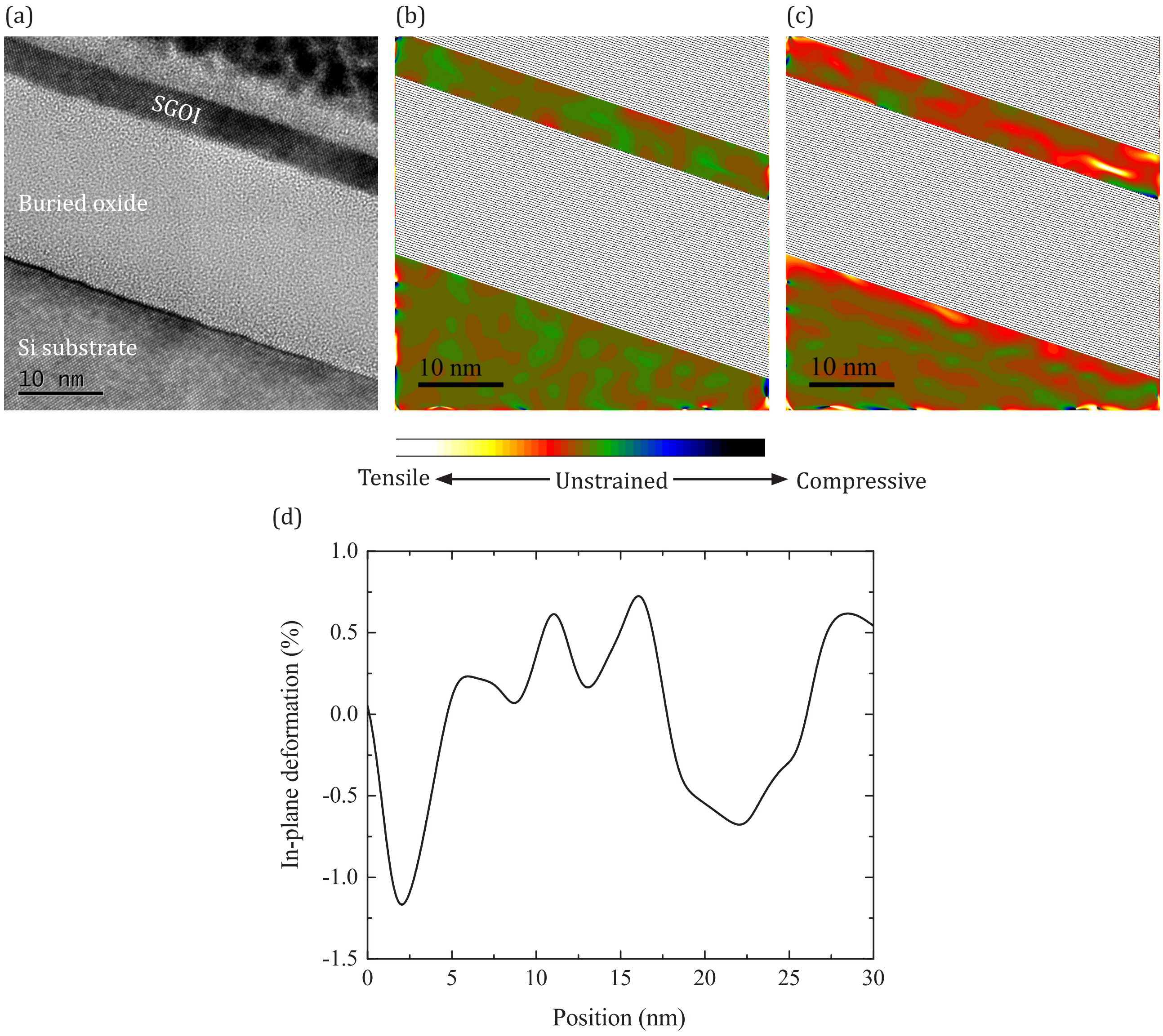

Figure IV.7: (a) HRTEM image of the SGOI26 layer, and (b) in-plane, (c) out-of-plane deformation maps measured by GPA and (d) compressive in-plane strain profile averaged over the thickness of the layer and plotted along the in-plane direction.

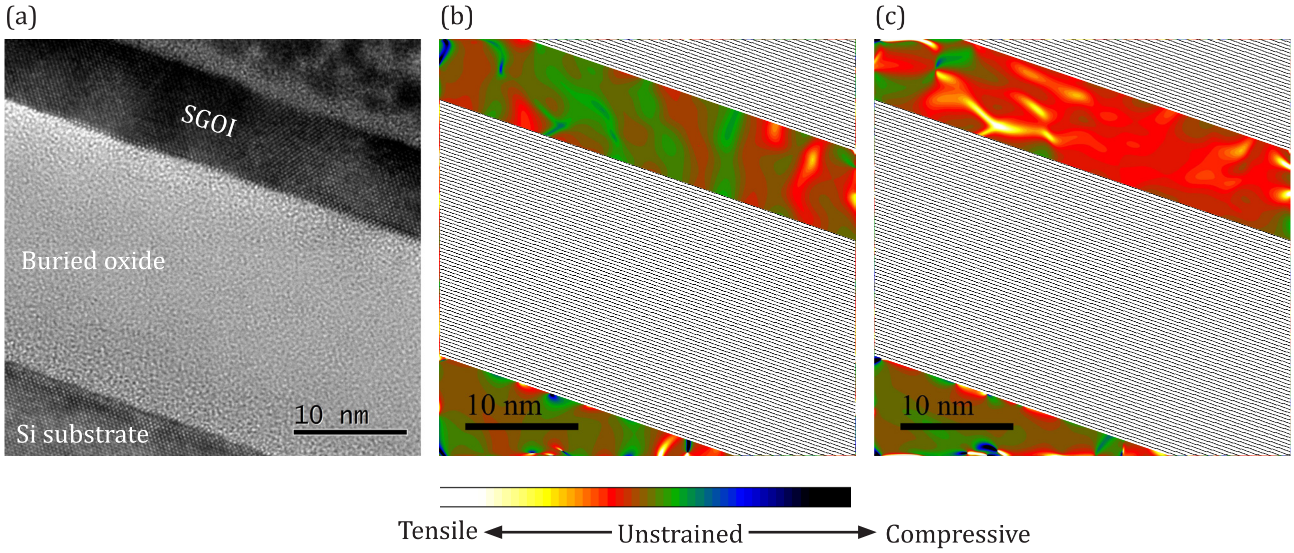
(a)
SGOI
Buried oxide
Si substrate
10 nm
(b)
10 nm
(c)
10 nm
Tensile
Unstrained
Compressive

Figure IV.8: (a) HRTEM image of the SGOI57 layer, and (b) in-plane and (c) out-of-plane deformation maps measured by GPA.

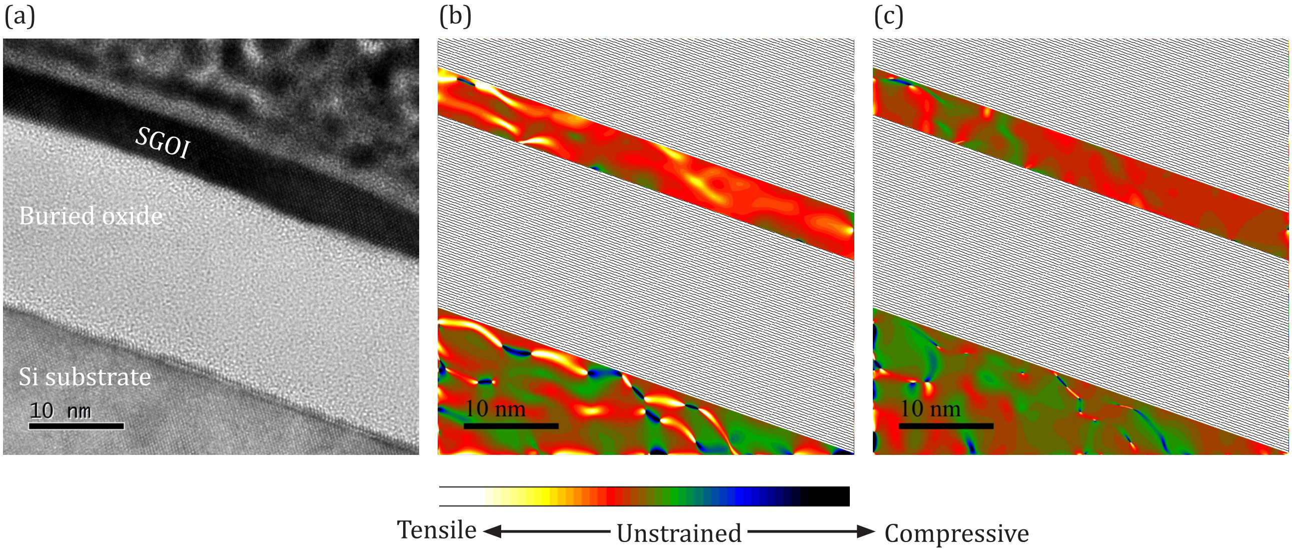

Figure IV.9: (a) HRTEM image of the SGOI77 layer, and (b) in-plane and (c) out-of-plane deformation maps measured by GPA.

Averaged values of compressive in-plane strains measured by GPA and Raman spectroscopy are reported on *Figure IV.10*. As described in *Section II.3.4.*, the Si-Si and the Ge-Ge modes were used for extraction by Raman spectroscopy of the in-plane strain of SGOI layers with Ge concentrations below and above 60% respectively. Due to the dependence of the uncertainty calculation on the mode used for extraction of strain, the uncertainty is higher with the Ge-Ge mode than with the Si-Si one. The line called "Fully strained SiGe" is the theoretical strain of a fully strained SiGe film calculated based on Poisson theory (see *Section I.2.2.3.*).

As for GPA, for each SGOI layer, the in-plane strain was extracted from the measurement of the in-plane deformation averaged over two HRTEM images acquired at two different locations of the TEM lamella, minus the areas where the measurement is obviously altered by either defects such as dislocations or by a contrast too low for robust GPA. We chose to use the in-plane deformation instead of the out-of-plane deformation because there are more atomic planes analyzed in the in-plane direction than in the out-of-plane one (about 40 nm is analysed with the GPA method in the in-plane direction instead of less than 10 nm in the out-of-plane direction), and thus a better statistical significance. Moreover, there may be some Ge concentration gradients in the out-of-plane direction because of the condensation process, while the Ge concentration is quite uniform in the in-plane direction thanks to the good within wafer uniformity of the SiGe epitaxy and condensation processes. This concentration gradient may cause a gradient in the out-of-plane deformation because of the Poisson effect, which in turns increases the uncertainty of averaging the out-of-plane deformation over a full HRTEM image. We finally highlight that quantitative uncertainties cannot be defined for the GPA method (see *Section II.3.5.*) so that values are to be considered with some caution.

It is firstly confirmed that the SiGe layer of the post epitaxy sample is fully strained. As condensation proceeds and as the Ge concentration increases, the compressive in-plane strain increases according to the theoretical strain of a fully strained SiGe film up to about 55-60% Ge concentration and even starts to decrease above 63% Ge concentration. Up to at least 45% Ge concentration, SGOI layers are fully strained, while the SGOI57 layer has a compressive in-plane strain slightly lower than the one of a fully strained SiGe layer. However, the difference between the two values corresponds to the measurement uncertainty so that we cannot claim for certain that this SGOI layer is partially relaxed. In short and in qualitative terms, the SGOI strain follows a "bell shape" as a function of the Ge concentration with a maximum strain value found to be 2.1% at 63% Ge concentration.

The GPA measurement of the same SGOI57 film gives the same strain value, which tends to confirm that this sample is likely to be slightly relaxed. GPA measurement gives a compressive in-plane value lower than the one extracted from Raman spectroscopy for the SGOI77 film. GPA measurement for this sample is likely less robust than Raman spectroscopy because of two reasons. Firstly, the TEM lamella of this sample was too thick for optimum contrast of the SGOI layer, and as a consequence for the GPA method. Secondly, as will be shown in *Section IV.A.4.3.*, the numerous extended defects of the SGOI77 layer alter the GPA measurement. Whatever the robustness of the GPA measurement for this SGOI layer is, both techniques qualitatively agree and show a strong strain relaxation of the SGOI77 film.

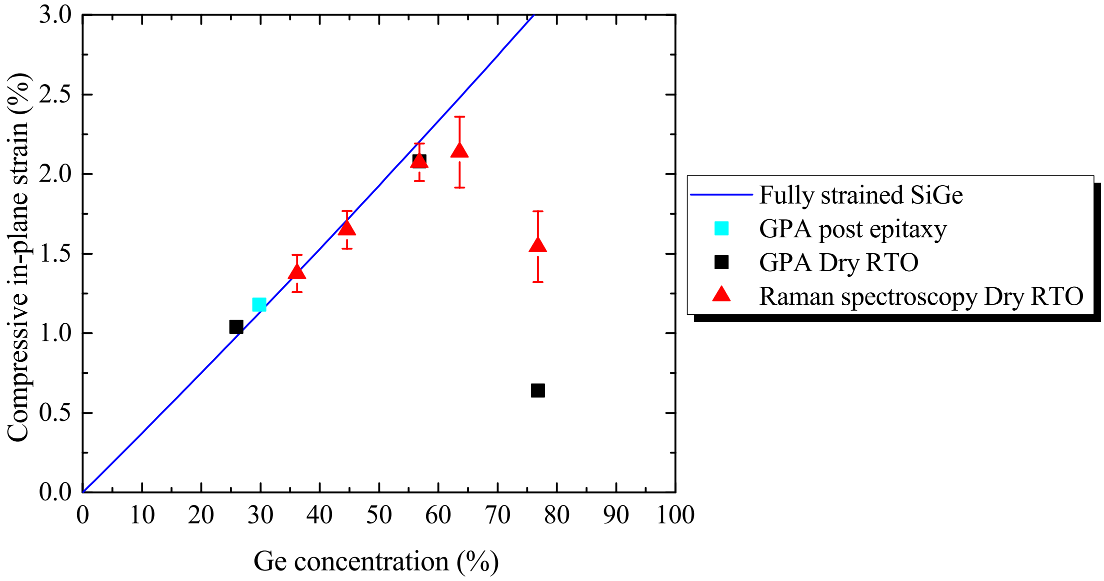

Figure IV.10: Compressive in-plane strain of SGOI layers measured by Raman Spectroscopy and GPA and plotted as a function of the Ge concentration.

IV.A.4.1.2. Comparison between Dry RTO and ISSG Oxidation

A study similar to the one conducted for dry RTO was conducted for condensation based on ISSG oxidation. *Figure IV.11* shows the measured compressive in-plane strain of SGOI films as a function of the Ge concentration for both dry RTO and ISSG oxidation. The SGOI31 layer fabricated by the latter process type is fully strained. However, the SGOI48 film seems to be already partially relaxed. As for the SGOI73 layer, it is also partially relaxed but still features a high compressive in-plane strain value of 2.2 %. The evolution of strain as a function of the Ge concentration follows similar trends for dry RTO and ISSG oxidation, but with a slight difference shown by the dotted lines on *Figure IV.11*. ISSG oxidation-based condensation seems to lead to strain relaxation for Ge concentration as low as 48% and to a maximum strain level attained at a higher Ge concentration than for dry RTO.

Two possible reasons for this difference are suggested. Firstly, and similarly to dry RTO, the temperature of condensation had to be lowered to 1000°C for fabrication of SGOI48 and SGOI73 by ISSG oxidation (see *Section IV.A.2.1.*). ISSG oxidation is faster than dry RTO at 1000°C (see *Section III.B.1.*), so that the SGOI film at the end of the condensation process is likely not as homogeneous as SGOI films fabricated by condensation based on dry RTO because of a stronger pile-up effect. As shown by Takagi et al., Ge concentration gradients tend to favor SGOI strain relaxation. Therefore, the fact that the SGOI48 sample is already partially relaxed could be due to a higher Ge concentration gradient for the case of ISSG oxidation than for dry RTO.

Secondly, oxidation of SiGe by means of dry oxidation is known to possibly inject Si and/or Ge interstitials into the SiGe film (see *Section III.A.1.3.3.*). We found no data on the injection of interstitials during ISSG oxidation of SiGe. If we assume that the mechanisms of strain relaxation of SGOI films (they will be discussed in *Section IV.A.4.1.5.* and *Section IV.A.4.1.6.*) are influenced by the injection of Si and/or Ge interstitials and that the two processes have different injection rates of interstitials, strain relaxation could be influenced by the process type. Strain relaxation might be favored in the case of ISSG oxidation compared with dry RTO for Ge concentration around 45%-50%, which would explain strain relaxation of the SGOI48 sample, while it might maintain a higher strain for Ge concentrations above 60%, which would correspond to the case of the SGOI73 sample. Especially, injection of interstitials is known to possibly play a role in the formation of extended defects in crystals, which are associated with plastic strain relaxation (the formation of extended defects will be discussed in *Section IV.A.4.3.*).

Studying more SGOI films with Ge concentrations above 50% is needed for a more accurate determination of the strain evolution of SGOI films formed by condensation based on high temperature ISSG oxidation.

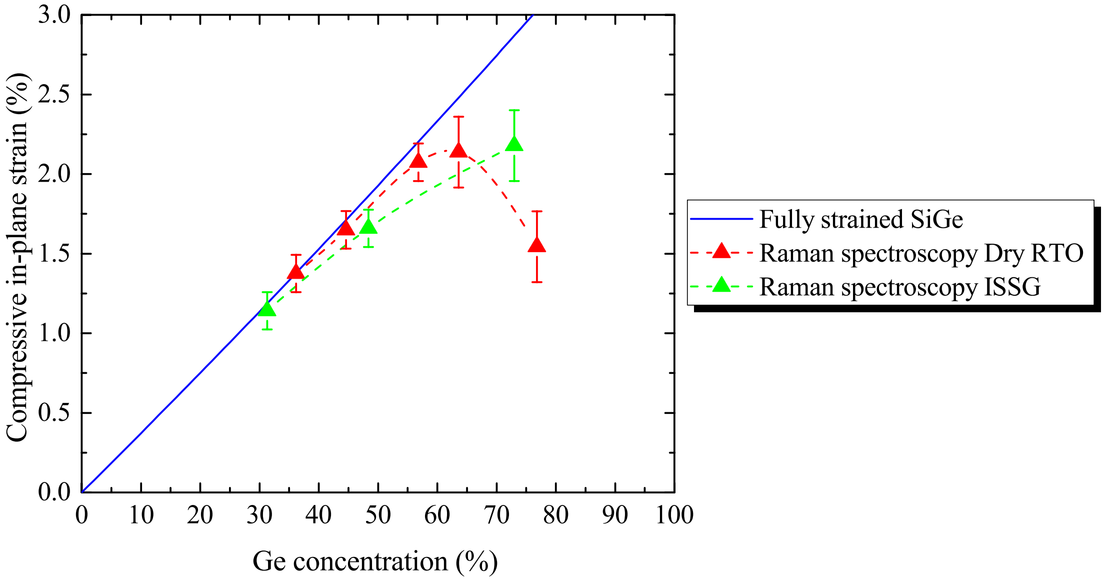

Figure IV.11: Compressive in-plane strain of SGOI layers measured by Raman Spectroscopy as a function of the Ge concentration. Dots are experimental data and dotted lines are guides for the eye.

IV.A.4.1.3. Comparison with Literature

Takagi et al. used a condensation process based on dry furnace oxidation to fabricate SGOI films with Ge concentrations up to 100% [Takagi10]. They also found that the compressive strain of the SGOI layer increases with the Ge content until a peak strain value. Above the Ge concentration that corresponds to this peak value, the compressive in-plane strain decreases. *Figure IV.12* shows the compressive in-plane strain values published by Takagi et al. and obtained with their best condensation process, and values from this work. We observe that the "bell shapes" of the evolution of the compressive in-plane strain as a function of the Ge concentration are very similar, with a maximum compressive strain of 2.2% at 60% Ge concentration for Takagi et al. and 2.1% at 63% Ge concentration for this work.

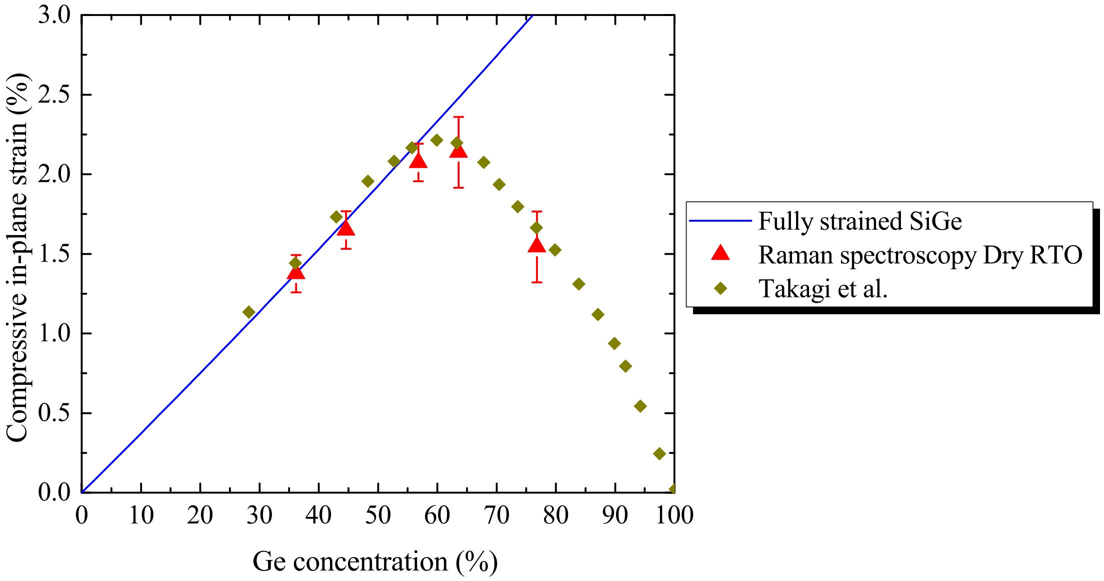

Figure IV.12: Compressive in-plane strain values published by Takagi et al. [Takagi10] and obtained with their best condensation process, and values from this work measured by Raman spectroscopy.

In this first approach, it seems that there is no difference between dry furnace oxidation and dry RTO in terms of strain evolution of SGOI films as a function of the Ge concentration. However, Takagi et al. pointed out that the analysis of the evolution of strain of SGOI films cannot be based on the consideration of the Ge concentration only. of the film especially must be considered. A more relevant analysis framework of these results is the one of elastic strain energy, as will be discussed into the next section.

IV.A.4.1.4. Comparison with SiGe Equilibrium Models

It appears necessary to identify the mechanisms that govern the evolution of strain of SGOI films. As already highlighted by Takagi et al., a common framework of the analysis of elastic strain is the one of the balance of elastic strain energy with plastic strain energy, the so-called equilibrium models of the critical thickness (see *Section I.2.4.2.*). These models were developed for SiGe epitaxial films and not for SGOI films but we will still compare Takagi et al. results and ours with these models.

Figure IV.13 plots the Ge concentration of SGOI films fabricated by condensation as a function of its thickness, for both this study and Takagi et al. one. Samples that are fully strained are indicated on *Figure IV.13*, and the SGOI57 sample, which is close to the onset of strain relaxation and likely slightly relaxed, is also indicated. The most common equilibrium models are Matthews and Blakeslee one and People and Bean one, and are also plotted on *Figure IV.13* for comparison [Matthews74][People85]. With fully strained SGOI layers above Matthews and Blakeslee critical thickness, both our study and Takagi et al. disagree with this model. Our study seems to be below People and Bean model, while Takagi et al. had fully strained SGOI films above People and Bean critical thickness. In summary, neither Takagi et al. data nor our study agrees with the most accepted equilibrium models of epitaxial SiGe-Si systems.

We suggest that the nature of the interfaces of the SiGe films, being with a Si crystal for the case of epitaxial SiGe systems while being with amorphous oxides for the case of SGOI films, influences strain relaxation of the SiGe crystal. We propose that SiGe-oxide interfaces might alter either the balance between elastic strain energy and plastic strain energy, which would explain the discrepancy with equilibrium models of epitaxial systems, or the generation, recombination and gliding of dislocations, which are known to nucleate at interfaces.

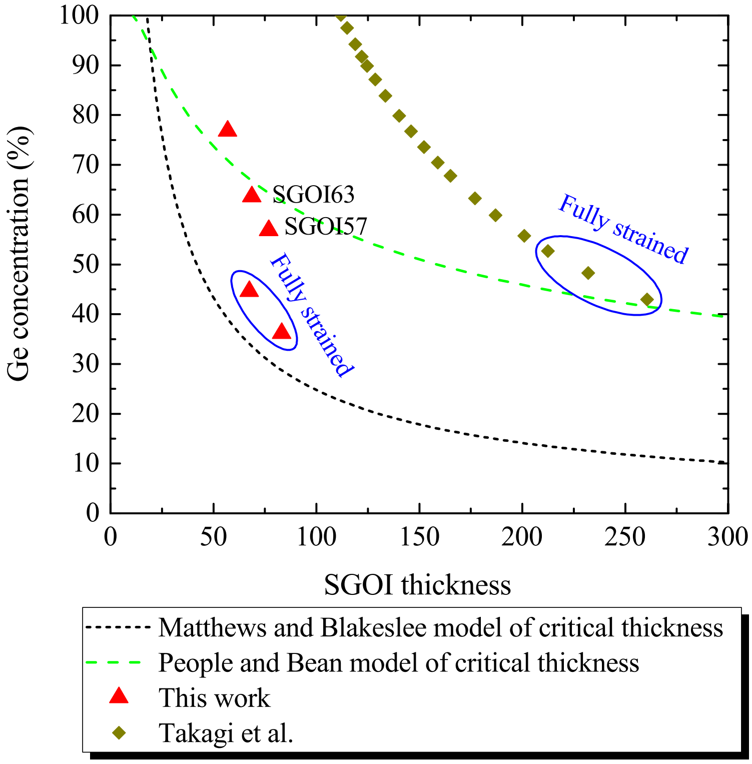

Figure IV.13: Ge concentration as a function of the SGOI thickness. This study experimental data and Takagi et al. experimental data [Takagi10] are plotted. The critical thickness of Matthews and Blakeslee model and the one of People and Bean model are also plotted as dashed lines [Matthews74][People85].

IV.A.4.1.5. Discussion about the Influence of the SGOI Thickness on Strain

Even if strain of SGOI films seem to disagree with the most accepted equilibrium models of epitaxial SiGe-Si systems, Takagi et al. still showed that the evolution of strain is not dependent on the Ge concentration only, as could imply *Figure IV.12.*. Takagi et al. discussed the effect of the thickness of SGOI films on strain using two key methods:

- They considered that the thickness of initial epitaxial SiGe films and SGOI films obtained by condensation of these initial films can be represented by the thickness of their equivalent GOI film. The equivalent GOI film thickness of an initial epitaxial SiGe film is the thickness of the GOI film obtained by condensation of this film until 100% Ge concentration is reached. For instance, a 40 nm-thick epitaxial $Si_{0.72}Ge_{0.28}$ film corresponds to a 11.2 nm-thick GOI film after condensation (see *Section IV.A.1.* for calculations) while a 40 nm-thick epitaxial $Si_{0.78}Ge_{0.22}$ film corresponds to a 8.8 nm-thick GOI film after condensation. We will also use this analysis methodology to discuss the effect of the thickness of SGOI films on strain.
- They studied SGOI films fabricated on tensily-strained SOI substrates (sSGOI). Tensily-strained SOI substrates (sSOI) are substrates whose SOI film is tensily strained with respect to relaxed Si.

Firstly, the comparison of strain of SGOI and sSGOI films made by Takagi et al. obviously shows that strain relaxation of SGOI layers is not dependent on the Ge concentration only. Indeed, the authors showed that the "bell shape" of the evolution of strain of sSGOI films is very similar to the one of condensation experiments performed with relaxed SOI substrates, except that it is shifted to higher Ge concentrations. We highlight that the authors found that the maximum strain values of SGOI and sSGOI films are similar (between 2.2% and 2.5%).

Secondly, as illustrated on *Figure IV.14*, Takagi et al. found that thicker sSGOI films yielded lower compressive strain at identical Ge concentrations. We also notice on *Figure IV.14* that the effect of the sSGOI thickness on elastic strain seems to be less and less important as sGOI thicknesses are reduced. If we assume that this tendency is also observed for SGOI films, we can suggest that as the GOI equivalent thickness is reduced to lower and lower values, the evolution of strain as a function of the Ge concentration gets closer to some sort of "asymptotic bell shape" curve with a maximum strain value between 2.2% and 2.5%. It also corresponds to a decreasing influence of the SGOI thickness on strain as this thickness is reduced. If we now look back to *Figure IV.11*, the fact that our results are aligned with Takagi et al. in terms of evolution of strain as a function of the Ge concentration is consistent with the idea of an "asymptotic bell shape". Indeed, data of Takagi et al. showed *Figure IV.11* corresponds to their thinner SGOI films and SGOI films of this study are even thinner.

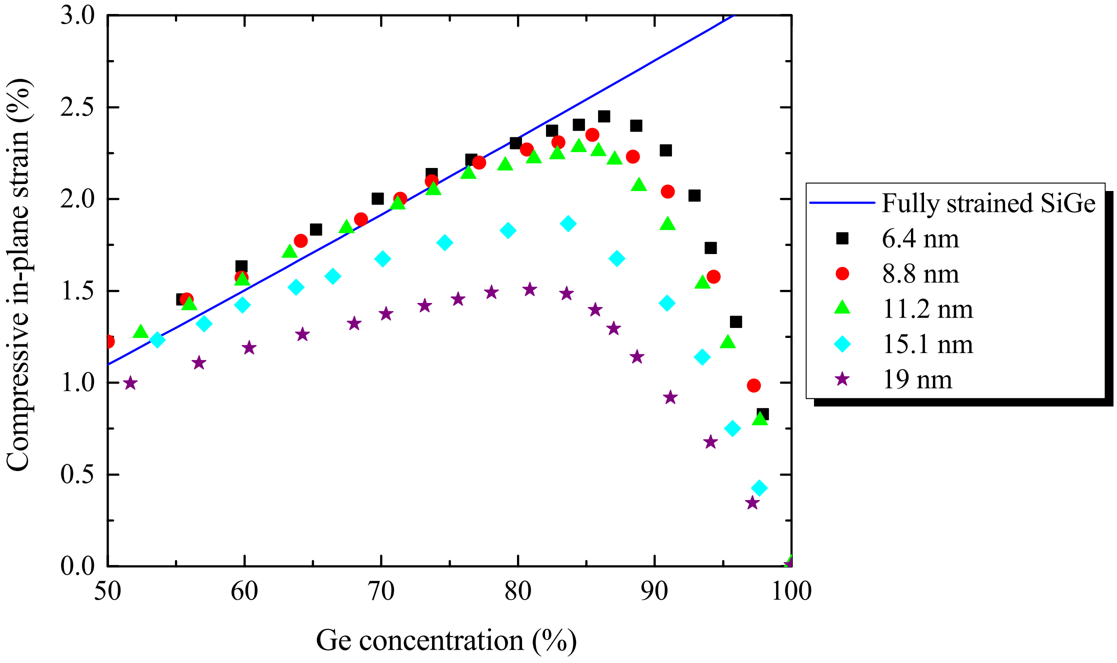

Figure IV.14: Compressive in-plane strain values of sSGOI films published by Takagi et al. [Takagi10]. sGOI equivalent thicknesses are indicated in the legend (see text for the definition of the sGOI equivalent thickness).

IV.A.4.1.6. Conclusion about Strain of SGOI Films Fabricated by High Temperature Condensation

In summary, the comparison of our results with Takagi et al. ones and with equilibrium models of epitaxial SiGe-Si models showed that SGOI strain relaxation is not governed by equilibrium models of epitaxial SiGe-Si systems. We argued that the Ge concentration alone is not a relevant parameter and that the SGOI thickness influences strain of SGOI films. However, it seems that the effect of the thickness of the SGOI film on strain relaxation is likely weak for SGOI thicknesses in the 10 nm range, a range which is relevant in light of today's technology needs. We finally highlight that the strain level is likely the key parameter of strain relaxation of thin SGOI films, with a threshold in the 2.2%-2.5% range for an optimized condensation process based high temperature oxidation. In terms of strain relaxation mechanisms, we highlighted that it is likely highly dependent on the nature of the SiGe-oxide interfaces.

As elastic strain relaxation is usually accompanied by generation of crystal defects such as dislocations, we study into the next section the formation of dislocations in SGOI films fabricated by condensation based on dry RTO.

IV.A.4.2. Strain of SGOI Films Fabricated by Low Temperature Condensation

As emphasized into the last section, SGOI strain relaxation is not governed by equilibrium models of epitaxial SiGe-Si systems and the nature of the interfaces with the SiGe film likely influences the mechanisms of strain relaxation. We performed condensation experiments at low temperature by means of ISSG oxidation at 850°C in order to study the influence of the temperature and of the nature of the interface with the SiGe film on strain relaxation. The process is schematically illustrated on *Figure IV.15*. As shown in *Section III.A.4.3.*, ISSG oxidation at 850°C of a $Si_{0.7}Ge_{0.3}$ film leads to formation of a pile-up layer with a Ge concentration of about 60%. Then, as condensation proceeds, the thickness of the pile-up layer increases while its Ge concentration is rather constant. The oxidation temperature being low, there is hardly any interdiffusion between the epitaxial layer and the SOI film. Finally, after the pile-up layer has "consumed" all the epitaxial SiGe layer, it starts to extend into the SOI layer until the bottom interface of the pile-up layer reaches the interface with the BOx layer. Oxidation durations were chosen based on kinetics results of *Section III.A.4.1.* so that it stops when the bottom interface of the pile-up layer reaches the interface with the BOx layer. As recipes are based on results of ISSG oxidation kinetics of SiGe layers on bulk Si substrates, there is some uncertainty on condensation kinetics (see *section IV.A.2.1.*). Two oxidation durations were thus chosen and final Ge concentrations were 53% and 58% based on measurement of the SGOI layer thicknesses by XRR.

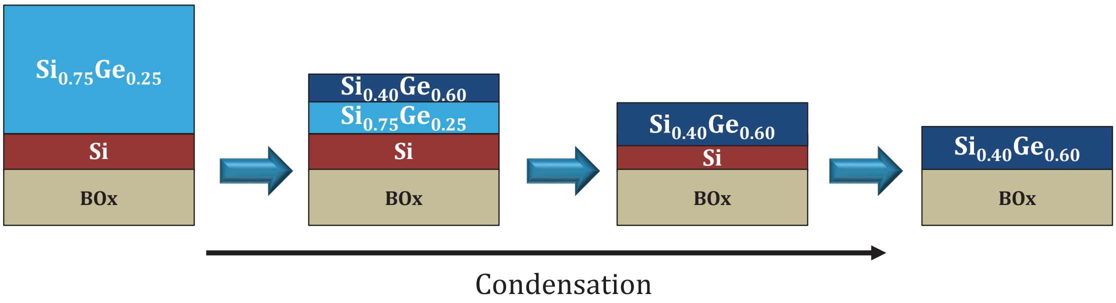

Figure IV.15: Schematic illustration of the condensation process based on low temperature ISSG oxidation to fabricate SGOI films with a Ge concentration of 60%. The thermal oxide is not shown for clarity considerations.

As shown *Figure IV.16*, Both samples have strain levels well below the ones of fully strained SiGe layers with the same SiGe compositions and obtained with high temperature oxidation. It is suggested that a SiGe layer on SOI has a crystalline interface that might favor strain relaxation via dislocations formation (a case that could be comparable to an epitaxial SiGe film on a Si bulk substrate). While for high temperature condensation, interdiffusion is fast enough for a quite homogeneous SGOI film to be formed quickly after the beginning of condensation. The interface between the strained SiGe layer and the underlying film is not a crystalline one anymore, but an interface with an amorphous oxide that might hinder strain relaxation up to higher strain levels.

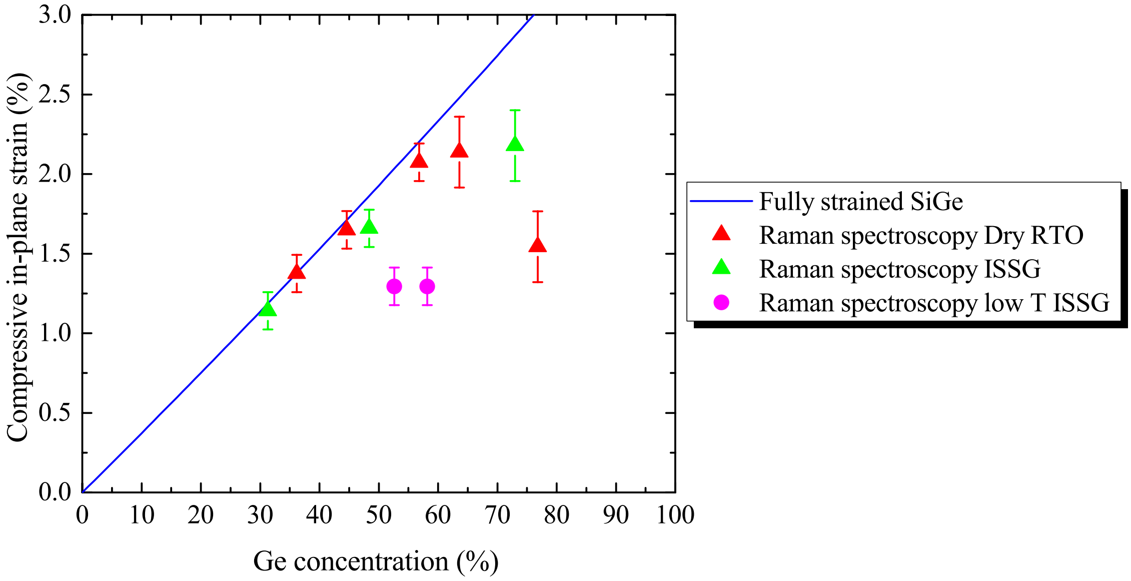

Figure IV.16: Compressive in-plane strain of SGOI layers measured by Raman Spectroscopy and plotted as a function of the Ge concentration for various condensation process types. "Low T" refers to samples fabricated by ISSG oxidation at 850°C and the others points are samples fabricated by high temperature condensation and already discussed into the last section.

IV.A.4.3. Extended Defects Revelation

AFM images of the surface of SGOI layers after oxide removal are shown on *Figure IV.17*. No specific pattern is observed for Ge concentrations up to 57% and Root Mean Squared (RMS, see *Appendice E*) are between 1.5 Å and 2 Å, which are typical values of SOI substrates. However, characteristic cross-hatched patterns are observed for SGOI63 and SGOI77 films. These patterns are formed by lines oriented in the <110> direction, and the spacing between lines is estimated to about 50 nm. These lines are due to atomic steps on the surface of the SiGe layer induced by dislocations gliding on {111} planes [Gunji11]. Strain relaxation of SGOI63 and SGOI77 samples measured by either Raman spectroscopy or TEM GPA (see *Section IV.A.4.1.1.*) is thus accompanied by generation of dislocations on {111} planes.

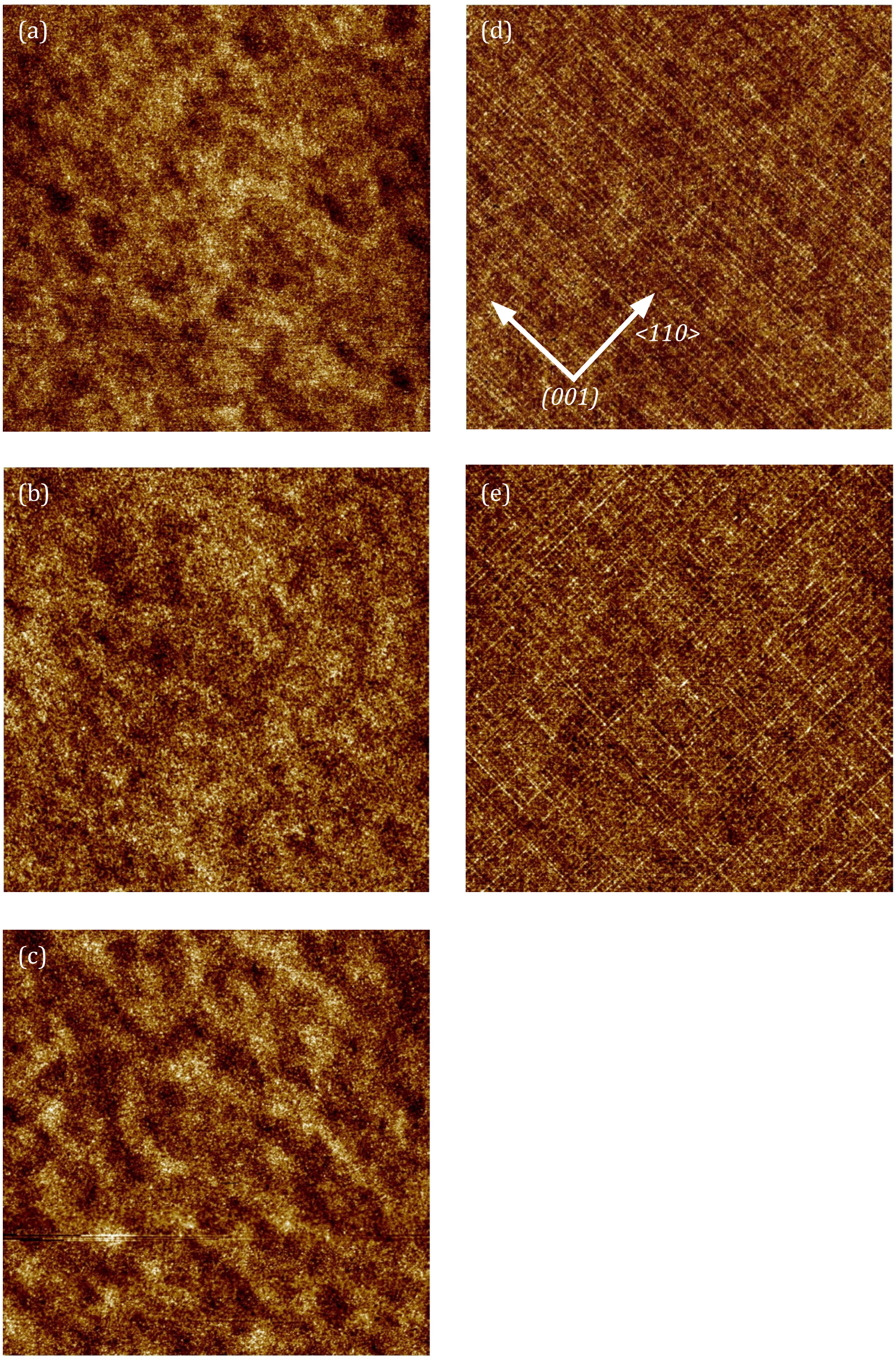

Figure IV.17: 5 µm x 5 µm AFM images of the surface of (a) SGOI36, (b) SGOI45, (c) SGOI57, (d) SGOI63 and (e) SGOI77 films.

We also acquired TEM images of some samples of this study to have a look at the films fabricated by condensation (and also to measure strain of SGOI films by GPA as shown in *Section IV.A.4.1.1.*). Indeed, while AFM is a convenient technique to identify the presence of dislocations at the surface of SGOI films, TEM is required to study the bulk of the SGOI films. These TEM images can be also used to obtain complementary information on the dislocations. Note that comparison between AFM and TEM results are not easy due of the different scales and views (edge view for the TEM section and plane view for AFM). From TEM images, dislocations can be evidenced using the Moiré technique. Numerical Moiré patterns of a chosen plane, such as (111), can be obtained by Fast Fourier Transform (FFT) of the HRTEM image, followed by filtering around the chosen diffraction spot, and finally inverse FFT to reconstruct the chosen planes. *Figure IV.18*, *IV.19*, *IV.20* and *IV.21* show HRTEM images and the (111) numerical Moiré patterns of Reference, SGOI25, SGOI57 and SGOI77 samples. No dislocations are observed in numerical Moiré patterns of Reference and SGOI25 samples while some are for SGOI57 and SGOI77 ones. TEM lamella preparation may be the source of some dislocations so that we cannot claim for sure that the dislocations observed in

HRTEM images and corresponding Moiré patterns are caused by the condensation process. However, TEM lamella preparation cannot make dislocations disappear so that we can claim that there is no dislocations in the bulk of the films of Reference and SGOI25 samples in the limited probed area of a TEM lamella.

Interestingly, dislocations were also observed in the Si substrate of the SGOI77 sample. If these dislocation are due to the condensation process and not to the TEM lamella preparation, we suggest that the substrate might be slightly strained by the SGOI layer even with the 20 nm-thick buried oxide film between the two layers. The Si substrate would be tensily strained and not compressively strained in this case. Properties of tensile Si might be a lot different from the ones of compressive Si, and might explain why there are dislocations into the substrate for low tensile strain levels. However, an in-depth study, based on dedicated experiments and mechanical simulations, seems required to further the discussion on these dislocations.

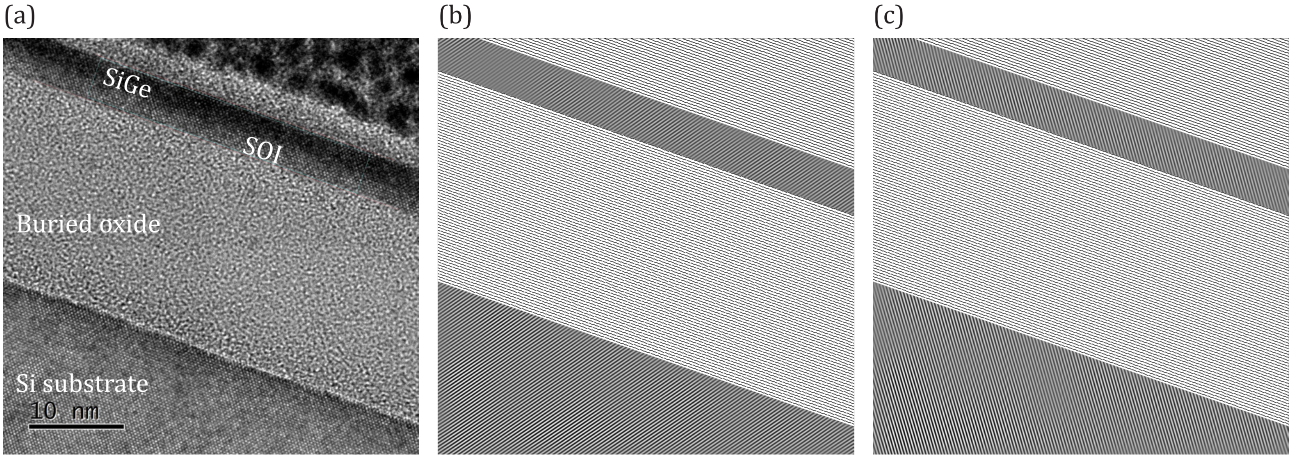

Figure IV.18: (a) HRTEM image of the Reference sample, and (b) and (c) numerical Moiré patterns of (111) planes.

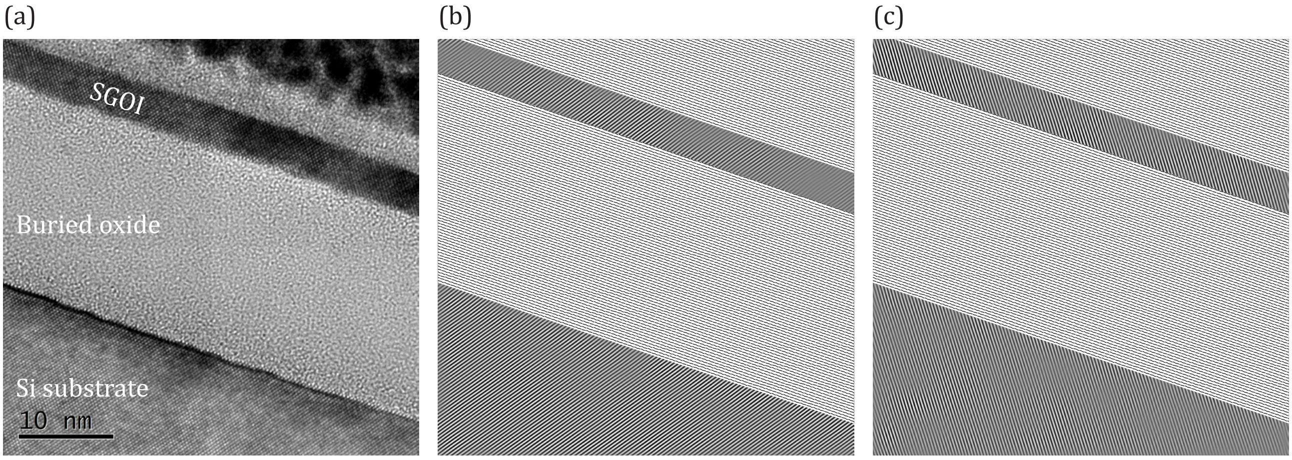

Figure IV.19: (a) HRTEM image of the SGOI25 sample, and (b) and (c) numerical Moiré patterns of (111) planes.

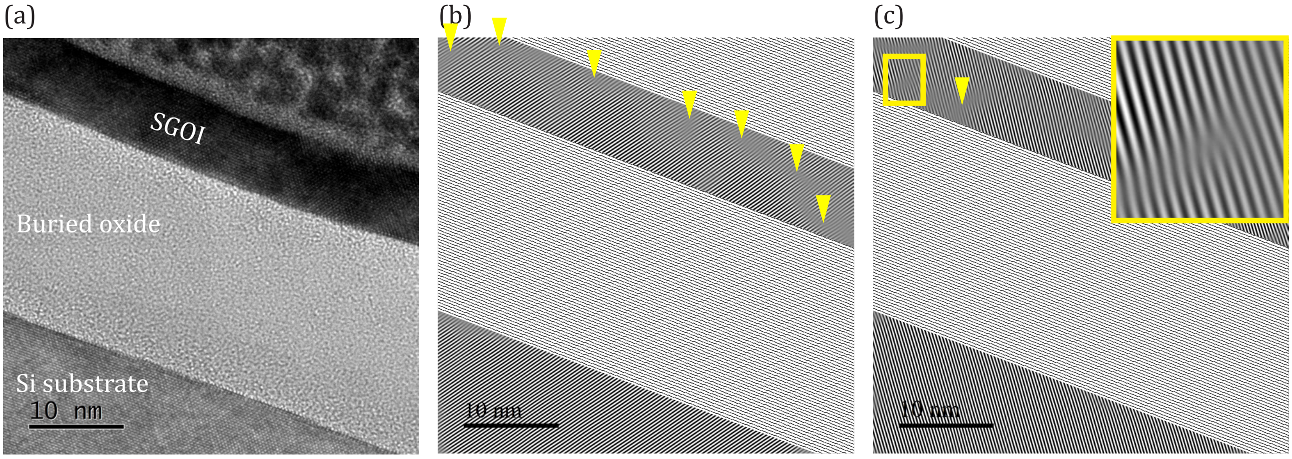

Figure IV.20: (a) HRTEM image of the SGOI57 sample, and (b) and (c) numerical Moiré patterns of (111) planes. Triangles indicate where missing half planes are observed and the insets of (b) and (c) are magnifications of the area where some of these missing half-planes are observed.

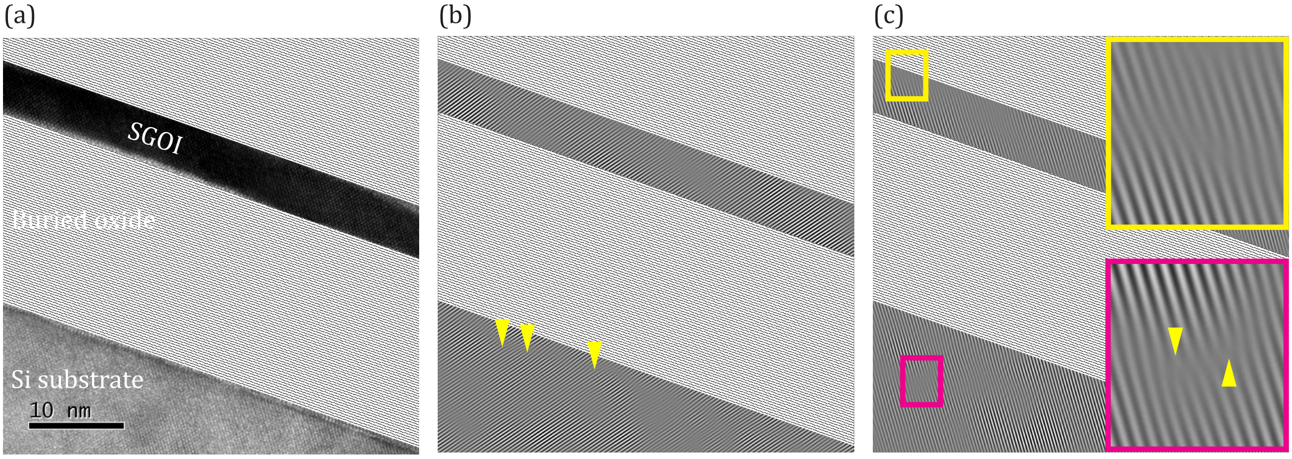

Figure IV.21: (a) HRTEM image of the SGOI77 sample, and (b) and (c) numerical Moiré patterns of (111) planes. Triangles indicate where missing half planes are observed and the insets of (b) and (c) are magnifications of the area where some of these missing half-planes are observed.

In summary, we showed that elastic strain relaxation of SGOI films measured by Raman spectroscopy is accompanied by formation of dislocations on {111} planes. Identifying the precise nature of these dislocations is however more difficult as TEM images are 2D projections of 3D samples, and as a consequence 2D projections of 3D dislocations. The absence of a sound consensus in the literature about the type of defects in partially relaxed SGOI layers also confirms the difficulty to study the nature of dislocations [Bedell04][Nakaharai06][Vincent07][Gunji11].

IV.A.4.4. Conclusion of Section IV.A.4.

We showed that strain of SGOI films fabricated by condensation based on high temperature dry RTO increases with the Ge concentration until a strain peak value of about 2.1% at 60% Ge concentration. It was also evidenced that the strain level is likely the key parameter of strain relaxation of thin SGOI films and not the Ge concentration, with a threshold in the 2.2%-2.5% range for an optimized condensation process based on dry oxidation at high temperature. In terms of strain relaxation mechanisms, we emphasized that the oxide-SiGe interfaces likely play a role in strain relaxation by hindering dislocations formation up to higher elastic strain values than at SiGe-Si interfaces. Finally, AFM imaging of the surface of SGOI films revealed that strain relaxation is accompanied by formation of dislocations in {111} planes.

IV.A.5. Characterization of SGOI Composition and Crystal Quality by MEIS

The former section focused on the evolution of elastic strain of SGOI films and its correlation with the formation of dislocations. The process conditions and mechanisms that lead to strain relaxation and formation of dislocations have been discussed. However, a finer characterization of the crystal quality as a function of depth into the SGOI film would be of great interest as the SiGe crystal quality influences its electrical properties. This is the object of this section. The composition and crystal quality of SGOI films fabricated by condensation is studied by MEIS. The three studied samples and experimental conditions of MEIS experiments are firstly introduced. In particular, the analysis methodology of MEIS random and channeling spectra is presented. The composition depth profiles are firstly studied because they must be fixed for the analysis of channeling spectra that allows to study the crystal quality of SGOI films. This section ends with the evolution during condensation of the crystal quality of SGOI films as a function of depth.

IV.A.5.1. Experimental

IV.A.5.1.1. Studied Samples and Experimental Configurations

MEIS spectra were acquired on the three different samples and in the three angular configurations shown *Table IV.1*. These three samples are not the same as the ones studied in *Section IV.A.4.* (except for one) and will thus be called differently. The three samples are:

- "Reference": it corresponds to a sample after SiGe epitaxy, so before condensation.
- "Low Ge": this SGOI sample has been fabricated by a condensation process close to the one used for fabrication of standard SGOI layers at STMicroelectronics Crolles fab (dry RTO at 1100°C). The 25% Ge concentration is also in the range of standard Ge concentrations of SGOI layers.
- "High Ge": it is the SGOI layer formed by condensation based on dry RTO that features the highest Ge concentration without any visible defects on AFM images (see *Figure IV.14*) and with a strain level very close to the one of a fully strained SiGe layer (see *Figure IV.10*). This sample is the SGOI57 film already studied in *Section IV.A.4.*.

For both "Low Ge" and "High Ge" samples, the thermal oxide grown during condensation was thinned down by HF treatment in order to decrease the "de-channeling" effect of amorphous layers located on top of multilayer systems (see *Section II.4.3.4.* for more details about de-channeling).

The MEIS angular configurations used in this study are (details about "random" and "channeling" modes are given *Section II.4.3.4.*):

- "Random 45-90": 45 corresponds to 45° between the incident ion beam and the normal to the surface of the sample, and 90° is the scattering angle. This configuration corresponds to the random mode.
- "Channeling 45-90": The angle configuration is similar to the one of "Random 45-90" but in channeling conditions. It corresponds to channeling in the [111] direction of the Si/SiGe crystal.
- "Random 66-76": the incident angle with respect to the normal of the surface of the sample is 66°.

Channeling conditions were chosen to be the ones that feature the smallest Ge peak.

Sample name	"Reference"	"Low Ge"	"High Ge"
Random 45-90	✓	✓	✓
Channeling 45-90	✓	✓	✓
Random 66-90		✓	

Table IV.1: MEIS acquisition conditions used for each sample.

IV.A.5.1.2. Identification of Peaks on MEIS Spectra

Section II.4.3. introduced the principles of the MEIS technique and discussed the dependence of the energy and of the probability of ion backscattering on the nature and depth of the scattering atom. The analysis of experimental MEIS spectra that is performed into the next sections requires the identification of the respective contributions of each element of each layer to the MEIS spectra for the specific samples of this study. This identification is conducted by simulation of each one of these contributions.

Figure IV.20 shows a simulated MEIS spectra of a thermal oxide-SGOI stack where the contribution of each element of each layer is shown. As explained in *Section II.4.3.3.*, the higher the atomic number of the scattering element of each layer is shown. As explained in *Section II.4.3.3.*, the higher the atomic number of the scattering element is, the higher the energy of backscattered ions is. We thus observe that the Ge peak of the SiGe layer is at a higher energy than the Si one of the same SiGe layer. We also notice that the peak area of Ge is higher than the one of Si while the simulation was performed for a $Si_{0.75}Ge_{0.25}$ layer which has more Si atoms than Ge atoms. Indeed, the probability of backscattering also increases with the atomic number, which makes the number of ions backscattered by Ge atoms higher than the one backscattered by Si atoms. These two effects are also evidenced when comparing the Si peak of the thermal oxide with the O peak of the same layer.

The dependence of the energy of backscattered ions on the depth at which they are backscattered is also observed. Ions backscattered by Ge atoms located at the top of the SiGe layer have the highest energy (around 92 keV for the example of *Figure IV.20*) while ions backscattered by Ge atoms at the bottom of the layer escape the top surface with a lower energy (around 85 keV for the example of *Figure IV.20*). The order of magnitude of the thickness dependence of the energy of backscattered ions is 1 keV for 1 nm. There are Si atoms in all layers of the simulated multilayer system so that Si peaks of each layer are consecutive from about 81 keV. We can also notice that the O peak of the thermal oxide layer, located at around 66 keV, is at the same energy as the Si peak of the bottom of the BOx layer.

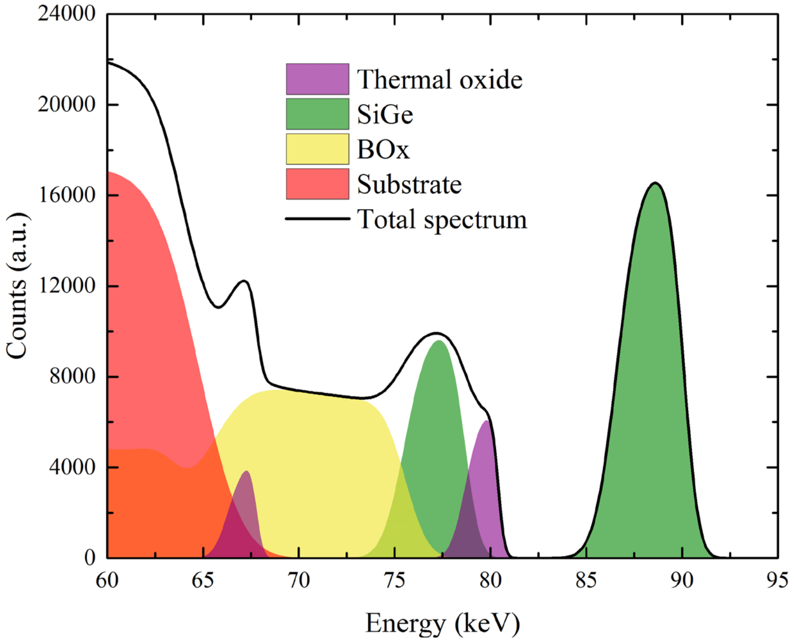

Figure IV.20: Simulated MEIS spectra of a thermal oxide-SGOI stack where the contribution of each element of each layer is shown.

As a conclusion, the dependence of the energy of backscattered ions and of the scattering probability on both the atomic number of the scattering element and the thickness at which ions are backscattered is clearly evidenced for samples and MEIS conditions used in this study. This identification allows us to analyse the experimental 2D MEIS maps presented into the next section.

IV.A.5.1.3. Experimental 2D MEIS Maps

Experimental MEIS spectra at a specific scattering angle were extracted from 2D maps such as the one shown *Figure IV.21*. These 2D maps represent the measured count of backscattered ions as a function of the energy and of the scattering angle. The scattering angular range is fixed by the detector to 40° around the central position, which is 90° on the example of *Figure IV.21*. Based on the simulated spectra of *Figure IV.20*, several peaks can be identified and associated with an element and a layer of the studied sample. The 2D map shown *Figure IV.21* was acquired in channeling conditions so that the peak corresponding to ions backscattered by Si atoms of the SiGe layer is lower in intensity than the one arising from the amorphous thermal oxide and BOx layers. It thus appears in blue on the 2D map. As explained in *Section II.4.3.3.* and illustrated *Figure IV.21*, the energy of the backscattered ions increases as the scattering angle decreases. We also observe that the angular dependence of the energy of backscattered ions is higher for Si atoms than for Ge atoms, as predicted by *Equation II.16* and illustrated *Figure II.18*.

MEIS spectra shown into the next section are extracted by summing ion counts over a narrow angle range in order to get reasonable statistics.

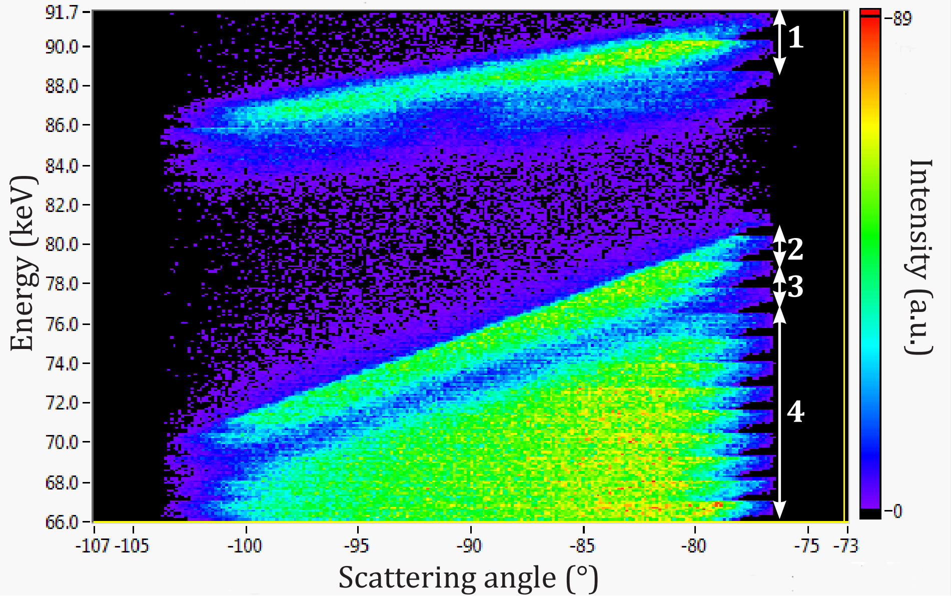

Figure IV.21: MEIS 2D map measured in channeling conditions with an incident angle of 45° and around a central scattering angle of 90°C. The arrows indicate the main peaks: (1) Ge peak of the SiGe layer, (2) Si peak of the thermal oxide, (3) Si peak of the SiGe layer appears lower in intensity (blue) because of the channeling conditions, and (4) Si peak of the BOx layer.

IV.A.5.2. Experimental and Simulated Spectra

Experimental and simulated spectra are shown *Figure IV.22*. Due to the experimental constraints described in *Section II.4.3.*, a trade-off between the scanned energy range and the counting time had to be chosen. Hence the scanned energy range is different from one spectrum to another depending on this trade-off. For "Reference 45-90" and "Low Ge 45-90" random and channeling spectra and "High Ge 45-90" channeling spectra, the scanned energy range was fixed to 65-92 keV. These spectra show the Ge peak and the Si peaks of the thermal oxide, of the SiGe layer and of a part of the BOx layer. While we can observe the O peak at about 67 keV for the "Low Ge 66-76" random spectrum. As for the "High Ge" random spectrum, the scanned energy range was 55-92 keV and thus allows the O peak at about 57 keV to be visible. All simulated spectra were simulated according to the procedure described in *Section II.4.3.6.*.

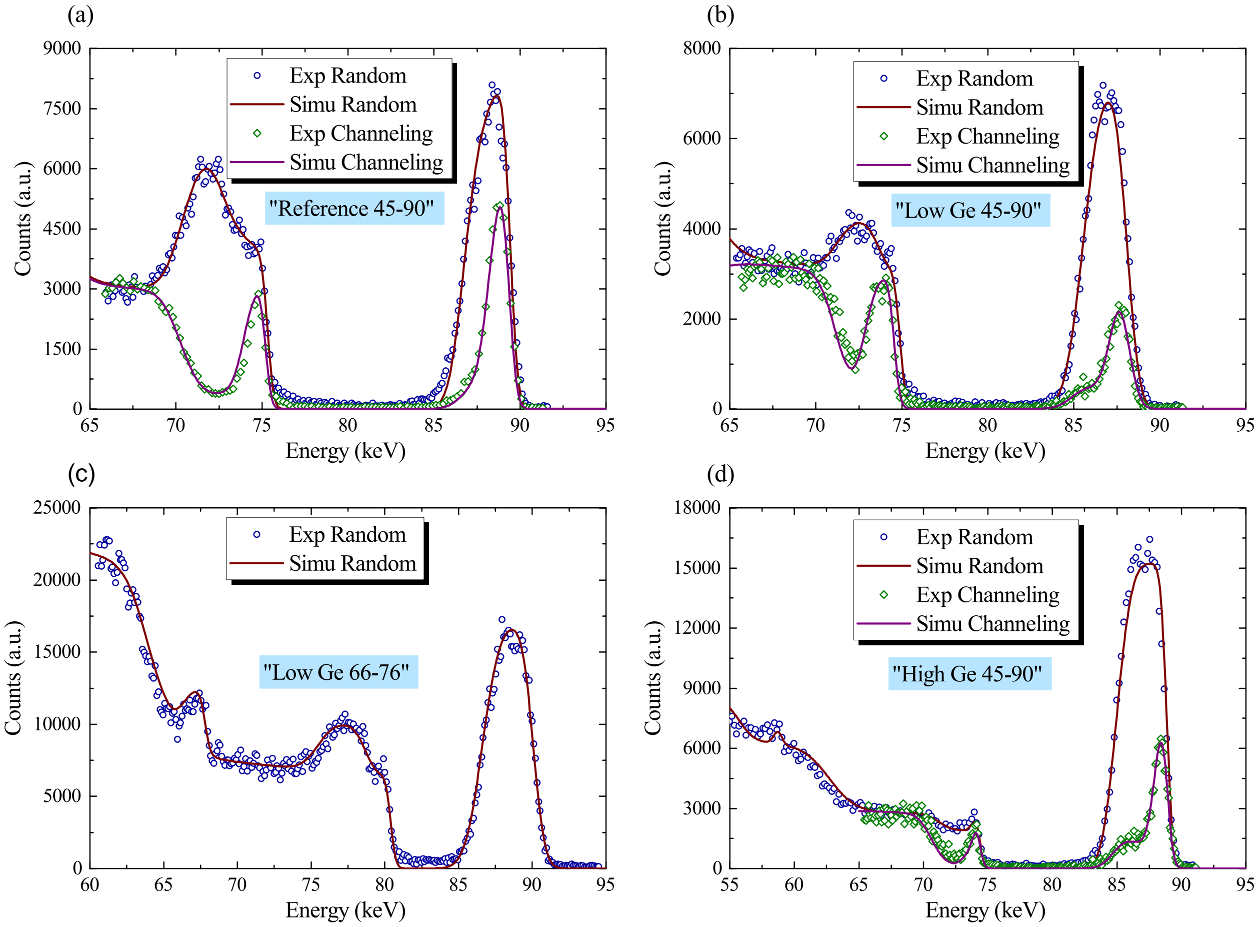

Figure IV.22: Experimental MEIS spectra and simulated ones for all configurations described in Section IV.A.5.1.1.: (a) "Reference" in random and channeling 45-90 configurations, (b) "Low Ge" in random and channeling 45-90 configurations, (c) "Low Ge" in random 66-76 configuration, and (d) "High Ge" in random and channeling 45-90 configurations.

Random spectra were firstly analyzed in order to retrieve the composition as a function of depth, which is the object of the next section. Then, the comparison with channeling spectra allows us to focus on the crystal quality in *Section IV.A.5.4.*.

IV.A.5.3. Chemical Composition Analysis

This section discusses the chemical composition profiles of the three studied samples. Fixing the composition of the samples is indeed required for analysing the channeling spectra in *Section IV.A.5.4.* (see *Section II.4.3.6.*).

The composition as a function of depth was extracted from MEIS spectra acquired in random conditions. A limited number of layers was used to fit experimental spectra so that composition gradients cannot be precisely retrieved. The composition of the top oxide and of the BOx layer were fixed to SiO_2 while the one of the SOI layer was fixed to pure Si. The Ge concentrations as a function of depth, taking the BOx-SGOI interface as zero depth and the *x* axis towards the surface of the sample, are plotted *Figure IV.23*. The BOx-SGOI interface was chosen to be the zero reference for the sake of consistency with the crystal quality results presented in *Section IV.A.5.4.*.

While a single homogeneous SiGe layer was used for fitting ellipsometry and XRR spectra of the "Reference" sample, two SiGe layers were used for fitting the MEIS random spectrum. Due to a limited number of layers used for fitting MEIS spectra (see *Section II.4.3.6.*), the inhomogeneity of the layer is represented by two SiGe layers with different concentrations. This SiGe bilayer is most certainly not real and a smooth gradient is more likely. Similarly, the values of the Ge concentrations of the two layers are not to be taken as absolute values but as average concentrations over the thickness of each of the two SiGe layers used for fitting.

As well as for the "Reference" sample, we used two SiGe layers to fit MEIS spectra in random 45-90 and 66-76 configurations for the "Low Ge" sample. However, even if this two SiGe layers system gives better fits than a single SiGe layer, the bottom SiGe layer is very thin and its composition is very close to the one of the top SiGe layer. As a consequence, it seems that the SiGe layer is fairly homogeneous. Such a homogeneous SGOI layer was expected because of the high temperature used for the condensation process (which tends to homogenize the SGOI layer as seen in *Section III.A.4.3.*).

Three SiGe layers were introduced to fit the experimental random spectrum of the "High Ge" sample. The top of the layer is found to feature a higher Ge concentration than the bottom (from 62% Ge concentration on top to 40% at the bottom). Again, a smoother composition gradient is more likely than three well-defined and homogeneous SiGe layers. We observe that the top of the SGOI layer seems quite homogeneous with a Ge concentration close to 62% while the Ge concentration over the deepest 3 nm of the SGOI layer is significantly lower. Contrary to the "Low Ge" sample, the composition inhomogeneity is significant. We propose that the SGOI layer was most likely homogeneous as long as the condensation temperature was 1100°C (until about 40% Ge concentration). Then, as the temperature was decreased to 1000°C, the pile-up effect was more pronounced and led to higher Ge concentration below the oxide. At the same time, SiGe interdiffusion drastically increases above 50% Ge concentration [Kube10][David15], which may lead to stabilization of the Ge concentration of the pile-up layer while interdiffusion is slowed down at the bottom of the layer. Hence the quite homogeneous SiGe layer on top (here with 62% Ge concentration) and the lower Ge concentration at the bottom (probably as low as 40%).

The chemical profiles of all three samples retrieved from random spectra were fixed for the analysis of channeling spectra performed into the next section.

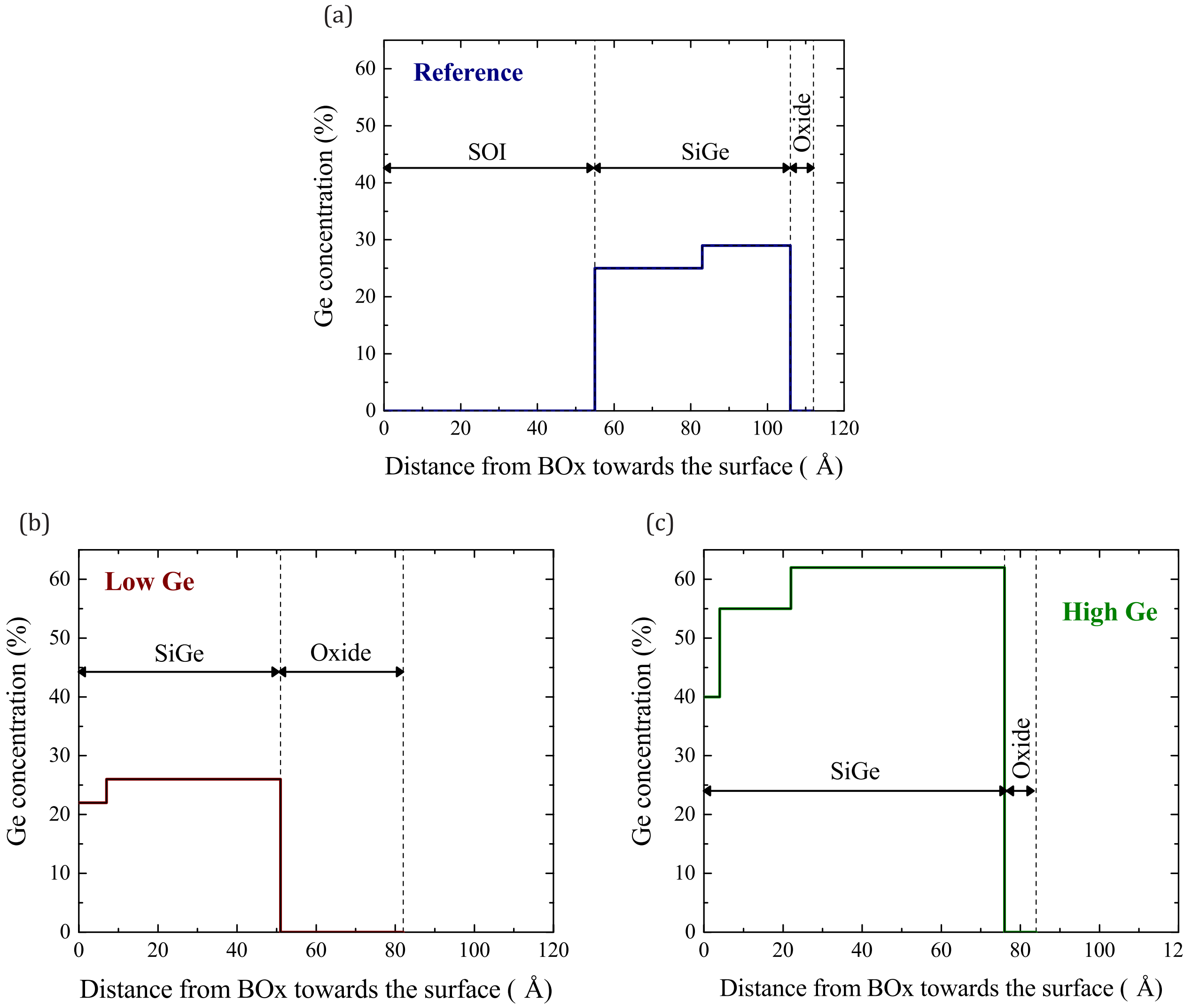

Figure IV.23: Ge concentration profiles extracted from random MEIS spectra. Profiles are plotted as a function of depth taking the BOx-SGOI interface as zero and the x axis towards the surface. (a) is for the "Reference" sample, (b) for the "Low Ge" one and (c) for the "High Ge" one.

IV.A.5.4. Crystal Quality Analysis

IV.A.5.4.1. Introduction and χ_{min} Definition

As described in *Section II.4.2.4.*, channeling is a mechanism that takes place when the ion beam is aligned with a crystallographic direction of the probed crystal. We evidenced in the previous section that there are Ge concentration gradients from the top to the bottom of SGOI films. These gradients induce out-of-plane lattice parameter changes from the top to the bottom of SGOI films. It results in deviations of crystallographic directions that must be evaluated for a rigorous analysis of MEIS channeling spectra, which is the subject of *Section IV.A.5.4.2.*.

Then, in *Section IV.A.5.4.3.*, we evaluate the surface peak caused by backscattering by the first atomic layers of the SGOI film, which are not included in the shadow cone (see *Section II.4.3.4.*).

Having assessed the two former effects that affect the channeling spectra, *Section IV.5.4.4.* discusses the depth profiles of the χ_{min} factor. As already introduced in *Section II.4.3.4.*, the χ_{min} factor is the percentage of atoms displaced from theoretical lattice sites. In the case of SiGe films, the theoretical lattice sites are the ones taking into account the Poisson effect.

IV.A.5.4.2. Channeling Angle and Angular Tolerance

The channeling angle along the [111] direction of an unstrained Si crystal is 45°. However, for the case of a fully strained SiGe film, the [111] channeling direction is disoriented with respect to 45° due to the Poisson effect. Channeling may still be observed if the incident beam is only slightly disoriented with respect to the considered crystal direction, here the [111] one. The angular tolerance is defined as the angular difference between the angle that gives the lowest χ_{min} factor (in other words the best channeling angular conditions) and the one that corresponds to an increase of the χ_{min} of 50% of the gap between the lowest χ_{min} factor and the one of random conditions. The angular tolerance is [Jalabert17]:

$$\psi^{1/2} = \sqrt{\frac{Z_I Z_A e^2}{2\pi\varepsilon_0 E d}}, \qquad \textbf{\textit{Equation IV.4}}$$

where Z_I is the atomic number of the incident ion, Z_A is the average atomic number of the considered material, e is the elementary charge, ε_0 is the dielectric constant of vacuum, E is the kinetic energy of incident ions and d is the average distance between atoms along atomic rows. Let us consider the case of a fully strained SiGe layer, which features the larger angular deviation with respect to unstrained Si. *Figure IV.24* shows the angular deviation with respect to 45° of the channeling angle along the [111] direction and the angular tolerance as a function of the Ge concentration. The angular tolerance and the angular deviation increase with the Ge concentration because of the increase of the average atomic number and because of the Poisson effect respectively. For Ge concentrations between 0% and 60%, the angular tolerance is always at least three times (which is the case of 60% Ge concentration) as large as the angular deviation.

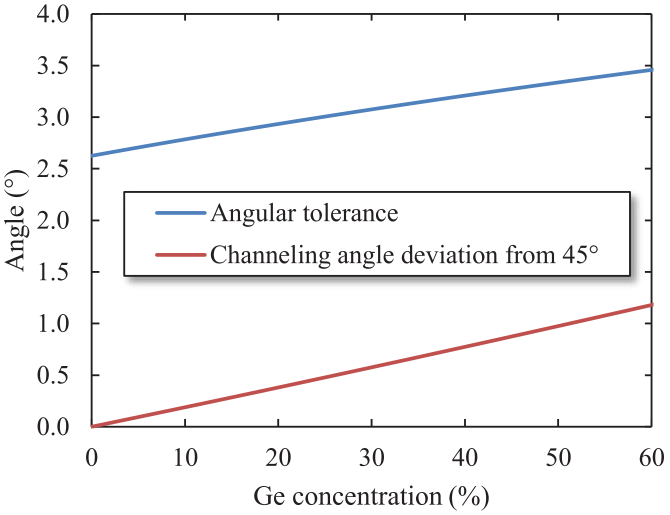

Figure IV.24: Calculated angular tolerance and channeling angle deviation from 45° for a fully strained SiGe layer and plotted as a function of the Ge concentration.

As a result, when the angle is fixed so that the χ_{min} factor is minimum in the SiGe layer of the "Reference" sample, the channeling conditions are still very close to the best ones for the SOI layer. And as for the "Low Ge" and "High Ge" samples, non-homogeneities of the Ge concentration are neither high enough to induce important variations of the χ_{min} factor. In summary, the χ_{min} factor is weakly sensitive to the elastic strain level variations of this study. And as a result, only atoms displaced from lattice sites in a significant manner, such as atoms of a dislocation core and in the immediate vicinity of it, or atoms in interstitial positions, significantly influence the χ_{min} factor.

IV.A.5.4.3. The Shadowing Effect and the Surface Peak

As briefly described in *Section II.4.3.4.*, in channeling conditions, deflection of incoming ions by the first nuclei of atomic rows is at the origin of a shadow cone (the so-called shadowing effect) that prevents ions from being backscattered by deeper atoms. The scattering yield of the first atomic layers is however the one of an amorphous layer as scattering of incoming ions is not prevented by this shadowing effect. It results in a peak, called surface peak, in spectra acquired in channeling conditions whose contribution must be quantified for a rigorous analysis.

The number of atoms per row to participate to the surface peak has been measured and simulated for various crystals, channeling directions and temperatures and was found to follow a trendline that only depends on the ratio ρ/R_m, where ρ is the amplitude of the thermal vibrations perpendicular to the channeling direction and R_m is the radius of the shadow cone [Jalabert17]. We calculated the radius of the shadow cone for a fully strained SiGe crystal as shown in [Jalabert17] and found that it is about 0.20 Å and rather constant over the full range of Ge concentration. Using the amplitude of thermal vibrations at room temperature of a Si crystal perpendicular to the [110] direction (we could not find values of amplitudes of thermal vibrations of a SiGe crystal in the perpendicular direction to [111], so that we assume that it is close enough to the case of a Si crystal in [110] channeling conditions to use the latest value), we can show that the ratio ρ/R_m is about 0.39. It corresponds to only one atom per atomic row to participate to the surface peak whatever the Ge concentration is.

In summary, with the conditions used for MEIS measurements, the surface peak of SGOI films is limited to backscattering of the first atomic layer of the film.

IV.A.5.4.4. Crystal Quality of SGOI Films

Figure IV.25 shows the Ge concentration and χ_{min} factor profiles extracted from random and channeling MEIS spectra. Some caution must be observed when discussing the χ_{min} factor profiles. Indeed, as we could not explore all possible solutions due to the manual fitting method, we cannot guarantee that the solutions reported here are the best ones and the closest to reality. Indeed, the contributions of each atomic layer overlap with each other because of the straggling effect (see *Figure IV.20* which shows that peaks overlap with each other). As a consequence, determination of the best χ_{min} factor profile is more difficult by a manual fitting method. If we look for instance at the "Reference" sample, we found that the top 2 nm of the SiGe films has a χ_{min} factor of 75 %. But the best solution could also be that the top 1.6 nm of the SiGe layer has a χ_{min} factor of 85 % as far as we cannot compare all χ_{min} factor profiles.

However, what we are more confident about is the total amount of atoms displaced from their lattice positions because this amount is more directly linked to the total area of the peak. For the sake of a more quantitative comparison between crystal qualities of samples, we define a term called Amorphous Atomic Layer Equivalent Number (*AmALEN*) which is proportional to the total amount of displaced atoms of the studied layer:

$$AmALEN = \frac{th \times \chi_{\min}}{d}, \qquad \textbf{\textit{Equation IV.5}}$$

where *th* is the thickness of the considered layer and *d* the distance between two atomic layers (in this case between two {111} planes because the chosen channeling direction is [111]). When the considered layer is the top part of the SiGe film, the *AmALEN* of the surface peak (see *Section IV.A.5.4.3.)*, which is equal to one, must be subtracted to the total *AmALEN* of the film.

Let us comment each sample:

- *Figure IV.25 (a)*: "Reference": SiGe epitaxial layer on SOI: the χ_{min} factor is found to be 5% in the whole SOI layer. It thus shows that the SOI crystal is not altered by the SiGe epitaxy process and still has a very low amount of atoms displaced from lattice sites. The bottom part of the epitaxial SiGe layer has a higher amount of atoms displaced from lattices than the SOI layer, even if it can be considered a high-quality crystal with a χ_{min} factor of 10%.

  Finally, the top part has an important amount of atoms displaced from lattice sites, with an *AmALEN* of about 3. The fact that the χ_{min} factor of the SOI layer, which is below the SiGe film, is as low as 5% rules out any disorientation with respect to channeling conditions as well as de-channeling of the ion beam through the top amorphous oxide as the possible explanations of such a high *AmALEN*. Neither roughness can account for such a high *AmALEN* because roughness only is not associated with SiGe crystal distortion. Roughness would result in the surface peak being "spread" over a wider energy range. Buckling, however, can be seen as roughness associated with crystal distortion and can contribute to such a high *AmALEN*.

- *Figure IV.25 (b)*: "Low Ge": Low Ge fraction SGOI films: the SiGe crystal sandwiched between the perturbed top part and the 1 nm-thick bottom part of the SGOI layer is as perfect as the SOI crystal. It shows that SiGe interdiffusion does not damage the crystal quality of the SOI layer during condensation.

  The *AmALEN* of the top part of the SiGe layer decreases from 3 for the "Reference" sample to 1. Two mechanisms are proposed to account for this decrease. Firstly, thermal oxidation may contribute to reorganize atoms of the top part of the SiGe crystal so that there are less atoms displaced from lattice sites after condensation. And secondly, the top part of the SGOI layer of the "Low Ge" sample corresponds to the former SOI film, whose χ_{min} factor is likely not altered by SiGe interdiffusion as suggested above.

  As for the bottom part of the SGOI layer, it seems that the presence of Ge at the interface with the BOx layer is associated with a degradation of the crystal in the immediate vicinity of the interface. Some authors showed that the higher the Ge concentration at an interface with a thermal SiO_2 film is, the higher the number of Ge dangling bonds is. They argued that these dangling bonds are formed in order to accommodate the stress at the semiconductor-oxide interface [Houssa11]. We suggest that while the crystal is not stressed at the interface with the BOx layer for the case of the SOI-BOx interface, it is stressed for the one of the SGOI-BOx interface, and that this stress may cause crystal distortion and/or damage. This mechanism could also account for at least a part of atoms displaced from lattices sites in the top part of the SGOI film.

- *Figure IV.25 (c)*: "High Ge": High Ge fraction SGOI films: The *AmALEN* of the top part of the SGOI layer is about 2. The fact that it is lower than the one of the "Reference" sample suggests that thermal oxidation tends to decrease the χ_{min} factor by reorganizing atoms below the oxidation front. Indeed, here the SGOI is thicker than the initial SOI so that the second mechanism proposed above for the case of the "Low Ge" sample can be ruled out in this case. The χ_{min} factor is also found to be higher close to the interface with the BOx layer. Finally, apart from the areas close to interfaces, the χ_{min} factor increases from 5% for low Ge fraction to about 10%, which shows that the SiGe crystal starts to be slightly degraded, possibly because of dislocations such as those evidenced by TEM GPA in *Section IV.A.4.1.3.*.

Having discussed in this section the crystal quality of the three studied samples individually, the key evolutions of the crystal quality of SGOI films during condensation are summarized in a concise and schematic manner into the next section.

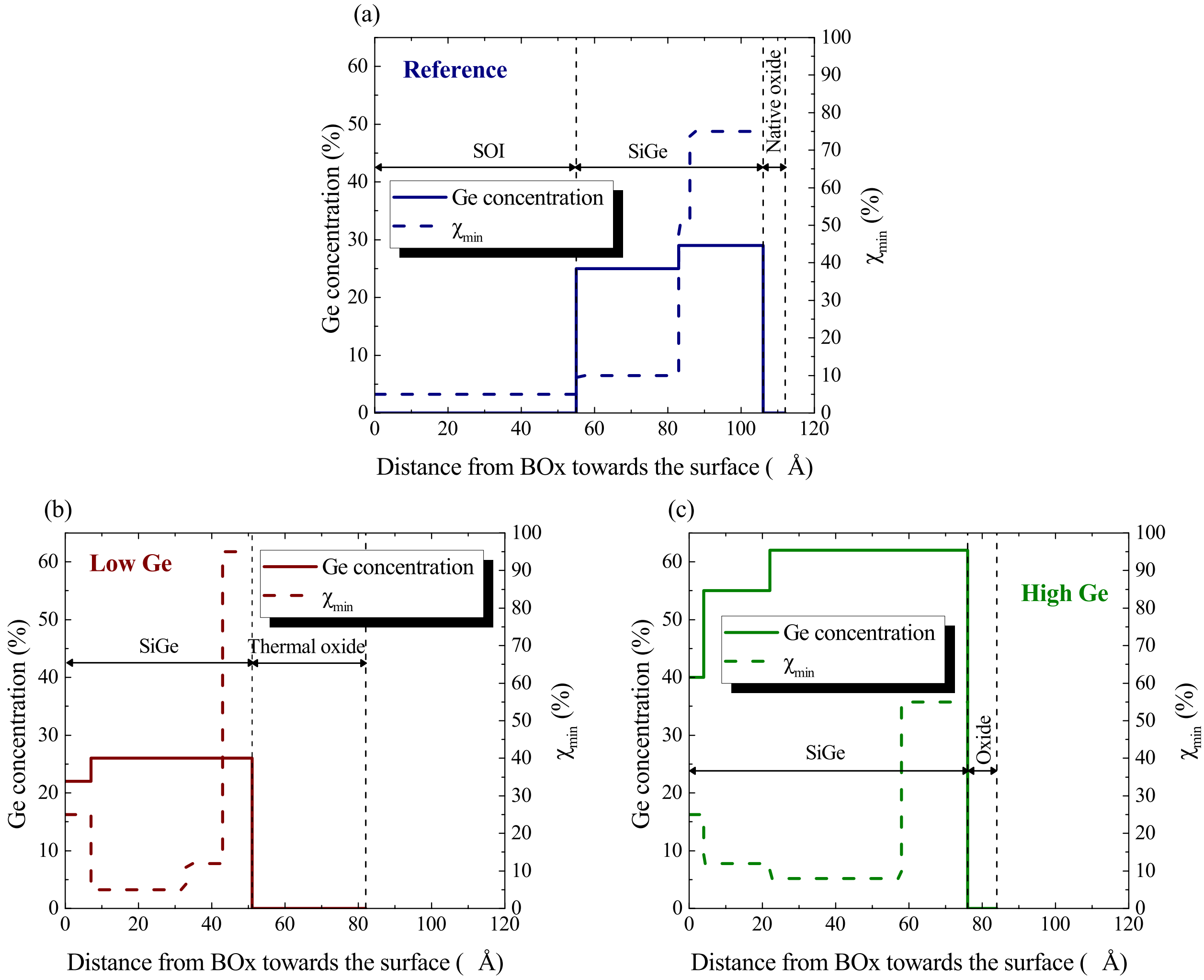

Figure IV.25: Ge concentration and χ_{min} *profiles extracted from random and channeling MEIS spectra. Profiles are plotted as a function of depth taking the BOx-SGOI interface as zero and the x axis towards the surface. (a) is for the "Reference" sample, (b) for the "Low Ge" one and (c) for the "High Ge" one.*

IV.A.5.5. Conclusion of Section IV.5.

We firstly discussed the composition profiles retrieved by the analysis of MEIS spectra. The composition of the SiGe films was found to be rather homogeneous. Then, the crystal quality of SGOI films, represented by χ_{min} factor which is the percentage of atoms displaced from lattice sites at a certain depth, was studied. Based on a schematic illustration, *Figure IV.26* summarizes the evolution of this crystal quality during condensation.

(a) **Reference**

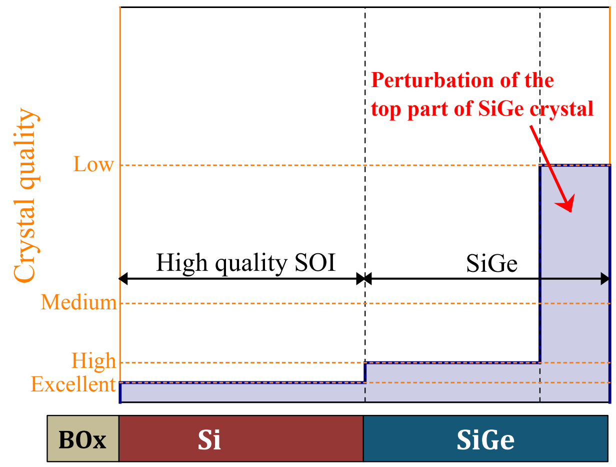
Perturbation of the top part of SiGe crystal
Crystal quality
Low
Medium
High
Excellent
High quality SOI
SiGe
BOx
Si
SiGe

- The SOI crystal quality is not altered by the SiGe epitaxy process.
- The SiGe crystal is degraded in the top 1-2 nm of the epitaxial SiGe layer.

(b) **After condensation - Ge% < 50%**

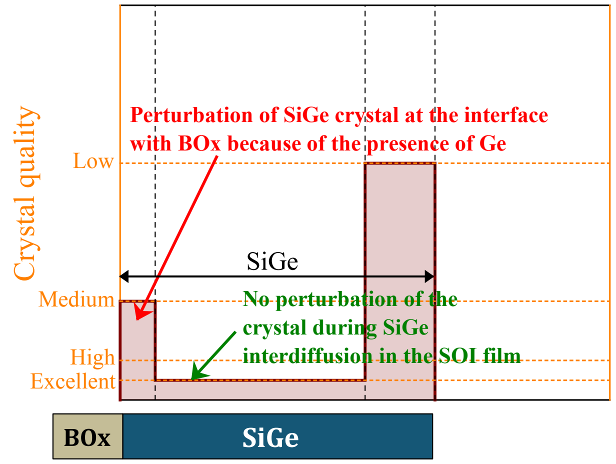
Perturbation of SiGe crystal at the interface with BOx because of the presence of Ge
Crystal quality
Low
Medium
High
Excellent
SiGe
No perturbation of the crystal during SiGe interdiffusion in the SOI film
BOx
SiGe

- Thermal oxidation may contribute to atomic rearrangement below the oxidation front and may tend to decrease the χ_{min} factor below it.
- The SOI crystal quality is not altered by SiGe diffusion for low Ge fraction SGOI layers.
- The presence of Ge, even at low fraction, seems to induce some crystal damage in the immediate vicinity of the SGOI-BOx interface.

(c) **After condensation - Ge% > 50%**

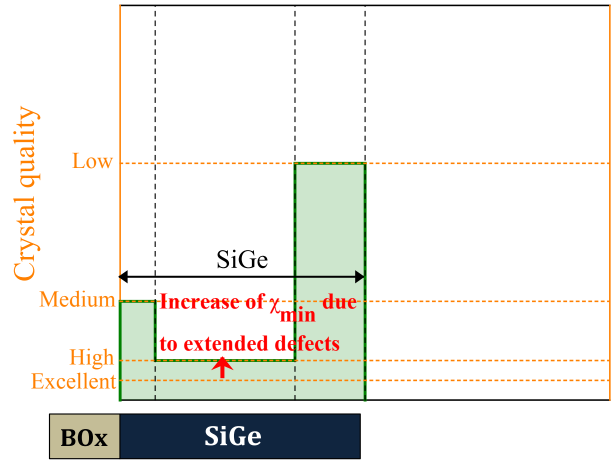
Crystal quality
Low
Medium
High
Excellent
SiGe
Increase of χmin due to extended defects
BOx
SiGe

- When the Ge concentration increases, the SiGe crystal quality starts to degrade, even far from interfaces with oxides.

Figure IV.26: Schematic illustration that summarizes the evolution of the amount of atoms displaced from lattice sites. (a) is for an epitaxial SiGe layer on SOI, (b) for a low Ge content SGOI film, and (c) for a high Ge content SGOI film. Key changes of the crystal quality from the epitaxial sample to the low Ge content SGOI film and finally to the high Ge content SGOI fims are indicated on the right side.

IV.A.6. Conclusion of Section IV.A.

We showed that strain of SGOI films fabricated by condensation based on high temperature dry RTO increases with the Ge concentration until a peak value of about 2.1% at 60% Ge concentration. We showed that the parameter that has the strongest influence on strain relaxation is the strain level and not the total elastic strain energy nor the Ge concentration and that strain relaxation is accompanied by formation of dislocations in {111} planes. Using Takagi et al. data for comparison [Takagi10], mechanisms of strain relaxation were discussed, and we emphasized that that the oxide-SiGe interfaces likely play a role in strain relaxation by hindering dislocations formation up to higher elastic strain values than at SiGe-Si interfaces. Low temperature condensation by means of ISSG oxidation was also performed but found to be not adequate for fabricating high Ge content fully strained SGOI films at the moment.

A finer characterization of the crystal quality as a function of depth into the SGOI film was performed by MEIS using the channeling effect. The evolution of the crystal quality of SGOI films during condensation is summarized in a few key points:

- The epitaxial SiGe crystal is already degraded in the top 1-2 nm.
- Thermal oxidation may contribute to atomic rearrangement below the oxidation front and may tend to decrease the χ_{min} factor below it.
- The SOI crystal quality is not altered by SiGe interdiffusion for low Ge fraction SGOI layers.
- After condensation, the presence of Ge, even at low fraction, seems to induce some crystal damage in the immediate vicinity of the SGOI-BOx interface.
- At high Ge concentrations (> 55%), the SiGe crystal quality starts to degrade, even far from interfaces with oxides.

IV.B. Strain Relaxation at the Edge of Active Areas

IV.B.1. Problem Definition

Strain of SGOI channels should be uniformly maintained in all pMOS active areas during fabrication of functional CMOS devices in order to fully benefit from the gain of strain on hole mobility. However, partial relaxation of the SGOI film at the frontier between pMOS active areas and Sallow Trench Isolation (STI) areas (see *Figure IV.27*) has been evidenced after the STI etch process step and shown to degrade electrical performances of transistors fabricated close to these frontiers [Andrieu16][Berthelon16]. It is crucial to understand and prevent as much as possible these effects as they induce a transistor performance dependency on chip design.

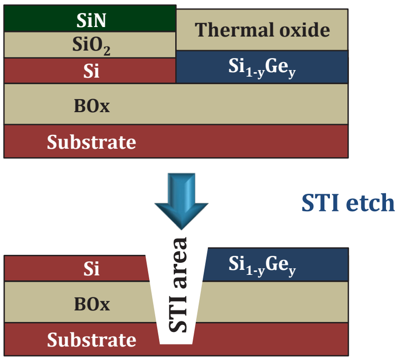

Figure IV.27: Integration of SGOI channels into pMOS active areas showing the STI etch process step after condensation. Intermediary process steps such as SiN film removal are not shown for clarity considerations.

SGOI strain profiles measured at the edge of active areas by Nano Beam Electron Diffraction (NBED) [Cooper16] and Dark Field Electron Hololography (DFEH – a strain characterization technique developed at CEMES laboratory [Hÿtch08]) were compared with FEM simulations based on the elastic theory [Boureau16]. As shown in *Figure IV.28*, the distance over which the SGOI film is partially relaxed after STI etch is much longer than the one predicted by the elastic theory. Usuda et al. also showed by Raman spectroscopy that relaxation of a SiGe film grown on Si agrees with the elastic theory while the SGOI films relaxation distance is longer [Usuda13].

Boureau showed that introducing a "sliding" mechanism at the thermal oxide-SGOI and BOx-SGOI interfaces in FEM simulation allows to reproduce experimental results (see *Figure IV.28*). As pointed out by Boureau, the agreement between the experimental results and simulations with the "sliding" mechanism suggests a special influence of the mechanical properties of the thermal oxide-SGOI and BOx-SiGe interfaces, even if it does not bring a physical meaning to the "sliding" mechanism. Usuda et al. also suggested that the BOx-SiGe interface may have mechanical properties that differ from the ones of the elastic theory.

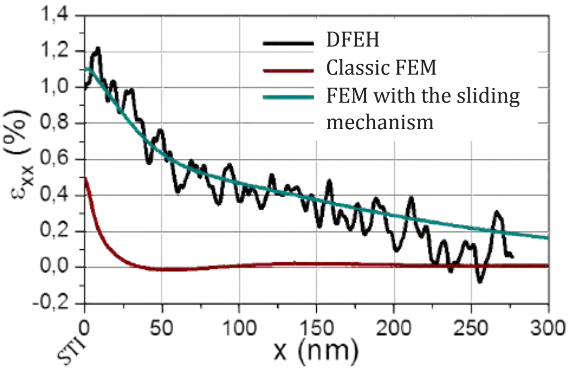

Figure IV.28: In-plane deformation measured by DFEH along with FEM simulations based on the elastic theory only, reffered as "classic FEM", and on the elastic theory with a sliding mechanism introduced at the SGOI-thermal oxide and SGOI-BOx interfaces, referred to as "FEM with the sliding mechanism". The standard condensation process was performed at 1100°C. Adapted from [Boureau16].

The condensation process allows fabrication of the SGOI film before the STI etch process step, and may alter the mechanical properties of the interfaces of the SGOI film with the thermal oxide and the BOx film. In *Section IV.B.*, we thus try to correlate the strain relaxation experimental results with the condensation process conditions and with the properties of the SGOI film and of its interfaces with the thermal oxide and the BOx layer. We identified two possible causes for this strain relaxation phenomenon and performed dedicated experiments to study them. They are presented in *Section IV.B.2.* and *Section IV.B.3.* respectively.

IV.B.2. Chemical Bonding at the SGOI-BOx interface Investigated by XPS

IV.B.2.1. Introduction

In this section, we investigate the chemical bonds at the SGOI-BOx interface, which then influence the mechanical properties of the interface. Kim et al. and Suh et al. mentioned that Ge-O bonds are weaker than Si-O bonds [Kim17][Suh16]. The presence of Ge-O bonds could induce weaker mechanical properties at the SiGe-oxide interface and account for the "sliding" mechanism suggested by Boureau [Boureau16]. No Ge-O bonds were evidenced at the SiGe-thermal oxide interface (see *Section III.A.3.*). However, the SiGe-BOx interface may be different from the top SiGe-thermal oxide interface because of different formation processes. The SGOI-thermal oxide one is the oxidation interface while the SGOI-BOx one is modified by diffusion of Ge atoms in its vicinity. We thus decided to investigate the chemical bonding properties of the SiGe-BOx interface by XPS. This study required a specific specimen preparation which is detailed into the next section.

IV.B.2.2. Experimental

Three specimens were studied:

- "Reference": a SOI substrate was oxidized by means of dry furnace oxidation at 900°C. This oxidation process is systematically performed prior to the oxide removal-SiGe epitaxy-condensation sequence. We chose to perform this process to discriminate the effect of the condensation process on the evolution of the chemical bonding at the SGOI-BOx interface from the effects of the inital oxidation process of the SOI substrate.
- "SGOI 1100°C": this sample is close to the standard condensation process and is known to suffer from the problem of strain relaxation at the edge of active areas. After epitaxial growth of SiGe on SOI, condensation was performed by means of dry RTO at 1100°C. An anneal in inert environment was performed in the same equipment at 1100°C for one minute to fully homogenize the SGOI film between the thermal oxide and the BOx layer. The final SGOI Ge concentration is about 25%.
- "SGOI 900°C annealed": a SiGe film was epitaxially grown on a SOI substrate and condensation was performed by means of dry RTO at 900°C. A furnace anneal in inert atmosphere for 8 hours at 900°C was then performed to fully homogenize the SGOI layer. This sample was fabricated in order to discriminate the effect of a lower oxidation temperature on chemical bonding at the SGOI-BOx interface. SiO_2 has been shown to be subjet to viscous flow at temperatures as low as 960°C, so that we decided to perform condensation below 960°C to discriminate the effect of viscous flow on strain relaxation [EerNisse77]. The final SGOI Ge concentration is also about 25%.

Then, the specimens were prepared for XPS measurements by the sequence described in *Figure IV.29*.

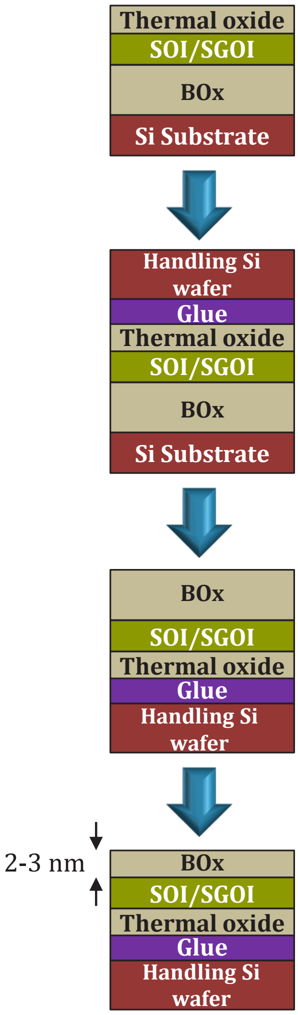

Bonding to a handling Si wafer

The multilayer system is returned and the Si substrate is removed by polishing and chemical etching

The BOx layer is thinned down until only 2-3 nm are left in order to preserve the BOx-SGOI interface from being modified by the chemical treatment

Figure IV.29: Schematic view of specimens preparation.

The chemical etching of Si was performed using Tetramethylammonium hydroxide (TMAH) and thinning of the BOx layer using HF solution. The HF etching process was calibrated on a dedicated sample and the residual BOx thickness was measured by ellipsometry.

IV.B.2.3. Ge-O Bonding

Figure IV.30 shows the experimental Ge3d and Ge2p XPS spectra of the two SGOI samples along with fitted peaks. During the photoelectron emission process, a part of the energy of the incoming X-Ray photons is transferred to the emitted electron as kinetic energy. The kinetic energy of electrons ejected from the Ge2p orbital is lower than the one of electrons ejected from the Ge3d spectrum (see also *Section II.3.3.* for a more detailed description of the XPS technique). As a consequence, the probing depth of the Ge2p spectrum is lower than the one of the Ge3d one (2.5 nm and 8.3 nm for the Ge2p and Ge3d orbitals respectively at a collection angle of 45°).

No Ge oxide peak is evidenced on any XPS spectrum except on the Ge2p spectrum of the "SGOI 1100°C" sample. The peak is very weak and no Ge oxide is evidenced on the Ge3d spectrum of the same sample. The Ge2p spectrum has a lower probing depth than the Ge3d one, which results in a lower contribution of metallic Ge atoms of the SGOI layer to the spectrum. The Ge oxide peak is therefore likely too weak to emerge from the foot of the metallic Ge peak on the Ge3d spectrum. As for the origin of this small amount of Ge oxides, we noticed that a first specimen preparation led to complete oxidation of Ge, most likely due to the chemical oxidation during BOx thinning. The small amount of Ge oxides observed on the Ge2p spectrum of the "SGOI 1100°C" sample might be due to the sample preparation.

We conclude on the absence of a noticeable quantity of Ge-O bonds at the SGOI-BOx interface for both investigated oxidation temperatures.

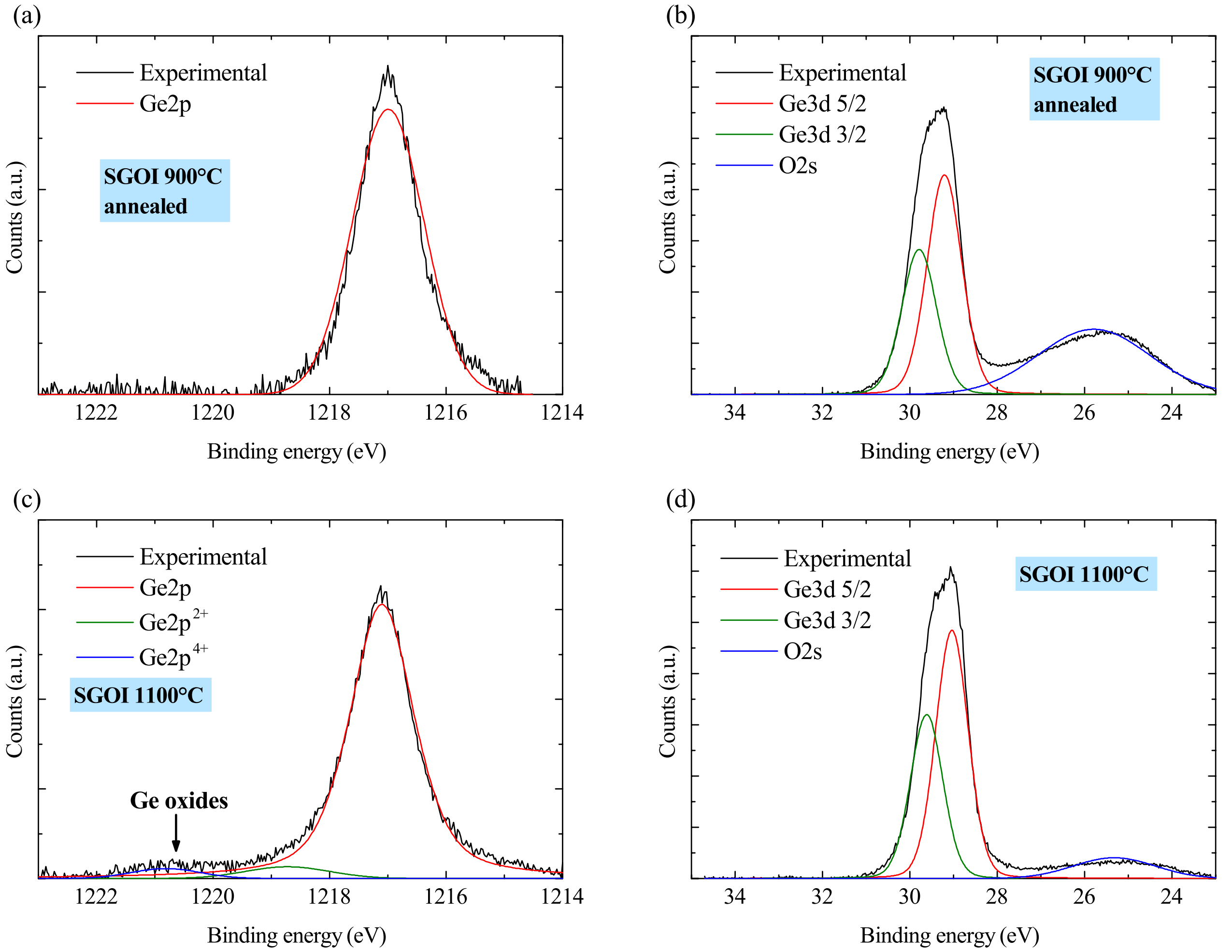

Figure IV.30: (a) Ge2p spectrum of "SGOI 900°C", (b) Ge3d spectrum of "SGOI 900°C annealed", (c) Ge2p spectrum of "SGOI 1100°C", and (d) Ge3d spectrum of "SGOI 1100°C".

IV.B.2.4. Si-O Bonding

We also seeked to compare the amount of Si sub-oxides at the SOI/SGOI-BOx interfaces, as a high amount of Si sub-oxides may be associated with a graded and/or a perturbed interface.

Experimental and fitted Si2p spectra are shown *Figure IV.31*. Neither precise evaluation of the quantity of Si sub-oxides nor reconstruction of depth profiles of each oxidation state is possible with a single XPS spectrum (see *Section II.3.3.* about the reconstruction of concentration depth profiles by Parallel Angle-Resolved XPS). Direct comparisons of peak areas is also difficult because of the varying oxide thicknesses from one sample to another one. We can reasonably assume that Si sub-oxides are sandwiched between a residual SiO_2 film and the SGOI/SOI film. In this case, the SiO_2 layer is on top of the multilayer system and its residual thickness can be evaluated by comparing Si^{4+} peak areas. The "SOI" and "SGOI 900°C annealed" have more similar residual SiO_2 thicknesses while the "SGOI 1100°C" has a lower SiO_2 residual thickness. We can reasonably give a direct comparison of the Si sub-oxides peak areas of the "SOI" and "SGOI 900°C annealed" samples. There is a higher amount of Si sub-oxides, especially Si^{3+}, for the case of the "SGOI 900°C annealed" sample than for the "SOI" one.

A semi-quantitative comparison of sub-oxide quantities with the "SGOI 1100°C" is now described. The "SGOI 900°C annealed" sample has a thicker SiO_2 residual film than the "SGOI 1100°C". It results in Si metallic atoms to be deeper and to have a lower contribution to the total spectrum for the "SGOI 900°C annealed" sample. Therefore, the "SGOI 900°C annealed" peak has a higher Si^{4+} peak area and a lower metallic Si peak area than the "SGOI 1100°C" sample. As a consequence, we suggest that the sum of the metallic Si peak area with the one of the Si^{4+} is rather similar in all three samples. The fact that the residual SiO_2 film is thicker also induces the sub-oxide peak area to be lower. However, we believe that the ratio of the total Si sub-oxides peak area to the one of the sum of the Si^{4+} and metallic Si can be considered a trend indicator of the total Si sub-oxide quantity. These ratio are 7%, 19% and 16% for the "SOI", "SGOI 900°C annealed" and "SGOI 1100°C" samples respectively. There is more Si sub-oxides in the "SGOI 900°C annealed" sample than in the "SOI" one in agreement with the first qualitative comparison made in the former paragraph. There seems to be roughly the same quantity of Si sub-oxides in the "SGOI 1100°C" sample as in the "SGOI 900°C annealed" one.

To summarize, the SGOI-BOx interface fabricated by condensation has more Si sub-oxides than the SOI-BOx. one.

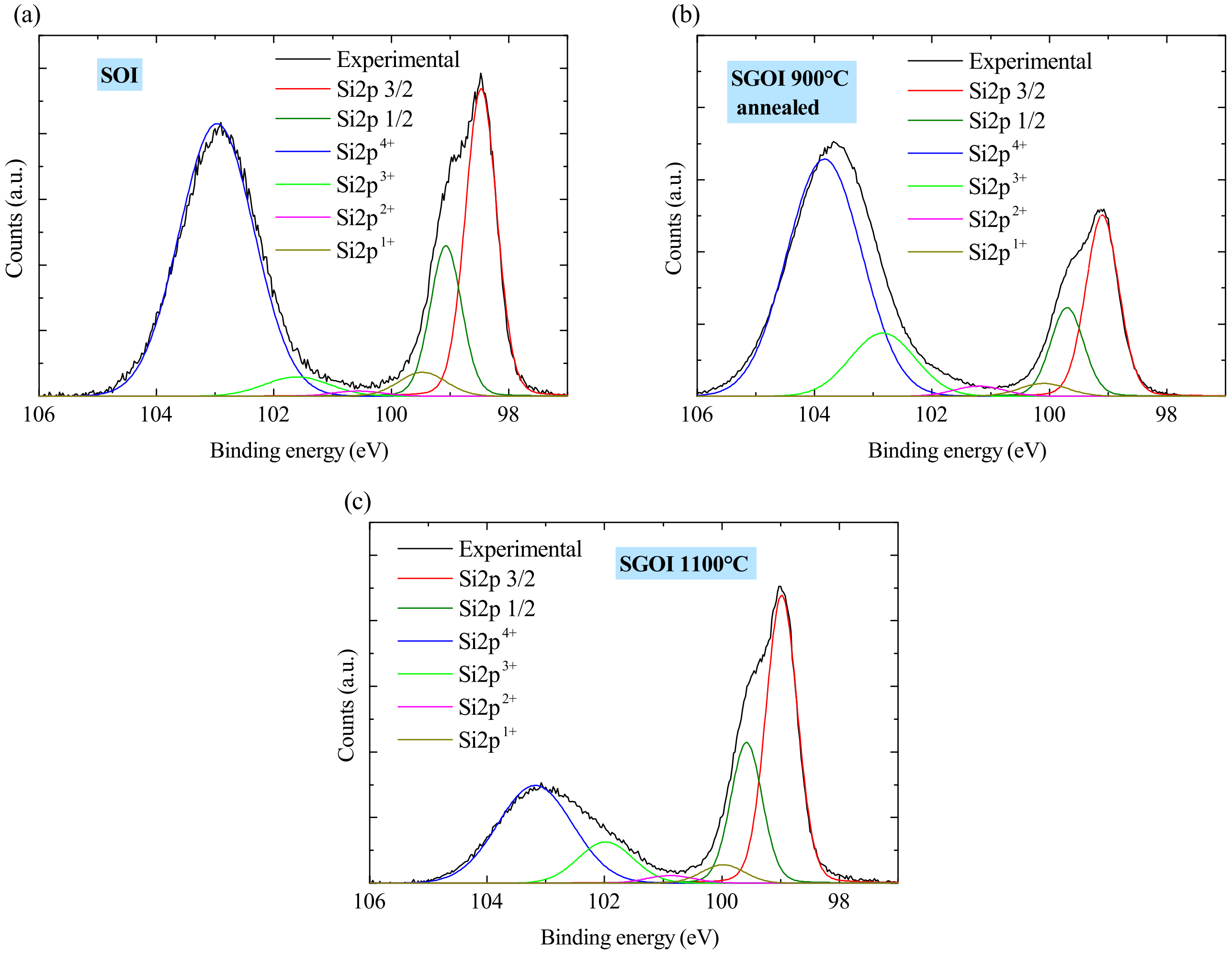

Figure IV.31: Si2p spectra of the (a) "SOI"*, (b) of the* "*SGOI 900°C annealed*"*, and (c) of the* "*SGOI 1100°C*"*.*

IV.B.2.5. Conclusion of Section IV.B.2.

A dedicated specimen preparation has been developed in order to study chemical bonding at the SGOI/SOI-BOx interface by XPS. It was firstly shown that there is no noticeable quantity of Ge-O bonds at the SGOI-BOx interface. It rules out weakened mechanical properties due to soft Ge-O bonds as a possible cause of the anomalous strain relaxation phenomenon described in *Section IV.B.1.*.

Then, a higher quantity of Si sub-oxides has been evidenced after condensation. LeGoues et al. and Kilpatrick et al. found that the SiGe-thermal SiO_2 interface has more Si atoms in intermediate oxidation states than the Si-thermal SiO_2 interface and that the higher the Ge concentration is, the higher this amount is [LeGoues89'] [Kilpatrick08]. It shows that even if the SOI-BOx interface is not the oxidation interface, diffusion of Ge atoms in the vicinity of the BOx film also raises the amount of Si sub-oxides.

We suggest that if there are Ge atoms in the last complete crystal monolayer at the interface with the BOx film, then there are less Si atoms in the last monolayer, and as a result less bonds between Si atoms of the SiGe crystal and Si and O atoms of the BOx film. This limited amount of bonds between the Si atoms of the SiGe crystal and the BOx film seems consistent with a higher amount of Si sub-oxides, even if atomic scale models of the SiGe-oxide interface are required to further confirm these results.

We showed by MEIS that the SiGe crystal is degraded at the interface with the BOx layer (see *Section IV.A.5.4.*)

and Afanas' ev et al. showed that there is a high amount of Ge dangling bonds at the SiGe-oxide interface [Afanas' ev09]. If they are Ge atoms in the last complete crystal monolayer at the interface with the BOx film, and if these Ge atoms are not bonded to any O atom of the BOx film as shown by XPS, Ge dangling bonds are indeed expected. As soon as they are dangling bonds in the crystal, some local bonds may be strained and atoms displaced from their expected lattice sites to compensate these dangling bonds in terms of total energy. In other words, come crystal disorder is expected in the vicinity of the interface with the BOx layer.

IV.B.3. Measurement of Hydrogen Concentration by Neutron Reflectivity Coupled with XRR

IV.B.3.1. Introduction

Segura-Ruiz et al. coupled XRR with neutron reflectivity to evidence the presence of hydrogen accumulation at the interface between a SiO_2 film and an amorphous carbon film [Segura15]. They showed that this H accumulation is correlated with higher local strain and hence a greater susceptibility to a mechanical weakness of the interface. As H is present in SiGe epitaxy processes (see *Section II.1.*), it was suggested that H might be incorporated into the SiGe-SOI-BOx stack during SiGe epitaxy and that it is accumulated at thermal oxide-SGOI and SGOI-BOx interfaces after condensation. This H accumulation could then weaken the mechanical properties of these interfaces and cause strain relaxation at the edge of active areas.

H is difficult to detect. Especially, H is too light to significantly influence the mass density of SiGe and SiO_2 films, so that it cannot be detected by XRR experiments. H background levels in SIMS measurements are too high to measure H concentrations below 10^{19} atoms.cm^{-3}, which is much higher than what can be expected in thin semiconductor films. However, as explained in *Section II.4.2.2.*, as opposed to O, Si and Ge elements, H has a strong negative neutron scattering length, which makes neutron reflectivity experiments very sensitive to its presence. As will be detailed in *Section IV.B.3.3.*, H concentration cannot be determined based solely on neutron reflectivity experiments, but must be coupled with at least another technique. We coupled neutron reflectivity experiments with XRR to measure H concentrations in three representative samples.

Experimental details on samples, neutron reflectivity and XRR are presented into the next section and results are shown and discussed in *Section IV.B.3.3.*.

IV.B.3.2. Experimental

Three specimens were studied and are illustrated *Figure IV.32*:

- "Reference epi": a SOI substrate was firstly oxidized by means of dry furnace oxidation at 900°C, and then a standard SiGe epitaxy process was performed (see *Section II.1.*).
- "SGOI 1100°C": this sample is the same as the one presented in *Section IV.B.2.2.*. This sample is close to the standard condensation process and is known to suffer from the problem of strain relaxation at the edge of active areas. After epitaxial growth of SiGe on SOI, condensation was performed by means of dry RTO at 1100°C. An anneal in inert environment was performed in the same equipment at 1100°C for one minute to fully homogenize the composition of the SGOI film between the thermal oxide and the BOx layer.
- "SGOI 900°C": a SiGe film was epitaxially grown on a SOI substrate and condensation was performed by means of dry RTO at 900°C. There is no or hardly any Ge at the interface with the BOx film while there is a high Ge concentration at the oxidation interface (about 45%) due to the low oxidation temperature (see *Section III.A.4.3.*). This sample was chosen because it was suggested that H might accumulate at oxide-SiGe interfaces only and not at oxide-Si ones.

Each specimen was characterized with XRR to measure the mass density of each layer and with neutron reflectivity to measure the neutron scattering length density of each layer.

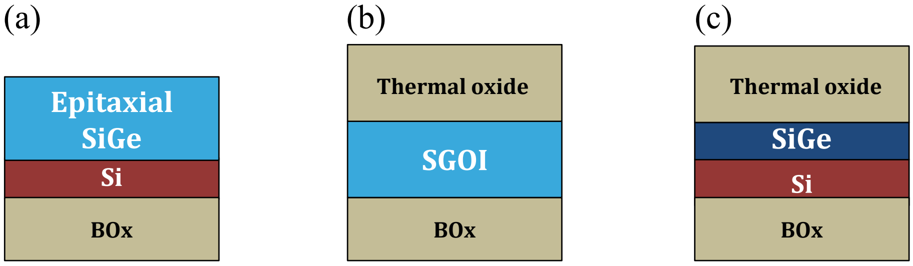

Figure IV.32: Schematic representation of (a) "Reference epi", (b) "SGOI 1100°C" and (c) "SGOI 900°C" samples.

IV.B.3.3. Results

Figure IV.33 shows experimental and fitted XRR and neutron reflectivity spectra of all samples. While the composition of oxides was assumed to be SiO_2 for fitting XRR spectra, fitting neutron reflectivity spectra with neutron scattering length densities does not require any assumption on the composition of the films. For neutron reflectivity, we only assumed a limited number of homogeneous layers. High fit qualities are obtained using the following models:

- "Reference epi": native oxide (assumed to be SiO_2) on top of a homogeneous SiGe film on a SOI substrate. A four layers model was used for neutrons (corresponding to a SiGe-SOI-SiO_2-Si substrate stack ; we indeed noticed that neutron reflectivity spectra are not sensitive to layers as thin as native oxides).
- "SGOI 1100°C": SiO_2 oxide on top of a SGOI film on the BOx layer. A four layers model was used for neutron reflectivity corresponding to a SiO_2-SGOI-SiO_2-Si substrate stack.
- "SGOI 900°C": a SiO_2-SiGe-Si-BOx-Si substrate model was used. A five layers model was used for neutron reflectivity corresponding to the same SiO_2-SiGe-Si-BOx-Si substrate stack.

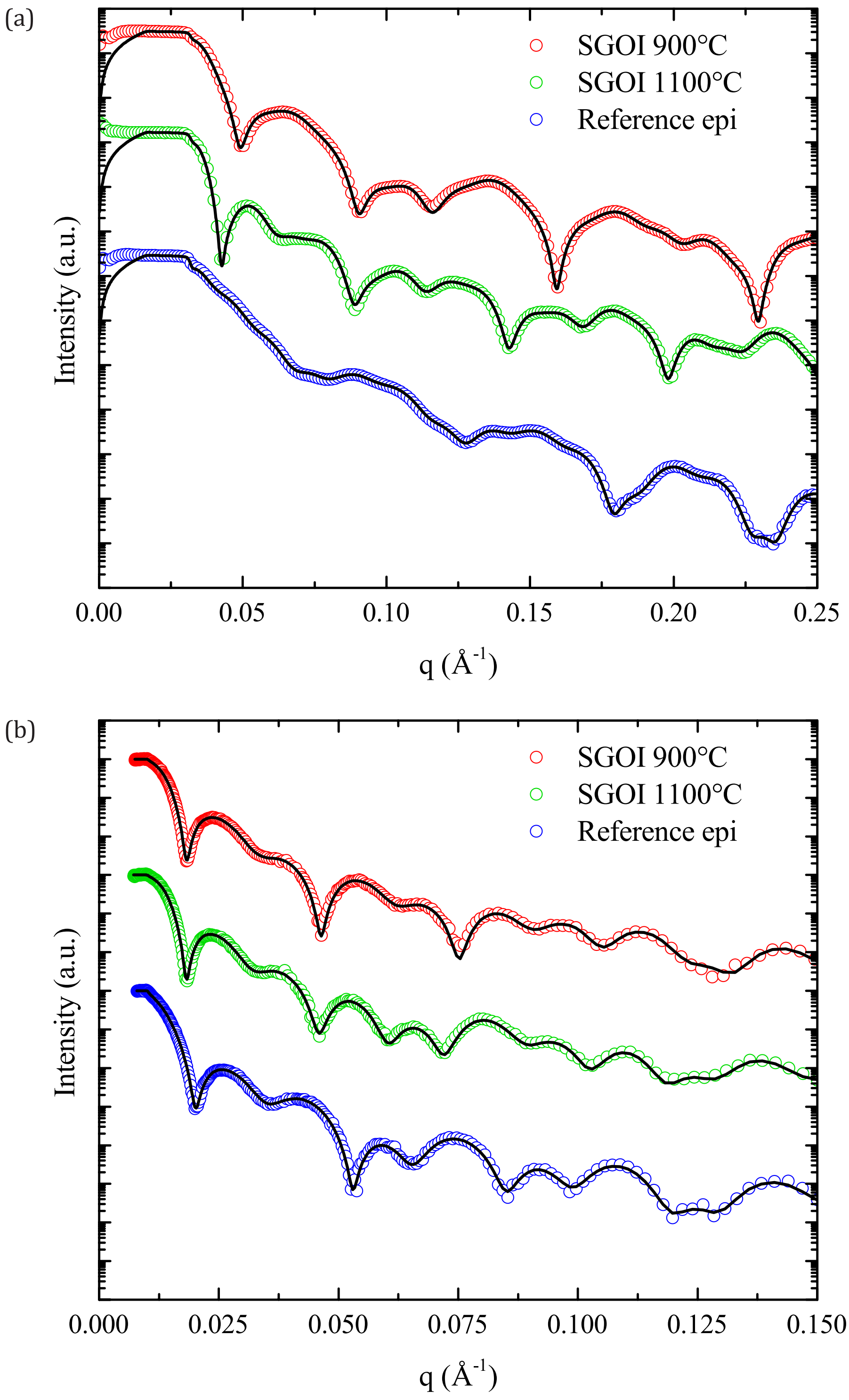

Figure IV.33: (a) XRR experimental and fitted spectra and (b) neutron reflectivity experimental and fitted spectra.

Mass densities determined by fitting XRR data and neutron scattering length densities determined by fitting neutron reflectivity data are shown *Table IV.2* and *Table IV.3* respectively. Mass densities of all SiGe and SiO_2 layers measured by XRR were found to be in good agreement with theoretical ones (SiGe mass densities can be calculated according to Poisson theory, as described in *Section I.2.2.3.* and SiO_2 mass densities are discussed in details in *Section III.A.5.*)

XRR		Reference epi	SGOI 1100°C	SGOI 900°C
Mass density (g.cm^{-3})	Thermal oxide		2.17	2.25
	SiGe top	3.24		3.78
	SOI/Si	2.27		2.23
	SGOI		2.97	
	BOx	2.21	2.20	2.23

Table IV.2: Mass densities determined by fitting XRR data.

Neutron reflectivity		Reference epi	SGOI 1100°C	SGOI 900°C
Scattering length density (×10^{-6} Å^{-2})	Thermal oxide		3.66	3.77
	SiGe top	2.68		2.92
	SOI/Si	2.07		2.06
	SGOI		2.53	
	BOx	3.51	3.53	3.53

Table IV.3: Neutron scattering length densities determined by fitting neutron reflectivity data.

On the first approach, we will assume that there is no H in any sample and that all layers are either $Si_{1-x}Ge_x$ or SiO_2 films, and see if measured neutron scattering length densities agree with predictions. The neutron scattering length densities of $Si_{1-x}Ge_x$ or SiO_2 are [Daillant08]:

$$SLD_{Si_{1-x}Ge_x} = N_A \rho \frac{(1-x) b_{Si} + x b_{Ge}}{(1-x) M_{Si} + x M_{Ge}} \qquad \textbf{\textit{Equation IV.6}}$$

$$SLD_{SiO_2} = N_A \rho \frac{b_{Si} + 2 b_O}{M_{Si} + 2 M_{Ge}}, \qquad \textbf{\textit{Equation IV.7}}$$

where N_A, ρ, b_O, b_{Si}, b_{Ge}, M_O, M_{Si}, M_{Ge} and x are the Avogadro number, the mass density of either $Si_{1-x}Ge_x$ or SiO_2, the scattering lengths of O, Si and Ge, the molar masses of O, Si and Ge and the Ge content.

Table IV.4 compares the measured SiGe SLDs with the theoretical ones calculated according to *Equation IV.6* and taking as input the measured SiGe mass density. The Ge content x of *Equation IV.6* is calculated according to Poisson theory (see *Section I.2.2.3.*) and oxides are assumed to be stoichiometric SiO_2. We observe that the measured SLD is systematically higher than the calculated one from XRR results. H has a negative scattering length so the presence of H in any of these layers could only decrease the measured SLD below the SLD calculated from XRR, as opposed to what is observed. Therefore, there is neither H after SiGe epitaxy nor after condensation.

		Reference epi	SGOI 1100°C	SGOI 900°C
Thermal oxide	Measured SLD ($\times10^{-6}$ Å^{-2})		3.66	3.77
	SLD calculated from XRR results ($\times10^{-6}$ Å^{-2})		3.43	3.55
SiGe	Measured SLD ($\times10^{-6}$ Å^{-2})	2.68	2.53	2.92
	SLD calculated from XRR results ($\times10^{-6}$ Å^{-2})	2.56	2.41	2.84
Si	Measured SLD ($\times10^{-6}$ Å^{-2})	2.27		2.23
	SLD calculated from XRR results ($\times10^{-6}$ Å^{-2})	2.02		1.98
BOx	Measured SLD ($\times10^{-6}$ Å^{-2})	3.51	3.53	3.53
	SLD calculated from XRR results ($\times10^{-6}$ Å^{-2})	3.49	3.47	3.52

Table IV.4: Measured SLDs and SLDs calculated from XRR results.

Differences between measured and calculated SLDs are indicated in *Table IV.5*. Interestingly, we observe that the differences are similar between the three different samples for the same layer. It is quite low for the BOx film (between 0.01×10^{-6} Å^{-2} and 0.06×10^{-6} Å^{-2}) while it is about 0.22×10^{-6} Å^{-2} and 0.25×10^{-6} Å^{-2} for the thermal oxide and the Si layer respectively. To explain this discrepancy, it was suggested that there might be another element at low concentrations in the SiGe film which has a scattering length high enough to significantly raise the scattering length density. Among the elements that have high positive scattering lengths (see *Section II.4.2.2.*) and that are present in processes performed to fabricate the samples, O and Cl are the only candidates. Cl is used in SiGe epitaxy processes (see *Section II.1.*), and there is always a more or less important O residual partial pressure in all semiconductor processes. *Figure IV.34* shows ToF-SIMS measurements of O and Cl concentrations in the "Reference epi" sample. The concentrations of both elements in the SiGe films are below the detection limit (< 0.1% concentration) hence well below levels that could raise the scattering length density of more than 0.1×10^{-6} Å^{-2}.

Measured SLD - SLD calculated from XRR ($\times10^{-6}$ Å^{-2})	Reference epi	SGOI 1100°C	SGOI 900°C
Thermal oxide	0.23	0.22	
SiGe	0.12	0.12	0.08
Si	0.25		0.25
BOx	0.02	0.06	0.01

Table IV.5: Difference betwenn measured SLD and SLD calculated from XRR results.

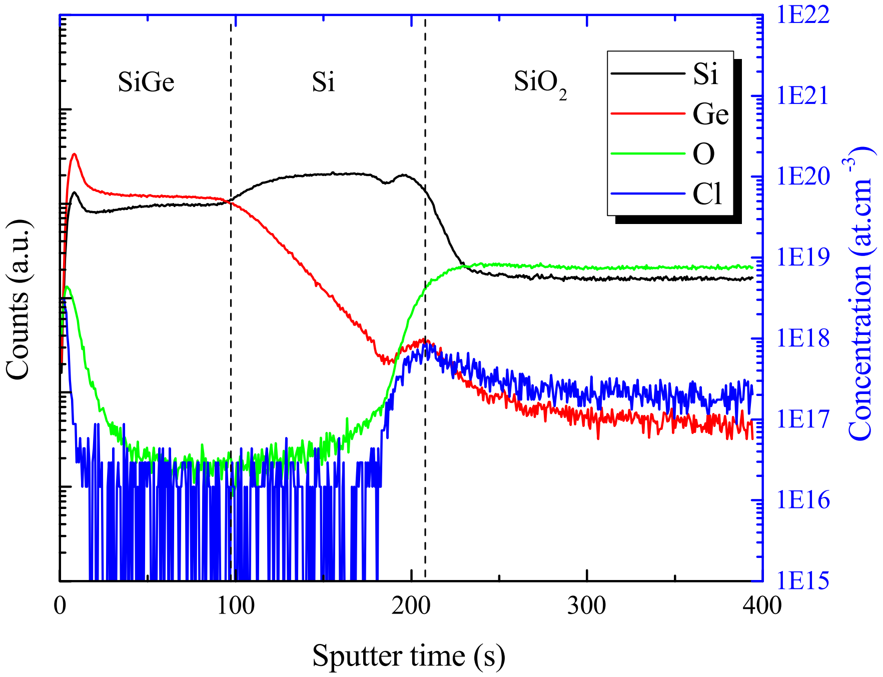

Figure IV.34: Si, Ge and O arbitrary concentration levels and Cl absolute concentration measured by ToF-SIMS in the "Reference epi" sample.

IV.B.3.4. Conclusion of Section IV.B.3.

We performed neutron reflectivity coupled with XRR to measure H concentrations in three representative samples. We showed that there is neither H after SiGe epitaxy on SOI substrates nor after condensation. To conclude, H is not the cause of strain relaxation of SGOI films after STI etch.

We observed that the measured scattering length density of SiGe films is systematically higher than the one calculated from XRR measurements. O and Cl presence in SiGe to explain this higher scattering length density has been dismissed by ToF-SIMS measurements. Further investigation is required to understand the anomalously high scattering length density of SiGe and thermal oxide films.

Conclusion of Chapter IV

In this chapter, we firstly studied strain levels and crystal qualities of SGOI films fabricated by various condensation processes based on dry RTO and ISSG oxidation.

We firstly discussed strain levels of SGOI films fabricated by condensation based on high temperature dry RTO and ISSG oxidation. We showed that in the case of SGOI films in the 10 nm thickness range, the parameter that has the strongest influence on strain relaxation is the strain level and not the total elastic strain energy nor the Ge concentration. In terms of strain relaxation mechanisms, we suggested that if strain relaxation is governed by strain energy balance, this balance is influenced by the nature of the underlying layer: a thermal oxide (BOx) for the case of SGOI films instead of crystalline Si for the case of epitaxial SiGe-Si systems. We also suggested that dislocation nucleation at SiGe-oxide interfaces may be hindered up to higher elastic strain values than at SiGe-Si interfaces. Low temperature condensation by means of ISSG oxidation was also performed but found to be not adequate for fabricating high Ge content fully strained SGOI films at the moment.

For technology applications, we highlight that the best condensation process that we studied is dry RTO at high temperature, with a threshold value of more than 2% for SGOI films in the 10 nm thickness range. Such a strain value corresponds to a Ge concentration of about 60%.

A finer characterization of the crystal quality as a function of depth into the SGOI film was performed by MEIS. Unfortunately, we cannot discuss optimization of the condensation process in terms of SGOI crystal quality with the characterization of three samples only. However, two conclusions can be drawn:

- The key crystal areas that are degraded and that must be particularly looked at for optimization of the condensation process are the interfaces of SiGe with oxides.
- The SOI crystal quality is not altered by SiGe interdiffusion for low Ge fraction SGOI layers, except when the Ge concentration increases above about 55%.

In the second part of this chapter, it was shown that the SGOI film is partially relaxed after the STI etch process step at the frontier between pMOS active areas and STI areas. Two possible causes to this strain relaxation phenomenon, and related to the condensation process, were suggested and investigated:

- The presence of Ge-O bonds at oxide-SGOI interfaces was thought to weaken the mechanical properties of oxide-SGOI interfaces and to cause a "sliding" mechanism of the SGOI film. We found that there is no noticeable quantity of Ge-O bonds at the SGOI-BOx interface and thus ruled out that proposition. Nevertheless, we observed a higher quantity of Si sub-oxides at the BOx-SGOI interface after condensation and discussed it in view of the crystal disorder evidenced by MEIS.
- H accumulation at SGOI-oxide interfaces was though to possibly induce mechanical weakness of the interfaces. By coupling neutron reflectivity with XRR, we found that there is neither H after SiGe epitaxy on SOI substrates not after condensation. To conclude, H is not the cause of strain relaxation of SGOI films after STI etch.

In summary, we ruled out two possible causes of the strain relaxation phenomenon and further investigation is therefore required to identify the cause of the strain relaxation mechanism.

Conclusion

The demand for higher speed and lower power consumption Integrated Circuits (ICs) has roused much interest into techniques that offer higher electron and hole mobility into channels of MOSFETs. Thanks to its high hole mobility, compressively strained SiGe is one of the most promising candidates for p-type MOSFET channel material. Moreover, advantages of strained SiGe in terms of hole mobility can be combined with the benefits of On Insulator (OI) structures, i.e., lower leakage current and better electrostatic control of the channel. Therefore, fabrication of SGOI structures may be a key milestone in enhancing performances of pMOSFETs. SGOI layers can be fabricated by the condensation technique. However, several challenges still need to be taken up for an efficient and optimized use of the condensation technique in an industrial environment. In order to complete these challenges, this thesis strived to bring understanding about thermal oxidation of SiGe, upon which the condensation technique is based, and solutions for optimizing the condensation process itself.

Chapter I has described the context, the theoretical and technological underpinnings of this thesis work. More precisely, the MOSFET technology has been introduced and its limitations to further downsizing have been described. New transistor architectures and high mobility channels, two main paths for enhancement of transistor performances, were reviewed. Among these performance "boosters", the benefits of using compressively strained SGOI films as channel material for p-type MOSFETs were presented. Specificities of the condensation technique, which allows the fabrication of SGOI films with possibly high strain levels, were described. Finally, the two main challenges of this thesis, which are addressed in *Chapter III* and *Chapter IV*, were defined:

- Understanding and controlling the mechanisms and kinetics of thermal oxidation of SiGe.

- Fabricating highly strained and high crystal quality SGOI films by the condensation technique.

Chapter II has reviewed the various processes, characterization techniques and the simulation tool used during this work. Techniques I personally used, either for the measurement and/or the analysis, were described in *Chapter II* while the other ones are presented in Appendices. Processes to fabricate samples, with a focus on the thermal oxidation processes used in this work, i.e. dry furnace oxidation, dry Rapid Thermal Oxidation (RTO) and In-Situ Steam Generation (ISSG) oxidation, were firstly presented. Then, characterization techniques using equipment considered as "common" equipment were reviewed: ellipsometry and XRR for thickness measurement, XPS for studying the chemical composition of thermal oxides grown on SiGe, Raman spectroscopy for measurement of strain of SGOI films, and GPA of HRTEM images for measurement of strain levels as well as for revealing crystal defects. Techniques that required the use of large-scale facilities were also reviewed: XRR experiments performed on SEXTANTS beamline at Soleil synchrotron in order to measure the density of thermal oxides, neutron reflectivity to identify whether or not there is hydrogen in SGOI films, and finally MEIS experiments to study the depth distribution of crystal perturbations and defects in SGOI films. This chapter ended with a description of the FEM and the environment of the developed simulation tool.

In the first part of *Chapter III* (*Section III.A*), an in-depth study of the mechanisms and kinetics of SiGe oxidations by means of three technology-relevant processes was carried out.

It was shown that, except possibly during the very first stages of oxidation (the temperature ramp up), the composition of oxides grown on SiGe is pure SiO_2 for all investigated oxidation processes, in agreement with thermodynamic calculations.

Then, we showed that oxidation of SiGe by means of dry furnace oxidation, dry RTO and ISSG oxidation is limited by diffusion of the oxidizing species through the growing oxide. A factor called Growth Rate Enhancement (GRE) was then defined to quantitatively compare the oxidation rates of Si and SiGe. We found that the GRE, and consequently oxidation kinetics, is correlated with the oxide density via the modulation of O_2 diffusivity. The influence of the process parameters on the oxide density, and as a result on oxidation kinetics, was finally clarified: the oxide density decreases when the oxidation temperature and the Ge concentration at the oxidation interface increase. Finally, we proposed a model of O_2 diffusivity that depends on the oxide density through the modulation of the diffusion barrier and which is consistent with our experimental data.

In the second part of this chapter (*Section III.B*), two technological applications based on the former results were presented. The first one is a graphic assessment of the oxide thickness and of the Ge diffusion length in SiGe, a key parameter of the evolution of the SiGe composition during oxidation, as a function of process parameters. The tool compares the relative importance of the Ge pile-up mechanism caused by the Si-selective oxidation with respect to SiGe interdiffusion. And secondly, a numerical simulation tool of thermal oxidation was adapted from the one of Morin et al. [Morin15]. The simulation model proved its worth in bringing more understanding of the dynamics of SiGe oxidation in spite of some remaining discrepancies with experimental data.

High strain levels and high crystal quality of SGOI films are needed for increasing the hole mobility. We thus compared in the first part of *Chapter IV* (*Section IV.A*) strain levels and crystal qualities of SGOI films fabricated by two industry-compatible condensation processes.

We firstly discussed strain levels of SGOI films fabricated by condensation based on high temperature dry RTO and ISSG oxidaion. We showed that in the case of SGOI films in the 10 nm thickness range, the parameter that has the strongest influence on strain relaxation is the strain level and not the total elastic strain energy nor the Ge concentration. Low temperature condensation by means of ISSG oxidation was also performed but found to be not adequate for fabricating high Ge content fully strained SGOI films. For technology applications, we highlight that the best condensation process that we studied is dry RTO at high temperature, with a threshold value of more than 2% for SGOI films in the 10 nm thickness range. Such a strain value corresponds to a Ge concentration of about 60%.

A finer characterization of the crystal quality as a function of depth into the SGOI film was performed by MEIS. Unfortunately, we cannot discuss optimization of the condensation process in terms of SGOI crystal quality with the characterization of three samples only. However, two conclusions can be drawn: the key crystal areas that are degraded and that must be particularly looked at for optimization of the condensation process are the interfaces of SiGe with oxides, and the SOI crystal quality is not altered by SiGe interdiffusion for low Ge fraction SGOI films.

In the second part of *Chapter IV* (*Section IV.B*), it was shown that the SGOI film is partially relaxed after the STI etch process step at the frontier between pMOS active areas and STI areas. Two possible causes to this strain relaxation phenomenon, and related to the condensation process, were suggested and investigated:

- The presence of Ge-O bonds at oxide-SGOI interfaces was proposed to weaken the mechanical properties of oxide-SGOI interfaces and to cause a "sliding" mechanism of the SGOI film. We found that there is no noticeable quantity of Ge-O bonds at the SGOI-BOx interface and thus ruled that proposition. Nevertheless, we observed a higher quantity of Si sub-oxides at the BOx-SGOI interface after condensation and discussed it in view of the crystal disorder evidenced by MEIS.

- H accumulation at SGOI-oxide interfaces was though to possibly induce mechanical weakness of the interfaces. By coupling neutron reflectivity with XRR, we found that there is H neither after SiGe epitaxy on SOI substrates not after condensation. To conclude, H is not the cause of strain relaxation of SGOI films after STI etch.

This work has brought more understanding about the mechanisms and kinetics of thermal oxidation of SiGe and about the evolution of the strain level and crystal quality of SGOI films fabricated by condensation. Perspectives to this work and questions left hanging in the air are numerous:

- What are the mechanisms that could account for the dependence of the oxide density on the oxidation temperature and on the Ge concentration at the oxidation interface? We suggested that the higher lattice parameter of SiGe with respect to Si could tend to accommodate the lattice mismatch between SiGe and SiO_2, and as a consequence decrease the density of the oxide. As for the effect of temperature, it was proposed that stress relaxation of SiO_2 via viscous flow could decrease the oxide density. We suggest that studying oxidation kinetics of fully relaxed SiGe films and varying the conditions of the temperature ramp up of each oxidation process (which are largely different from dry RTO to dry furnace oxidation) could shed light on the mechanisms that induce this dependence.

- What are the causes of the discrepancies of the simulation model and how could it be improved? It was suggested that dedicated experiments to calibrate the diffusion model on the specific processes performed in this work would help improve the model.

- Optimizing the condensation process requires a sound understanding of the mechanisms of strain relaxation of SGOI films fabricated by condensation experiments, which are not fully identified yet. In terms of strain relaxation mechanisms, we suggested that if strain relaxation is governed by strain energy balance, this balance is influenced by the nature of the underlying layer: a thermal oxide (BOx) for the case of SGOI films instead of crystalline Si for the case of epitaxial SiGe-Si systems. We also suggested that dislocation nucleation at SiGe-oxide interfaces may be hindered up to higher elastic strain values than at SiGe-Si interfaces. Condensation based on other processes, such as dry furnace oxidation and ISSG oxidation with a different O_2/H_2 ratio for instance could contribute to a better understanding of these mechanisms.

- The cause to the SGOI strain relaxation phenomenon at the edge of active areas has not been determined yet.

Bibliography

A

[Afanas’ ev09] Afanas’ ev, V. V., et al. "Electronic properties of Ge dangling bond centers at $Si_{1-x}Ge_x/SiO_2$ interfaces." *Applied Physics Letters* (2009): vol. 95, no 22, p. 222106.

[Akiyama08] Akiyama, T., et al. "Impact of oxidation-induced strain on microscopic processes related to oxidation reaction at the SiO_2/Si(100) interface." *Physical Review B*, 77(11) (2008), 115356.

[Andrieu14] Andrieu, F., et al. "Strain and Layout Management in dual Channel (sSOI substrate, SiGe channel) planar FDSOI MOSFETs." *Solid State Device Research Conference (ESSDERC)*, 2014 44th European. IEEE, 2014.

[Andrieu16] Andrieu, F., et al. "UTBB FDSOI PMOSFETs Including Strained SiGe Channels at the 14nm Technology Node and Beyond." *ECS Transactions*, 75(8) (2016), 3-14.

[Awaji96] Awaji, N., et al. "High-density layer at the SiO_2/Si interface observed by difference X-ray reflectivity." *Japanese Journal of Applied Physics* 35.1B (1996): L67.

B

[Bai94] Bai, G., et al. "Strain relief of metastable GeSi layers on Si (100)." *Journal of Applied Physics* 75.9 (1994): 4475-4481.

[Balk71] Balk, P. "Surface Properties of Oxidized Germanium-Doped Silicon." *Journal of The Electrochemical Society* 118.3 (1971): 494-495.

[Bardeen50] Bardeen, J., et al. "Deformation potentials and mobilities in non-polar crystals." *Physical Review* 80.1 (1950): 72.

[Barin77] Barin, I., et al. "Tables. Thermochemical properties of inorganic substances." *Springer Berlin Heidelberg*, 1977. 1-861.

[Bean84] Bean, J. C., et al. "Ge_xSi_{1-x}/Si strained-layer superlattice grown by molecular beam epitaxy." *Journal of Vacuum Science & Technology A* 2.2 (1984): 436-440.

[Bedell04] Bedell, S. W., et al. "Defects and strain relaxation in silicon-germanium-on-insulator formed by high-temperature oxidation." *Applied Physics Letters* 85.24 (2004): 5869-5871.

[Bedell06] Bedell, S. W., et al. "Strain and lattice engineering for Ge FET devices." *Materials Science in Semiconductor Processing* 9.4 (2006): 423-436.

[Berthelon16] Berthelon, R., et al. "Design/technology co-optimization of strain-induced layout effects in 14nm UTBB-FDSOI CMOS: Enablement and assessment of continuous-RX designs." *VLSI Technology*, 2016 IEEE Symposium on. IEEE, 2016.

[Bongiorno03] Bongiorno, A., et al. "Atomistic structure of the Si (100)-SiO_2 interface: A synthesis of experimental data." *Applied Physics Letters* 83.7 (2003): 1417-1419.

[Bongiorno03’] Bongiorno, A., et al. "Transition Structure at the Si (100) − SiO_2 Interface." *Physical Review Letters* 90.18 (2003): 186101.

[Bongiorno04] Bongiorno, A., et al. "Multiscale modeling of oxygen diffusion through the oxide during silicon oxidation." *Physical Review B* 70.19 (2004): 195312.

[Bongiorno04’] Bongiorno, A., et al. "Reaction of the Oxygen Molecule at the Si(100)-SiO_2 Interface During Silicon Oxidation." *Physical Review Letters* 93.8 (2004): 086102.

[Borisenko97] Borisenko, V., et al. "Rapid thermal processing of semiconductors" *Microdevices*, 1997.

[Boureau16] Boureau, V. "Déformations introduites lors de la fabrication de transistors FDSOI : une contribution de l’holographie électronique en champ sombre" *PhD dissertation*, Université de Toulouse, 2008.

C

[Cooper16] Cooper, D., et al. "Strain mapping of semiconductor specimens with nm-scale resolution in a transmission electron microscope." *Micron* 80 (2016): 145-165.

[Costello84] Costello, J. A., et al. "Isotope Labeling Studies of the Oxidation of Silicon at 1000° and 1300° C." *Journal of The Electrochemical Society* 131.8 (1984): 1944-1947.

[Cui09] Cui, H., et al. "Size-dependent oxidation behavior for the anomalous initial thermal oxidation process of Si." *Applied Physics Letters* 94.8 (2009): 083108.

[CXRO] Center for X-Ray Optics, http://www.cxro.lbl.gov/

D

[Daillant08] Daillant, J., et al. "X-ray and neutron reflectivity: principles and applications" Vol. 770. *Springer*, 2008.

[David15] David, T., et al. "Kinetics and Energetics of Ge Condensation in SiGe Oxidation." *The Journal of Physical Chemistry C* 119.43 (2015): 24606-24613.

[David16] David, T., et al. "Remarkable Strength Characteristics of Defect-Free SiGe/Si Heterostructures Obtained by Ge Condensation." *The Journal of Physical Chemistry C* 120.36 (2016): 20333-20340.

[Deal65] Deal, B. E., et al. "General relationship for the thermal oxidation of silicon." *Journal of Applied Physics* 36.12 (1965): 3770-3778.

[DeSalvo14] DeSalvo, B., et al. "A mobility enhancement strategy for sub-14nm power-efficient FDSOI technologies." *Electron Devices Meeting (IEDM), 2014 IEEE International*. IEEE, 2014.

[Dennard74] Dennard, R. H., et al. "Design of ion-implanted MOSFET’s with very small physical dimensions." *Solid-State Circuits, IEEE Journal of* 9.5 (1974): 256-268.

[Di05] Di, Z., et al. "Strain relaxation mechanism in SiGe-on-insulator fabricated by Ge condensation." *Journal of Crystal Growth* 281.2 (2005): 275-280.

[Diebold99] Diebold, A. C., et al. "Characterization and production metrology of thin transistor gate oxide films." *Materials Science in Semiconductor Processing* 2.2 (1999): 103-147.

[Dismukes64] Dismukes, J. P., et al. "Thermal and Electrical Properties of Heavily Doped Ge-Si Alloys up to 1300° K." *Journal of Applied Physics* 35.10 (1964): 2899-2907.

[Dodson87] Dodson, B. W., et al. "Relaxation of strained-layer semiconductor structures via plastic flow." *Applied Physics Letters* 51.17 (1987): 1325-1327.

[Dong12] Dong, Y., et al. "A unified interdiffusivity model and model verification for tensile and relaxed SiGe interdiffusion over the full germanium content range." *Journal of Applied Physics* 111.4 (2012): 044909.

[Dong14] Dong, Y., et al. "On the role and modeling of compressive strain in Si-Ge interdiffusion for SiGe heterostructures." *Semiconductor Science and Technology* 29.1 (2014): 015012.

[Dong14] Dong, Y., et al. "On the role and modeling of compressive strain in Si-Ge interdiffusion for SiGe heterostructures." *Semiconductor Science and Technology* 29.1 (2014): 015012.

[Doremus84] Doremus, R. H. "Oxidation of silicon: strain and linear kinetics." *Thin Solid Films* 122.3 (1984): 191-196.

[Doremus89] Doremus, R. H. "Oxidation of silicon: Is there a slow interface reaction?" *Journal of Applied Physics* 66.9 (1989): 4441-4443.

[Dunham86] Dunham, S. T., et al. "Point-defect generation during oxidation of silicon in dry oxygen. I. Theory." *Journal of Applied Physics* 59.7 (1986): 2541-2550.

E

[EerNisse77] EerNisse, E. P. "Viscous flow of thermal SiO_2." *Applied Physics Letters* 30.6 (1977): 290-293.

[Elzo12] Elzo, M., et al. "X-ray resonant magnetic reflectivity of stratified magnetic structures: Eigenwave formalism and application to a W/Fe/W trilayer." *Journal of Magnetism and Magnetic Materials* 324.2 (2012): 105-112.

F

[Fauquier17] Fauquier, L., et al. "Benefits of XPS nanocharacterization for process development and industrial control of thin SiGe channel layers in advanced CMOS technologies" *Materials Science in Semiconductor Processing* 70 (2017): 105-110.

[Ferain11] Ferain, I., et al. "Multigate transistors as the future of classical metal-oxide-semiconductor field-effect transistors." *Nature* 479.7373 (2011): 310-316.

[Fischetti96] Fischetti, M. V., et al. "Band structure, deformation potentials, and carrier mobility in strained Si, Ge, and SiGe alloys." *Journal of Applied Physics* 80.4 (1996): 2234-2252.

[Frank11] Frank, M. M. "High-k/metal gate innovations enabling continued CMOS scaling." *ESSCIRC (ESSCIRC)*, 2011 Proceedings of the IEEE, 2011.

G

[Ghani03] Ghani, T., et al. "A 90nm high volume manufacturing logic technology featuring novel 45nm gate length strained silicon CMOS transistors." *Electron Devices Meeting*, 2003. IEDM'03 Technical Digest. IEEE International. IEEE, 2003.

[Gourhant14] Gourhant, O., et al. "Ge Condensation Using Rapid Thermal Oxidation for SGOI Substrate Preparation." *ECS Transactions* 64.6 (2014): 469-478.

[Gunji11] Gunji, M., et al. "Strain relaxation mechanisms in compressively strained thin SiGe-on-insulator films grown by selective Si oxidation." *Journal of Applied Physics* 109.1 (2011): 014324.

[Gusev95] Gusev, E. P., et al. "Growth mechanism of thin silicon oxide films on Si (100) studied by medium-energy ion scattering." *Physical Review B* 52.3 (1995): 1759.

H

[Himpsel88] Himpsel, F. J., et al. "Microscopic structure of the SiO_2/Si interface." Physical Review B 38.9 (1988): 6084.

[Hirose07] Hirose, K., et al. "Photoelectron spectroscopy studies of SiO_2/Si interfaces." *Progress in Surface Science* 82.1 (2007): 3-54.

[Holland87] Holland, O. W., et al. "Novel oxidation process in Ge^+-implanted Si and its effect on oxidation kinetics." *Applied Physics Letters* 51.7 (1987): 520-522.

[Houghon91] Houghton, D. C. "Strain relaxation kinetics in $Si_{1-x}Ge_x$/Si heterostructures." *Journal of Applied Physics* 70.4 (1991): 2136-2151.

[Houssa11] Houssa, M., et al. "Experimental and theoretical investigation of defects at (100) $Si_{1-x}Ge_x$/oxide interfaces." *Microelectronic Engineering* 88.4 (2011): 383-387.

[Hÿtch98] Hÿtch, M. J., et al. "Quantitative measurement of displacement and strain fields from HREM micrographs" *Ultramicroscopy* 74.3 (1998): 131-146.

I

[IOFFE] Ioffe Physico-Technical Institute, http://www.ioffe.ru/SVA/NSM/

J

[Jaouen04] Jaouen, N., et al. "An apparatus for temperature-dependent soft X-ray resonant magnetic scattering." *Journal of synchrotron radiation* 11.4 (2004): 353-357.

[Jalabert17] Jalabert, D., et al. "Swift Ion Beam Analysis in Nanosciences" *John Wiley & Sons*, 2017.

K

[Kahng63] Kahng, D. "Electric field controlled semiconductor device." U.S. Patent No. 3,102,230. 27 Aug. 1963.

[Kazor95] Kazor, A. "Space-charge oxidant diffusion model for rapid thermal oxidation of silicon." *Journal of Applied Physics* 77.4 (1995): 1477-1481.

[Kee00] Kee, R. J., et al. "The influence of pressure, fluid flow, and chemistry on the combustion-based oxidation of silicon." *Proceedings of the Combustion Institute* 28.1 (2000): 1381-1388.

[Kilpatrick97] Kilpatrick, S. J., et al. "A diffusional model for the oxidation behavior of $Si_{1-x}Ge_x$ alloys." *Journal of Applied Physics* 81.12 (1997): 8018-8028.

[Kilpatrick03] Kilpatrick, S. J., et al. "Experimental study of the oxidation of silicon germanium alloys." *Journal of Applied Physics* 93.8 (2003): 4896-4901.

[Kilpatrick08] Kilpatrick, S. J., et al. "An angle-resolved study of early oxidation (< 3.0 nm) of Si–Ge alloys." *Journal of Applied Physics* 103.4 (2008): 043514.

[kim17] Kim, W-K., et al. "High performance 4.5-nm-thick compressively-strained Ge-on-insulator pMOSFETs fabricated by Ge condensation with optimized temperature control." *VLSI Technology*, 2017 Symposium on. IEEE, 2017.

[Kosowsky97] Kosowsky, S. D., et al. "Evidence of annealing effects on a high-density Si/SiO_2 interfacial layer." *Applied Physics Letters* 70 (1997): 3119-3121.

[Kube10] Kube, R., et al. "Composition dependence of Si and Ge diffusion in relaxed $Si_{1-x}Ge_x$ alloys." *Journal of Applied Physics* 107.7 (2010): 073520.

[Kuhn12] Kuhn, K. J. "Considerations for ultimate CMOS scaling." *IEEE Trans. Electron Devices* 59.7 (2012): 1813-1828.

L

[Labrot16] Labrot, M., et al. "Low thermal budget for Si and SiGe surface preparation for FD-SOI technology." *Applied Surface Science* 371 (2016): 436-446.

[LeGoues89] LeGoues, F. K., et al. "Kinetics and mechanism of oxidation of SiGe: dry versus wet oxidation." *Applied Physics Letters* 54.7 (1989): 644-646.

[LeGoues89’] LeGoues, F. K., et al. "Oxidation studies of SiGe." *Journal of Applied Physics* 65.4 (1989): 1724-1728.

[Ligenza60] Ligenza, J. R., et al. "The mechanisms for silicon oxidation in steam and oxygen." *Journal of Physics and Chemistry of Solids* 14 (1960): 131-136.

[Lilienfeld30] Lilienfeld E. J. "Method and apparatus for controlling electric currents." U.S. Patent No. 1,745,175. 28 Jan. 1930.

[long12] Long, E., et al. "A comparative analysis of oxidation rates for thin films of SiGe versus Si." *Physica Status Solidi (a)* 209.10 (2012): 1934-1939.

[lundstrom02] Lundstrom, M., et al. "Essential physics of carrier transport in nanoscale MOSFETs." I*EEE Transactions on Electron Devices* 49.1 (2002): 133-141.

M

[Manasevit82] Manasevit, H. M., et al. "Electron mobility enhancement in epitaxial multilayer Si-$Si_{1-x}Ge_x$ alloy films on (100) Si." *Applied Physics Letters* 41.5 (1982): 464-466.

[Marée87] Marée, P. M. J., et al. "Generation of misfit dislocations in semiconductors." *Journal of Applied Physics* 62.11 (1987): 4413-4420.

[Margalit72] Margalit, S., et al. "Oxidation of silicon-germanium alloys." *Journal of Crystal Growth* 17 (1972): 288-297.

[Massoud85] Massoud, H. Z., et al. "Thermal Oxidation of Silicon in Dry Oxygen Growth-Rate Enhancement in the Thin Regime I. Experimental Results." *Journal of the Electrochemical Society* 132.11 (1985): 2685-2693.

[Massoud85’] Massoud, H. Z., et al. "Thermal Oxidation of Silicon in Dry Oxygen: Growth-Rate Enhancement in the Thin Regime II. Physical Mechanisms." *Journal of The Electrochemical Society* 132.11 (1985): 2693-2700.

[Matthews70] Matthews, J. W., et al. "Accommodation of misfit across the interface between crystals of semiconducting elements or compounds." *Journal of Applied Physics* 41.9 (1970): 3800-3804.

[Matthews74] Matthews, J. W., et al. "Defects in epitaxial multilayers: I. Misfit dislocations." *Journal of Crystal Growth* 27 (1974): 118-125.

[Mehrer07] Mehrer, H. "Diffusion in Solids: Fundamentals, Methods, Materials, Diffusion-Controlled Processes" *Springer* (2007): 547-552.

[Menéndez09] Menéndez, J. "Analytical strain relaxation model for $Si_{1-x}Ge_x$/Si epitaxial layers." *Journal of Applied Physics* 105.6 (2009): 3519.

[Moore65] Moore, G. E. "Cramming more components onto integrated circuits." *Electronics Magazine* (1965):4.

[Morin15] Morin, P. F., et al. "Mechanical analyses of extended and localized UTBB stressors formed with Ge enrichment techniques." *ECS Transactions* 66.4 (2015): 57-65.

[Morin15’] Morin, P., et al. "A review of the mechanical stressors efficiency applied to the ultra-thin body & buried oxide fully depleted silicon on insulator technology." *Solid-State Electronics* 117 (2016): 100-116.

[Moulder92] Moulder, J. F., et al. Handbook of X-ray Photoelectron Spectroscopy: A Reference Book of Standard Spectra for Identification and Interpretation of XPS Data. Physical Electronics Division, *Perkin-Elmer Corporation*, 1992.

[Muller99] Muller, D. A., et al. "The electronic structure at the atomic scale of ultrathin gate oxides." *Nature* 399.6738 (1999): 758-761.

[Munkholm04] Munkholm, A., et al. "Ordering in thermally oxidized silicon." *Physical Review Letters* 93.3 (2004): 036106.

N

[Nakaharai03] Nakaharai, S., et al. "Characterization of 7-nm-thick strained Ge-on-insulator layer fabricated by Ge-condensation technique." *Applied Physics Letters* 83.17 (2003): 3516-3518.

[Nakaharai06] Nakaharai, S., et al. "The generation of crystal defects in Ge-on-insulator (GOI) layers in the Ge-condensation process." *Semiconductor Science and Technology* 22.1 (2006): S103.

[Nakaharai09] Nakaharai, S., et al. "Formation process of high-purity Ge-on-insulator layers by Ge-condensation technique." *Journal of Applied Physics* 105.2 (2009): 024515.

[Napolitani05] Napolitani, E., et al. "Silicon interstitial injection during dry oxidation of SiGe/Si layers." *Journal of Applied Physics* 97.3 (2005): 036106.

[Nayak92] Nayak, D. K., et al. "Rapid isothermal processing of strained GeSi layers." *IEEE Transactions on Electron Devices* 39.1 (1992): 56-63.

[Nayak15] Nayak, M., et al. "Determining Chemically and Spatially Resolved Atomic Profile of Low Contrast Interface Structure with High Resolution." *Scientific Reports* 5 (2015).

[Nolot14] Nolot, E., et al. "Optical Constants Determination of Pseudomorphic $Si_{1-x}Ge_x$ Layers on Si(001), with $0<x<0.54$" *ECS Transactions* 64(6), 455–465 (2014).

[Norton61] Norton, F. J. "Permeation of gaseous oxygen through vitreous silica." *Nature* 191.4789 (1961): 701-701.

O

[Oh01] Oh, J. H., et al. "Chemical structure of the ultrathin SiO_2/Si(100) interface: An angle-resolved Si2p photoemission study." *Physical Review B* 63.20 (2001): 205310.

[Olesinski84] Olesinski, R. W., et al. "The Ge−Si (germanium-silicon) system." *Journal of Phase Equilibria* 5.2 (1984): 180-183.

[Ouellette15] Ouellette, K. "Advances in Applications and Ecosystem for FDSOI technology" *Tokyo SOI Meeting (2015)*.

P

[Paine91] Paine, D. C., et al. "Oxidation of $Si_{1-x}Ge_x$ alloys at atmospheric and elevated pressure." *Journal of Applied Physics* 70.9 (1991): 5076-5084.

[Park08] Park, T. J., et al. "Effects of surface treatments using O_3 and NH_3 on electrical properties and chemical structures of high-k HfO_2 dielectric films on strained $Si_{1-x}Ge_x$/Si substrates." *Journal of Applied Physics* 103.8 (2008): 084117.

[pd.chem] Properties of the neutron: http://pd.chem.ucl.ac.uk/pdnn/inst3/neutrons.htm

[People85] People, R., et al. "Erratum: Calculation of critical layer thickness versus lattice mismatch for Ge_xSi_{1-x}/Si strained-layer heterostructures [Appl. Phys. Lett. 47, 322 (1985)]." *Applied Physics Letters* 49.4 (1986): 229-229.

[Pillarisetty11] Pillarisetty, R. "Academic and industry research progress in germanium nanodevices." *Nature* 479.7373 (2011): 324-328.

[Prabkakaran93] Prabhakaran, K., et al. "In situ oxidation of a thin layer of Ge on Si (001): Observation of GeO to SiO_2 transition." *Applied Physics Letters* 62.8 (1993): 864-866.

[Prabkakaran00] Prabhakaran, K., et al. "Distinctly different thermal decomposition pathways of ultrathin oxide layer on Ge and Si surfaces." *Applied Physics Letters* 76.16 (2000): 2244-2246.

R

[Robertson15] Robertson, J., et al. "High-K materials and metal gates for CMOS applications." *Materials Science and Engineering: R: Reports* 88 (2015): 1-41.

[Rochet97] Rochet, F., et al. "Suboxides at the Si/SiO_2 interface: a Si2p core level study with synchrotron radiation." *Journal of Non-crystalline Solids* 216 (1997): 148-155.

[Rosencher79] Rosencher, E., et al. "An ^{18}O study of the thermal oxidation of silicon in oxygen." *Applied Physics Letters* 34.4 (1979): 254-256.

[Rouchon14] Rouchon, D., et al. "Germanium content and strain in $Si_{1-x}Ge_x$ alloys characterized by Raman spectroscopy." *Journal of Crystal Growth* 392 (2014): 66-73.

S

[Schäffler97] Schäffler, F. "High-mobility Si and Ge structures." *Semiconductor Science and Technology*, 12(12), (1997): 1515.

[Segura15] Segura-Ruiz, J., et al. "Hydrogen accumulation as the origin of delamination at the a-carbon/SiO_2 interface." *Journal of Applied Physics* 117.21 (2015): 215302.

[Shimura10] Shimura, T., et al. "Residual order in the thermal oxide of a fully strained SiGe alloy on Si." *Physical Review B* 81.3 (2010): 033308.

[Smith54] Smith, C. S. "Piezoresistance effect in germanium and silicon." *Physical Review* 94.1 (1954): 42.

[Souriau08] Souriau, L., et al. "High Hole Mobility SGOI Substrates Obtained by the Germanium Condensation Technique." *ECS Transactions* 16.10 (2008): 79-89.

[Spadafora03] Spadafora, M., et al. "Oxidation rate enhancement of SiGe epitaxial films oxidized in dry ambient." *Applied Physics Letters* 83.18 (2003): 3713-3715.

[Spadafora05] Spadafora, M., et al. "Dry oxidation of MBE-SiGe films: rate enhancement, Ge redistribution and defect injection." *Materials Science in Semiconductor Processing* 8.1 (2005): 219-224.

[Suh16] Suh, J., et al. "Effects of additional oxidation after Ge condensation on electrical properties of germanium-on-insulator p-channel MOSFETs." *Solid-State Electronics* 117 (2016): 77-87.

[Sun09] Sun, Y., et al. "Strain effect in semiconductors: theory and device applications." *Springer Science & Business Media*, 2009.

[Sze06] Sze, S. M., et al. Physics of semiconductor devices. *John wiley & sons*, 2006.

T

[Takagi94] Takagi, S., et al. "On the universality of inversion layer mobility in Si MOSFET's: Part I-effects of substrate impurity concentration." *Electron Devices, IEEE Transactions on* 41.12 (1994): 2357-2362.

[Takagi08] Takagi, S., et al. "Carrier-transport-enhanced channel CMOS for improved power consumption and performance." *Electron Devices, IEEE Transactions on* 55.1 (2008): 21-39.

[Takagi10] Takagi, S., et al. "Critical Factors for Enhancement of Compressive Strain in SGOI Layers Fabricated by Ge Condensation Technique." *ECS Transactions* 33.6 (2010): 501-509.

[Takagi15] Takagi, S., et al. "III–V/Ge channel MOS device technologies in nano CMOS era." *Japanese Journal of Applied Physics* 54.6S1 (2015): 06FA01.

[Tatsumura04] Tatsumura, K., et al. "Residual order within thermally grown amorphous SiO_2 on crystalline silicon." *Physical Review B* 69.8 (2004): 085212.

[Tatsumura05] Tatsumura, K., et al. "Reactions and diffusion of atomic and molecular oxygen in the SiO_2 network." *Physical Review B* 72.4 (2005): 045205.

[Tezuka01] Tezuka, T., et al. "A novel fabrication technique of ultrathin and relaxed SiGe buffer layers with high Ge fraction for sub-100 nm strained silicon-on-insulator MOSFETs." *Japanese Journal of Applied Physics* 40.4S (2001): 2866.

[Thompson04] Thompson, S. E., et al. "A 90-nm logic technology featuring strained-silicon." *Electron Devices, IEEE Transactions on* 51.11 (2004): 1790-1797.

[Tiilikainen07] Tiilikainen, J., et al. "Accuracy in x-ray reflectivity analysis." *Journal of Physics D: Applied Physics* 40.23 (2007): 7497.

[Trimaille89] Trimaille, I., et al. "Use of ^{18}O isotopic labelling to study thermal dry oxidation of silicon as a function of temperature and pressure." *Applied Surface Science* 39.1-4 (1989): 65-80.

[Tsetseris06] Tsetseris, L., et al. "Oxygen Migration, Agglomeration, and Trapping: Key Factors for the Morphology of the Si– SiO_2 Interface." *Physical Review Letters* 97.11 (2006): 116101.

U

[Uchida05] Uchida, K., et al. "Physical mechanisms of electron mobility enhancement in uniaxial stressed MOSFETs and impact of uniaxial stress engineering in ballistic regime." *Electron Devices Meeting*, 2005. IEDM Technical Digest. IEEE International. IEEE, 2005.

[Usuda13] Usuda, Koji, et al. "Characterization of anisotropic strain relaxation after isolation for strained SGOI and SiGe/Si structure with newly developed high-NA and oil-immersion Raman method." *Solid-State Electronics* 83 (2013): 46-49.

V

[Vincent07] Vincent, B., et al. "Stacking fault generation during relaxation of silicon germanium on insulator layers obtained by the Ge condensation technique." *Applied Physics Letters* 90.7 (2007): 074101.

[Vincent08] Vincent, B., et al. "The Ge condensation technique: A solution for planar SOI/GeOI co-integration for advanced CMOS technologies?" *Materials Science in Semiconductor Processing* 11.5 (2008): 205-213.

W

[Wang01] Wang, T. C., et al. "Dislocation dynamics of strain relaxation in epitaxial layers." *Journal of Applied Physics* 89.11 (2001): 6069-6072.

[Wanlass67] Wanlass, F. M. "Low stand-by power complementary field effect circuitry." U.S. Patent No. 3,356,858. 5 Dec. 1967.

[Watanabe06] Watanabe, T., et al. "New linear-parabolic rate equation for thermal oxidation of silicon." *Physical Review Letters* 96.19 (2006): 196102.

[Welser92] Welser, J., et al. "NMOS and PMOS transistors fabricated in strained silicon/relaxed silicon-germanium structures." *Electron Devices Meeting*, 1992. IEDM'92. Technical Digest., International. IEEE, 1992.

[Williams98] Williams, D., et al. "Transmission electron microscopy: a textbook for materials science" Vol. 10. No. 10.6. *Springer*, 1998.

Y

[Yang03] Yang, M., et al. "Performance dependence of CMOS on silicon substrate orientation for ultrathin oxynitride and HfO_2 gate dielectrics." *Electron Device Letters, IEEE* 24.5 (2003): 339-341.

[Young87] Young, E. M., et al. "Ultraviolet light stimulated thermal oxidation of silicon." *Applied Physics Letters* 50.2 (1987): 80-82.

[Young87'] Young, E. M., et al. "Rate constants for light-enhanced thermal oxidation of silicon." *Journal of Applied Physics* 62.5 (1987): 2086-2094.

Z

[Zienkiewicz77] Zienkiewicz, O. C., et al. "The finite element method." Vol. 3. London: *McGraw-hill*, 1977.

Appendices

A. Stress and Strain

This appendice complements *Section I.2.2.* by giving a more general and complete description of stress and strain laws. Such a description is needed as soon as studied systems are more complex than full-sheet layer. Investigating the mechanical behaviour of 2D or 3D nanoscale transistors, such as in [Morin15'], indeed requires the full knowledge of elastic moduli or compliance tensors.

Strain is defined as the relative lattice displacement created by deformation of the crystal structure of the material. Strain is fully characterized by the following second-order tensor:

$$\overset{=}{\varepsilon} = \begin{pmatrix} \varepsilon_{xx} & \varepsilon_{xy} & \varepsilon_{xz} \\ \varepsilon_{yx} & \varepsilon_{yy} & \varepsilon_{yz} \\ \varepsilon_{zx} & \varepsilon_{zy} & \varepsilon_{zz} \end{pmatrix}, \qquad \textbf{\textit{Equation A.1}}$$

with $\varepsilon_{\alpha\beta} = \frac{\partial u_\alpha}{\partial x_\beta}$, $u_\alpha = u_x, u_y, u_z$ and $x_\beta = x, y, z$ and where u_α is the displacement of the lattice point along x_α.

The strain tensor is symmetric:

$$\varepsilon_{\alpha\beta} = \varepsilon_{\beta\alpha} = \frac{1}{2}\left(\frac{\partial u_\alpha}{\partial x_\beta} + \frac{\partial u_\beta}{\partial u_\alpha} \right). \qquad \textbf{\textit{Equation A.2}}$$

Stress is defined as the force responding to strain in a unit area and is fully defined by the second-order stress tensor:

$$\overset{=}{\sigma} = \begin{pmatrix} \sigma_{xx} & \sigma_{xy} & \sigma_{xz} \\ \sigma_{yx} & \sigma_{yy} & \sigma_{yz} \\ \sigma_{zx} & \sigma_{zy} & \sigma_{zz} \end{pmatrix} \text{ with } \sigma_{\alpha\beta} = \sigma_{\beta\alpha}. \qquad \textbf{\textit{Equation A.3}}$$

As schematiccaly represented *Figure A.1*, σ_{xy} is the force applied in the *x* direction to a unit area in the plane which is normal to the *y* direction.

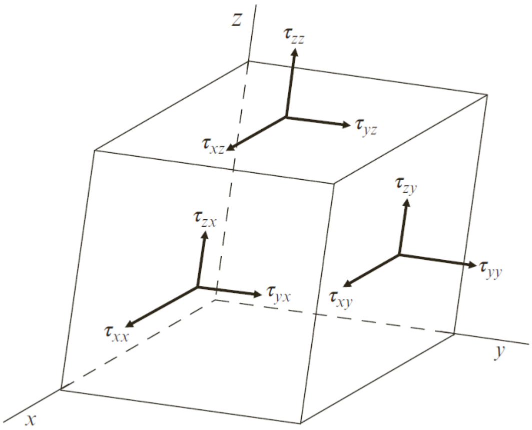

Figure A.1: Schematic representation of stress components on surfaces of an infinitesimal cube. From [Sun09].

Within the linear elastic theory, stress and strain are related by Hooke's law:

$$\bar{\bar{\sigma}} = \bar{\bar{\bar{\bar{C}}}}.\bar{\bar{\varepsilon}} \text{ or } \bar{\bar{\varepsilon}} = \bar{\bar{\bar{\bar{S}}}}.\bar{\bar{\sigma}},$$ **Equation A.4**

where $\bar{\bar{\bar{\bar{C}}}}$ and $\bar{\bar{\bar{\bar{S}}}}$ are the elastic moduli and compliances fourth-order tensors. $\bar{\bar{\bar{\bar{C}}}}$ and $\bar{\bar{\bar{\bar{S}}}}$ are inverse to each other. Symmetry relations induce:

$$C_{ijkl} = C_{jikl} = C_{ijlk} = C_{klij}.$$ **Equation A.5**

The elastic moduli tensor has therefore 21 independent components. A matrix notation, called Voigt notation, is usually used to take into account symmetry considerations. It uses the indices I, J according to the rule:

(i,j)/(k,l)	(1,1)	(2,2)	(3,3)	(2,3)	(3,1)	(1,2)
I/J	1	2	3	4	5	6

Table I.1: Voigt notation.

Hooke's law is then expressed in Voigt notation as:

$$\begin{pmatrix} \sigma_{xx} \\ \sigma_{yy} \\ \sigma_{zz} \\ \sigma_{yz} \\ \sigma_{zx} \\ \sigma_{xy} \end{pmatrix} = \begin{pmatrix} C_{11} & C_{12} & C_{13} & C_{14} & C_{15} & C_{16} \\ C_{12} & C_{22} & C_{23} & C_{24} & C_{25} & C_{26} \\ C_{13} & C_{23} & C_{33} & C_{34} & C_{35} & C_{36} \\ C_{14} & C_{24} & C_{34} & C_{44} & C_{45} & C_{46} \\ C_{15} & C_{25} & C_{35} & C_{34} & C_{55} & C_{56} \\ C_{16} & C_{26} & C_{36} & C_{46} & C_{56} & C_{66} \end{pmatrix} \begin{pmatrix} \varepsilon_{xx} \\ \varepsilon_{yy} \\ \varepsilon_{zz} \\ 2\varepsilon_{yz} \\ 2\varepsilon_{zx} \\ 2\varepsilon_{xy} \end{pmatrix}.$$ **Equation A.6**

Using Voigt notation, symmetry relations of cubic systems such as Si and SiGe reduce the elastic moduli tensor to:

$$\underline{\underline{C}} = \begin{pmatrix} C_{11} & C_{12} & C_{12} & 0 & 0 & 0 \\ C_{12} & C_{11} & C_{12} & 0 & 0 & 0 \\ C_{12} & C_{12} & C_{11} & 0 & 0 & 0 \\ 0 & 0 & 0 & C_{44} & 0 & 0 \\ 0 & 0 & 0 & 0 & C_{44} & 0 \\ 0 & 0 & 0 & 0 & 0 & C_{44} \end{pmatrix}.$$ **Equation A.7**

The elastic moduli coefficients of SiGe are [IOFFE]:

$$C_{11} = 165.8 - 37.3x$$
$$C_{12} = 63.9 - 15.6x \quad \text{where } x \text{ is the Ge fraction.}$$
$$C_{44} = 79.6 - 12.8x,$$

Equation A.8

B. Secondary Ion Mass Spectroscopy (SIMS)

Secondary-Ion-Mass Spectroscopy (SIMS) is a chemical composition characterization technique based on sputtering by ion bombardment. The incident ions, called primary ions, are focused on the sample with a kinetic energy from a few keV to a few hundreds keV, which induce sputtering of various particles, among which ions which are called secondary ions, from the surface of the sample. The chemical composition of the surface of the sample is extracted from the analysis of secondary ions by a mass spectrometer. A schematic view of the SIMS apparatus is shown *Figure B.1*. As the surface of the sample is eroded by the incident ion beam, chemical composition profiles as a function of depth can be extracted assuming sound understanding of the ionization probabilities of the studied materials and proper calibration of the sputter rate.

Time-of-Flight SIMS (ToF-SIMS) uses a Time-of-Flight mass spectrometer instead of a magnetic spectrometer. Separation of elements is performed by measuring the time of flight between the sample and the detector, which depends on the mass of each element. ToF-SIMS thus uses a pulsed primary ion beam, usually with a frequency in the 10 kHz range.

SIMS and ToF-SIMS using a 300 V O_2^+ beam (CAMECA IMS Wf) were performed to measure the Ge concentration as a function of depth after oxidation. Ge concentration quantification was performed on $Si_{0.8}Ge_{0.2}$ well known samples prior to any SIMS characterization. The variation of the sputter rate with the Ge concentration is low for Ge concentrations in the 20%-30% range. We can therefore reasonably extract Ge concentrations as a function of depth for most of the samples of this study. No conclusion is based on the depth dependence of the Ge concentration when the Ge concentration is higher, even if Ge concentration profiles are plotted as a function of depth as well for direct comparison.

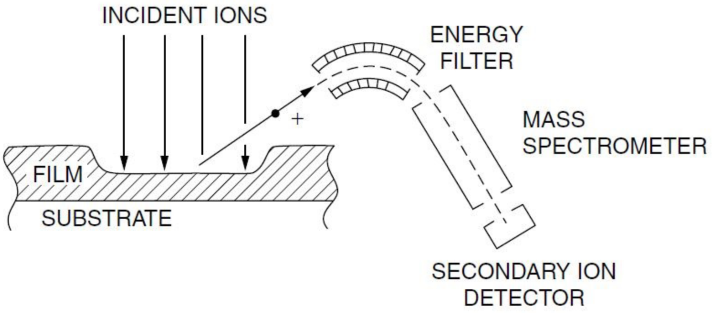

Figure B.1: Schematic illustration of SIMS principles.

C. Wavelength Dispersive X-Ray Fluorescence (WDXRF)

X-Ray Fluorescence (XRF) is a technique used to qualitatively and sometimes quantitatively study the chemical composition of materials. The principles of the technique are illustrated *Figure C.1*. When an incoming X-Ray photon is absorbed by the material, its energy can be transfered to the core electron of an atom. The core electron then goes onto an unoccupied higher energy level or becomes a free electron. The formerly occupied level is almost immediately filled with an electron of a higher energy level. The energy gap between these two levels is evacuated through the emission of either a X-Ray photon or an electron called Auger electron. X-Rays emitted through this process have energies which are specific to the probed atom energy levels and thus allow identification of the probed element

Fluorescence spectral lines, which are specific to each element, are usually named according to Siegbahn notation. X-Rays are hardly absorbed in films a few nanometers-thick so that we can assume that the intensity of the spectral lines is proportional to the total quantity of the probed element. As a result, in identical acquisition conditions, comparison of the areas of Kα and Lα spectral lines of Ge gives a relative comparison between the total quantities of Ge atoms in various SiGe films.

XRF Kα and Lα Ge lines were measured in Wavelength Dispersive mode (based on the selective reflection of a specific wavelength on a crystal according to Bragg's law) on a Rigaku AZX400 equipped with a Rhodium source, ten different crystals for the wavelength selection and two different detectors (a scintillation counter and a gaseous proportional counter).

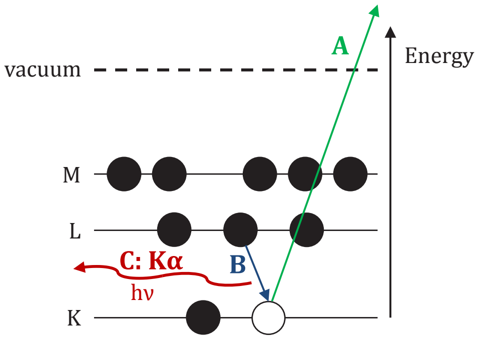

Figure C.1: Illustration of the process on which the XRF technique is based. The process follows the sequence A-B-C. With A: A core electron of the K-shell is emitted into vacuum due to the incoming X-Ray beam. B: An electron of the L-shell filled in the hole of the K-shell. C: the energy set free by process B induces emission of a X-Ray photon with a specific wavelength corresponding to the Kα spectral line.

D. X-Ray Diffraction (XRD)

X-Ray Diffraction (XRD) is a technique used to probe the crystal structure of materials. At the atomic scale, XRD corresponds to scattering of X-Ray waves by atoms organized in spatially periodic structures. The scattering process of X-Rays by a periodic structure results in constructive and destructive interferences which carry information about the crystal structure and the nature of the scattering elements. The intensity diffracted by a family of lattice planes {hkl} is maximum according to Bragg's law (see *Figure D.1*):

$$2d\sin\theta = n\lambda, \qquad \textbf{\textit{Equation D.1}}$$

where λ is the X-Ray wavelength, θ the angle between the incident wave vector and the family of diffracting planes {hkl}, and n the diffraction order.

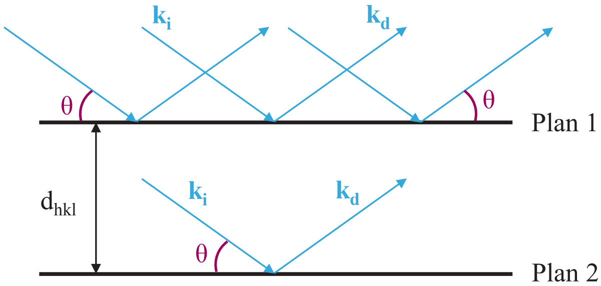

Figure D.1: Illustration of Bragg's conditions for diffraction by a family of planes {hkl}.

While there are many possible XRD experimental conditions, only one experimental set-up was used in this work to extract the composition and thickness of strained SiGe layers. As illustrated *Figure D.2*, the analysis was performed in a θ-2θ scan along the (004) direction perpendicular to the surface. A typical XRD spectra of a fully strained and homogeneous SiGe layers on a Si substrate is shown *Figure D.3*. In this case, the out-of-plane SiGe lattice parameter is higher than the one of Si according to Poisson's effect (see *Section I.2.2.3.*). It results in the {004} family of SiGe planes to have Bragg's conditions different from the ones of the Si substrate, and as a consequence a (004) diffraction peak shifted with respect to the one of Si.

The (004) SiGe peak position is only dependent on the out-of-plane SiGe lattice parameter at a fixed X-Ray wavelength. Assuming that the SiGe layer is fully strained, the Ge concentration can be extracted from Dismuke's law and Poisson's effect [Dismukes64]. The SiGe layer thickness can be extracted from the width of the main peak and of the interference fringes. The width of the main peak is inversely proportional to the thickness of the SiGe layer. One limitation of XRD is that the signal-to-noise ratio becomes too low for proper fitting for very thin films because the number of diffracting (004) planes is reduced to a few ones. Moreover, the width of the main peak is inversely proportional to the thickness of the SiGe layer so that interference fringes disappear when the SiGe thickness decreases. This effect also reduces fitting robustness.

XRD measurements were performed on a commercial Jordan Valley JVX7300 equipment in STMicroelectronics Crolles clean room.

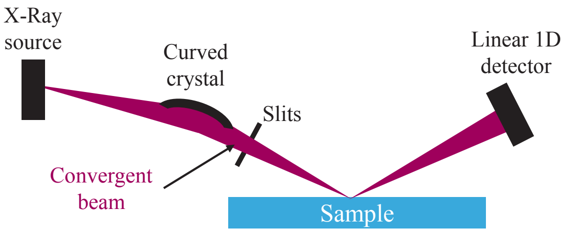

Figure D.2: JVX7300 diffraction setup.

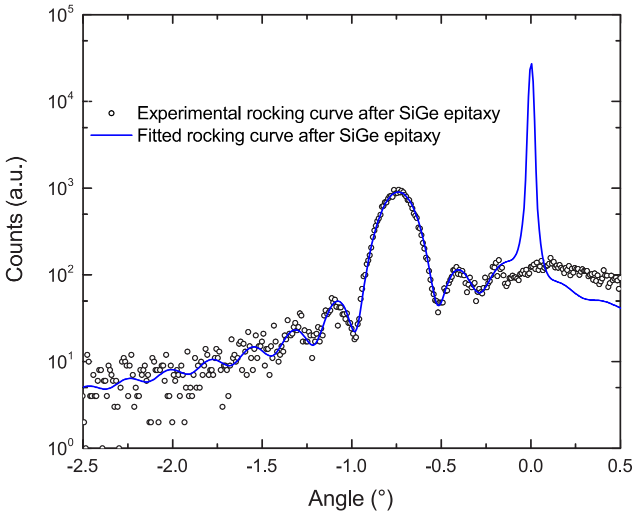

Figure D.3: Experimental and fitted rocking curves of an epitaxial SiGe layer on a bulk Si substrate. The Si peak is cut on the experimental rocking curve.

E. Atomic Force Microscopy (AFM)

Atomic Force Microscopy (AFM) is a surface characterization technique based on the measurement of interaction forces, among which electrostatic forces, van der Walls forces and short-range chemical forces, between the surface of the sample and a sharp tip attached to the free end of a cantilever. While many properties of the surface of the layer can be measured by AFM, such as viscoelasticity or adhesion strength, topography measurements only were performed in this study. As illustrated *Figure E.1*, the interaction forces induce a deflection of the cantilever, which is then measured thanks to the deflection of the reflected laser beam. Measurements were performed on 5x5 µm^2 squared surfaces on a Bruker Icon Head tool in tapping mode. There are two main formula of interest used in this manuscript about AFM characterization:

- Root Mean Squared (*RMS*): standard deviation of the *Z* (height) values with a given area:

$$RMS = \sqrt{\frac{\sum_{i=1}^{N}(Z_i - Z_{ave})}{N}}, \qquad \textbf{Equation E.1}$$

where Z_i is the current Z value, Z_{ave} the averaged Z with a given area and N the number of points with a given area.

- R_{max}: difference in height between the lowest and highest point on the surface relative to the mean plane.

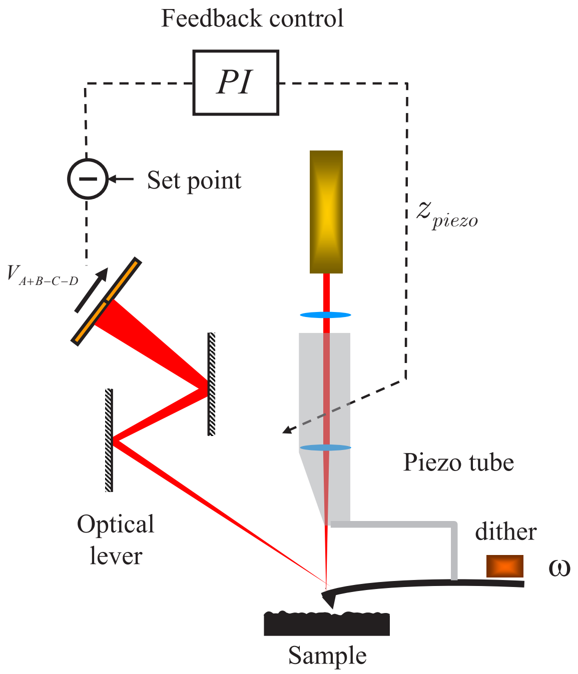
Feedback control
PI
Set point
z_{piezo}
$V_{A+B-C-D}$
Optical lever
Piezo tube
dither
ω
Sample

Figure F.1: Schematic view of principles and apparatus of the AFM characterization technique.

F. Transmission Electron Microscopy (TEM)

Transmission Electron Microscopy (TEM) is a technique that allows a broad range of characterization techniques, from imaging to diffraction and chemical analysis, at the nanometric scale. TEM is described in depth in many textbooks such as [Williams98] and the apparatus of a transmission electron microscope is shown *Figure F.1*. High Resolution TEM (HRTEM) with atomic resolution, which is a specific mode of TEM imaging, was performed in this thesis. In HRTEM mode, a parallel electron beam is formed through specific electromagnetic lenses and directed towards a thin lamella (less than 100 nm thick). The contrast of the image is a phase contrast due to interferences between the transmitted and diffracted beams. HRTEM is particularly dependent on the quality of the TEM lamella, and interpretation of HRTEM images must be cautiously done.

TEM lamella were prepared using standard Focused Ion Beam (FIB) and imaged in a JEOL 2010 equipped with a LaB_6 electron gun, and with an accelerating voltage of 200 kV.

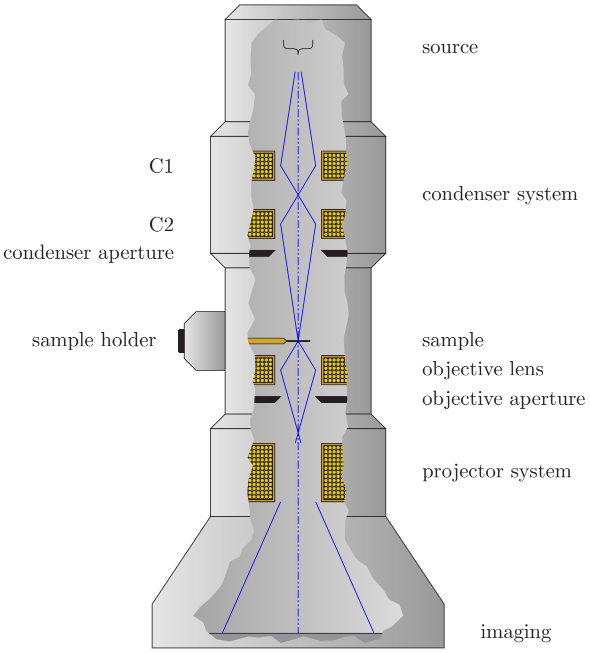
source
C1
C2
condenser aperture
condenser system
sample holder
sample
objective lens
objective aperture
projector system
imaging

Figure F.1: Schematic view of a Transmission Electron Microscope.

Résumé en français

Sommaire

Introduction **205**

Chapitre I - La technique de condensation appliquée aux technologies CMOS FD-SOI **206**

Introduction au Chapitre I 206

I.1. La technologie MOSFET, les films SGOI et la technique de condensation : limitations, potentiel, et problématiques 206

I.2. Procédés d'oxydation 207

Chapitre II - Les mécanismes et la cinétique de l'oxydation thermique du SiGe **208**

Introduction au Chapitre II 208

II.1. Cinétique d'oxydation et évolution de la composition du film SiGe 208

II.1.1. Le modèle de Deal et Grove *208*

II.1.2. Protocole expérimental *209*

II.1.3. Régime d'oxydation *209*

II.1.4. Méthode d'analyse: définition du Growth Rate Enhancement (GRE) *210*

II.1.5. Dépendance du GRE à la concentration initiale en Ge et à la température *210*

II.1.6. Evolution de la composition du film SiGe pendant l'oxydation *211*

II.1.7. Dépendance de la cinétique d'oxydation à la concentration en Ge à l'interface d'oxydation *212*

II.1.8. Conclusion de la partie II.1. *212*

II.2. Corrélation entre cinétique d'oxydation et densité de l'oxyde 212

II.2.1. Protocole expérimental *212*

II.2.2. Densité des oxydes thermiques *213*

II.2.3. Dépendance de la densité de l'oxyde aux paramètres du procédé d'oxydation *213*

II.2.4. Dépendance de la cinétique d'oxydation à la densité de l'oxyde *214*

II.2.5. Dépendance de la diffusion de l'O_2 à la densité de l'oxyde *214*

II.2.6. Conclusion de la partie II.2. *215*

Conclusion du Chapitre II 215

Chapitre III - Déformation et qualité cristalline de films SGOI fabriqués par condensation **217**

Introduction au Chapitre III 217

III.1. Déformation et défauts cristallins des films SGOI 217

III.1.1. Protocole expérimental *217*

III.1.2. Evolution de la déformation de films SGOI en fonction de la concentration en Ge *218*

III.1.3. Comparaison avec la littérature *218*

III.1.4. Discussion autour des mécanismes de relâchement de la déformation *219*

III.1.5. Révélation de défauts cristallins *220*
III.1.6. Conclusion de la partie III.1. .... *220*
III.2. Mesure de la qualité cristalline des films SGOI 221
III.2.1. Introduction à la technique MEIS *221*
III.2.2. Protocole expérimental *222*
III.2.3. Spectres MEIS *222*
III.2.4. Qualité cristalline des films SGOI *223*
Conclusion du Chapitre III 224

Conclusion **226**

Références **227**

Introduction

Entre une minute à consulter les réseaux sociaux sur son smartphone et une autre à lire le dernier best-seller sur sa liseuse, levons les yeux vers la façade d'un immeuble d'une mégalopole recouvert de panneaux publicitaires géants, approchons notre carte de transport d'une borne magnétique dans un tramway d'une ville moyenne, ou encore écoutons les signalements sonores indiquant le passage d'un train à une intersection avec une route de campagne, et nous voilà face à une débauche de systèmes électroniques aussi variés dans leur fonctionnement que dans leur application. Un point commun toutefois à ces systèmes ? Oui, le transistor. La complexification galopante des systèmes électroniques repose en effet principalement sur la miniaturisation de la brique élémentaire de ces systèmes électroniques qu'est le transistor.

Jusque dans les années 2000, la réduction des dimensions des transistors a obéit à une loi, ou plutôt une prophétie auto-réalisatrice, édictée par Gordon Moore en 1965 et nommée d'après lui. La loi de Moore prédit que la taille des transistors est divisée par deux tous les deux ans. Cette loi, dont la force est sa capacité à constituer un objectif clair et simple dans sa formulation pour l'industrie de la microélectronique, se heurte toutefois à des obstacles croissants à mesure que les dimensions des transistors se rapprochent de celles de quelques couches atomiques. La loi de Moore est désormais poussée dans ses retranchements grâce à l'introduction dans le transistor d'éléments nouveaux permettant d'augmenter les performances et/ou de réduire la consommation de ce dernier.

Parmi ces éléments figurent l'intégration d'un nouveau matériau, le SiGe contraint en compression, dans le canal d'un transistor dont l'architecture non-conventionnelle est de type FD-SOI (Fully-Depleted Silicon-On-Insulator). L'intérêt de films SiGe ultra-minces, contraints en compression, et sur isolant (SGOI: SiGe-On-Insulator) est double : ils bénéficient de la forte mobilité des trous dans le SiGe contraint en compression ainsi que du meilleur contrôle électrostatique des structures dites « sur isolant ». Les films SGOI présentant une forte concentration en Ge et une importante contrainte peuvent être fabriqués par une technique industrielle appelée condensation. Cette technique repose sur deux processus simultanés : l'oxydation thermique et sélective du SiGe (seul le Si est oxydé) et l'inter-diffusion du SiGe entre l'oxyde thermique et l'oxyde enterré qui se comporte comme une barrière à la diffusion.

L'utilisation de cette technique dans un environnement industriel nécessite de relever deux défis : maîtriser les mécanismes et la cinétique d'oxydation, et atteindre les plus fortes contraintes et qualités cristallines pour les films SGOI. L'organisation de ce résumé en français est la suivante :

- Le *Chapitre I* présente le contexte dans lequel s'inscrit ce travail de thèse et les fondements de ce dernier.
- Le *Chapitre II* traite des mécanismes et de la cinétique d'oxydation du SiGe.
- Le *Chapitre III* porte sur la caractérisation des contraintes et de la qualité cristalline des films SGOI fabriqués par condensation.

Chapitre I - La technique de condensation appliquée aux technologies CMOS FD-SOI

Introduction au *Chapitre I*

Dans ce premier chapitre, nous introduisons tout d'abord la brique élémentaire d'une majorité des systèmes électroniques : le MOSFET (Metal Oxide Semiconductor Field Effect Transistor). Ses limitations et l'intérêt que présente l'utilisation de canaux de type SGOI pour le MOSFET de type p (dont la conduction est assurée par les trous) sont soulignés. La technique de condensation et les deux problématiques de cette thèse, adressées dans les *Chapitre II* et *Chapitre III* respectivement, sont ensuite présentées. Enfin, les procédés d'oxydation thermique utilisés sont décrits.

I.1. La technologie MOSFET, les films SGOI et la technique de condensation : limitations, potentiel et problématiques

Si la technologie MOSFET a évolué sous de nombreux aspects depuis le premier circuit intégré commercialisé en 1971, ses principes de fonctionnement sont restés identiques. Ce travail portant sur le MOSFET de type p, représenté *Figure I.1*, nous nous concentrerons désormais sur ce dernier. La conductivité du canal entre la source et le drain, qui représente l'information binaire (« 0 » ou « 1 ») des systèmes logiques, est contrôlée par la tension appliquée à la grille.

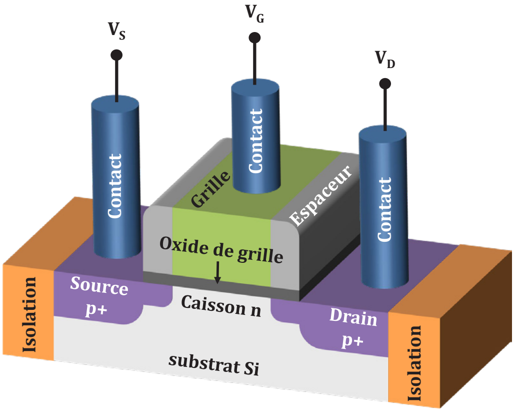

Figure I.1: Illustration schématique d'un MOSFET de type p.

Quant aux performances intrinsèques du transistor, elles sont fortement dépendantes au contrôle électrostatique du canal par la grille et à la mobilité des trous dans le canal. Tandis que l'architecture de type FD-SOI permet un meilleur contrôle électrostatique du canal par rapport aux architectures de transistor traditionnelles, les films SiGe contraints en compression présentent des mobilités de trous supérieures [Pillarisetty11]. Afin de bénéficier de ce double avantage, il est nécessaire de pouvoir fabriquer des films SiGe ultra-minces, contraints en compression, et sur isolant (SGOI : SiGe-On-Insulator) à l'aide d'un procédé industriel: la condensation [Tezuka01]. Cette technique, illustrée *Figure I.2*, repose sur deux processus simultanés : l'oxydation thermique et sélective du SiGe (seul le Si est oxydé) et l'inter-diffusion du SiGe entre l'oxyde thermique et l'oxyde enterré qui se comporte comme une barrière à la diffusion. Trois caractéristiques font de ce procédé l'un des plus pertinents pour la fabrication de ces films dans un environnement industriel :

- La condensation permet la fabrication de films SGOI dans les zones de transistors de type p uniquement (les films SGOI ne présentent pas d'intérêt pour les transistors de type n)

- Des films SGOI non-relaxés (ou autrement dit totalement contraints à la maille du Si), de quelques nanomètres seulement, et présentant des concentrations en Ge de l'ordre de 50% peuvent être fabriqués.

- La condensation ne nécessite l'usage que de substrats conventionnels et de procédés compatibles avec le reste de la chaîne de production des systèmes électroniques.

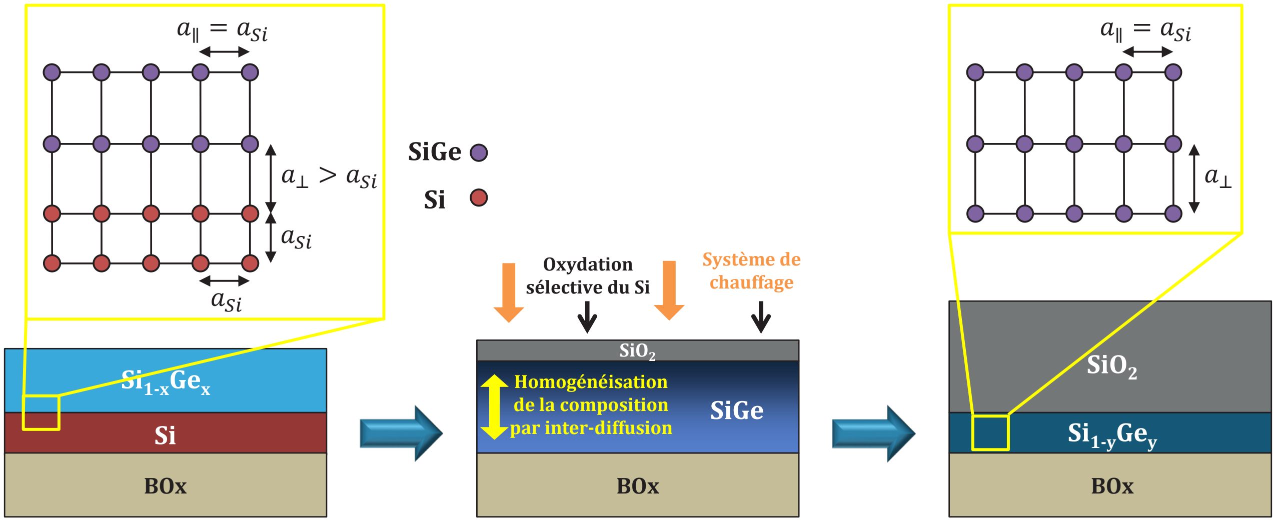

Figure I.2: Schéma de principe du procédé de condensation. BOx est l'abréviation de «Buried Oxide» pour «oxyde enterré», a_{Si}, $a_{\perp}$ et $a_{//}$ sont les paramètres de maille du Si relaxé, du SiGe dans le plan et du SiGe hors-plan.

L'utilisation de cette technique dans un environnement industriel nécessite de relever deux défis :

- **Maîtriser les mécanismes et la cinétique d'oxydation**. Il est important d'étudier plusieurs procédés d'oxydation à la fois industriels et pertinents au regard des besoins technologiques actuels. Cette problématique fait l'objet du *Chapitre II*.

- **Atteindre les plus fortes contraintes et qualités cristallines pour les films SGOI**. Dans cette optique, la compréhension de l'évolution des contraintes et de la qualité des films SGOI en fonctions des paramètres du procédé de condensation se révèle indispensable pour l'optimisation de ce dernier. Cette problématique est adressée au *Chapitre III*.

I.2. Procédés d'oxydation

Deux principales caractéristiques sont associées aux procédés d'oxydation thermique : le type d'équipement et la chimie d'oxydation. Les types d'équipement utilisés pendant cette thèse sont :

- Le four : les gaz introduits dans la chambre sont chauffés par des résistances et ce type d'équipement permet de traiter plusieurs dizaines de plaquettes à la fois.
- Les systèmes de recuit rapide (RTP : Rapid Thermal Processing). Une unique plaquette est chauffée par le rayonnement émis par un réseau de lampes halogènes au tungstène situé au-dessus de la plaquette. Ce type d'équipement permet des montées et descentes en température bien plus agressives que le four (de l'ordre de 50°C/s pour le RTP contre 50°C/minute pour le four).

Les deux atmosphères oxydantes utilisées pendant cette thèse sont :

- O_2 pur à 740 Torr, appelée oxydation sèche.
- 33% H_2 + 66% O_2 à une pression totale de 7 Torr, appelée oxydation ISSG (In-Situ Steam Generation). Il a été démontré que cette atmosphère conduit à la génération de radicaux d'oxygène O* qui sont l'espèce oxydante principale de cette atmosphère [Kee00].

Les procédés d'oxydation étudiés et combinant un de ces types d'équipement et une de ces chimies sont :

- Oxydation sèche en four
- Oxydation sèche par RTP
- Oxydation ISSG par RTP, abrégée par la suite en oxydation ISSG

Chapitre II - Les mécanismes et la cinétique de l'oxydation thermique du SiGe

Introduction au Chapitre II

La cinétique de l'oxydation sèche en four et par RTP et de l'oxydation ISSG est tout d'abord décrite en fonction de l'évolution de la composition du film SiGe sous l'oxyde. La deuxième partie de ce chapitre se penche sur la corrélation entre la cinétique d'oxydation et la densité de l'oxyde thermique en croissance. Enfin, la dépendance de la diffusion de l'O_2 dans SiO_2, dont dépend la cinétique de l'oxydation sèche, est discutée.

II.1. Cinétique d'oxydation et évolution de la composition du film SiGe

II.1.1. Le modèle de Deal et Grove

La « consommation » d'un volume de Si conduit à la croissance de 2.25 volumes de SiO_2 en raison de la différence de densité entre les deux matériaux. Quant à la cinétique de l'oxydation du SiGe, elle est généralement décrite par le modèle de Deal et Grove [Deal65]. Le modèle, illustré en *Figure II.*1, décrit l'oxydation par l'enchaînement des trois étapes suivantes :

- L'espèce oxydante est absorbée en surface de l'oxyde depuis l'atmosphère.
- L'espèce oxydante diffuse à travers l'oxyde en direction de l'interface oxyde-SiGe. Ce processus obéit à la loi de Fick.
- L'espèce oxydante réagit à l'interface oxyde-SiGe avec les atomes de Si pour former du SiO_2.

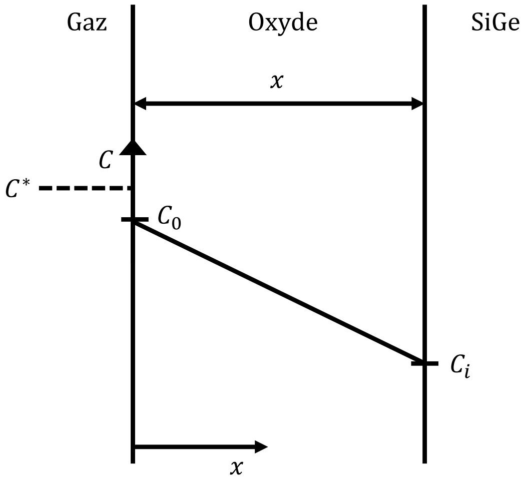

Figure II.1: Le modèle de Deal et Grove de l'oxydation thermique du silicium. C est la concentration en espèces oxydantes à une profondeur donnée et x l'épaisseur d'oxyde. Adapté de [Deal65].

Le traitement mathématique de ces étapes conduit à l'établissement d'une loi cinétique dite linéaire-parabolique :

$$\frac{x(t)}{A/2} = \left[1 + \frac{t+\tau}{A^2/4B}\right]^{\frac{1}{2}} - 1, \qquad \textbf{\textit{Equation II.1}}$$

où x, t et τ sont l'épaisseur d'oxyde, le temps d'oxydation et une constante, et où B/A, la constante linéaire, et B, la constance parabolique, dépendent des paramètres physiques du modèle et du procédé d'oxydation.

Nous pouvons remarquer que lorsque $t \gg \frac{A^2}{4B}$, la loi cinétique est correctement décrite après approximation par l'équation parabolique suivante:

$$x(t)^2 \simeq Bt. \qquad \textbf{\textit{Equation II.2}}$$

Dans ce cas, la cinétique d'oxydation est imitée par le processus de diffusion de l'espèce oxydante à travers l'oxyde.

II.1.2. Protocole expérimental

Trois concentrations en Ge (0%, 10% et 30%) ont été utilisées afin d'identifier l'influence de la composition du film SiGe sur la cinétique d'oxydation. Les films SiGe contraints en compression par le substrat, tel qu'illustré *Figure I.2*, et déposés par épitaxie, présentent des épaisseurs de l'ordre de 20 nm. Pour chacun des procédés d'oxydation décrit en *partie I.2.*, différentes températures et durées d'oxydation ont été utilisées. L'épaisseur des oxydes thermiques ainsi formés et la composition des films SiGe en fonction de la profondeur ont été déterminés par ellipsométrie et par spectrométrie de masse à ionisation secondaire (SIMS : Secondary Ion Mass Spectroscopy) respectivement.

Deux hypothèses de travail, sur lesquelles repose le principe de la technique de condensation, ont été vérifiées au préalable:

- Une étude par spectroscopie de photoélectrons à rayons X (XPS : X-Ray Photoelectron Spectroscopy) nous a permis de montrer que l'oxyde thermique formé sur SiGe est le SiO_2 (dioxyde de silicium) en phase amorphe quel que soit le procédé d'oxydation utilisé.

- La conservation de la totalité du Ge, repoussé dans le film SiGe à l'interface avec l'oxyde lors de l'oxydation, a été démontrée par fluorescence de rayons X (XRF : X-Ray Fluorescence).

II.1.3. Régime d'oxydation

Pour les trois procédés d'oxydation, plus la concentration en Ge du film SiGe initial est élevée, plus l'oxyde est épais à température et temps d'oxydation égaux (voir *Figure II.2*). Il est à souligner que l'effet de la concentration en Ge sur la cinétique d'oxydation est nettement moins important pour le cas de l'oxydation ISSG que pour les oxydations sèches. L'effet du Ge sur la cinétique d'oxydation est également observé pour les oxydations sèches par RTP à 1000°C et 1100°C, et pour les oxydations ISSG à 850°C et 1050°C.

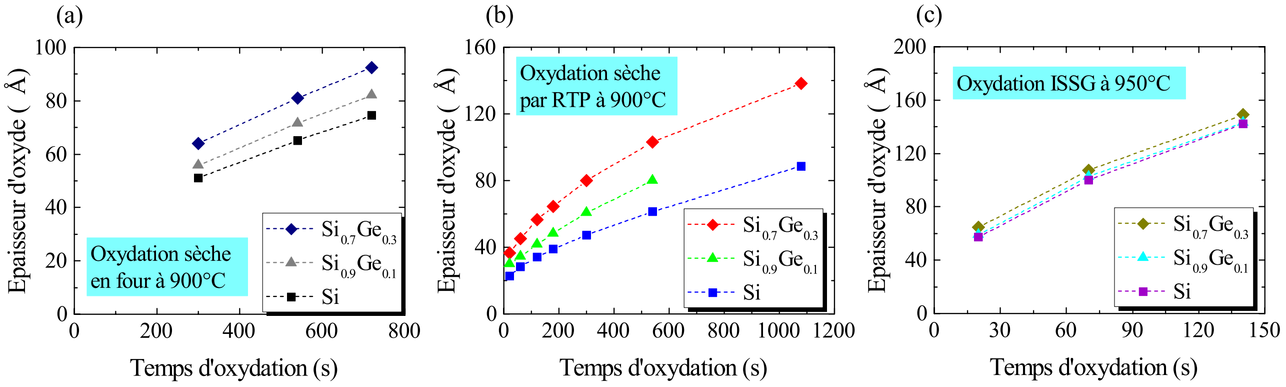

Figure II.2: Epaisseur d'oxyde en fonction du temps d'oxydation pour (a) l'oxydation sèche en four à 900°C, (b) l'oxydation sèche par RTP à 900°C et (c) pour l'oxydation ISSG à 950°C de couches Si, $Si_{0.9}Ge_{0.1}$ et $Si_{0.7}Ge_{0.3}$. Les points sont les épaisseurs expérimentales.

La relation linéaire entre le carré de l'épaisseur d'oxyde et le temps d'oxydation mise en évidence en *Figure II.3* montre la nature parabolique du régime d'oxydation. D'après le modèle de Deal et Grove présenté en *partie II.1.*, ce régime correspond à une oxydation limitée par la diffusion de l'espèce oxydante, O_2 dans le cas des oxydations sèches et O* dans celui de l'oxydation ISSG, à travers l'oxyde thermique en croissance.

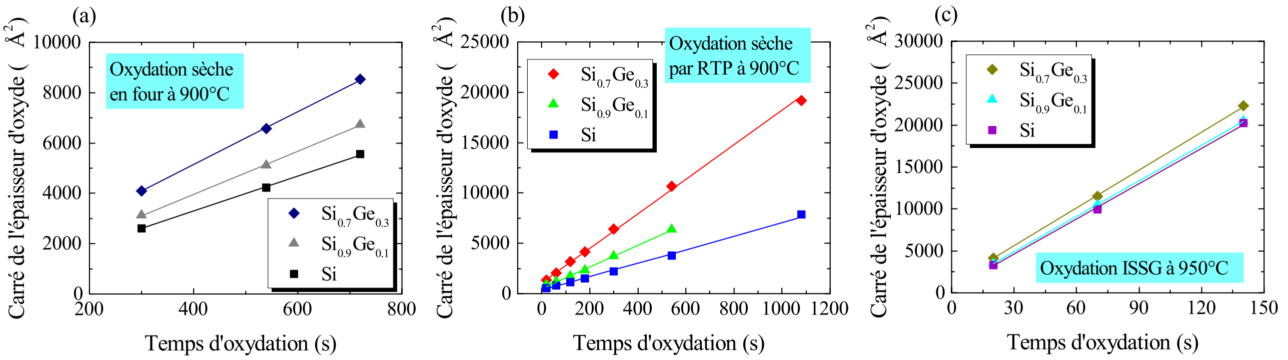

Figure II.3: Carré de l'épaisseur d'oxyde en fonction du temps d'oxydation pour (a) l'oxydation sèche en four à 900°C, (b) l'oxydation sèche par RTP à 900°C et pour (c) l'oxydation ISSG à 950°C de couches Si, $Si_{0.9}Ge_{0.1}$ et $Si_{0.7}Ge_{0.3}$. Les points sont les épaisseurs expérimentales et les lignes sont les résultats des ajutements des lois paraboliques aux points expérimentaux.

II.1.4. Méthode d'analyse: définition du Growth Rate Enhancement (GRE)

La méthode d'analyse quantitative développée lors de ce travail de thèse est désormais décrite. Elle repose sur la définition d'un terme noté GRE (Growth Rate Enhancement) et définit comme le rapport, à temps d'oxydation égal, de la vitesse de croissance de l'oxyde sur SiGe à celle de l'oxyde crû sur Si. En termes qualitatifs, le GRE est un indicateur de l'augmentation de la vitesse d'oxydation causé par la présence de Ge. Du fait de la nature parabolique du régime d'oxydation, le GRE se réduit à une valeur unique pour une combinaison unique type de procédé-concentration initiale en Ge-température d'oxydation et est égal au rapport des coefficients paraboliques:

$$GRE = \frac{\alpha\left(Concentration\ initiale\ SiGe, Procédé, T\right)}{\alpha\left(Si, Procédé, T\right)}, \qquad \textbf{Equation II.3}$$

où α, *Concentration initiale SiGe*, *Procédé* et T sont la constante parabolique extraite de l'ajustement des données expérimentales à une loi parabolique (voir *Figure II.3*), la concentration en Ge du film SiGe épitaxié (0%, 10% ou 30%), le procédé d'oxydation (oxydation sèche en four, oxydation sèche par RTP ou oxydation ISSG) et la température. Cette définition est doublement justifiée: les mécanismes de l'oxydation (diffusion des espèces oxydantes etc...) font intervenir la vitesse de croissance de l'oxyde et non directement l'épaisseur d'oxyde; et deuxièmement, cette définition nous permet de nous affranchir de la diminution de la vitesse d'oxydation du simple fait de l'épaisseur croissante d'oxyde, et donc de décorréler cet effet de l'influence du procédé d'oxydation et du Ge sur la cinétique d'oxydation. La définition du GRE est illustrée en *Figure II.4*.

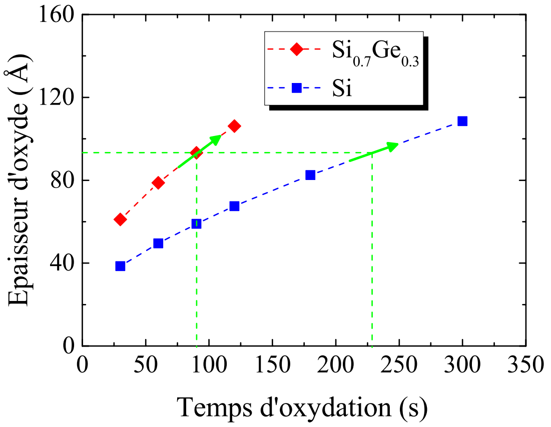

Figure II.4: Représentation schématique de la définition du GRE pour le cas de l'oxydation sèche par RTP de $Si_{0.7}Ge_{0.3}$ à 1000°C. Les flèches sont tangentes aux courbes et représentent les vitesses de croissance de l'oxyde.

II.1.5. Dépendance du GRE à la concentration initiale en Ge et à la température

La *Figure II.5* nous permet de mettre en évidence l'influence de nombreux paramètres sur le GRE :

- (1) la concentration initiale en Ge
- (2) la manière dont l'énergie thermique est apportée au système (oxydation sèche en four versus oxydation sèche par RTP)
- (3) la température
- *Figure II.5 (a)* versus *Figure II.5 (b)* - la nature de l'espèce oxydante: O_2 ou O* (oxydation sèche par RTP versus oxydation ISSG)

Néanmoins, ces multiples influences ne permettent pas d'identifier les mécanismes influençant directement la cinétique d'oxydation. Nous proposons de considérer par la suite l'évolution de la composition du film SiGe pendant son oxydation, que nous savons dépendre de tous les paramètres précédemment cités, afin d'apporter davantage de compréhension à propos du GRE.

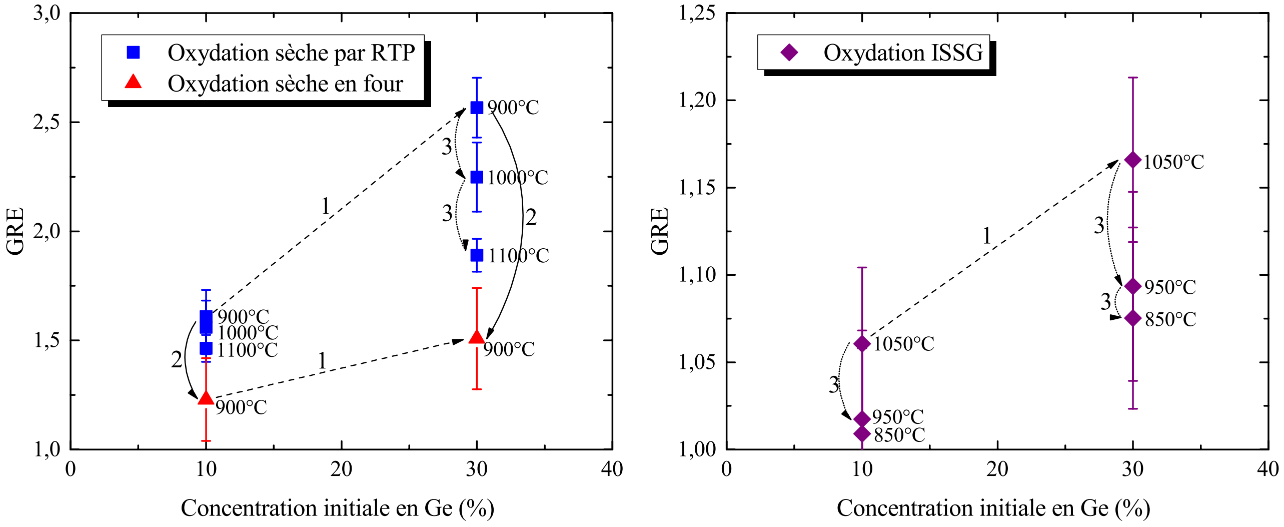

Figure II.5: GRE en fonction de la concentration initiale en Ge pour (a) l'oxydation sèche en four et par RTP et pour (b) l'oxydation ISSG. L'influence de (1) la concentration initiale en Ge, de (2) la manière dont l'énergie thermique est apportée au système et de (3) la température est indiquée par des flèches.

II.1.6. Evolution de la composition du film SiGe pendant l'oxydation

Deux mécanismes thermiquement activés sont à l'origine de l'évolution du profil en concentration en Ge du film SiGe :

- L'oxydation sélective du Si repousse le Ge sous l'oxyde en croissance et tend donc à augmenter la concentration en Ge à l'interface oxyde-SiGe : c'est l'effet « pile-up ».
- L'inter-diffusion du SiGe, à l'inverse, tend à lisser le profil en concentration en Ge.

L'évolution du profil en concentration en Ge, et en particulier la concentration à l'interface oxyde-SiGe, dépend de la compétition entre ces deux mécanismes. A basse température, l'inter-diffusion dans le SiGe est très faible et l'effet « pile-up » dominant, ce qui conduit à la formation d'une couche riche en Ge sous l'oxyde (entre 45% et 50% de concentration en Ge pour le cas de l'oxydation sèche par RTP de $Si_{0.7}Ge_{0.3}$ à 900°C), comme illustré en *Figure II.6 (a)*. Lorsque la température augmente, les deux mécanismes s'accélèrent. Du fait d'une importante énergie d'activation (autour de 4 eV [Kube10]), l'inter-diffusion accélèrent de façon plus marquée que l'oxydation (qui présente des énergies d'activation de l'ordre de 2 eV et 1 eV pour l'oxydation sèche par RTP et l'oxydation ISSG respectivement).

La *Figure II.6* nous permet de souligner un deuxième point : la variation de la concentration en Ge à l'interface oxyde-SiGe est faible au cours du temps et reste, pour le cas de l'oxydation sèche par RTP, autour de 33% à 1100°C, 42% à 1000°C, et 48% à 900°C.

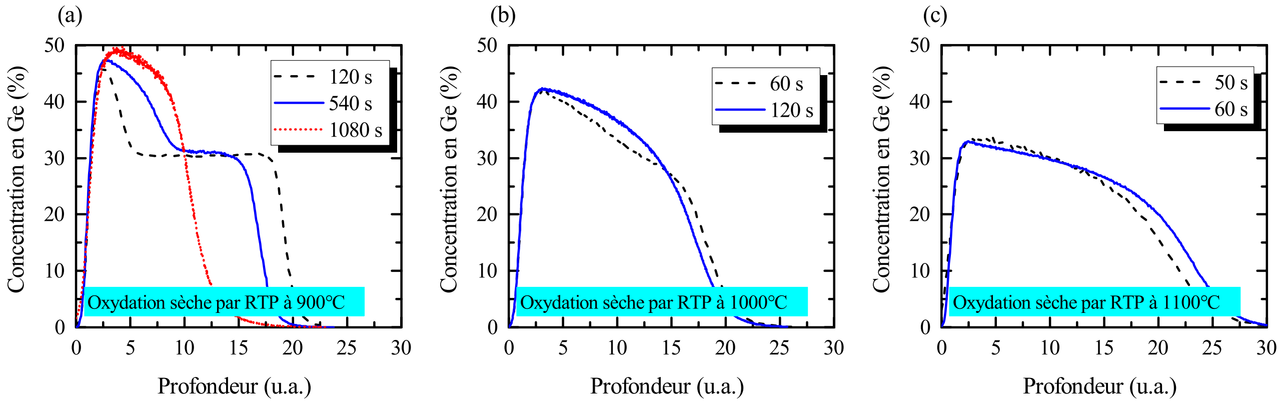

Figure II.6: Profils en concentration en Ge après oxydation sèche par RTP à (a) 900°C, (b) 1000°C and (c) 1100°C. L'axe des x est systématiquement décalé afin de positionner l'interface oxyde-SiGe à la profondeur 0.

II.1.7. Dépendance de la cinétique d'oxydation à la concentration en Ge à l'interface d'oxydation

Nous pouvons observer en *Figure II.7* que le GRE augmente avec la concentration en Ge à l'interface oxyde-SiGe pour chacun des trois procédés d'oxydation. Pour l'oxydation sèche par RTP, les influences de la concentration initiale en Ge et de la température discutées en *partie II.5.* sont ainsi réduits à une unique influence de la concentration en Ge à l'interface oxyde-SiGe.

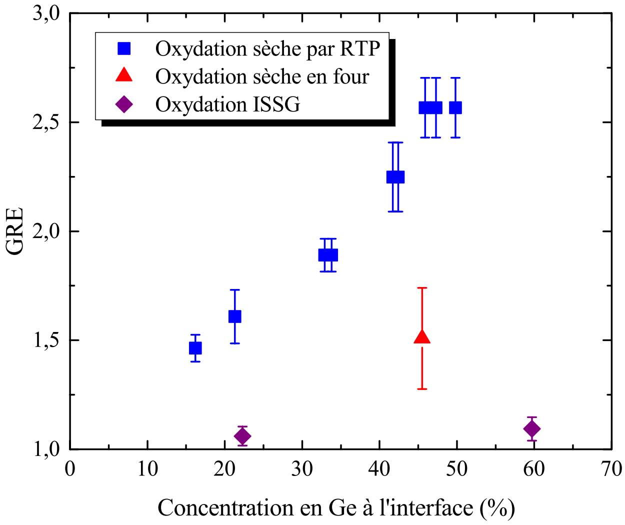

Figure II.7: GRE en fonction de la concentration en Ge à l'interface oxyde-SiGe.

II.1.8. Conclusion de la partie II.1.

La cinétique d'oxydation est faiblement dépendante de la concentration en Ge pour le cas de l'oxydation ISSG tandis qu'elle se trouve accélérée par la présence de Ge pour le cas de l'oxydation sèche. Ayant montré que la cinétique d'oxydation est limitée par la diffusion de l'espèce oxydante à travers l'oxyde, il semble que la présence de Ge influence la diffusion de l'espèce oxydante à travers l'oxyde. Il a été démontré dans la littérature que la diffusion d'O_2 dans SiO_2 dépend de la densité de l'oxyde. C'est pourquoi nous nous penchons dans la partie suivante sur la dépendance de la densité de l'oxyde thermique crût sur SiGe aux conditions du procédé d'oxydation.

II.2. Corrélation entre cinétique d'oxydation et densité de l'oxyde

II.2.1. Protocole expérimental

Les densités des oxydes thermiques crûs sur Si et SiGe par différents procédés d'oxydation ont été mesurées par réflectivité de rayons X à 500 eV sur la ligne SEXTANTS du synchrotron Soleil. Les spectres de réflectivité ont ensuite été ajustés aux spectres théoriques à l'aide du programme dyna.

II.2.2. Densité des oxydes thermiques

L'évolution de la densité en fonction des paramètres du procédé d'oxydation et de la concentration en Ge est mise en évidence en *Figure II.8* :

- 1: Concentration initiale en Ge : pour l'oxydation sèche par RTP et l'oxydation ISSG, la densité de l'oxyde diminue lorsque la concentration initiale en Ge augmente.
- 2: Type de procédé : la densité de l'oxyde crû sur $Si_{0.7}Ge_{0.3}$ par oxydation sèche en four est plus élevée que celle de l'oxyde crût par oxydation sèche par RTP.
- 3: Température : la densité des oxydes crûs sur $Si_{0.7}Ge_{0.3}$ par oxydation sèche par RTP augmente avec la température, à l'inverse des oxydes crûs sur Si par le même procédé.

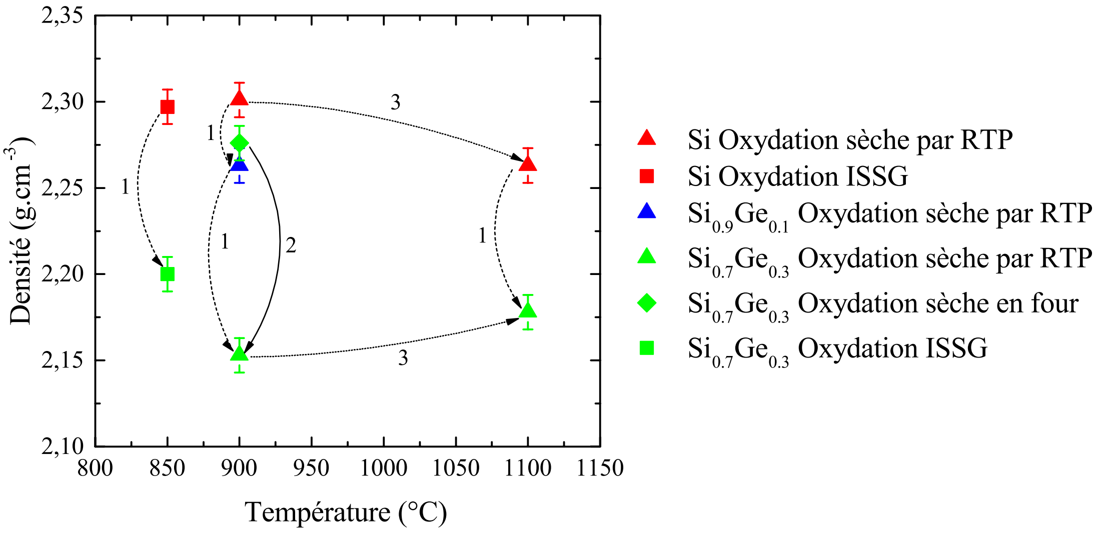

Figure II.8: Evolution de la densité des oxydes crûs sur Si et SiGe en fonction de la concentration initiale en Ge et des paramètres du procédé d'oxydation. Les influences de la concentration initiale en Ge, du type de procédé et de la température sont indiquées par des flèches (voir texte).

Dans la continuité de la conclusion de la *partie II.1.5.*, nous ne pouvons pas identifier les mécanismes à l'origine directe des variations de densité observées en *Figure II.8*. Nous considérons dans la partie suivante la concentration en Ge à l'interface oxyde-SiGe.

II.2.3. Dépendance de la densité de l'oxyde aux paramètres du procédé d'oxydation

La *Figure II.9* montre que plus la concentration en Ge à l'interface est élevée, plus la densité de l'oxyde est faible. Tel que proposé par Holland et al. [Holland87], nous suggérons que le plus grand paramètre de maille du SiGe pourrait réduire le stress compressif dans l'oxyde à l'interface oxyde-SiGe engendré par la différence de densité atomique entre les deux matériaux. La réduction de ce stress serait alors à l'origine de la croissance d'un oxyde moins dense. La densité systématiquement plus faible à 1100°C qu'à 900°C pour l'oxydation sèche par RTP pourrait quant à elle provenir du fluage de l'oxyde qui tendrait à diminuer le stress et par conséquent la densité de l'oxyde [EerNisse77]. Enfin, nous soulignons que, tous paramètres égaux par ailleurs, l'oxyde crû par oxydation sèche en four est plus dense que celui crû par oxydation sèche par RTP.

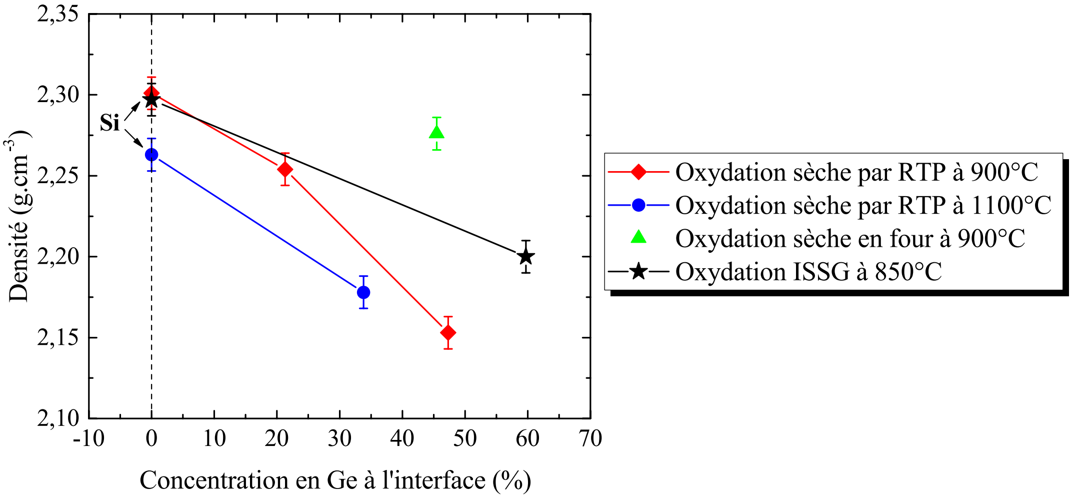

Figure II.9: Evolution de la densité de l'oxyde en fonction de la concentration en Ge à l'interface.

Ayant montré et commenté les influences des paramètres matériaux et du procédé d'oxydation sur le densité de l'oxyde, nous nous penchons désormais sur la dépendance de la cinétique d'oxydation à cette densité.

II.2.4. Dépendance de la cinétique d'oxydation à la densité de l'oxyde

Conformément à une oxydation limitée par la diffusion d'O_2 à travers l'oxyde, la cinétique de l'oxydation sèche augmente lorsque la densité de l'oxyde diminue (voir *Figure II.10*). En effet, les molécules d'O_2 diffusent à travers le SiO_2 de site interstitiel en site interstitiel d'autant plus rapidement que la densité de l'oxyde est faible et donc les sites interstitiels grands [Bongiorno04]. Le fait que le cas de l'oxydation sèche en four à 900°C soit aligné avec l'oxydation sèche par RTP à la même température confirme la dépendance directe de la cinétique d'oxydation et de la diffusion d'O_2 à travers l'oxyde à la densité. Quant au décalage précédemment mentionné dû à la seule température, il sera discuté en partie suivante.

La densité de l'oxyde n'influence presque pas la cinétique d'oxydation ISSG. Il est logique, compte tenu de la petite taille des radicaux d'oxygène par rapport aux molécules d'O_2, que la diffusion de ces radicaux ne soit pas affectée, ou ne le soit que faiblement, par la densité de l'oxyde.

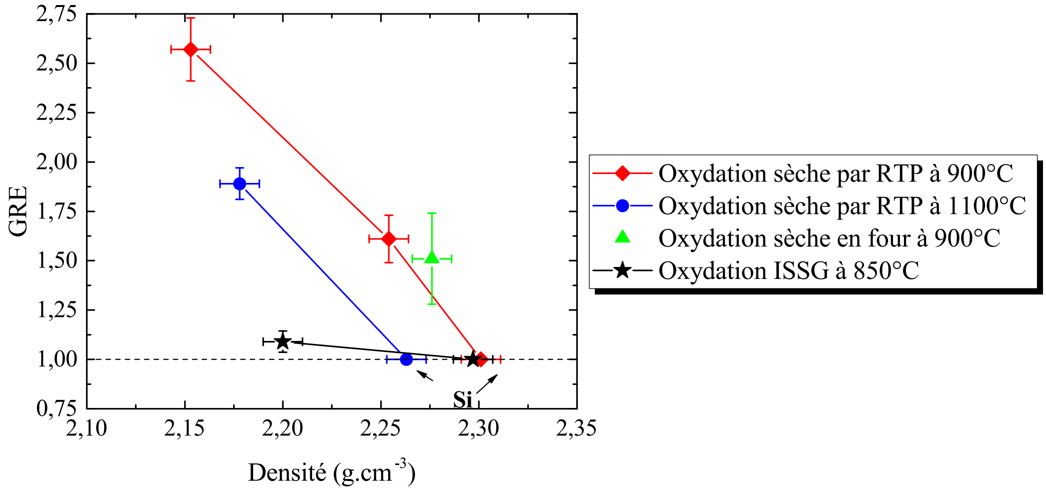

Figure II.10: Evolution du GRE en fonction de la densité de l'oxyde.

Grâce à la dépendance du GRE au coefficient de diffusion de l'espèce oxydante dans l'oxyde, nous pouvons discuter spécifiquement de l'influence de la densité de l'oxyde sur la diffusion de l'O_2 dans SiO_2.

II.2.5. Dépendance de la diffusion de l'O_2 à la densité de l'oxyde

Des considérations thermodynamiques quant à la dépendance du coefficient de diffusion à la température et à la pression nous permettent de proposer le modèle suivant pour le coefficient de diffusion d'O_2 dans SiO_2

[Mehrer07] :

$$D = \begin{cases} D_0 \exp\left(-\dfrac{E}{k_B T}\right) & \text{dans l'oxyde crû sur Si} \\ D_0 \exp\left(-\dfrac{E+\Delta E}{k_B T}\right) & \text{dans l'oxyde crû sur SiGe} \end{cases} , \qquad \textbf{Equation II.4}$$

où T est la température, k_B la constante de Boltzmann, E l'énergie d'activation de la diffusion d'O_2 dans un SiO_2 crû sur Si et ΔE la modulation de la barrière à la diffusion induite par la variation de densité. Il est à noter que la variation de densité induite par la seule température d'oxydation est incluse dans le terme E. Combinant l'*Equation II.1* à l'*Equation II.3* et à la dépendance de la constante parabolique au coefficient de diffusion démontrée par Deal et Grove [Deal65], le GRE s'écrit :

$$GRE = \exp\left(-\frac{\Delta E}{k_B T}\right). \qquad \textbf{Equation II.5}$$

Nous observons expérimentalement que la modulation de la barrière à la diffusion augmente linéairement avec la densité de l'oxyde (voir *Figure II.11*), conformément aux prédictions théoriques de Cui et al. [Cui09].

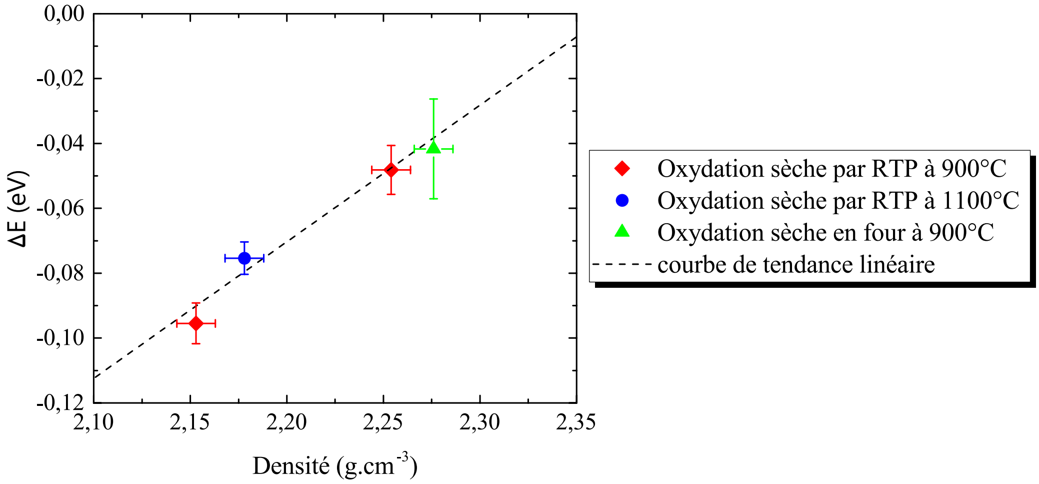

Figure II.11: Evolution de la modulation de la barrière à la diffusion d'O_2 dans SiO_2 en fonction de la densité du SiO_2.

II.2.6. Conclusion de la partie II.2.

L'influence de chacun des paramètres d'oxydation (chimie d'oxydation : oxydation sèche versus ISSG, type de procédé : four versus RTP, concentration initiale en Ge, température et concentration en Ge à l'interface) a été discutée. Nous retiendrons en particulier que tous paramètres égaux par ailleurs, plus la concentration en Ge à l'interface oxyde-SiGe est importante, moins l'oxyde formé est dense. La densité de l'oxyde est également d'autant plus faible que la température d'oxydation est élevée.

La dépendance directe de la cinétique d'oxydation sèche à la densité a ensuite été mise en évidence : moins l'oxyde est dense, plus la diffusion d'O_2 dans SiO_2, et par conséquent la cinétique d'oxydation, sont rapides. Quant à l'oxydation ISSG, elle ne dépend pratiquement pas de la densité de l'oxyde, indiquant ainsi la faible dépendance de la diffusion des radicaux d'oxygène O* à la densité de l'oxyde.

Enfin, un modèle du coefficient de diffusion de l'O_2 dans SiO_2 a été proposé. Ce dernier dépend de la densité de l'oxyde à travers la modulation de la barrière à la diffusion, modulation qui se trouve observer une variation linéaire par rapport à la densité.

Conclusion du Chapitre II

Ce chapitre a permis d'apporter davantage de compréhension concernant les mécanismes et la cinétique d’oxydation du SiGe qui doivent être finement maîtrisés pour une utilisation industrielle du procédé de condensation.

Nous avons dans un premier temps montré que pour les trois procédés d’oxydation étudiés, l’oxydation sèche en four, l’oxydation sèche par RTP et l’oxydation ISSG, la cinétique d’oxydation est déterminée par la diffusion de l’espèce oxydante à travers l’oxyde. Tandis que l’oxydation ISSG est peu dépendante à la présence de Ge, l’oxydation sèche du SiGe est plus rapide que celle du Si. La définition d’une méthode d’analyse pertinente au regard du régime d’oxydation observé nous a permis de mettre en évidence une corrélation entre la cinétique d’oxydation, la diffusion d’O_2 dans SiO_2 et la densité de l’oxyde. La diffusion des radicaux d’oxygène O*, qui sont les principales espèces oxydantes de l’oxydation ISSG, est largement indépendante de la densité de l’oxyde. Nous avons ensuite clarifié l’influence du Ge et de la température d’oxydation sur la densité de l’oxyde: la densité diminue lorsque la concentration en Ge à l’interface avec l’oxyde et la température augmentent. Le plus grand paramètre de maille du SiGe pourrait être à l’origine de la variation de densité de l’oxyde due à la présence de Ge tandis que le fluage de l’oxyde à haute température a été suggéré en tant que mécanisme à l’origine de l’influence de la température sur la densité. Enfin, cette étude s’est conclue avec la proposition d’un modèle de coefficient de diffusion de l’O_2 dans SiO_2, qui se trouve dépendre de la densité à travers la modulation de la barrière à la diffusion.

Chapitre III - Déformation et qualité cristalline de films SGOI fabriqués par condensation

Introduction au Chapitre III

Nous commençons par décrire l’évolution de la contrainte des films SGOI fabriqués par condensation à haute température en fonction de la concentration en Ge. Les mécanismes de relâchement des contraintes sont discutés à la lumière de la comparaison avec la littérature, de la nature des interfaces du film SGOI et des contraintes des films SGOI fabriqués par condensation à basse température. Ensuite, le nombre d’atomes déplacés des sites cristallins des films SGOI, qui est un indicateur de la qualité cristalline, est mesuré en fonction de la profondeur dans le film. Les effets du procédé de condensation et de la présence intrinsèque de Ge sur la qualité cristalline sont soulignés.

III.1. Déformation et défauts cristallins des films SGOI

III.1.1. Protocole expérimental

Deux types de procédé de condensation, dont les profiles en température sont représentés en *Figure III.1*, sont discutés dans cette *partie III.1.* :

- L’oxydation sèche par RTP à haute température : la température de condensation est réduite par paliers de 100°C, en commençant à 1100°C, afin que cette dernière demeure toujours inférieure à la température de fusion du SiGe qui, elle, diminue au cours du procédé du fait de l’augmentation de la concentration en Ge. Ce type de procédé conduit à l’élaboration de films SGOI relativement homogènes en composition grâce à une forte diffusion du SiGe (voir *partie II.1.6.*).

- L’oxydation ISSG à basse température : l’oxydation ISSG à 850°C d’un film $Si_{0.7}Ge_{0.3}$ conduit à la formation sous l’oxyde thermique d’une couche enrichie à 60% de Ge par effet « pile-up » (voir *partie II.1.6.*). La faible température du procédé ne permet pas la diffusion à l’interface $Si_{0.7}Ge_{0.3}$-Si. La condensation est arrêtée lorsque la couche enrichie à 60% de Ge constitue la totalité du film SGOI tel qu’illustré en *Figure III.2*.

Les temps des procédés de condensation ont été calibrés grâce aux résultats de cinétique d’oxydation présentés en *Chapitre II*.

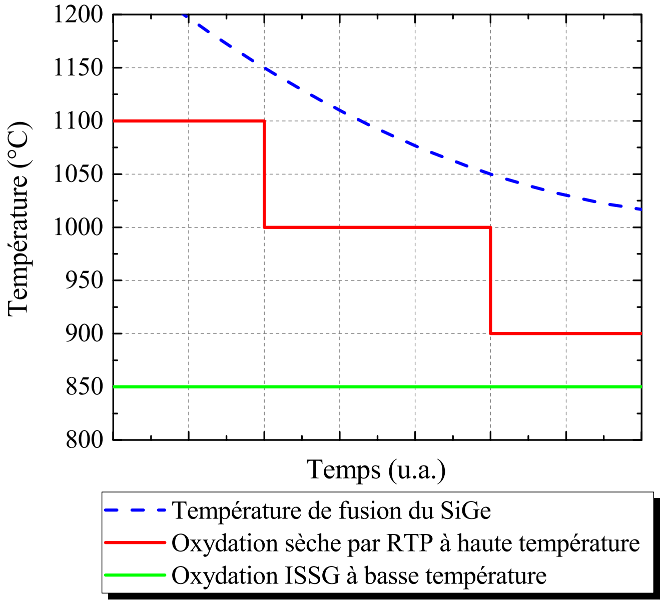

Figure III.1: Evolution de la température de fusion du SiGe au cours du procédé de condensation et des températures des deux procédés de condensation décrits dans le texte. Pour l’oxydation sèche par RTP à haute température, la température de condensation est réduite de 100°C lorsque l’écart entre cette dernière et la température de fusion du SiGe n’est plus que de 50°C.

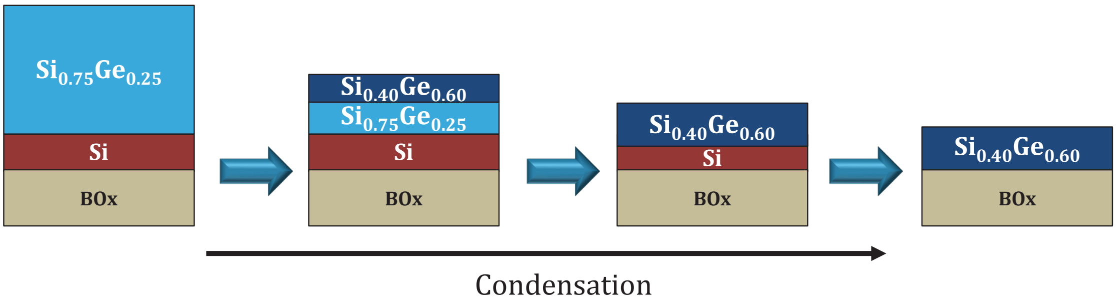

Figure III.2: Illustration du procédé de condensation basé sur l'oxydation ISSG à basse température et utilisé pour fabriquer des films SGOI présentant des concentrations en Ge de 60%. L'oxyde thermique n'est pas montré sur la figure.

III.1.2. Evolution de la déformation de films SGOI en fonction de la concentration en Ge

Les contraintes (que nous assimilons à la contrainte relative au paramètre de maille du SiGe non contraint et non à celui du Si) des films SGOI fabriqués par oxydation sèche par RTP à haute température sont tracées en fonction de la concentration en Ge en *Figure III.3*. La courbe « pseudomorphique SiGe » correspond à la contrainte théorique d'un film SiGe dont le paramètre de maille dans le plan est exactement celui du Si. La contrainte expérimentale des films SGOI suit la courbe théorique jusqu'à une concentration en Ge au moins égale à 45%. Le cas du film SGOI à 57% de concentration en Ge est délicat car sa contrainte est très légèrement inférieure à la contrainte théorique. La contrainte continue néanmoins d'augmenter jusqu'à un maximum de 2.1% à 63% de concentration en Ge, puis diminue au-delà de cette concentration.

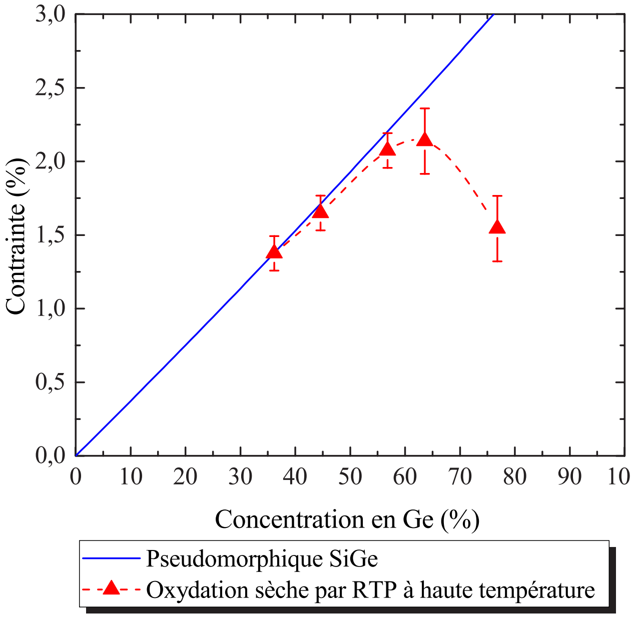

Figure III.3: Evolution de la contrainte des films SGOI fabriqués par un procédé de condensation reposant sur l'oxydation sèche par RTP à haute température.

III.1.3. Comparaison avec la littérature

La forme en « cloche » de cette évolution de la contrainte des films SGOI est très semblable à celle publiée par Takagi et al. pour le cas de films SGOI fabriqués par un procédé de condensation reposant sur l'oxydation sèche en four à haute température [Takagi10] (voir *Figure III.4*). Le type de procédé, four ou RTP, ne semble pas avoir d'effet sur l'évolution de la contrainte des films SGOI. Alors que la comparaison entre ces deux jeux de données pourrait laisser supposer que l'évolution de la contrainte est dépendante uniquement de la concentration en Ge, un troisième jeu de données, publié par Takagi et al. et portant sur la contrainte de films SGOI fabriqués sur substrats sSOI (substrats dont le SOI est contraint en tension) montre qu'il n'en est rien. En effet, la forme en « cloche » de l'évolution de la contrainte de ces films semble simplement décalée vers de plus fortes concentrations en Ge. Au vu de la comparaison de ces trois jeux de données, le paramètre semblant déterminer l'évolution de la contrainte, et en particulier l'existence d'une contrainte maximale, est la valeur de la contrainte elle-même, avec un maximum entre 2.2% et 2.5%.

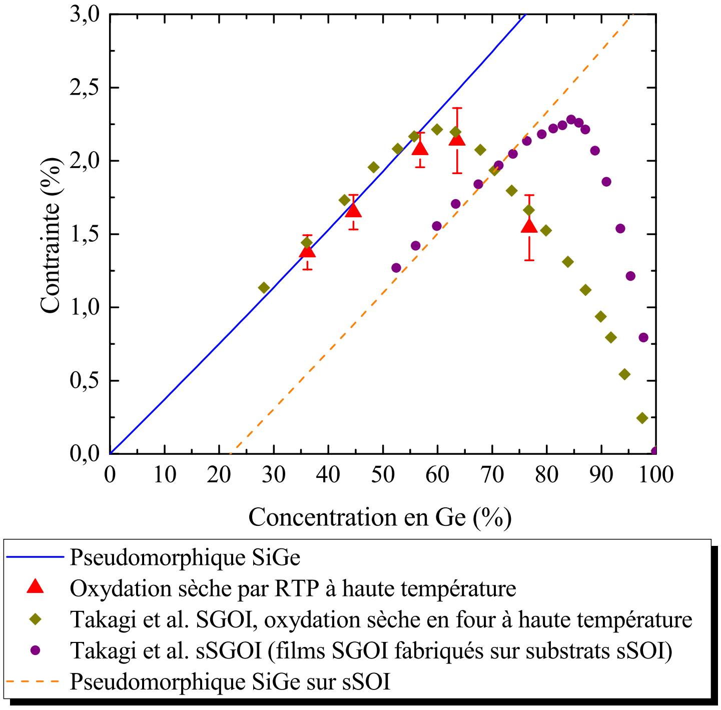

Figure III.4: Evolution de la contrainte des films SGOI fabriqués par un procédé de condensation reposant sur l'oxydation sèche par RTP à haute température (déjà présentées en Figure III.3), ainsi que les données publiées par Takagi et al. sur les contraintes de films SGOI fabriqués sur substrats SOI et sSOI par un procédé de condensation reposant sur une oxydation sèche en four à haute température [Takagi10].

Cependant, il est à noter que les épaisseurs des films SGOI fabriqués par Takagi et al. sont très différentes de celles des films SGOI de cette étude. Or, on pourrait logiquement s'attendre à une forte influence de l'épaisseur, comme c'est le cas pour les films SiGe épitaxiés sur Si. Cette observation suggère des mécanismes de relâchement de la contrainte propres aux films SGOI.

III.1.4. Discussion autour des mécanismes de relâchement de la déformation

Certains des films SGOI de cette étude et de ceux fabriqués par Takagi et al. sont totalement contraints alors que les contraintes des films SiGe de même épaisseur et de même composition sont partiellement relâchées d'après les modèles de référence de Matthews et de People [Matthews74][People85]. Le relâchement plastique des contraintes des films SGOI n'obéit donc pas aux mécanismes de relâchement des contraintes des films SiGe sur Si.

Afin d'évaluer l'influence de la nature des interfaces des films SiGe (cristal-cristal dans le cas de films SiGe épitaxiés sur Si contre cristal-oxyde amorphe dans le cas de films SGOI), nous avons comparé les contraintes des échantillons fabriqués par condensation à haute température avec celles des films SGOI fabriqués par le procédé de condensation à basse température décrit en *partie III.1.1.*. Tandis que la condensation à haute température conduit rapidement à la formation d'un film SGOI relativement homogène en composition, la condensation à basse température permet la formation par oxydation d'une couche SiGe à 60% de concentration en Ge environ sur le cristal de $Si_{0.7}Ge_{0.3}$ puis sur celui de Si du SOI. La nature des interfaces lors de la condensation est donc radicalement différente entre les deux procédés.

Les contraintes des films fabriqués par condensation à basse température sont fortement relâchées et inférieures aux contraintes des films SGOI de composition identique mais fabriqués par condensation à haute température (voir *Figure III.5*). Les interfaces SiGe-Si semblent donc favoriser le relâchement plastique des contraintes par rapport aux interfaces SiGe-oxyde amorphe. Nous suggérons que ces interfaces SiGe-oxyde amorphe modifient l'équilibre entre énergie élastique et énergie plastique et/ou retarde la formation de dislocations, qui sont les défauts cristallins accompagnant le relâchement des contraintes comme nous le verrons en partie suivante, dans le film SGOI.

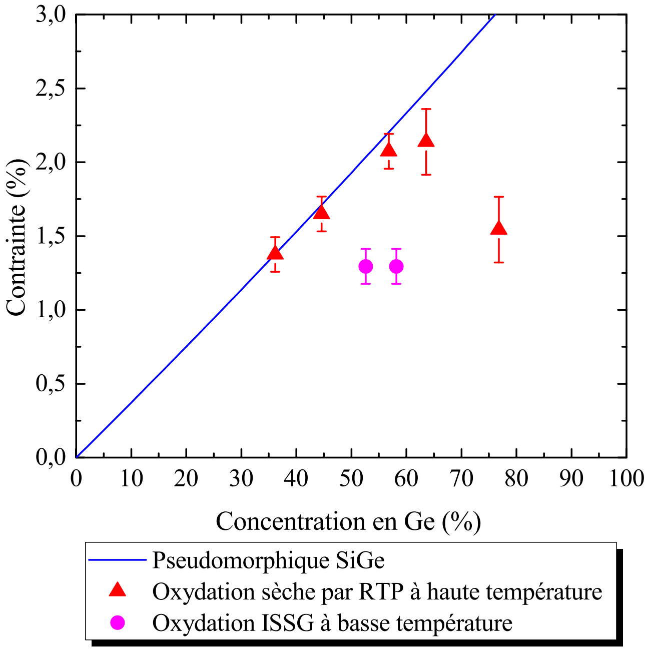

Figure III.5: Evolution de la contrainte des films SGOI fabriqués par condensation à haute température (par oxydation sèche par RTP) et à basse température (par oxydation ISSG).

III.1.5. Révélation de défauts cristallins

Les images de microscopie à force atomique (AFM : Atomic Force Microscopy), dont certaines sont représentées en *Figure III.6*, révèlent la présence de motifs particuliers en surface des films SGOI présentant des concentrations en Ge supérieures ou égales à 63% et fabriqués par condensation à haute température. Ces motifs sont constitués de lignes orientées dans les directions <110> et sont révélatrices de dislocations dans les plans {111} du cristal de SiGe [Gunji11]. Les films SGOI dont les contraintes sont relâchées avec certitude (dont les concentrations en Ge sont 63% et 77%) présentent donc des dislocations.

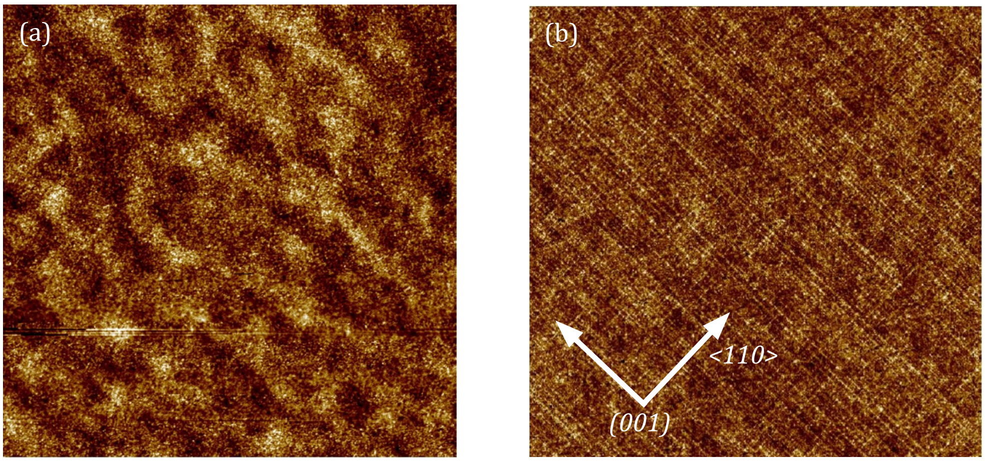

Figure III.6: Images 5×5 μm^2 par microscopie à force atomique (AFM) de la surface de films SGOI fabriqués par condensation à haute température et présentant des concentrations en Ge de (a) 57% et de (b) 63%.

En résumé, le relâchement des contraintes s'accompagne de la formation de dislocations dans les plans {111} du SiGe. Le cas du film SGOI à 57% de concentration en Ge est difficile à trancher du fait de la contradiction entre l'image AFM qui ne révèle pas de dislocations sur une surface d'échantillon de 5×5 μm^2, la GPA qui en révèle sur des lames minces pour TEM.

III.1.6. Conclusion de la partie III.1.

Nous avons montré que la contrainte des films SGOI fabriqués par condensation à haute température augmente avec la concentration en Ge jusqu'à une valeur maximale d'environ 2.1% à 60% de concentration en Ge, puis diminue au-delà de cette concentration. Le relâchement des contraintes est associé à la génération de dislocations dans les plans {111} du cristal de SiGe. Toutefois, les mécanismes du relâchement des contraintes demeurent indéterminés, même si nous avons montré que l'influence de la nature des interfaces du cristal SiGe, avec un oxyde amorphe dans le cas de films SGOI, semble être majeure, et que le paramètre déterminant est la contrainte en elle-même, avec un maximum entre 2.2% et 2.5%.

Après avoir identifié les paramètres permettant l'obtention de contraintes maximales dans les films SGOI continus et fabriqués par condensation, nous nous attelons dans la partie suivante à caractériser finement la qualité cristalline de ces films.

III.2. Mesure de la qualité cristalline des films SGOI

III.2.1. Introduction de la technique MEIS

La technique Medium Energy Ion Scattering (MEIS), ou rétrodiffusion d'ions de moyenne énergie, permet de déterminer le profil de composition en profondeur et certaines propriétés physiques, telle que la qualité cristalline, de couches minces [Jalabert17]. La technique repose sur la mesure du nombre d'ions rétrodiffusés par les atomes de l'échantillon, ainsi que de leur angle de rétrodiffusion et leur énergie. A angle fixé, la mesure MEIS se présente sous la forme de spectres en énergie tel que celui représenté en *Figure III.7*, où la contribution de chaque élément de chaque couche est identifiée.

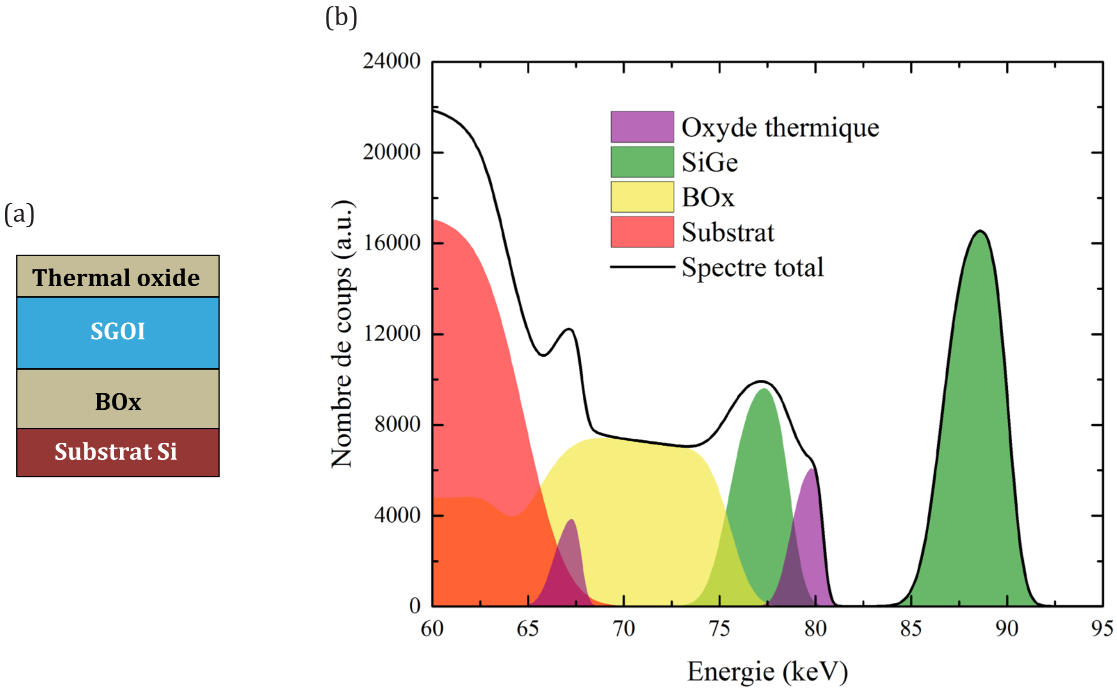

Figure III.7: (a) Représentation de l'empilement dont le spectre MEIS simulé est représenté en (b). La contribution de chaque couche est indiquée en (b).

Lorsque le faisceau d'ions parallèle est orienté dans une direction cristallographique particulière d'une couche cristalline de l'échantillon, ce dernier peut théoriquement traverser la totalité de la couche sans rétrodiffusion. C'est l'effet de canalisation, illustré en *Figure III.8*, qui du point de vue de la mesure diminue le nombre d'ions rétrodiffusés par les atomes du cristal. Le facteur de réduction du nombre d'ions rétrodiffusés par effet de canalisation est appelé χ_{min}. Ce facteur est le pourcentage d'atomes déplacés des sites du cristal, qui peuvent être des atomes en sites interstitiels ou situés au cœur de dislocations par exemple. Le χ_{min} est égal à 100% pour un matériau totalement amorphe et à 5% pour un cristal de Si d'excellente qualité. En résumé, ce facteur est un indicateur de la qualité cristalline.

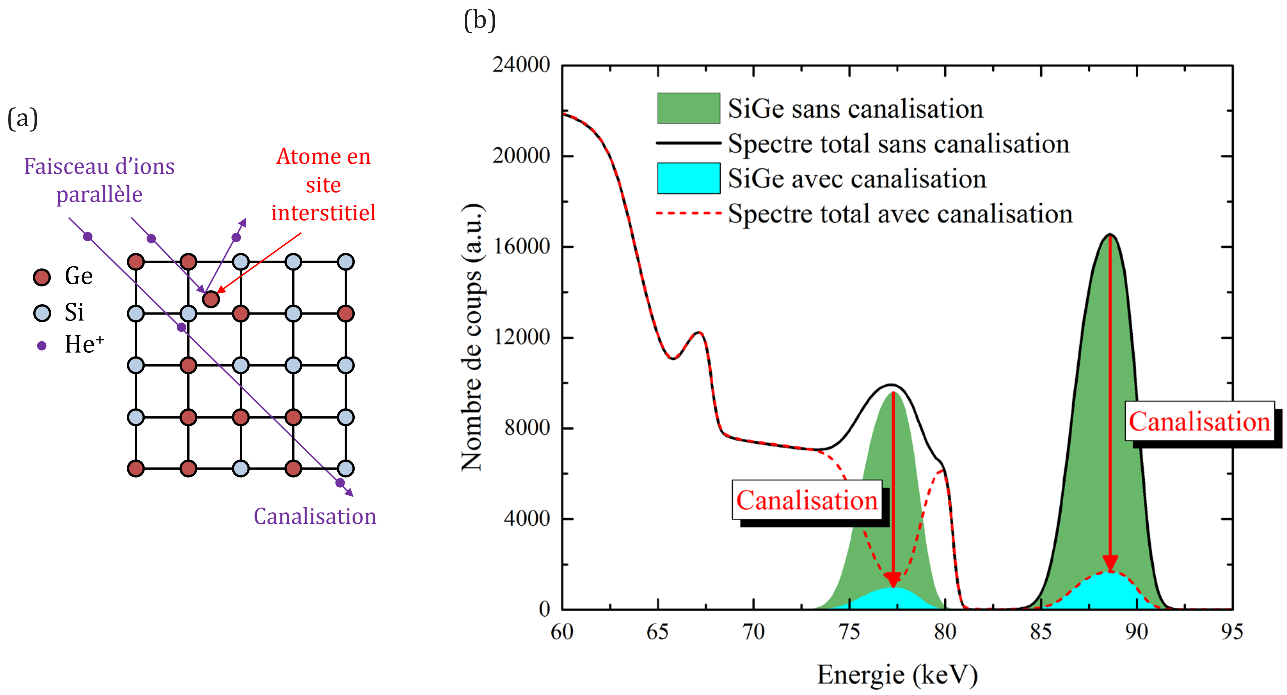

Figure III.8: (a) Représentation du principe de la canalisation dans un cristal de SiGe et (b) spectres MEIS simulés du même empilement qu'en Figure III.8, en conditions normales (non canalisées) et en conditions de canalisation.

III.2.2. Protocole expérimental

Les mesures de spectres MEIS ont été réalisées sur l'équipement du LETI avec un faisceau d'ions He^+ accéléré à 100 kV. Les spectres ont ensuite été analysés à l'aide d'un programme de simulation [Jalabert17]. Trois échantillons ont été mesurés :

- « Référence » : il s'agit d'un film SiGe épitaxié sur SOI, donc avant condensation.

- « Faible Ge » : le film SGOI, dont la composition est de l'ordre de 25% en concentration de Ge, a été réalisé par un procédé de condensation reposant sur une oxydation sèche par RTP à 1100°C.

- « Fort Ge » : d'une concentration moyenne en Ge de 57%, il s'agit du même film SGOI que celui discuté en *partie III.1.*. Ce film SGOI est celui présentant le maximum de contrainte sans révélation de dislocations par mesure AFM dela surface du film.

III.2.3. Spectres MEIS

Les spectres MEIS expérimentaux et ajustés pour chaque échantillon et chaque condition (conditions de canalisation ou non) sont représentés en *Figure III.9*. Nous observons pour chacun des échantillons une réduction plus ou moins prononcée du nombre d'ions rétrodiffusés aux énergies correspondant aux couches SOI, SiGe et SGOI (entre 85 keV et 90 keV et autour de 72.5 keV). Chacun des spectres expérimentaux a été ajusté à l'aide d'un programme dont les modèles des empilements sont définis par un nombre fini de couches homogènes en composition et en χ_{min}. Même si un nombre fini de couches ne peut pas reproduire exactement la réalité des profils en composition et en χ_{min}, l'ajustement aux spectres expérimentaux est jugé suffisamment bon avec un nombre fini de couches pour en extraire des tendances de variation de χ_{min} en profondeur. Ces tendances sont présentées et discutées en partie suivante.

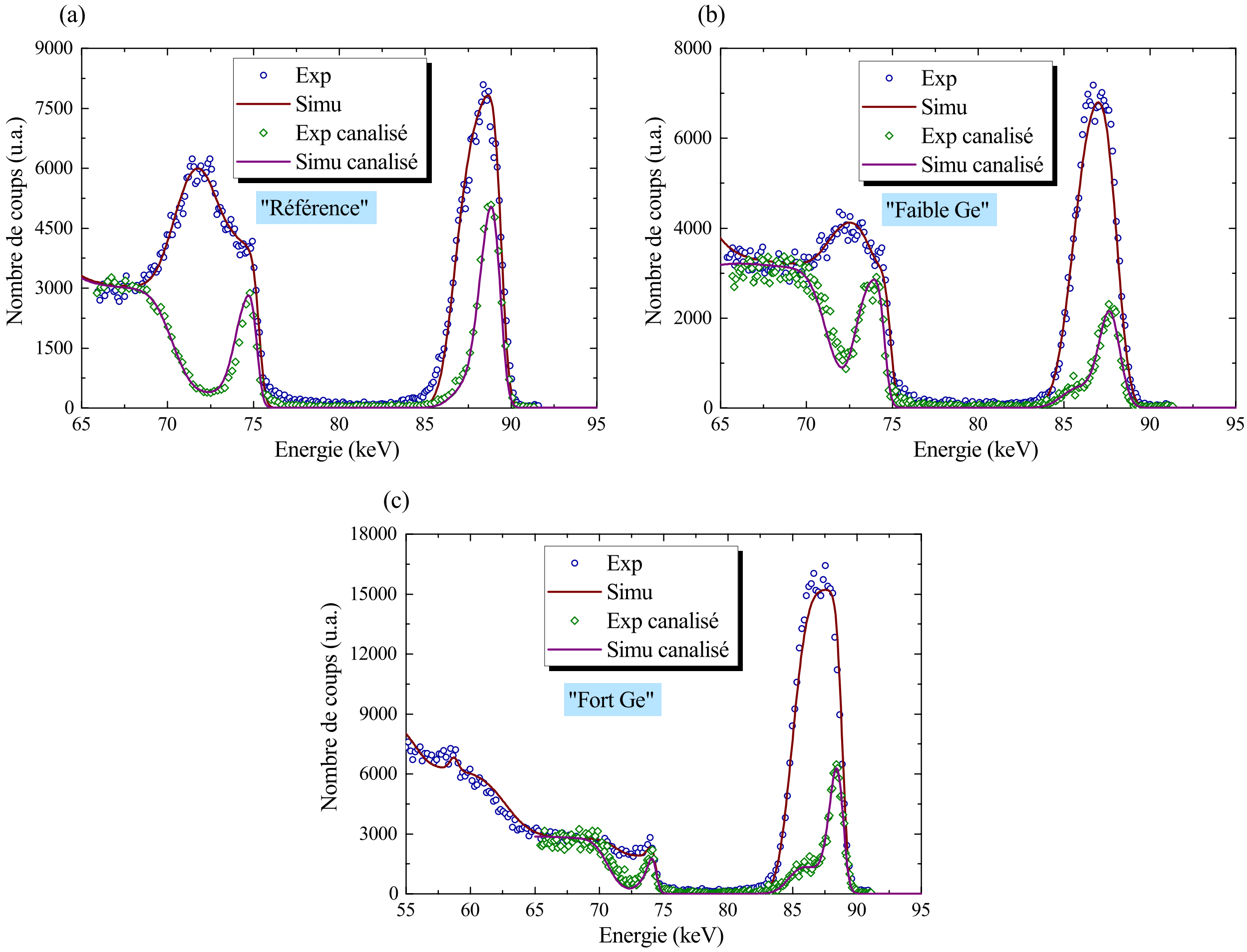

Figure III.9: Spectres expérimentaux (notés « Exp ») et spectres simulés (notés « Simu ») par ajustement aux spectres expérimentaux pour les échantillons (a) « Référence », (b) « Faible Ge » et (c) « Fort Ge ». Les spectres obtenus en conditions de canalisation sont aussi représentés et identifiés dans la légende

III.2.4. Qualité cristalline des films SGOI

Nous soulignons tout d'abord que la composition des films SiGe et SGOI est relativement homogène en profondeur (cette discussion, reposant sur l'analyse des spectres MEIS hors conditions de canalisation seulement, n'est pas détaillée ici). La *Figure III.10* résume l'évolution au cours de la condensation du profil en profondeur du nombre d'atomes déplacés des sites cristallins, représenté par le facteur χ_{min}, depuis l'état avant condensation (« Référence »), en passant par un film SGOI faiblement contraint du fait d'une faible concentration en Ge (« Faible Ge ») et jusqu'au film SGOI fortement contraint et à forte concentration en Ge (« Fort Ge »). Nous avons choisi de tracer les profils en profondeur du χ_{min} en prenant comme origine de l'axe des abscisses l'interface avec l'oxyde enterré et en allant vers la surface de l'échantillon pour les valeurs positives des x.

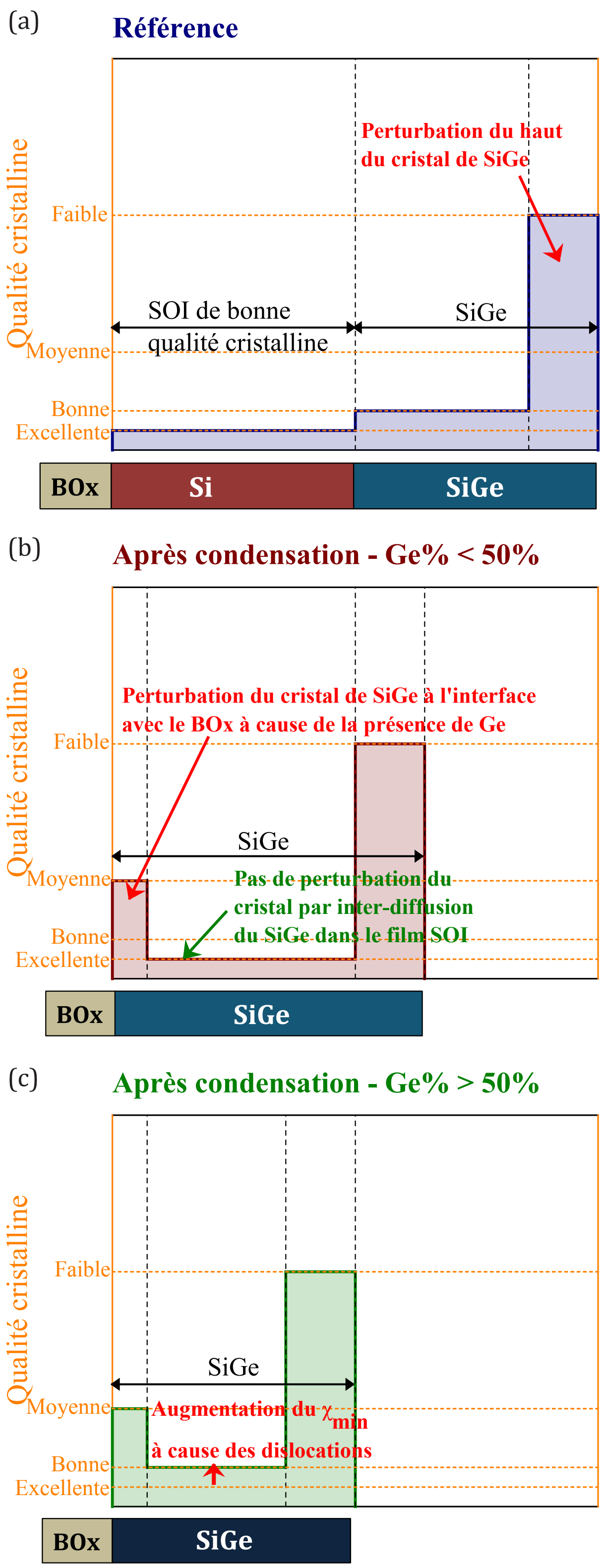
(a)
Référence
Qualité cristalline
Faible
Moyenne
Bonne
Excellente
Perturbation du haut du cristal de SiGe
SOI de bonne qualité cristalline
SiGe
BOx
Si
SiGe
(b)
Après condensation - Ge% < 50%
Qualité cristalline
Faible
Moyenne
Bonne
Excellente
Perturbation du cristal de SiGe à l'interface avec le BOx à cause de la présence de Ge
SiGe
Pas de perturbation du cristal par inter-diffusion du SiGe dans le film SOI
BOx
SiGe
(c)
Après condensation - Ge% > 50%
Qualité cristalline
Faible
Moyenne
Bonne
Excellente
SiGe
Augmentation du χmin à cause des dislocations
BOx
SiGe

- La qualité cristalline du SOI n'est pas altérée par le procédé d'épitaxie du film SiGe.
- Le cristal de SiGe est dégradé dans les 1 à 2 nm de profondeur du haut du film.

- L'oxydation thermique est susceptible de modifier l'arrangement atomique immédiatement sous l'oxyde en croissance et ainsi diminuer le χ_{min} sous ce dernier.
- La qualité cristalline du SOI n'est pas dégradée par la diffusion de Ge pour de faibles valeurs de concentration en Ge.
- La présence de Ge, même à faible concentration, semble provoquer une dégradation de la qualité cristalline du film SGOI à l'interface avec l'oxyde enterré (BOx) sur environ 1 nm.

- Lorsque la concentration en Ge augmente vers de fortes valeurs (50% et plus), la qualité cristalline du film SGOI commence à diminuer, et ce loin des interfaces avec les oxydes thermique et enterré.

Figure III.10: Illustration de l'évolution du nombre d'atomes déplacés des sites atomiques du cristal. (a) correspond à un film SiGe épitaxié sur SOI (« Référence »), (b) à un film SGOI de faible concentration en Ge (« Faible Ge ») et (c) à un film de forte concentration en Ge (« Fort Ge »). Les changements majeurs de la qualité cristalline, représentée par le facteur χ_{min}*, au cours de la condensation sont indiqués point par point à droite de chaque sous-figure. L'axe des abscisses correspond à la profondeur dans le film en partant de l'interface avec l'oxyde enterré (BOx) et en allant vers la surface. L'oxyde thermique n'est pas représenté sur les schémas des empilements sous chaque sous-figure.*

Conclusion du Chapitre III

Afin de bénéficier d'un gain maximal sur la mobilité des trous dans le canal des transistors de type p, les films SGOI fabriqués par condensation doivent présenter des contraintes importantes et une excellente qualité cristalline.

Nous avons discuté de l'évolution des contraintes en fonction des paramètres du procédé de condensation, et sommes parvenus à identifier le procédé parmi ceux étudiés conduisant à une contrainte maximale d'environ 2.1% à 60% de concentration en Ge. Il s'agit de l'oxydation sèche par RTP dont la température est aussi haute que possible sans faire entrer le SiGe en fusion.

Deux aspects clés du procédé de condensation et des films SGOI ont été soulignés grâce à la caractérisation de la qualité cristalline de ces films :

- Les zones dégradées du cristal, et qui méritent donc de recevoir une attention particulière lors de l'optimisation du procédé de condensation, sont les interfaces avec les oxydes thermique et enterré.

- L'excellente qualité cristalline du SOI est maintenue lors de la condensation jusqu'à des concentrations en Ge de l'ordre de 50%, et ce malgré la diffusion de Ge dans le film.

Conclusion

L'intégration de films SiGe contraints en compression sur isolant (SGOI) dans le canal du transistor de type p apparait comme l'une des alternatives aux transistors traditionnels les plus pertinentes. L'utilisation dans un milieu industriel de la technique de condensation, qui permet de fabriquer de tels films, nous astreint à maîtriser à la fois la cinétique de l'oxydation thermique du SiGe et la contrainte et la qualité cristalline du film SGOI ainsi formé.

Dans le *Chapitre II*, nous nous sommes penchés sur le premier de ces défis. Nous avons identifié les mécanismes d'oxydation du SiGe pour trois procédés d'oxydation appropriés à la condensation. Nous avons ainsi relié la cinétique d'oxydation avec la diffusion de l'espèce oxydante à travers l'oxyde en croissance et avons corrélé cette diffusion à la densité de l'oxyde. L'application de ces résultats fondamentaux à la condensation est double :

- Nous pouvons estimer graphiquement la cinétique d'oxydation du SiGe à l'aide d'abaques, dont la construction n'est pas détaillée dans ce résumé, et ce pour trois procédés d'oxydation et de larges gammes de concentrations en Ge et de températures.

- Un programme de simulation par éléments finis, basé sur celui développé par Morin [Morin15], permettrait de poursuivre l'étude de la dynamique de l'oxydation du SiGe et de prédire avec précision les épaisseurs et compositions des films SGOI fabriqués par condensation.

Le *Chapitre III* a porté quant à lui sur l'évolution de la contrainte et de la qualité cristalline des films SGOI. Les paramètres de condensation permettant d'atteindre les plus fortes contraintes, supérieures à 2% relativement au SiGe relâché, ont été discutés. La qualité cristalline des films SGOI a pu être finement caractérisée, et les zones du cristal dégradées et les causes de dégradation, partiellement identifiées. Cette étude soulève une autre question : comment la contrainte et la qualité cristalline des films SGOI changent pendant la suite de la fabrication des transistors, et quel est le procédé de condensation adéquat au regard de toute la chaîne de fabrication ? Cette problématique a fait l'objet de deux études, l'une portant sur la nature des liaisons chimiques entre le film SGOI et l'oxyde enterré, et l'autre sur l'incorporation involontaire d'hydrogène au cours de la fabrication des films SGOI.

Les réponses aux problématiques précédemment définies ont aussi soulevé de nouvelles questions :

- Nous avons montré dans le *Chapitre II* que plus la concentration en Ge à l'interface et la température d'oxydation sont élevées, moins l'oxyde est dense. Les mécanismes qui en sont à l'origine n'ont toutefois pas été identifiés, malgré deux suggestions, à savoir que le plus grand paramètre de maille du SiGe et le fluage de l'oxyde à haute température tendrait à réduire la densité de l'oxyde.

- S'il a été mis en exergue, le rôle que joue la nature des interfaces du cristal de SiGe avec les autres couches dans les mécanismes de relâchement des films SGOI n'a pas été déterminé et mérite donc une attention particulière.

Références

[Bongiorno04] Bongiorno, A., et al. « Multiscale modeling of oxygen diffusion through the oxide during silicon oxidation. » *Physical Review B* 70.19 (2004): 195312.

[Cui09] Cui, H., et al. « Size-dependent oxidation behavior for the anomalous initial thermal oxidation process of Si. » *Applied Physics Letters* 94.8 (2009): 083108.

[Deal65] Deal, B. E., et al. « General relationship for the thermal oxidation of silicon. » *Journal of Applied Physics* 36.12 (1965): 3770-3778.

[EerNisse77] EerNisse, E. P. « Viscous flow of thermal SiO_2. » *Applied Physics Letters* 30.6 (1977): 290-293.

[Gunji11] Gunji, M., et al. « Strain relaxation mechanisms in compressively strained thin SiGe-on-insulator films grown by selective Si oxidation. » *Journal of Applied Physics* 109.1 (2011): 014324.

[Holland87] Holland, O. W., et al. « Novel oxidation process in Ge^+-implanted Si and its effect on oxidation kinetics. » *Applied Physics Letters* 51.7 (1987): 520-522.

[Jalabert17] Jalabert, D., et al. « Swift Ion Beam Analysis in Nanosciences » *John Wiley & Sons*, 2017.

[Kee00] Kee, R. J., et al. « The influence of pressure, fluid flow, and chemistry on the combustion-based oxidation of silicon. » *Proceedings of the Combustion Institute* 28.1 (2000): 1381-1388.

[Kube10] Kube, R., et al. « Composition dependence of Si and Ge diffusion in relaxed $Si_{1-x}Ge_x$ alloys. » *Journal of Applied Physics* 107.7 (2010): 073520.

[Matthews74] Matthews, J. W., et al. « Defects in epitaxial multilayers: I. Misfit dislocations. » *Journal of Crystal Growth* 27 (1974): 118-125.

[Mehrer07] Mehrer, H. « Diffusion in Solids: Fundamentals, Methods, Materials, Diffusion-Controlled Processes » *Springer* (2007): 547-552.

[Morin15] Morin, P. F., et al. « Mechanical analyses of extended and localized UTBB stressors formed with Ge enrichment techniques. » *ECS Transactions* 66.4 (2015): 57-65.

[People85] People, R., et al. « Erratum: Calculation of critical layer thickness versus lattice mismatch for Ge_xSi_{1-x}/Si strained-layer heterostructures [Appl. Phys. Lett. 47, 322 (1985)]. » *Applied Physics Letters* 49.4 (1986): 229-229.

[Pillarisetty11] Pillarisetty, R. « Academic and industry research progress in germanium nanodevices. » *Nature* 479.7373 (2011): 324-328.

[Takagi10] Takagi, S., et al. « Critical Factors for Enhancement of Compressive Strain in SGOI Layers Fabricated by Ge Condensation Technique. » *ECS Transactions* 33.6 (2010): 501-509.

[Tezuka01] Tezuka, T., et al. « A novel fabrication technique of ultrathin and relaxed SiGe buffer layers with high Ge fraction for sub-100 nm strained silicon-on-insulator MOSFETs. » *Japanese Journal of Applied Physics* 40.4S (2001): 2866.

Bibliography of the author

Publications in Regular Journals

- **Rozé, F.**, Gourhant, O., Blanquet, E., Bertin, F., Juhel, M., Abbate, F., Pribat, C. & Duru, R. (2017). Oxidation kinetics of Si and SiGe by dry rapid thermal oxidation, in-situ steam generation oxidation and dry furnace oxidation. *Journal of Applied Physics*, 121(24), 245308.

- Fauquier, L., Pelissier, B., Jalabert, D., Pierre, F., Hartmann, J. M., **Rozé, F.**, Doloy, D., Le Cunff, D., Betia, C. & Baron, T. (2016). Benefits of XPS nanocharacterization for process development and industrial control of thin SiGe channel layers in advanced CMOS technologies. *Materials Science in Semiconductor Processing*.

Publications in Conference Proceedings

- **Rozé, F.**, Gourhant, O., Blanquet, E., Bertin, F., Juhel, M., Abbate, F., Pribat, C. & Duru, R. (2016). Comparative Analysis of Growth Rate Enhancement and Ge Redistribution during Silicon-Germanium Oxidation by Rapid Thermal Oxidation. *ECS Transactions*, 75(8), 67-78.

- **Rozé, F.**, Gergaud, P., Jaouen, N., Gourhant, O., Blanquet, E., Bertin, F., Juhel, M., Abbate, F., Pribat, C. & Campidelli, Y. (2017). SiGe Oxidation Kinetics and Oxide Density Measured by Resonant Soft X-Ray Reflectivity. *12th IEEE Nanotechnology Materials and Devices Conference (NMDC)*.

- Berthelon, R., Andrieu, F., Perreau, P., Cooper, D., **Roze, F.**, Gourhant, O., Rivallin, P., Bernier, N., Cros, A., Ndiaye, C., Baylac, E., Souchier, E., Dutartre, D., Claverie, A., Weber, O., Josse, E., Vinet, M., Haond, M. & Baylac, E. (2016, December). A novel dual isolation scheme for stress and back-bias maximum efficiency in FDSOI Technology. In Electron Devices Meeting (IEDM), 2016 IEEE International (pp. 17-7). IEEE.

Talks in International Conferences

- **Rozé, F.**, Gourhant, O., Blanquet, E., Bertin, F., Juhel, M., Abbate, F., Pribat, C. & Duru, R. (2016). Comparative Analysis of Growth Rate Enhancement and Ge Redistribution during Silicon-Germanium Oxidation by Rapid Thermal Oxidation. *ECS Prime Meeting*, 2016, Honolulu, Hawaii, USA.

- **Rozé, F.**, Gourhant, O., Bertin, F., Blanquet, E., Pierre, F., Rouchon, D., Guyader, V., Fauquier, L., Pribat, C. & Campidelli, Y. (2017). Strain and Crystal Quality of High Ge Content SiGe-On-Insulator Films Fabricated by the Condensation Technique. *European Congress and Exhibition on Advanced Materials and Processes (Euromat)*, 2017, Thessaloniki, Greece.

- **Rozé, F.**, Gergaud, P., Jaouen, N., Gourhant, O., Blanquet, E., Bertin, F., Juhel, M., Abbate, F., Pribat, C. & Campidelli, Y. (2017). SiGe Oxidation Kinetics and Oxide Density Measured by Resonant Soft X-Ray Reflectivity. *12th IEEE Nanotechnology Materials and Devices Conference (NMDC)*, 2017, Singapore.

TITLE: Study of Thermal Oxidation of SiGe for Advanced CMOS FD-SOI Technologies

ABSTRACT

The tremendous spread of electronic devices and networks into our day-to-day life has been enabled by the constant downscaling of transistors since the 60's. However, downsizing transistors has become increasingly difficult in the past few years and going to the nanometer scale brings new detrimental effects that have put power consumption and performances on quasi-plateaux for a few years. To overcome these limitations, high mobility channels based on new materials and new transistor architectures are being introduced. Ultrathin compressively strained SiGe-On-Insulator (SGOI) films benefit from the advantages of both the higher hole mobility of compressively strained SiGe as well as of the better electrostatic control of On-Insulator structures. The condensation technique is a CMOS-compatible technique that allows fabrication of such films with possibly high Ge content and high strain levels. The technique is based on Si-selective thermal oxidation of SiGe and concurrent SiGe diffusion between the thermal oxide and the buried oxide layer that acts as a diffusion barrier.

Two main challenges still need to be taken up for an efficient and optimized use of the condensation technique in an industrial environment: oxidation mechanisms and kinetics must be well controlled, and strain and crystal quality of the SGOI film must be as high as possible.

Firstly, this work bridges the gap between previous studies by covering various oxidation processes relevant to today's technological needs with a new and quantitative analysis methodology of oxidation kinetics. A correlation is established between the diffusivity of the oxidizing species that governs oxidation kinetics, the Ge concentration at the oxidation interface, and the oxide density measured by X-Ray Reflectivity on a synchrotron beamline.

Secondly, SGOI films with Ge concentrations up to 80% were fabricated by the condensation technique. The evolution of strain of SGOI films is discussed as a function of process parameters and strain energy levels. How the condensation technique alters the crystal quality, both at interfaces with oxides and in the bulk of the SiGe crystal, is evaluated by the Medium Energy Ion Scattering (MEIS) technique by using the channeling effect.

KEY WORDS

CMOS, high mobility channels, SiGe, SiGe-On-Insulator (SGOI), strain, condensation, thermal oxidation, SiO_2

TITRE: Etude de l'oxydation thermique du SiGe pour application aux technologies CMOS FD-SOI avancées

RESUME

La réduction continue des dimensions des transistors depuis les années 60 est à l'origine de l'explosion des usages de l'électronique. Toutefois, la réduction des dimensions à l'échelle nanométrique s'accompagne de nouvelles difficultés qui tendent à limiter les gains des transistors en termes de performances et de consommation. Afin de surmonter ces obstacles et maintenir cette dynamique, des canaux à base de nouveaux matériaux à forte mobilité et de nouvelles architectures de transistors sont désormais utilisées ou à l'étude. L'intérêt de films SiGe contraint en compression sur isolant (SGOI: SiGe-On-Insulator) ultra-minces est double : ils bénéficient de la forte mobilité des trous du SiGe contraint en compression ainsi que du meilleur contrôle électrostatique des structures dites « sur isolant ». Des films SGOI présentant une forte concentration en Ge et une importante contrainte peuvent être fabriqués par une technique industrielle appelée condensation. Cette technique repose sur deux processus simultanés : l'oxydation thermique et sélective du SiGe (seul le Si est oxydé) et l'inter-diffusion du SiGe entre l'oxyde thermique et l'oxyde enterré qui se comporte comme une barrière à la diffusion.

L'utilisation de cette technique dans un environnement industriel nécessite de relever deux défis : maîtriser les mécanismes et la cinétique d'oxydation, et atteindre les plus fortes contraintes et qualités cristallines pour les films SGOI.

La cinétique de plusieurs procédés d'oxydation industriels et pertinents au regard des besoins technologiques actuels est étudiée à l'aide d'une nouvelle méthodologie d'analyse quantitative. Nous établissons une corrélation entre le coefficient de diffusion de l'espèce oxydante, qui détermine la cinétique d'oxydation, la concentration en Ge à l'interface d'oxydation, et la densité de l'oxyde mesurée par réflectivité de rayons X sur une ligne de synchrotron.

Puis, nous avons fabriqué des films SGOI présentant des concentrations en Ge jusqu'à 80%. Nous discutons l'évolution de la contrainte de ces films en fonction des paramètres du procédé et des niveaux de contrainte. Enfin, nous mettons en évidence les effets du procédé de condensation sur la qualité cristalline du film SiGe aux interfaces avec les oxydes grâce à l'effet de canalisation d'une technique de rétrodiffusion d'ions à moyenne énergie (MEIS : Medium Energy Ion Scattering)

MOTS CLES

CMOS, canal à haute mobilité, SiGe, SiGe-On-Insulator (SGOI), contrainte, condensation, oxydation thermique, SiO_2